UNIVERSITY OF CALIFORNIA SAN DIEGO

Multifunctional Electrochemistry and Molecular Designs for Energy Storage and Conversion

A dissertation submitted in partial satisfaction of the requirements
for the degree Doctor of Philosophy

in

Nanoengineering

by

Hongyao Zhou

Committee in charge:

Professor Ping Liu, Chair
Professor Renkun Chen
Professor Zheng Chen
Professor Darren Lipomi
Professor Valerie Schmidt

2020

The Dissertation of Hongyao Zhou is approved, and it is acceptable in quality and form for publication on microfilm and electronically:

_____

_____

_____

_____

_____

Chair

University of California San Diego

2020

TABLE OF CONTENTS

LIST OF ABBREVIATIONS

(Abbreviation)	(Full name)
AC	alternate current
AFM	AFM
Al_2O_3	aluminum oxide
ALD	atomic layer deposition
AlF_3	aluminum trifluoride
ATR	attenuated total reflectance
C_2Cl_4	perchloroethylene
CE	coulombic efficiency
CNT	carbon nanotube
cryo	cryogenic-temperature
Cu||Li	two-electrode cell with copper as working and lithium metal as reference and counter electrodes
DCM	dichloromethane
DEC	diethyl carbonate
DMC	dimethyl carbonate
DMC	dimethyl carbonate
DME	dimethoxyethane
DME	dimethyl ether
DMF	N,N'-dimethyl formamide
DOL	1,3-dioxolane
EC	ethylene carbonate
ED	electron diffraction
EDX	energy dispersive X-ray
EELS	electron energy-loss spectroscopy
EIS	electrochemical impedance spectroscopy
EMC	ethyl methyl carbonate
FEC	fluoroethylene carbonate
FTIR	Fourier transform infrared spectroscopy
GF	fluorinated graphene
GO	graphene oxide
HF	hydrogen fluoride
LFP	lithium iron phosphate ($LiFePO_4$)
Li	lithium
Li||Li	two-electrode cell with lithium metal at both sides
Li_2CO_3	lithium carbonate
Li_2O	lithium oxide
Li_2S	lithium disulfide

Li_2S_6	dilithium hexasulfide
Li_3P	lithium phosphide
Li_3PO_4	lithium phosphate
Li_3PS_4	lithium phosphorous sulfide
LiBOB	lithium bis(oxalato)borate
LiCl	lithium chloride
$LiClO_4$	lithium perchlorate
LiF	Lithium fluoride
LiI	lithium iodide
Li-Nafion	lithiated Nafion
$LiNO_3$	lithium nitrate
LiOH	lithium hydroxide
$LiPF_6$	lithium hexafluorophosphate
LiPON	Lithium phosphorous oxynitride
LiTFSI	lithium bis(trifluoromethanesulfonyl)imide
LLCZN	$Li_7La_{2.75}Ca_{0.25}Zr_{1.75}Nb_{0.25}O_{12}$
LLZO	$Li_7La_3Zr_2O_{12}$
LMC	lithium methyl carbonate
LP30	commercial electrolyte composed of EC:DMC = 1:1 + 1 M $LiPF_6$
MLD	molecular layer deposition
MoS_2	molybdenum disulfide
MPS	3-mercaptopropyl trimethoxysilane
NCA	$LiNi_{0.8}Co_{0.15}Al_{0.05}O_2$
NCM 523	$LiNi_{0.5}Co_{0.2}Mn_{0.3}O_2$
NM	nitromethane
NMC	lithium nickel manganese oxide ($LiNi_{1-x-y}Mn_xCo_yO_2$)
NMC 111	$LiNi_{1/3}Co_{1/3}Mn_{1/3}O_2$
NMC811	$LiNi_{0.8}Mn_{0.1}Co_{0.1}O_2$
NMP	N-methyl-2-pyrrolidone
P_2S_5	diphosphorous pentasulfide
PAN	polyacrylonitrile
PC	propylene carbonate
PCl_3	phosphorous trichloride
PDMS	polydimethyl siloxane
PEDOT	poly(3,4-ethylenedioxythiophene)
PEGDA	polyethylene glycol diacrylate
PEO	poly(ethylene oxide)
PFT	peak force tapping
poly(Imide-DOL)	poly((*N*-2,2-dimethyl-1,3-dioxolane-4-methyl)-5-norbornene-*exo*-2,3-dicarboximide)

poly(SF-DOL)	poly(vinyl sulfonyl fluoride-*ran*-2-vinyl-1,3-dioxolane)
PTFE	tetrafluoroethylene
PTMEG	poly(tetrametylene ether glycol
PVDF	polyvinylidene fluoride
PVDF-HFP	polyvinylidene fluoride-*co*-hexafluoropropylene
QCM	quartz crystal microbalance
Q_p	capacity obtained after complete plating of Li metal on Cu electrode
Q_s	capacity obtained after complete stripping of Li metal from Cu electrode
RPC	reactive polymer coating
sat.	saturated
SEI	solid electrolyte interface
SEM	scanning electron microscopy
SF	sulfonyl fluoride, $-SO_2F$ group
$SnCl_4$	tin tetrachloride
STEM	scanning transmission microscopy
t-BuOLi	lithium *tert*-buthoxide
TEM	transmission electron microscopy
TEOS	tetraethoxysilane
THF	tetrahydrofurane
t_{Li+}	transference number of Li^+
VC	vinylene carbonate
XPS	X-ray photoelectronic spectroscopy
XRD	X-ray diffraction
ZnO	zinc oxide

LIST OF FIGURES

LIST OF TABLES

ACKNOWLEDGEMENTS

Here I would like to express my sincere appreciation to Prof. Ping Liu for the guidance and mentoring through my entire PhD study, and to Prof. Darren Lipomi, Prof. Renkun Chen, Prof. Valerie Schmidt and Prof. Zheng Chen for their valuable comments to the work. The work is completed with the help and advice from the group members: Dr. Haodong Liu, Dr. Xiujun Yue, Dr. Yejing Li, Xing Xing, Zhaohui Wu, Matthew Gonzalez, Victoria Petrova, John Holoubek, and Sicen Yu. The work is greatly supported by the interdisciplinary collaborations with Prof. Ying Shirley Meng, Prof. Jonathan Pokorski, Prof. Eric Fullerton, Prof. Shengqian Cai, Prof. David Fenning, Dr. Gabriel Veith (Oakridge National Lab), Dr. Xuefeng Wang, Dr. Derek Church, Haowen Ren, Zijun Wang and Taewoo Kim.

Chapter 1, in full, is a reprint of materials published in the following paper: Hongyao Zhou, Sicen Yu, Haodong Liu* and Ping Liu*, "Protective coatings for lithium metal anodes: recent progress and future perspectives" *J. Power Sources*, **2020**, 450, 227632. The dissertation author was the primary researcher for the data presented and was the primary author of this publication. The permissions to reproduce this material were granted by Elsevier, copyright 2020.

Chapter 2 contains materials that is currently being prepared for submission for publication. The dissertation author is the primary researcher for the data presented and is the primary author of the manuscript. The work is supervised by Prof. Ping Liu and supported by Dr. Gabriel Veith, Dr. Haodong Liu, Xing, Sicen Yu and Zijun Wang.

Chapter 3, in full, is a reprint of materials published in the following paper: Hongyao Zhou, Haodong Liu, Yejing Li, Xiujun Yue, Xuefeng Wang, Matthew Gonzalez, Ying Shirley Meng and Ping Liu*, "*In situ* formed

polymer gel electrolyte for lithium batteries with inherent thermal shutdown safety features" *J. Mater. Chem. A*, **2019**, 7, 16984. The dissertation author was the primary researcher for the data presented and was the primary author of this publication. The permissions to reproduce this material were granted by Royal Society of Chemistry, copyright 2019.

Chapter 4, in full, is a reprint of materials published in the following paper: Hongyao Zhou and Ping Liu*, "High Seebeck Coefficient Electrochemical Thermocells for Efficient Waste Heat Recovery" *ACS Appl. Energy Mater.* **2018**, 1, 1424. The dissertation author was the primary researcher for the data presented and was the primary author of this publication. The permissions to reproduce this material were granted by American Chemical Society, copyright 2018.

VITA

2016 Bachelor of Engineering, Materials Science and Engineering, Kyushu University, Fukuoka, Japan

2018 Master of Science, Nanoengineering, University of California San Diego, La Jolla, California

2020 Doctor of Philosophy, Nanoengineering, University of California San Diego, La Jolla, California

PUBLICATIONS

1. **Zhou, H.**; Yamada, T.; Kimizuka, N. Supramolecular Thermo-Electrochemical Cells: Enhanced Thermoelectric Performance by Host–Guest Complexation and Salt-Induced Crystallization. *J. Am. Chem. Soc.* **2016**, *138*, 10502–10507. https://doi.org/10.1021/jacs.6b04923.
2. Liu, H.; **Zhou, H.**; Lee, B. S.; Xing, X.; Gonzalez, M.; Liu, P. Suppressing Lithium Dendrite Growth with a Single-Component Coating. *ACS Appl. Mater. Interfaces* **2017**, *9* (36), 30635–30642. https://doi.org/10.1021/acsami.7b08198.
3. Liu, H.; Wang, X.; **Zhou, H.**; Lim, H.-D.; Xing, X.; Yan, Q.; Meng, Y. S.; Liu, P. Structure and Solution Dynamics of Lithium Methyl Carbonate as a Protective Layer for Lithium Metal. *ACS Appl. Energy Mater.* **2018**, *1* (5), 1864–1869. https://doi.org/10.1021/acsaem.8b00348.
4. **Zhou, H.**; Liu, P. High Seebeck Coefficient Electrochemical Thermocells for Efficient Waste Heat Recovery. *ACS Appl. Energy Mater.* **2018**, *1428* (2). https://doi.org/10.1021/acsaem.8b00247.
5. **Zhou, H.**; Yamada, T.; Kimizuka, N. Thermo-Electrochemical Cells Empowered by Selective Inclusion of Redox-Active Ions by Polysaccharides. *Sustain. Energy Fuels* **2018**, *2*, 472–478. https://doi.org/10.1039/C7SE00470B.
6. Coaty, C.; **Zhou, H.**; Liu, H.; Liu, P. A Scalable Synthesis Pathway to Nanoporous Metal Structures. *ACS Nano* **2018**, *12*, 432–440. https://doi.org/10.1021/acsnano.7b06667.
7. Liang, Y.; **Zhou, H.**; Yamada, T.; Kimizuka, N. A Theoretical Basis for the Enhancement of Seebeck Coefficients in Supramolecular Thermocells. *Bull. Chem. Soc. Jpn.* **2019**, *92*, 1142–1147. https://doi.org/10.1246/bcsj.20190062.
8. **Zhou, H.**; Liu, H.; Li, Y.; Yue, X.; Wang, X.; Gonzalez, M.; Meng, Y. S.; Liu, P. In Situ Formed Polymer Gel Electrolytes for Lithium Batteries with Inherent Thermal Shutdown Safety Features. *J. Mater. Chem. A* **2019**, *7*, 16984–16991. https://doi.org/10.1039/C9TA02341K.
9. Liang, Y.; Yamada, T.; **Zhou, H.**; Kimizuka, N. Hexakis(2,3,6-Tri-: O -Methyl)-α-Cyclodextrin-I5- Complex in Aqueous I-/I3- Thermocells and Enhancement in the Seebeck Coefficient. *Chem. Sci.* **2019**, *10* (3), 773–780. https://doi.org/10.1039/c8sc03821j.

10. Liu, H.; Yue, X.; Xing, X.; Yan, Q.; Huang, J.; Petrova, V.; **Zhou, H.**; Liu, P. A Scalable 3D Lithium Metal Anode. *Energy Storage Mater.* **2019**, *16*, 505–511. https://doi.org/10.1016/j.ensm.2018.09.021.
11. Gonzalez, M. S.; Yan, Q.; Holoubek, J.; Wu, Z.; **Zhou, H.**; Patterson, N.; Petrova, V.; Liu, H.; Liu, P. Draining Over Blocking: Nano-Composite Janus Separators for Mitigating Internal Shorting of Lithium Batteries. *Adv. Mater.* **2020**, 1906836. https://doi.org/10.1002/adma.201906836.
12. Li, Y.; Wang, X.; **Zhou, H.**; Xing, X.; Banerjee, A.; Holoubek, J.; Liu, H.; Meng, Y. S.; Liu, P. Thin Solid Electrolyte Layers Enabled by Nanoscopic Polymer Binding. *ACS Energy Lett.* **2020**, *5*, 955–961. https://doi.org/10.1021/acsenergylett.0c00040.
13. Yin, Y.; Arca, E.; Wang, L.; Yang, G.; Schnabel, M.; Cao, L.; Xiao, C.; **Zhou, H.**; Liu, P.; Nanda, J.; Teeter, G.; Eichhorn, B.; Xu, K.; Burrell, A.; Ban, C. Nonpassivated Silicon Anode Surface. *ACS Appl. Mater. Interfaces* **2020**, *12* (23), 26593–26600. https://doi.org/10.1021/acsami.0c03799.
14. **Zhou, H.**; Yu, S.; Liu, H.; Liu, P. Protective Coatings for Lithium Metal Anodes: Recent Progress and Future Perspectives. *J. Power Sources* **2020**, *450*, 227632. https://doi.org/10.1016/j.jpowsour.2019.227632.

FIELDS OF STUDY

Major Field: Engineering

Studies in Applied Chemistry
Professors Teppei Yamada and Nobuo Kimizuka

Studies in Applied Electrochemistry
Professor Ping Liu

ABSTRACT OF THE DISSERTATION

Multifunctional Electrochemistry and Molecular Designs for Energy Storage and Conversion

by

Hongyao Zhou

Doctor of Philosophy in Nanoengineering

University of California San Diego, 2020

Professor Ping Liu, Chair

In realization of carbon neutral and sustainable society, it is an imperative duty to develop giant energy storage systems for solar/wind power plants and for electrified automotive vehicles. Rechargeable lithium (Li) metal battery, once abandoned three decades ago due to the safety issues, has been gaining increasing attention from the battery scientists again to surpass the energy density of the contemporary Li-ion cells. One approach to stabilize the interface between Li metal and organic liquid electrolytes is to passivate the Li surface by protective coatings, which can reduce permeation rate of the liquid electrolyte and improve the morphology of electroplated Li deposits. In Chapter 1, recent progress of the protective coatings is summarized, and the material properties are categorized according to the proposed protection mechanisms. Ion conduction through the inorganic coatings is determined by the intrinsic ion conductivity of the material itself and independent from the liquid electrolytes. In contrast, the ion

conductivity of polymer coatings is dependent on the swelling behavior in the liquid electrolytes. However, there is a dearth of understanding on factors controlling the swelling ratio of polymer coatings and the influence on ion-transport properties. To answer these questions, we carry out quantitative analysis on the effect of solvent polarity and cross-link density to the ion-transport and rheological properties of a polymer coating in Chapter 2. In Chapter 3, we develop a gel polymer electrolyte for Li metal battery, which can stabilize the surface of Li metal by in-situ formation of robust passivation layer. The electrolyte also possesses a safety feature which can shut-down the battery cycling under the condition of abusive thermal runaway. In addition to the energy storage systems, we also study an electrochemical method to recover energy from waste heat resources. In Chapter 4, we report the method of using vaporization of a volatile redox couple to achieve the highest conversion ratio of voltage (Seebeck coefficient) generated from the temperature gradient. This dissertation contributes to the development of high-density energy storage system and waste heat recovery by leveraging the multifunctional electrochemistry and through the molecular designs of electrolyte materials.

Chapter 1 Recent progress and future perspectives of protective coatings for lithium metal anodes

1.1 Introduction

Booming popularity of electric vehicles requires batteries to increase the energy density to more than 500 Wh kg^{-1}.[1] Conventional Lithium(Li)-ion battery has achieved excellent cycling performance through the intercalation chemistries, however, the low theoretical capacity of graphite anode limits the energy density of the battery. Li metal anode uses reversible electroplating and stripping of metallic Li to store energy.[2] The theoretical capacity of Li metal anode (3860 mAh g^{-1}) is ten times higher than the value of graphite (372 mAh g^{-1}). Therefore, Li metal is regarded as the anode for next-generation high energy density Li batteries. Li metal anode is widely studied for the application in both liquid-electrolyte-based and all-solid-state batteries. Advantages of liquid-electrolyte-based Li metal battery are the fast ion transport at the electrode-electrolyte interface, and the mature battery mass production process. Recently, liquid electrolyte based Li metal battery with an energy density of 300 Wh kg^{-1} and 86% capacity retention for 200 cycles is reported.[3] However, the cycling life still needs to be improved for practical applications.

Failure of Li metal battery often stems from the Li anode side: The Li metal foil, initially of a shiny metallic color, turns black after several cycles, because the Li metal forms a microporous and mossy structure (**Figure 1-1a**).[3,4] The surface of this mossy Li metal is covered with a passivation (solid electrolyte interface, SEI) layer, and isolation of these Li microparticle from the current collector (formation of “dead Li”) results in loss of anode capacity.[5] Furthermore, the porous Li metal with high surface area promotes the side reactions and quickly consumes the liquid electrolyte, which results in increased cell impedance.

Several strategies have been reported to improve the cycle life of Li metal anode, primarily based on the hypotheses of minimizing reactions between lithium metal and the electrolyte and maintaining electric contact between deposited lithium metal particles. These approaches include: 1) electrolytes with low chemical reactivity with Li metal, for example using highly concentrated salt or fluorinated solvent;[6–8] 2) additives to passivate the surface of Li metal and regulate the morphology;[9,10] 3) surface modifications of the polymer separator;[11,12] 4) current collectors with 3D framework to guide the deposition of Li metal;[13–16] 5) surface pretreatments of Li metal or the current collector with a protective coating to stabilize the interface between Li metal and electrolyte (focus of this review); 6) high external pressure to promote flat depositions of Li metal.[17,18]

Protective coatings are ion-conductive or electrolyte-permeable layers underneath which Li metal can be electrodeposited (**Figure 1-1b**). As Li ions pass through the coating layer, the ion flux becomes more homogeneous at the electrode surface, leading to uniform Li metal deposition.[19,20] The protective layer also reduces the contact area between the electrolyte and Li, thus suppresses the side reactions. In contrast to SEI layer formed by the side reaction inside the battery, protective coatings for Li metal can be viewed as a preformed, artificial SEI layer. The composition of the coating materials can be tuned to optimize the ionic conductivity, the mechanical strength, and the permeability to the solvent.[21,22]

Previously, protective coatings were reviewed as one approach to stabilize the electrolyte-Li metal interface, as reported by Archer, Cui, Zhang et al, respectively.[2,20,23,24] More recently, a comprehensive review covering the interface engineering at Li metal anode was published by Zhang et al.[25] These reviews provide excellent and extensive summaries of synthesis approaches for protective coatings, and descriptions of how different coatings improve lithium metal anode cycling performance.

The continuous publication of many peer-reviewed studies on the protective coating motivated us to focus our review on works published from 2017 to 2019. We chose references reporting the results of Li||Li symmetric cycling, Cu||Li CE test, Li||cathode cell test with well-described testing conditions (discussed in Section 1.5) to allow precise comparisons among different coating materials. Instead of providing a comprehensive account of published literature, this review attempts to analyze reported literature based on how different coating materials accomplish both protective and ion-conducting functions simultaneously and the intrinsic tradeoff between them. We hypothesized that the protection mechanism of coatings to be: 1) mechanical suppression of dendritic Li; 2) reduced side reaction by chemical selectivity. In addition to these two protection mechanisms, ionic conductivity is an essential feature of the coating, because Li ion is required to transport through the layer.

Chapter 1 is organized as the following: proposal of the functioning mechanisms of the coating layer based on previous studies of interfacial physics and chemistry between Li metal and the electrolyte (Section 1.2), review of various techniques for the preparation of coating layers (Section 1.3), the characterization techniques of the coatings (Section 1.4), and the performance evaluation of the coatings (Section 1.5). The protective coatings are divided into inorganic materials (Section 1.6) and polymeric materials (Section 1.7), and the material properties and the stabilization effect on Li metal are discussed in detail. Composite coatings of inorganic and polymer materials are also discussed in Section 1.7. Based on the reported results and discussions, we provide guidelines for designing effective coating layers and suggest testing protocols to rigorously evaluate the performance of protective coatings on Li metal under practical cell conditions (Section 1.8).

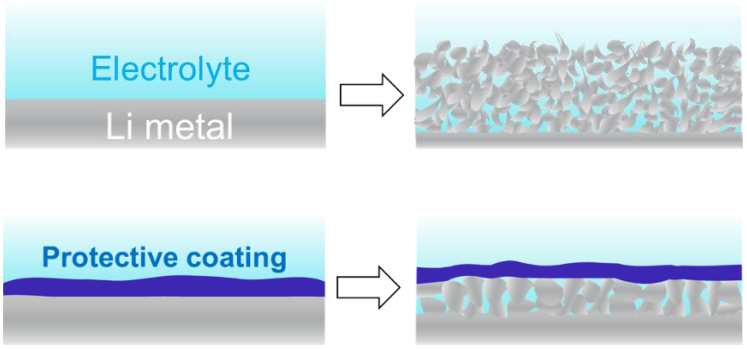

Figure 1-1 Porous morphology of electroplated Li metal after long period of cycling. (b) Dense morphology of Li metal electroplated underneath the protective coating. The coating also protects Li metal from side reactions with the electrolyte.

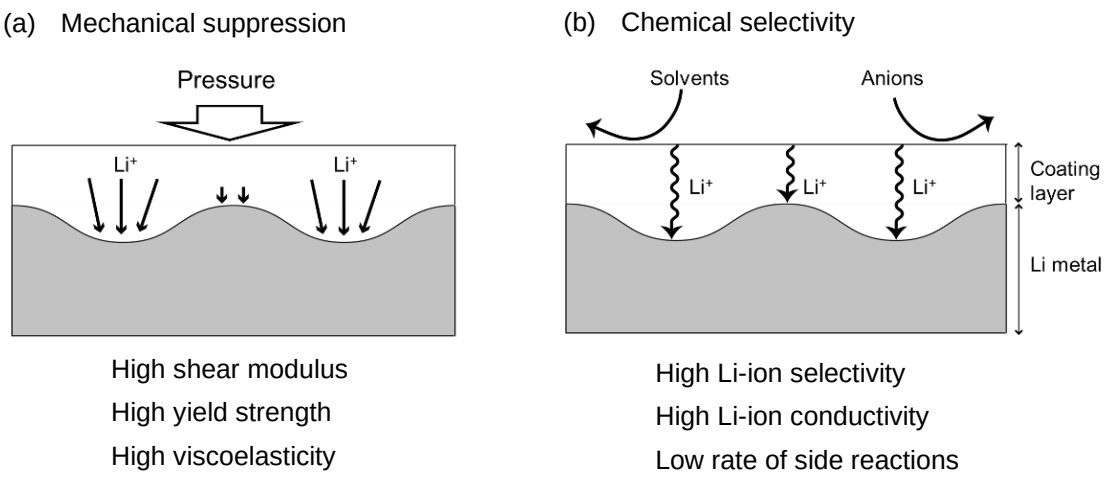

Figure 1-2 (a) Mechanical suppression of dendrite growth. A coating layer with high shear modulus (> 8 GPa) promotes Li metal deposition at the concave regions to reduce the surface roughness. (b) Selective conduction of Li cations through the coating layer. Less permeation of solvents and anions reduces the rate of side reactions with Li metal.

1.2 Protection mechanism and key requirements for the coating layers

Protection mechanism of coating layers on Li metal can be categorized into two types: Mechanical suppression of Li dendrite; and high selectivity toward Li ion transport. For the mechanical suppression, a theoretical calculation by Newman et al. showed that compressive forces on the Li metal surface can promote Li deposition at the concave area, if the surface layer has more than two-times higher shear modulus than Li metal (**Figure 1-2a**).[26,27] This theory supports the basic idea of using hard inorganic materials to suppress the dendritic growth of Li metal. For example, a ceramic solid ion conductor, $Li_7La_3Zr_2O_{12}$ (LLZO), has the shear modulus of 56-61 GPa, one order of magnitude higher than the value of Li metal (4.25 GPa) to effectively suppress the Li dendrites.[28]

Unlike inorganic materials, the shear modulus of organic polymer materials (e.g. 26.2 MPa for PEO [29]) are significantly lower than the value of Li metal to validate the Newman model. Srinivasan modified the Newman model by taking into account for the plastic deformation of Li metal under a high mechanical pressures.[30] The authors showed that increasing yield strength of the polymer layer (i.e. lower elasticity) promotes plastic deformation of Li metal and hence suppresses Li dendrite. In contrast, Archer et al. showed increasing viscoelasticity of electrolytes suppresses the Li dendrite growth based on the theory of electro-convection.[31,32] This theory supports the stabilization effect of Li metal by soft and gel-like polymer coatings.[33,34]

Selective lithium ion transport means the coating layer selectively conducts Li ion while expelling solvent or anion molecules from Li metal surface (**Figure 1-2b**). Li ion is always solvated by solvent molecules or anions,[35–37] and the contact between the Li metal and solvent molecules/anions is inevitable during the electrodeposition. The contact between liquid electrolytes and Li metal triggers side reactions and decreases the CE by consuming the active Li metal. Desolvation of the solvent/anion molecules from the coordinating Li ion at the

coating surface can solve this problem. Solid state electrolyte has ideally the highest selectivity for Li ion (transference number = 1), because Li ion migrates via hopping mechanism in the crystal structure. Abe and Janek et al. respectively reported that Li-ion transport at the interface between liquid electrolyte and solid state electrolyte has the highest activation energy and is the rate-limiting step.[38,39] This activation energy is related to the desolvation energy of solvent molecules from Li ion.[38] Additionally, Janek reported the formation of inorganic/organic composite layer at the interface between the solid state electrolyte and the liquid electrolyte, which increases the interfacial resistance.[39]

Solid state electrolytes are the ideal coating material for selective transport of Li ions; however, the layer is brittle and usually has cracks and voids. At the plating step, Li metal can eventually grow through these defects and reach the liquid electrolyte. In contrast, polymer materials can realize uniform and defect-free coating thanks to the soft and deformable nature. The disadvantage of using the polymer materials is, however, the selectivity toward Li ions is generally lower than the inorganic solid ion conductors. To enhance the selectivity of polymer coatings, understandings on the swelling ratio of polymer films in the electrolytes is critical, as this parameter is closely related to the chemical selectivity (or repelling ability) of the polymer against the solvents. For example, Whitesides et al. reported swelling ratio of PDMS in various solvent systems.[40] PDMS shows one order of higher swelling ratio in ether solvent such as THF and dimethoxyethane than in carbonate solvent such as DMC. This result indicates PDMS film repels more carbonate solvent than ether solvent. It is important to note that less solvent in the polymer film results in lower ionic conductivity because ion conduction is carried by the solvent molecules incorporated inside the polymer. Therefore, the balance between the chemical selectivity and ionic conductivity must be precisely tuned by swelling ratio of polymer film in the electrolyte.

To summarize, there are four major requirements for protective coatings in Li metal battery. 1) uniform and crack-free coating layer to build a uniform current distribution over the entire electrode surface. High Li-ion flux at the cracks leads to dendritic growth of Li metal. On this point, flexible polymeric coatings have advantages over brittle inorganic coatings. 2) Mechanical properties such as high shear modulus, high yield strength, and high viscoelasticity of the coating help to suppress Li dendrite growth. High mechanical strength also enables the coating layer to survive long-term cycling of batteries. 3) Chemical selectivity toward Li ion over solvents/anions to reduce the rate of side reactions and increase the lifetime of Li metal anode. 4) High ionic conductivity, because a sluggish ion conduction builds up concentration gradient of Li ion and promotes dendritic plating of Li metal.[19] In addition, at high-rate charging/discharging, the energy loss by Ohmic resistance can be minimized by higher ionic conductivity.

1.3 Approaches for the formation of protective layers on Li metal surface

Various approaches have been reported to form protective coatings on Li metal surface. The range of obtainable thickness is dependent on the coating methods, as summarized in **Figure 1-3a**. Depositions using gas-phase precursors (e.g. ALD, MLD, sputtering, see below) generally produce thinner coatings with thicknesses ranging from couple of nanometers to hundred nanometers. Methods using solution-phase precursors (e.g. spin, dip, cast, and spray coatings) generate submicron to a few micrometer thick coatings. Furthermore, the coating methods can be categorized into those using inert substrate (**Figure 1-3b–d**), and those using reactivity of Li metal to initiate the formation of coating products (**Figure 1-3e, f**).

ALD is a versatile technique of preparing high-quality thin layer of inorganic materials.[41] Based on the sequential and self-limiting chemical reactions, gaseous precursors deposit on a solid surface layer-by-layer at a growth rate of a few Angstroms per cycle.[42] For example, a thin film of LiF can be prepared by ALD from *t*-BuOLi and HF (**Figure 1-3b**).[42] In addition to the nanometer-level control of the thickness, ALD produces a smooth and uniform coating, which is beneficial for the protection of the electrode. MLD is a similar technique to ALD and can prepare organic or inorganic/organic hybrid films.[43] The organic components provide flexibility and functional groups to the film.[44] The working mechanism of MLD is pulsing two reactants to a solid surface alternatively and the polymerization takes place in a layer-by-layer manner. For instance, Sun et al reported a fabrication of polyurea layer on Li metal by MLD from ethylenediamine and 1,4-phenylene diisocyanate.[45]

Sputtering is also a versatile coating technique and able to deposit nanometer-thick film of metal or oxide/sulfide materials on wide range of substrates.[46–48] Because sputtering technique only requires the vacuum environment and the external field to ionize the noble gas atoms, it is more cost-effective to produce inorganic thin

films, compared to the ALD technique. MoS_2, (**Figure 1-3c**), Al_2O_3, and Li_3PO_4 coating layer were successfully prepared on Li foil either by electron-based sputtering or by magnetron sputtering.[47–49]

For a solution-based precursor, spin, dip, cast, and spray coating methods are used to form protective coatings. Spin coating produces a thin polymer film on a rotating disk as the liquid droplet is spread out by the centrifugal force while the solvent evaporates.[50] The coating thickness ranges from nanometers to a few micrometers and is controllable through the rotation speed and the concentration of the polymer solution. Dip coating is a simple method to produce a thin film by immersing the substrate into a polymer solution and drying in air. Multiple factors affect the thickness and morphology of the coating layer, such as surface condition of the substrate, the immersion time, the lifting speed, the number of dipping cycles, the operation temperature, and the humidity.[51] Cast coating is a scalable and versatile technique to make thin polymer films, often used in both laboratories and industries.[52] Thickness of coatings are tunable by various parameters, such as viscosity of the polymer solution, volatility of the solvent, and the drying temperatures. To prepare a film by cast coating, a homogeneous polymer solution is dropped on a flat substrate and casted with a blade, followed by a drying process. Cast coating is suitable for thin layer preparation in a range of sub-micrometers to micro-level thickness.[53–55] Spray coating uses a stream of fine droplets striking at the target substrates at high velocity to form a uniform layer.[56] This technique is suitable for mass production due to its high efficiency, low cost, and high reproducibility. For instance, Wei et al employed spray coating technology to fabricate a graphene oxide layer on Li foil (**Figure 1-3d**).[57]

Highly reactive surface of Li metal can be used as the initiator to grow protective coatings on top of the Li metal. The thickness of protecting layer can be controlled by the reaction time and the concentration of the reactant.

Cui et al. used a solid-gas reaction of sulfur vapor on the reactive Li metal surface to form a homogenous Li_2S layer *in-situ* (**Figure 1-3e**).[58] LiF coating layers are prepared by the reduction of fluorine-containing gas on the Li metal surface.[59,60] Hybrid silicate is synthesized by reacting vapor of MPS and TEOS on the surface of Li metal.[61]

Solid-solution reaction is also widely applied to produce a variety of coating materials on Li metal surface. Wu et al reported a simple method to coat a uniform LiF/polymer composite layer on Li metal surface by reacting with PVDF dissolved in DMF (**Figure 1-3f**).[62] Polymerization of ethyl α-cyanoacrylate on the surface of Li metal was reported by Cui et al.[63] Li_3PS_4 layer is produced on Li metal surface inside the battery by the reduction reaction of Li_2S_6/P_2S_5 in an ether electrolyte.[64]

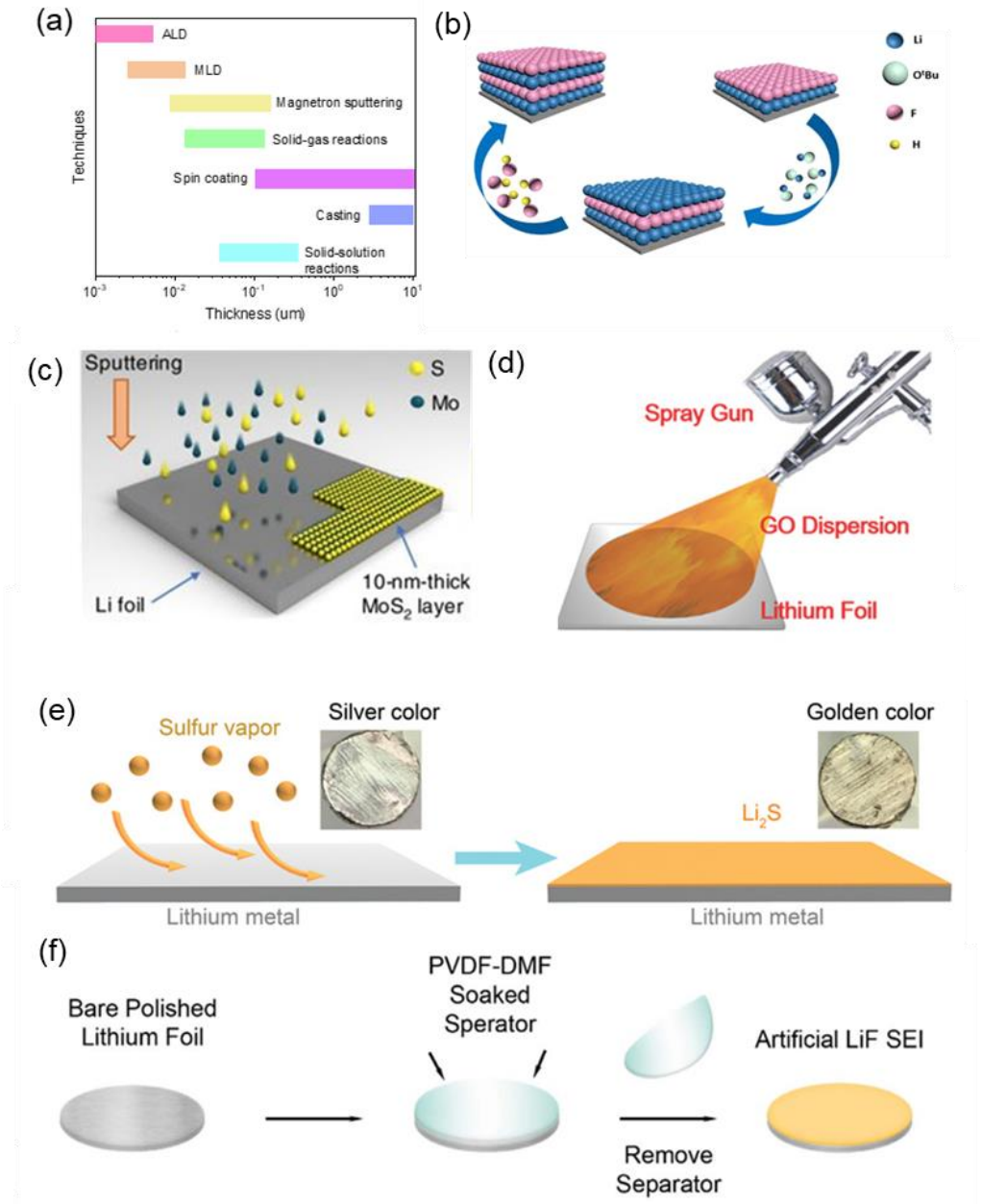

Figure 1-3 (a) Thickness range of the protective coatings achievable by the various techniques. Versatile coating methods independent of surface reactivity of the substrate: (b) LiF coating on Li metal by ALD;[42] (c) MoS_2 coating on Li electrodes by sputtering;[48] (d) Graphene oxide coating on Li foil by spray coating.[57] Li-specific coating methods dependent on the reactivity of Li metal: (e) Li_2S coating produced from the reduction of sulfur vapor on Li metal surface;[58] (f) LiF/polymer composite coating formed from the reduction of PVDF solution in DMF on Li metal surface.[62]

1.4 Characterization techniques for physical and chemical properties of the protective coatings

The characterization of surface coating on Li mainly focuses on the composition, morphology, and mechanical property. **Figure 1-4** summarizes the tools for characterizing the coating layer, SEI layer, Li layer, and their interfaces. The EDX, XPS, XRD, FTIR, Raman spectroscopy, ED, and EELS are widely used for composition analysis. The morphology of the protective layer, SEI layer, and Li are studied by SEM and TEM. *In-situ* techniques for the analysis of electrode-electrolyte interfaces are reviewed in detail by Wang et al.[65]

XRD is a rapid analytical method used for crystalline phase identification. Benefiting from the high flux of synchrotron light sources, the current synchrotron based XRD allows us to identify the nanometer-scale crystalline components such as Li, Li_2O, Li_2CO_3, and LiF in the SEI layer.[58,66] Furthermore, the *Operando* synchrotron XRD is currently under development, which is able to monitor the evolution of Li and crystalline SEI components throughout plating and stripping of Li. Consequently, this technique provides qualitative and quantitative information on chemically reacted Li, physically orphaned Li, and electrochemically active Li in real time.[1]

XPS is a surface-specific analytical tool probing the outermost region limited to 8-10 nm of the sampling depth. To avoid the reactions between Li sample and air, the XPS for Li metal study is usually equipped with an argon filled glovebox. Another approach to eliminate the air contamination is using a customer designed air-tight sample transfer arm to send the sample from glovebox to the XPS. In addition to identify the chemical species, XPS can quantify the ratio of chemical compounds at the sample surface. By etching the surface layer, the depth profile of the chemical compositions from the outermost surface layer to the bulk regions can be analyzed.[22,58] The depth profile of the coating layer produced from the solid-gas reaction of sulfur vapor and Li metal are shown in **Figure 1-4a** as an example.[58] According to the S 2p and Li 1s spectra, the outmost layer of the coating is

composed of multiple compounds such as Li_2CO_3, Li_2S, $LiSO_3$, $LiSO_2$, and Li_2SO_4. In contrast, the main components from the middle to the bulk layer are simply Li_2S and Li_2CO_3. The gradation of sulfide compounds represents that the degree of sulfur reduction varies with the distance from the reductive surface of Li metal.

FTIR and Raman spectroscopy are often employed to analyze the composition of Li metal surface.[55,61,62,67] ATR-FTIR is particularly sensitive to the sample surface and suitable for the surface analysis. For example, a thin PVDF film coated on Cu current collector is analyzed by this technique (**Figure 1-4b**).[67] ATR technique can be applied to *in-situ* analysis of SEI composition on the anode surface.[68] As such, *in-situ* characterization of the protective coating during plating/stripping of Li metal can potentially provide useful information on the swelling behavior or the compositional change in the coating. *In-situ* stimulated Raman scattering has been demonstrated to monitor the concentration gradient of anion at the electrolyte-Li interface, and the growth of Li metal under a Li_3PO_4 coating.[19]

SEM is frequently used to study the morphologies of the coating layer, the cross-sectional interface layer. Observation of Li metal electrodeposited after varied times provides the time evolution of nucleation and growth of Li metal particles or the dendrites inside the battery cell.[34,69] The intensity of electron beam used in SEM is much lower than TEM, and therefore minimum beam damage is expected in SEM.[70] However, the resolution of SEM is not high enough to observe a nanometer-thick coatings (those formed by ALD or sputtering techniques) and the SEI layer. In contrast, TEM enables observation of SEI layer under the high-energy electron beam. The challenge of TEM characterization has been the beam damage to thin Li and organic samples (**Figure 1-4d**, left), and then cryo-TEM which operates at cryogenic temperature is developed by Cui,[71] Meng,[72] Kourkoutis et al.,[73] respectively, to minimize the beam damage on Li metal (**Figure 1-4d**, right).[71]

A few other analytical tools for elemental or chemical characterizations are often paired with electron microscopies. EDX is generally combined with SEM to provide elemental mapping along with sample morphology. Elemental Li is inactive in EDX analysis and therefore observed as a black region in the EDX mapping image. The cross-sectional EDX mapping of the coated Li metal can identify the thickness and uniformity of the coating layer on the Li metal. For example, cross-section of the MoS_2-coated Li metal was characterized by Mo and S signals in the EDX analysis, which shows that MoS_2 layer on Li foil is structurally stable, and the uniform film is observable after 300 cycles..[48]

EELS provides abundant chemical information of the sample such as the atomic composition, chemical bonding, and valence. EELS instrument is generally combined with TEM. In contrast to EDX, signals from light elements such as Li is observable in EELS. Electron diffraction is another analytical technique combined with TEM imaging to determine the crystal structure of the sample at a particle or even at an atomic level. Because high-energy electron beam can damage organic samples and Li metal, cryogenic condition has been used in EELS (**Figure 1-4c**),[73] electron diffraction (**Figure 1-4d**, inset),[71] to evaluate the chemical composition or determine the crystal orientation of Li metal and the SEI layer.[74] Kourkoutis et al. combined cryo-STEM and EELS to obtain the nanoscale structure and composition of intact SEI on Li metal, revealing the structure of Li dendrites and the SEI layers. [73]

AFM probes the surface morphology and mechanical properties of the samples, which achieves high vertical resolution of 0.1 nm.[63] AFM is unique for its capability of evaluating the Young's modulus of the coating layer by measuring the van der Waals forces between the probing tip and the surface.[22,75] Qian measured the mechanical properties of Li_3P/LiCl coating layer on Li metal by AFM in peak force tapping (PFT) mode. As

shown in **Figure 1-4e**, Li_3P/LiCl layer on the Li surface shows high Young's modulus, which suppresses the growth of Li dendrites.[22,75]

QCM techniques measure nanogram-scale mass changes of the electrode during the electrochemical reactions.[76,77] For instance, Sun et al. used QCM to evaluate the growth rate of polyurea on Li foil (**Figure 1-4f**).[45] QCM can quantify and accurately control the film thickness coated on Li foil, which has prominent influence on the ionic conductivity of the film.

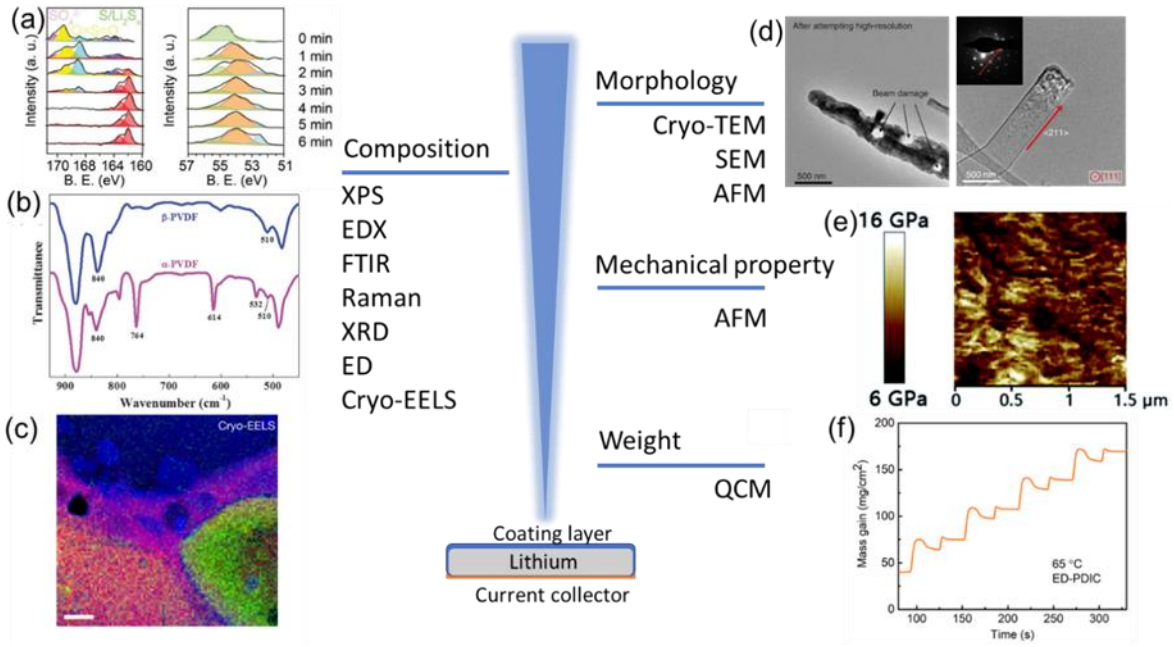

Figure 1-4 Characterization techniques for the coating layers or the SEI layers on lithium metal anode: (a) Depth profile of the XPS spectra of Li2S coating layer on Li metal after varied sputtering times;[58] (b) FTIR spectra of α phase and β phase PVDF coatings;[67] (c) EELS elemental mapping of the SEI layer on Li metal;[73] (d) TEM images of the Li metal dendrite observed under standard TEM (left); and under cryo-TEM (right), which is free from the beam damage;[71] (e) AFM image of Li3P/LiCl composite layer showing high Young's modulus of the coating;[75] and (f) QCM analysis of the mass gain of polyurea thin film growing on Li metal.[45]

1.5 Morphology of Li metal and electrochemical method to evaluate the protective function of coating layers

Protective effects of a coating layer on Li metal are usually evaluated by observation of the morphology of electroplated Li metal, electrochemical performance in a Li||Li symmetric cell, Cu||Li cell, and Li||cathode full cell. An effective coating layer leads to a dense and dendrite-free deposition of Li metal even after extensive numbers of cycles. Long cycle life and stable voltage curve in Li||Li symmetric cell, especially under large current and capacity, indicate stable deposition of Li metal. CE in plating/stripping cycle of Li metal can be evaluated by Cu||Li cell and enables a quantitative evaluation of Li loss during the cycles. Practical application of a protective coating can be assessed by cycling the protected Li metal anode paired with a cathode. We briefly summarize the key information obtainable from these characterization and cell testing, the required condition for the testing, and the way of interpreting the results. This section is intended to make the comparisons of the protection performance more comprehensive between different coating materials as discussed in Section 1.6 and 1.7.

1.5.1 Morphology of Li metal

SEM is a common tool to investigate the morphologies of the coating layer and deposited Li. SEM measurements provides three key information. 1) Position of electrodeposited Li metal. To exert the protective function of the coating layer, Li metal has to be deposited underneath the coating layer. 2) Morphology of electrodeposited Li metal particles. Round shape and large particles (> 5 μm of diameter) has smaller contact area with the electrolyte than fibrous and dendritic shape, and thus less side reaction is expected.[8] 3) Total thickness of deposited Li metal on the current collector. To reduce the contact area with the electrolyte, low pore volume inside the deposited Li metal is desirable. The porosity in Li metal can be evaluated from the total thickness of deposited Li metal. A useful standard is that 1 mAh cm^{-2} of Li metal with zero porosity yields a deposition thickness of 4.85 μm.

Assuming an isotropic pore, total thickness as d μm, the porosity in Li metal deposited after Q_p mAh cm^{-2} can be calculated from the formula, $(d - 4.85Q_p)/d$.

1.5.2 Li||Li symmetric cell cycling

Cycling the Li||Li symmetric cell at different current densities with various areal capacities is the first approach to assess the performance of the surface protected Li. Voltage curves reflect the morphology evolution of Li metal. There are two typical symptoms of cell failure due to the Li dendrite growth (**Figure 1-5a**). The voltage suddenly drops to 0 V as a result of Li dendrites penetrating the separator and shorting the cell (**Figure 1-5b**, pure Li metal).[58] Another phenomenon is the dramatic increase of the cell polarization, which is also associated with dendritic Li formation leading to high surface area porous Li deposition. (**Figure 1-5b**, Li_2S_8 preplant Li) The Li metal with high surface area not only reacts with the electrolyte to generate highly resistive side reaction products, but also absorbs the electrolyte into the pores. Although the cell is not shorted, the increase of the polarization and unstable voltage curves indicate massive Li dendrites formation. Long-term cycling without apparent increase of voltage polarization is a good indication of stabilization of Li metal (**Figure 1-5b**, Li_2S-coated Li). Because Li metal becomes less stable at higher current density and higher capacity, Li||Li cycling test at such conditions can clearly show the validity of protective coatings. It is worth mentioning that the Li||Li cycling test fails to distinguish the internally-shorted cell, when the voltage curve appears smooth and stable for long period of time, while the voltage does not reach 0 V (often referred as soft short). Then, EIS test is required to prove the cell is not shorted.

1.5.3 Coulombic efficiency

CE test is conducted in a two-electrode cell with Cu as the working, and Li as both counter and reference electrodes. Li metal is repetitively plated on and stripped from Cu electrode. CE is calculated from the ratio of stripping capacity to plating capacity ($CE = Q_s/Q_p$). CE less than unity means loss of Li metal in the plating/stripping cycles. Influence of current density, Q_s, Q_p on CE and other cycling protocols is detailed elsewhere. [78] The irreversible loss of the Li originates from either chemical reaction with the electrolyte to form SEI, or formation of electrically isolated Li particles. The effectiveness of a protective coating is evaluated by comparing the CEs with or without the coating covered on the Cu working electrode. An effective coating layer suppresses the irreversible chemical reaction by reducing the contact between the Li and electrolyte and mitigates the formation of isolated Li metal particles by promoting dense uniform Li deposition.

1.5.4 Full cell

Li||cathode full cell is the ultimate evaluation of the coating, which provides insight for practical application. Depending on the compatibility between the coating and the electrolyte solvent, the cathode for the full cell testing is usually LFP, sulfur, and NMC. Although there are reports of stable cycling at high current densities in Li||Li cells, the reported current density used in Li||cathode full cell is usually much lower than the value used in Li||Li cells. Cathode with high loading of active materials are required to test the full cell at higher current density. The benefits from the coating are obvious when limited Li and/or lean electrolyte is used. For instance (**Figure 1-5c**), high CEs of >99.8% are reported as Li efficiencies with more than 10-fold excess of Li in the full cell. However, the excess Li means the reported efficiency value is really a measure of the cathode reversibility.[79] In comparison, **Figure 1-5d** shows the performance of Li||NMC 811 cells with one-fold excess of Li. Before the excess Li is

consumed the capacity of the cell is stable and the CE is 99.93%, which represents the CE of the cathode.[80] Once the excess Li is consumed, the capacity of the cell decay much faster and the CE of the cell reflects the efficiency of the Li anode. Since the CE of the full cell with excess Li is basically the CE of the cathode, a proper way to evaluate the CE of Li metal in a full cell is to test the anode free cell, which only utilize the Li from cathode side.

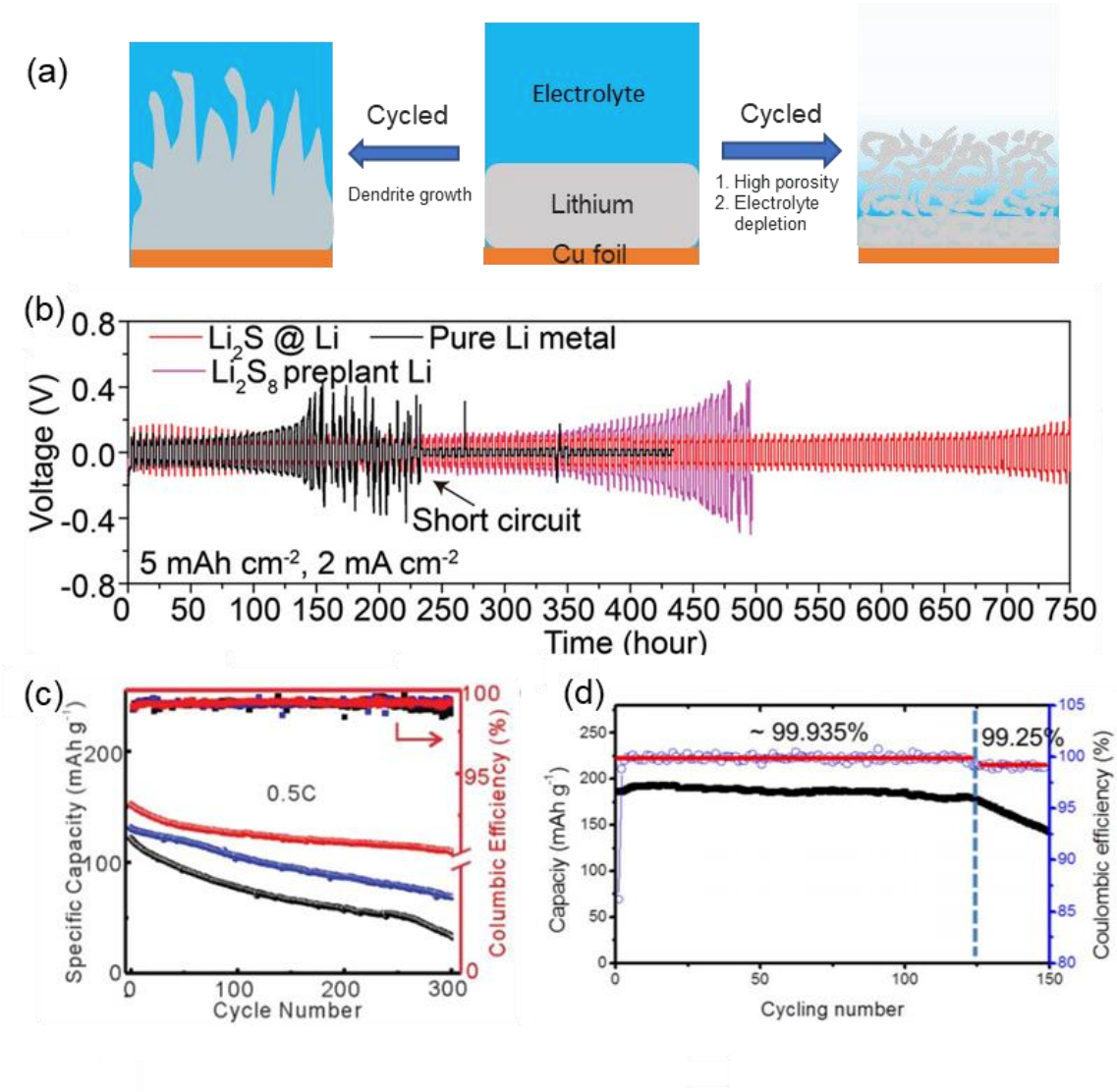

Figure 1-5 (a) Schematic diagram of two possible Li failure mechanisms. (b) Li||Li symmetric cell cycling with/without coating.[58] (c) Cycling stability of Li||LCO cells tested under 17-fold excess amount of Li metal.[79] (d) Cycling stability of Li||NMC811 cells tested with one-fold excess of Li metal.[80]

1.6 Inorganic coating

Inorganic coatings generally possess high shear modulus and can serve as a physical barrier to Li metal dendrite.[26,28] **Table 1-1** lists the intrinsic shear modulus and ionic conductivity of inorganic materials used as the protective coating on Li metal.Al_2O_3, fluorinated graphene (GF), LiF shows notably high shear modulus, while sulfide-based materials such as MoS_2 and Li_3PS_4 shows lower shear modulus. Materials with high ionic conductivity is expected to transport Li cations via hopping mechanism and show the highest selectivity toward Li cations. Meanwhile, ion transport through non-conductive coating layer is only possible in the liquid electrolyte permeating the layer, and therefore, the selectivity toward Li ion through non-conductive layer is limited. In short, high ionic conductivity of inorganic coating materials directly leads to high selectivity of Li cation. This relation is only true for single-ion conductor and not true for polymeric materials (Section 1.7).

Coating uniformity is the essential factor which determines the performance of inorganic coating. Presence of defects, grain boundaries, and pores in coating layer significantly reduce shear modulus, ionic conductivity, and the Li^+ selectivity. Most of the inorganic coatings is directly formed on the Li surface by ALD, sputtering, or solution-phase reaction (**Table 1-1**). Then, high-pressure compression or high-temperature sintering to eliminate the defects in the coating layer is not available,[81] because those processes result in deformation or melt-down of metallic Li.

Performance of inorganic coating is often evaluated as the cycling life of Li||Li symmetric cell (**Table 1-1**). Longer cycle numbers at higher current density and higher capacity indicate superior protection effect on the Li metal. However, one must note that Li metal foil used in the cell is usually very thick (>250 μm), corresponding to nearly 50 mAh cm^{-2} in capacity. Given such an excess amount of Li as a reservoir, the cycle life of the cell is

determined by the rate of electrolyte consumption or cycle life before internal shorting, rather than by the consumption rate of metallic Li. Measurement of CE or use of thin (controlled amount of) Li foil is highly recommended to evaluate the reduction rate of side reactions by protective coatings (Section 1.5.3).

Table 1-1 Conditions and cycle numbers of Li||Li symmetric cells with various inorganic coatings on the Li metal. Note thick Li metal foil (> 250 μm) is used in the test. Reference for ionic conductivity at room temperature: LiF=ref[82]; Al_2O_3=ref[83]; LiPON($Li_{3.3}PO_{3.8}N_{0.22}$)=ref[84]; Li_3PS_4=ref[81]; Li_3P=ref[85], Reference for shear modulus: LiF/LiCl=ref[86]; Al_2O_3=ref[87]; LiPON=ref[88]; Li_3PS_4=ref[89]; MoS_2=ref[90]; GF=ref[91]

Material	Ionic conductivity (S cm^{-1})	Shear modulus (GPa)	Coating method	Thickness	Electrolyte	Current (mA cm^{-2})	Capacity (mAh cm^{-2})	Cycle number
LiF	10^{-13}-10^{-7}	76 (LiF)	ALD	8 nm	EC/EMC (3:7), 1M $LiPF_6$	1	1	130
LiF	10^{-13}-10^{-7}	76 (LiF)	Solid-gas reaction	380 nm	EC/DEC (1:1), 1M $LiPF_6$	5	1	300
LiF + polymer	10^{-13}-10^{-7}	76 (LiF)	Solution reaction	300 nm	EC/DEC (1:1), 1M $LiPF_6$	3	1	300
Al_2O_3	10^{-30} (amorphous Al_2O_3)	165 (Al_2O_3)	Magnetron sputtering	20 nm	EC/DEC/DMC (1:1:1), 1M $LiPF_6$	0.5	0.5	600
LiPON + polymer	2.4×10^{-6} (LiPON)	31 (LiPON)	ALD	15 nm	EC/DEC (1:1), 1.5M $LiPF_6$	2	2	100
Li_3PS_4 +LSPS	3×10^{-4} (Li_3PS_4)	8.7 (Li_3PS_4)	Solution reaction	2 μm	DOL/DME, 1M LiTFSI, 25mM Li_2S_6/P_2S_5	4	1	800
Li_3P + LiCl	10^{-4} (Li_3P)	34 (LiCl)	Solution reaction	15 μm	EC/DMC/EMC (1:1:1), 1M $LiPF_6$, 5% FEC	3	2	100
$Li_{13}In_3$ + LiCl	Mixed conductor	-	Solution reaction	10 μm	DOL/DME (1:1) 1M LiTFSI	2	2	600
MoS_2	Mixed conductor	18 (MoS_2)	Sputtering	10 nm	DOL/DME (1:1), 1M LiTFSI, 0.25M $LiNO_3$	10	5	300
GF + LiF	Mixed conductor	140 (GF)	Solid-solid reaction	1 μm	EC/DEC (1:1), 1M $LiPF_6$	10	1	165

1.6.2 Ionically non-conductive materials

1.6.2.1 Lithium halide

LiF is a major SEI compound formed from the decomposition of fluorinated salts or fluorinated organic solvents.[92–94] Because Li metal generally shows stable cycling in those fluorinated electrolytes, LiF is believed to protect Li metal surface. Rochefort et al. reported that Li metal immersed in FEC solvent can be cycled in acetonitrile (1 M $LiPF_6$ as the salt), a solvent known to react with Li metal.[95] XPS and AFM analysis of the SEI layer on Li metal after the immersion in FEC revealed the existence of LiF, Li_2CO_3, and polymeric compounds. The authors suggested that the soft polymeric components also play the important role in protecting Li metal surface.

Mechanism of ion transport and the exact ionic conductivity in LiF is still unclear today. A theoretical study showed defects in LiF can contribute to the ionic conductivity.[96] Pan et al shows Schottky pairs are likely formed at the anode side, and the ionic conductivity of LiF is estimated as 10^{-31} S cm^{-1}. On the cathode side, *p*-type defect is formed, and the ionic conductivity of LiF is estimated as 10^{-12} S cm^{-1}. The authors suggested doping divalent cation (e.g. Mg^{2+}) in LiF increases the carrier concentration and improve the ionic conductivity. Greeley et al. calculated the conductivity of LiF to be in the range of 10^{-7}-10^{-13} S cm^{-1}, much higher than the value reported by Pan et al.[82] Li et al. reported that LiF thin film deposited on silica (0001) surface is structurally disordered, and the ionic conductivity is experimentally evaluated as 6×10^{-6} S cm^{-1} at 50 °C.[97] The cause of high conductivity is attributed to the interface region between the amorphous and the crystalline phases in LiF. The authors reported thermal annealing of the LiF film at a moderate temperature (350 °C) is the key to growing the amorphous-crystalline interface.

Several methods have been reported to form LiF layers directly on Li metal. Elam et al. used ALD with *t*-BuOLi and HF as the precursors.[42] Cui et al. produced LiF layer by the direct reaction of fluorine (F_2) gas on Li metal surface (**Figure 1-6a**).[60] The F_2 gas is generated from thermal decomposition of perfluoro-3-butenyl vinyl ether (commercially known as Cytop) and diffuses to the Li surface to initiate the formation of LiF. Li||Li symmetric cell with the LiF layer (380 nm) cycles for 300 cycles at 5 mA cm^{-2}, 1 mAh cm^{-2} in an electrolyte composed of EC and DEC with 1 M of $LiPF_6$ (**Figure 1-6b**). Wu et al. reported that Li metal immediately reacts with a DMF solution of PVDF to form a composite film (300 nm thick in total) of LiF and polymers derived from PVDF.[62] Li||Li symmetric cell with the LiF/polymer coating cycles for 300 cycles at 3 mA cm^{-2} and 1 mAh cm^{-2} in a carbonate electrolyte (EC/DEC (1:1) + 1 M $LiPF_6$).

LiCl is another Li halide salt having higher shear modulus (34 MPa) than Li metal. Yang et al. prepared a LiCl/polymer composite layer from the reaction between C_2Cl_4 and LiOH on the Li metal surface.[98] Lithiophilic nature of LiCl surface facilitates the Li^+ transport through the composite layer. The surface-modified Li||Li cell cycles for 1000 hours without increase of voltage hysteresis at 2 mA cm^{-2} and 1 mAh cm^{-2} in ether electrolyte (DOL/DME + 1 M LiTFSI + 2% $LiNO_3$).

1.6.2.2 Aluminum oxide

An ultrathin coating of Al_2O_3 is commonly prepared by ALD technique (Section 1.3), using a reactive organometallic precursor (trimethylaluminum) and water vapor. Nanometer-thin amorphous Al_2O_3 layer has been proven to protect cathode materials from the decomposition reaction by HF in the electrolyte.[99] To understand the ion transport through amorphous Al_2O_3 layer, Wolverton et al. calculated the Li diffusivity as 2.7×10^{-14} m^2 s^{-1} at 600

K.[83] Based on this result, the conductivity of Al_2O_3 is estimated as only 10^{-30} S cm^{-1} at 300 K. Such low ionic conductivity requires Al_2O_3 layer to be nanometer-thin to allow Li^+ diffuse through.

On the surface of Li metal, reduction of Al_2O_3 produces $LiAl_5O_8$ phase. Recent ab initio calculation shows $LiAl_5O_8$ has a lower Li-ion migration barrier (0.33 eV) and higher Li-ion diffusivity (3.6×10^{-8} cm^2 s^{-1}) than Al_2O_3 (2.69 eV, and 9.3×10^{-48} cm^2 s^{-1}, respectively).[100] Therefore, $LiAl_5O_8$ coating layer is expected to be a more ideal single-ion conductive coating layer than Al_2O_3.

Hu et al. coated ultrathin layer of Al_2O_3 on a garnet Li-ion conductor , LLCZN.[101] The lithiophilic nature of Al_2O_3 interface layer results in intimate contact between the Li metal and LLCZN, and the interfacial impedance is reduced significantly. TEM/EELS analysis reveals that Al_2O_3 is converted into $Li_2Al_4O_7$ (another Li-ion conductive phase) at the interface with Li metal. Their study provides a perspective for solving the inherent problem of high interfacial resistance in all-solid-state Li metal batteries.[102]

Li et al. used magnetron sputtering to coat Al_2O_3 layer directly on Li surface.[47] The authors compared the Li||Li cycling life with different thickness of Al_2O_3 layer (0, 7, 20, 40 nm) in a carbonate electrolyte, and 20 nm-thick Al_2O_3 layer showed the longest cycling life (> 1,000 hours at 0.5 mA cm^{-2}, 0.5 mAh cm^{-2}). Interestingly, the authors observed Li metal deposited on top of the Al_2O_3 layer rather than underneath the layer. This result indicates the ionic conductivity of 20-nm-thick Al_2O_3 layer is too low, and Li metal deposits through the cracks in the Al_2O_3 layer.

1.6.2.3 Lithium methyl carbonate

LMC is another class of SEI component often observed in carbonate electrolytes.[103] Liu et al. demonstrated that a uniform coating of LMC can be formed on Li metal surface by a selective demethylation of

DMC, catalyzed by LiI (**Figure 1-6c**).[104–106] Because LMC is soluble in EC/DMC solvent, the electrolyte is saturated with LMC powder to suppress the dissolution of the LMC coating layer. The CE of Li deposition of LMC-coated Li metal in LMC-saturated carbonate electrolyte (EC/DMC (1:1) + 1 M $LiPF_6$ + sat. LMC) is 96%, which is higher than the efficiency in a commercial LP30 carbonate electrolyte (EC/DMC (1:1) + 1 M $LiPF_6$) (**Figure 1-6d**).[105]

1.6.2.4 Lithium sulfide

Li_2S is often observed on the Li metal anode in Li||S batteries due to the reaction between polysulfide and Li metal.[107] Although the formation of Li_2S on the anode decreases the amount of active sulfur, the solid Li_2S layer is believed to hinder the growth of Li dendrite. Cui et al. made a dense layer of Li_2S (62 nm thick) on Li surface via solid-gas reaction between vaporized sulfur and solid Li metal.[58] The CE of Li deposition is evaluated by measuring the consumption rate of thin Li metal anode (10 mAh cm^{-2} capacity) in a ether electrolyte (DOL /DME (1:1) + 1 M LiTFSI), and the efficiency is 98.9%.

1.6.3 Ion-conductive materials

1.6.3.1 Lithium phosphorous oxynitride

LiPON is an amorphous solid-state electrolyte, which can be prepared either by radio frequency reactive sputtering or ALD techniques. Xie et al. coated 2 um-thick LiPON on both Cu current collector and Li metal, each of which were assembled into a pouch cell.[108] The authors demonstrated prolonged cycle life in both LiPON-coated Cu||$LiCoO_2$ cell and LiPON-coated Li||$LiCoO_2$ cell. However, when NCA and elemental sulfur are used as the cathode materials, LiPON coating deteriorates the cycle life. Because the capacity of NCA and sulfur is

higher than the $LiCoO_2$, larger amount of Li metal is deposited during the charging cycle, which leads to the crack formation in LiPON layer and eventually causes the deterioration of the cycling performance.

To overcome this brittle nature of LiPON, Noked et al. put a 800-nm-thick polymer layer underneath a LiPON layer (15 nm).[109] The polymer layer is prepared by electrochemical polymerization of DOL on Li metal surface. However, thermal expansion of the underlying polymer layer during the 150 °C ALD process results in formation of cracks in the top LiPON layer. After 100 cycles of plating/stripping, electroplated Li metal is observed at the surface cracks in LiPON layer. Although the surface of Li metal is exposed to the electrolyte, the morphology of Li metal was smooth and densely packed on top of the LiPON layer. This result indicates that the surface composition of the substrate can alter the electroplating behavior of Li metal.

1.6.3.2 Lithium phosphorous sulfide

Li_3PS_4 is a glassy solid-state electrolyte widely used in solid state Li metal battery. Compared to garnet type solid electrolyte, Li_3PS_4 is more malleable and ductile, offering great processing ability to form a thin film.[110] Li_3PS_4 can be synthesized from a solution phase, which enables a facile way to form a uniform coating on Li metal surface.[111] Nazar et al. formed Li_3PS_4 coating directly on Li surface by soaking a Li foil into a DOL/DME mixed solution of Li_2S_6 and P_2S_5.[64] The resulting layer is a mixture of conductive Li_3PS_4 and non-conductive phosphorous sulfide species. Thickness of the resulting Li_3PS_4 coating was approximately 2 μm (**Figure 1-6e**). In the electrochemical test, Li_2S_6 and P_2S_5 are added directly into the electrolyte to form Li_3PS_4 layer *in-situ* on the surface of Li metal electrode. As a result, Li metal can be stably plated/stripped for 400 hours at a high current density of 4 mA cm^{-2} (**Figure 1-6f**), and no dendritic nor mossy Li is observed during the cycling under the optical microscopy. Sun et al. used an alternative pathway to form Li_3PS_4 layer on Li metal surface, where Li foil is soaked

in a solution of P_4S_{16} in NMP.[112] The authors showed improved capacity retention of Li||S battery with the Li_3PS_4 coating.

1.6.3.3 Lithium phosphide

Yang et al. prepared Li_3P from the direct reaction between Li metal and PCl_3.[75] Li_3P is known as a fast Li-ion conductor (10^{-4} S cm^{-1} at room temperature).[85] The overpotential of Li_3P-coated Li||Li symmetric cycling is reduced and achieves 100 cycles at 3 mA cm^{-2} and 2 mAh cm^{-2} in a carbonate electrolyte (EC /DMC/ EMC (1:1:1) + 1 M $LiPF_6$ + 5% FEC).

1.6.4 Mixed ion-electron conductor

1.6.4.1 Composite of metal and lithium halide

Nazar et al. formed a layer of lithium alloy (e.g. $Li_{13}In_3$, LiZn, Li_3Bi, Li_3As) by soaking a lithium metal in THF solution of metal chloride (MCl_x; M = In, Zn, Bi or As).[113] LiCl is a byproduct in the reaction and remained in the alloy layer. The $Li_{13}In_3$ coating layer shows particularly effective protection on Li metal. $Li_{13}In_3$-coated Li||Li symmetric cell cycles for 1200 hours at 2 mA cm^{-2} and 2 mAh cm^{-2} in an ether electrolyte (DOL/DME (1:1) + 1 M LiTFSI).

Xie et al. prepared a composite Li-Sn alloy/polymer layer by soaking a Li metal into a THF solution of $SnCl_4$.[114] $SnCl_4$ reacts with Li metal to form Li-Sn alloy and LiCl, while THF polymerizes into PTMEG. Li metal with the composite coating becomes more resistant against water. With the Li-Sn/polymer coating, Li||Li cycling achieves 1000 hours at 1 mA cm^{-2}/1 mAh cm^{-2} in an ether electrolyte (DOL/DME + 1 M LiTFSI + 1 wt% $LiNO_3$). In addition, a Cu||Li cell achieves 200 cycles at 0.5 mA cm^{-2}/1 mAh cm^{-2} with a CE of over 95%.

Yan et al. reported a LiF/Cu composite layer prepared by the reduction of CuF_2 on the Li metal surface.[115] LiF/Cu layer is mixed conductor and the electronic and ionic conductivities are 2.06×10^{-3} S cm^{-1} and 1.79×10^{-4} S cm^{-1}, respectively. CE of Li metal covered with LiF/Cu layer is evaluated as 96.3% under 0.5 mA cm^{-2} with 0.5 mAh cm^{-2} in a carbonate electrolyte (EC/DEC (1:1) + 1 M $LiPF_6$).

1.6.4.2 2D materials and carbon nanotube

2D materials such as graphene, GO, GF and MoS_2 can conduct Li ion in between the layered structures. These layers are highly selective toward Li ion and expected to expel the solvent molecules from the Li metal surface. Cui et al. studied electroplating of Li metal on Cu foil where the surface is covered with boron nitride or graphene nanosheets.[116] Li metal plating through the 2D layers forms dense morphology, and the CE is increased to 97% at the cycling condition of 0.5 mA cm^{-2} and 5 mAh cm^{-2} in a carbonate electrolyte (EC/DEC + 1 M $LiPF_6$). Choi et al. coated MoS_2 layer directly on Li metal via sputtering technique (Section 1.3).[48] The authors demonstrated stable cycling of MoS_2-coated Li metal at high current density (10 mA cm^{-2}) and large capacity (5 mAh cm^{-2}).

Qian et al. reported another composite coating of LiF with graphene fluoride (GF), which was prepared by reacting GF with molten Li metal.[117] The GF-LiF coating suppresses growth of Li dendrite and enables stable Li||Li cycling at high current density (10 mA cm^{-2}) in a carbonate electrolyte. The coating is hydrophobic and protects Li metal from moisture damage when exposed to ambient air.

Carbon nanotube (CNT) is an electron conductive material, and Li metal is expected to grow on the top when placed on Li metal anode. However, lithiophobic nature of CNT prohibit Li metal to deposit directly on CNT surface. Zhang et al. prepared a multilayer ZnO/CNT coating film with lithiophilic-lithiophobic gradient where the

inner layer of CNT is coated with ZnO to alter the surface nature to be more lithiophilic, while outer layer of CNT remains bare and lithiophobic.[118] The gradual increase of lithiophilicity of the ZnO/CNT film towards Li metal surface guides uniform deposition of Li metal underneath the coating layer. Stable Li||Li cycling was demonstrated under 10 mA cm^{-2} with 1 mAh cm^{-2} in coin cell, and 1 mA cm^{-2} with 1 mAh cm^{-2} in pouch cell.

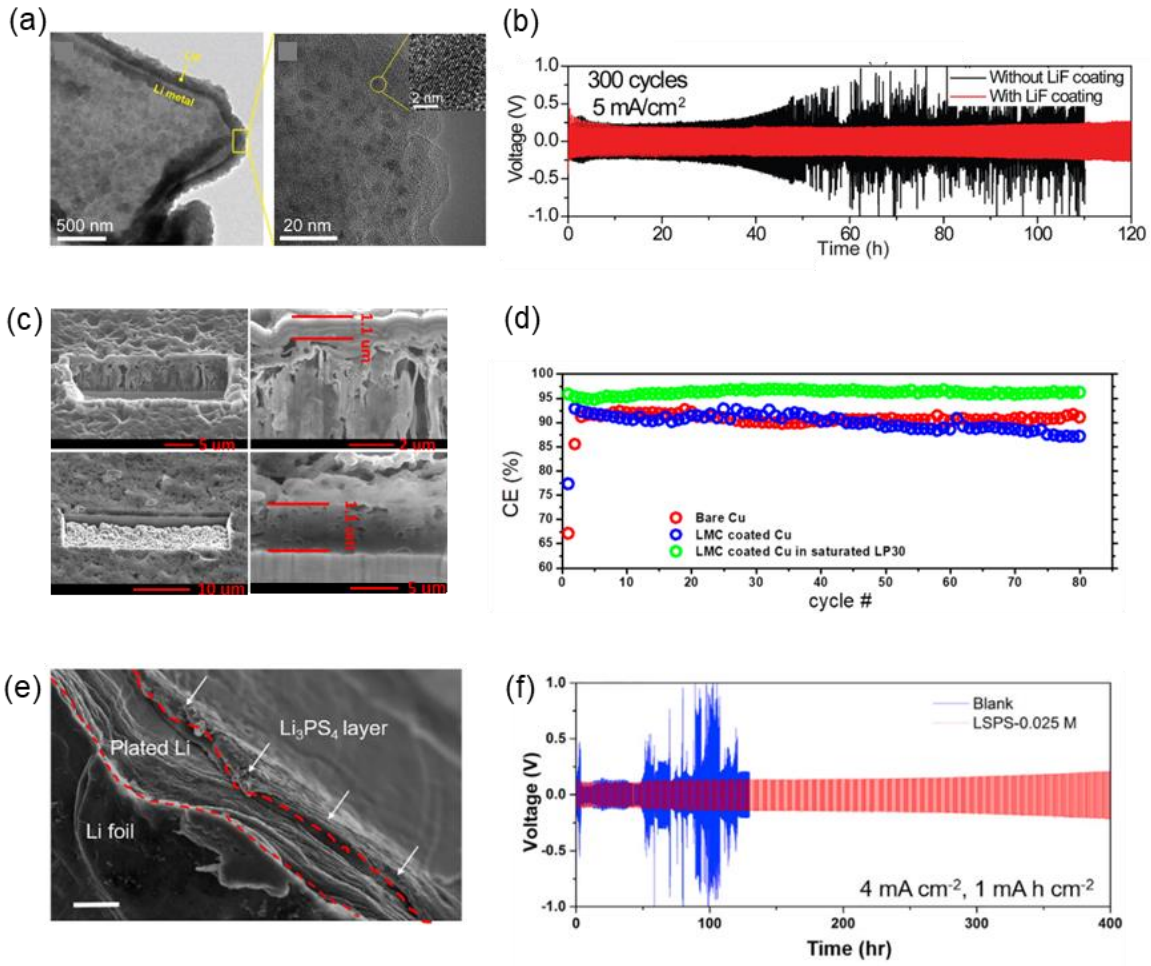

Figure 1-6 (a) TEM images of LiF coating on Li metal surface. (b) Li||Li symmetric cell cycling in EC/DEC electrolyte at 5 mA cm^{-2} and 1 mAh cm^{-2} with/without LiF coating.[60] (c) Cross-sectional SEM images of Cu current collector after 1 mAh cm^{-2} of Li metal is deposited (top) and then stripped (bottom) in 0.2 M LiI EC/DMC solution. A layer of 1 μm-thick lithium methyl carbonate (LMC) is observed on the surface. (d) CE of Li plating/stripping on Cu current collector without coating, with LMC coating in normal LP 30 electrolyte (EC/DMC + 1 M $LiPF_6$), and with LMC coating in LP30 electrolyte saturated with LMC.[105] (e) Cross-sectional SEM image of Li metal after 4 mAh cm^{-2} of Li is plated in 0.025M of L_2S_6/P_2S_5 (LSPS) ether solution. A layer of Li_3PS_4 is formed on the Li surface. Scale bar = 20 μm. (f) Li||Li symmetric cell cycling at 4 mA cm^{-2} and 1 mAh cm^{-2} in DOL/DME electrolyte added with L_2S_6/P_2S_5.[64]

1.7 Polymer and polymer/inorganic composite coatings

Polymer coatings are more flexible, and elastic compared to inorganic coatings and thus more capable of accommodating volume change during Li plating/stripping. Intimate contact between polymer layer and Li metal is often observed because polymer itself or the liquid that swells the polymer wets the surface of Li metal better than rigid inorganic precursors. Polymer can be made into a uniform film by spin coating, solution casting, and even direct polymerization on Li metal surface. Thickness is controllable by the concentration of the polymer solution used in the coating process or by the reaction times. Thinner coating can increase the ionic conductivity of the polymer film, while thicker coating can enhance the film toughness and the selectivity toward the conduction of Li^+.[119]

In addition to film thickness, ionic conductivity of polymer films depends on the swelling ratio in the electrolyte. Hildebrand solubility parameter is a square-root of intermolecular cohesive energy within a unit volume of material (unit = $MPa^{1/2}$).[40] Solubility parameter is useful to predict the swelling behavior of polymers in solvents: Polymer swells more in a solvent with similar solubility parameter as the polymer. Solubility parameter is higher in polar solvent because of stronger dipole-dipole interaction. For example, solubility parameter of ethers ranges between 15-20 $MPa^{1/2}$ (e.g. diethyl ether = 15.8; 1,4-dioxane = 20.5); linear carbonates range between 17-20 $MPa^{1/2}$ (e.g. DEC = 17.9; DMC =19.4); cyclic carbonates range between 27-30 $MPa^{1/2}$ (e.g. PC = 27.3; EC = 29.6). [40,120] Solubility parameters of polymer films used as protective coating of Li metal is listed in **Table 1-2**. Solubility parameters of some polymers have not been reported in literature. In this case, we listed the solubility parameter of the solvent which dissolves the polymer, since the solubility parameter of the polymer is expected to be similar to the value of the solvent.

Polymer materials are categorized into three types based on the solubility parameters: Non-polar polymer (Section 1.7.1) with solubility parameter below 16 $MPa^{1/2}$; polar polymer (Section 1.7.2) with solubility parameter in the range of 20-25 $MPa^{1/2}$; strongly-polar polymer (Section 1.7.3) with solubility parameter above 26 $MPa^{1/2}$. A Polymer film swells and becomes ion-conductive only in a solvent with similar solubility parameter as the polymer. Therefore, non-polar polymer coating is usually used with less polar electrolyte such as ether electrolytes to maximize the film conductivity, except in the case the film has pores to let the solvent permeate through. Polar polymer films are conductive in both less-polar ether electrolyte, and polar carbonate electrolytes. Strongly-polar polymer films are only conductive in polar carbonate electrolytes. Chemical selectivity is generally observed in strongly-polar polymer, which is advantageous as a protective coating of Li metal (Section 1.2). For example, electrostatic interaction between Li^+ and sulfonate group enables a selective conduction of Li^+ through Nafion film (Section 1.7.3.1). Dipole-dipole interaction between EC and nitrile group of PAN reduces the reactivity of EC with Li metal (Section 1.7.3.2). On the other hand, polar group is generally at high oxidation state and therefore tends to be reduced by Li metal. Addition of a designed functional group to the polymer backbone which can form a stable SEI layer on Li metal can mitigate decomposition of both the coating layer and the electrolyte (Section 1.7.2.5–6).

Inorganic components such as LiF, Al_2O_3, L_3PS_4, graphene oxide can be mixed with polymers to increase the mechanical strength of the protective layer. High shear modulus of inorganic compounds can suppress the dendrite growth (Section 1.2). In polymer/inorganic composite film, the polymer matrix glues the inorganic components together to enhance the film elasticity. Uniform distribution of the inorganic components, and the higher degree of bonding between the inorganic and polymer phases are the important conditions to realize uniform current distribution through the film.

Coulombic efficiencies of Li plating/stripping on polymer-coated Cu or inert metal electrode (stainless steel) are summarized in **Table 1-2**. High CE over 99% in a carbonate electrolyte was reported recently, which makes polymer or polymer/inorganic composite a promising material for stabilization of the electrolyte-Li interface.

Table 1-2 Conditions and CE of Li metal plating/stripping with various polymer or composite coatings on a flat working electrode. (continued)

Material	Solubility parameter ($MPa^{1/2}$)	Coating method	Thickness	Electrolyte	Current ($mA\ cm^{-2}$)	Capacity ($mAh\ cm^{-2}$)	CE
PDMS (dense)	15.5	Melt casting	1 μm	DOL/DME (1:1), 1M LiTFSI, 1wt% $LiNO_3$	1	1	98.3%
PDMS (porous)	15.5	Spin coating	500 nm	EC/DEC (1:1), 1M $LiPF_6$	0.5	1	-
PVDF-HFP + LiF	20.0 (acetone)	Solution casting	12 μm	DOL/DME (1:1) 1M LiTFSI, 2% $LiNO_3$	0.5	1	-
Poly(SF-DOL) + GO	20.3 (DCM)	Solution casting	3 μm	EC/EMC (3:7), 1M $LiPF_6$, 2% LiBOB	1	1	92%
β-PVDF	23.2	Solution casting	4 μm	DOL/DME (1:1), 1M LITFAppendix, 3wt% $LiNO_3$	1	0.5	-
Nafion	31 & 21	Spray coating	4 μm	EC/DEC (1:1), 1M $LiPF_6$	-	-	-

Note all electroplated Li metal is stripped at the end of each cycle. Solubility parameters of the solvent of the polymer are listed in case the value of polymer is not available in literatures. Reference of solubility parameters: ref[129] for polymers, and ref[120] for solvents

Material	Solubility parameter ($MPa^{1/2}$)	Coating method	Thickness	Electrolyte	Current ($mA\ cm^{-2}$)	Capacity ($mAh\ cm^{-2}$)	CE
Poly(Imide-DOL)	24.8 (DMF)	Solution casting	2 μm	EC/EMC/FEC (3:7:1), 1M LiPF6	0.5	1	98.3%
PEDOT-PEO	25.1 (NM)	Spin coating	380 nm	EC/DMC (1 :1), 1 M $LiClO_4$	-	-	-
PAN	26.1	Thermal crosslinking	40-200 μm	EC/DEC (1:3), 1 M $LiPF_6$	-	-	-
Li-Nafion + Al_2O_3	27.3 (PC)	Solution casting	200 nm	EC/DMC (1:1), 1 M $LiPF_6$, 10% FEC, 1% VC	3	3	92%
Polyurea	30.1	MLD	4 nm	EC/DEC/DMC (1:1:1), 1 M $LiPF_6$	-	-	-
Nafion	31 & 21	Spray coating	4 μm	EC/DEC (1:1), 1M $LiPF_6$	-	-	-

1.7.2 Non-polar polymer

1.7.2.1 Poly(dimethyl siloxane)

PDMS is widely used because of the chemical stability against metallic Li, and the elastic property enables PDMS to form a thin film.[121] The protective function of PDMS film is often evaluated in an ether electrolyte consisting of DOL/DME as the mixed solvent, LiTFSI as the salt, and $LiNO_3$ as the additive. The ether electrolyte itself shows high CE without any coating layer (>98.5%),[122] and the efficiency with PDMS film in ether electrolyte shows limited increase. Meanwhile, PDMS coating enables longer cycle life (> 100 cycles) of Li deposition/stripping, compared to bare electrodes.[54,123]

PDMS is a non-polar material and thus no Li salt can directly dissolve into this polymer.[124] The ion conduction through the PDMS layer must be mediated by the solvent molecules dissolved inside the film. PDMS film swells more in ether electrolytes because the solubility parameter of PDMS (15.5 $MPa^{1/2}$) is closer to that of the ether electrolyte. In contrast, swelling ratio of PDMS is much lower in carbonate electrolytes, and thus the film is non-conductive. Zhu et al. reported a treatment of PDMS film with hydrofluoric acid (HF) creates nanopores to increase the ionic conductivity of PDMS film in carbonate electrolytes.[125] An average CE with the HF-treated PDMS film in a carbonate electrolyte (EC/DEC (1:1) + 1 M $LiPF_6$) reaches 94.5%.

Bao and Cui et al. studied flowable PDMS films, which can deform as Li dendrite grows.[54] Dynamic crosslinking between the polymer chains imparts fluid-like property to the coating layer and successfully suppress the dendritic growth of Li metal. With the flowable PDMS film coated on Cu electrode, the average CE achieves 97.0% over 100 cycles in an ether electrolyte (DOL/DME (1:1) + 1 M LiTFSI + 1wt% $LiNO_3$) at 1 mA cm^{-2} and 1 mAh cm^{-2}. The authors also reported fluid-like polymer film made from polyamine.[126] Biased random walk

simulation suggests that reduced ion conductivity in the fluid-like polymer coating may contribute to uniform deposition of Li metal.[126]

Nazar et al. used PDMS as an elastic polymer support for Li_3PS_4 solid ion conductor.[127] Li_3PS_4 powder is cold pressed into a solid ion-conductive layer, and then the *in-situ* crosslinking among PDMS oligomers fills the void inside the Li_3PS_4 layer. An average CE of 95.8% over 200 cycles (1 mA cm^{-2}, 1 mAh cm^{-2}) is reported in an ether electrolyte with the Li_3PS_4-PDMS composite coating. While the presence of PDMS clearly improved the cycling stability, the moderate efficiency values indicate that significant electrolyte permeation takes place which reacts with lithium metal.

1.7.3 Polar polymers

1.7.3.1 Poly(vinylidene fluoride) and poly(vinylidene fluoride-co-hexafluoropropylene)

PVDF can react with Li metal to produce LiF at the interface. PVDF film contains both polar and non-polar phases, depending on the conformation of electronegative fluorine (F) atoms on the polymer chains: In α-phase, F atoms take alternating trans-gauche conformation with antiparallel dipole moments, and thus α-PVDF film exhibits nonpolar property; In β-phase, F atoms take all trans conformation with parallel dipole moments, and thus β-PVDF film exhibits polar property. Wu et al. observed a flat deposition of Li metal on β-PVDF-coated Cu substrate, in contrast to the dendritic Li metal on bare Cu (**Figure 1-7a**). [67] The CE of Li plating in an ether electrolyte reaches 98% in the first 10 cycles on a copper electrode coated with polar β-PVDF film (**Figure 1-7b**). Meanwhile, with the nonpolar α-PVDF coating, the initial CE begins from only 85% and then gradually improves to 98% after 200 cycles. The voltage hysteresis of polar β-PVDF coated copper is the same as the bare copper, while the hysteresis is doubled

with non-polar α-PVDF coating. The polar β-PVDF film provides more conductive pathways to Li ion to diffuse through the polymer coating and plate underneath the coating layer.

PVDF-HFP is a highly fluorinated version of PVDF possessing trifluoro methane group. Because of uniform distribution of the dipole moment, PVDF-HFP is less polar than PVDF, and the surface energy is extremely low.[128] Huang et al. reported a composite film of PVDF-HFP and LiF microparticles to increase the mechanical strength of the polymer film.[66] The CE of Li deposition through the PVDF-HFP/LiF composite film in an ether electrolyte with $LiNO_3$ additive is 97.2%. Although the CE shows little increase from the bare Cu electrode, the protected Cu||Li cell cycled longer than the control cell (120 cycles).

1.7.3.2 Poly(3,4-ethylenedioxythiophene-*co*-ethylene oxide)

PEDOT is an electron-conductive polymer, while PEO is a Li^+-conductive polymer. The direct use of PEO (solubility parameter = 24.0 $MPa^{1/2}$, [129]) as the coating layer is not feasible due to its solubility in common organic electrolytes. Kim et al. reported the copolymer of PEDOT and PEO (PEDOT-*co*-EO), which is insoluble in organic electrolytes and strongly adheres to Li metal surface.[130] PEDOT-*co*-EO swells in a carbonate electrolyte (EC/DMC + 1 M $LiClO_4$) and shows high ionic conductivity (3.5×10^{-3} S cm^{-1}). The cycled life of Li||$LiCoO_2$ cell is increased when Li metal anode is coated with PEDOT-*co*-EO coating. Kim et al. also incorporated AlF_3 particles in PEDOT-*co*-EO to form a composite coating.[131] AlF_3 is expected to serve as a solid component to mechanically suppress growth of the Li dendrite. As a result, the voltage polarization is reduced by this composite coating, and cycling life of a Li||O_2 cell is extended.

1.7.3.3 Alucone

Alucone is a hybrid metal-organic material where ethylene oxide units are bridged by aluminum cation. Alucone is directly grown from Li metal surface by MLD with trimethyl aluminum and ethylene glycol as the precursors. Elam et al. reported that the Li||Li cycling life is enhanced in a carbonate electrolyte with 6-nm-thick alucone coating.[44] The morphology of electrodeposited Li is denser with the alucone coating, however, no significant increase of the CE was observed despite a longer cycling life compared to the control cell.

1.7.3.4 Poly((*N*-2,2-dimethyl-1,3-dioxolane-4-methyl)-5-norbornene-*exo*-2,3-dicarboximide)

Ether-based organic electrolyte is known to show better cycle life for Li metal compared to carbonate electrolyte. This exceptional stability is believed to be the result of decomposition of ether solvents on the Li surface to form polymeric SEI layers. Wang et al. designed a copolymer, poly(Imide-DOL), where a DOL is attached to a norbornene-*exo*-dicarboximide main chain poly(Imide-DOL).[53] The cyclic ether group decomposes on Li surface to produce ether-based SEI layer, while the rigid cyclic carboximide group imparts stiffness to the entire film. A moderate degree of polymer swelling in carbonate electrolytes provides ionic conductivity to the polymer film. The CE of Li deposition/dissolution with this polymer coating is increased to 98.3% over 200 cycles in a carbonate electrolyte with FEC as the additive (EC/EMC/FEC (3:7:1) + 1 M $LiPF_6$). This efficiency is close to the value of ether electrolytes.

1.7.3.5 Poly(vinyl sulfonyl fluoride-*ran*-2-vinyl-1,3-dioxolane)

Wang et al. also reported another type of copolymer, poly(SF-DOL) composed of DOL, and sulfonyl fluoride (-SO_2F, SF) groups.[22] SF group is reduced on the lithium surface to produce LiF as the SEI component (**Figure 1-7c**). GO nanosheets is mixed into the polymer layer to further enhance the interface stability. This

polymer/GO coating is named as reactive polymer coating (RPC) after the designed reactivity with Li metal. CE of Li metal deposition on a flat stainless-steel electrode achieves 99.3% at 1 mA cm^{-2} and 1 mAh cm^{-2} in a carbonate electrolyte (EC/EMC/FEC (3:7:1) + 1 M $LiPF_6$ + 2%LiBOB). Poly(SF-DOL) coating is applied on a carbon-based 3D host, and the CE achieves 99.1% at high current density (2.0 mA cm^{-2}) and high capacity (4.0 mAh cm^{-2}) (**Figure 1-7d**). Poly(SF-DOL)-coated 3D host can be lithiated to form Li-containing anode and paired with NCM 523 cathode. Impressively, under limited amount of Li metal (1.9-fold excess) plated inside the RPC-protected 3D host, and limited volume of electrolyte (7 μL mAh^{-1}), the Li||NCM 523 cell retained 90% of the initial capacity after 200 cycles (**Figure 1-7e**).

1.7.4 Strongly-polar polymer

1.7.4.1 Nafion

Nafion is an ionomer where sulfonate group is tethered onto PTFE backbone. Nafion has two solubility parameters, 21 $MPa^{1/2}$ (attributed to the PTFE backbone) and 31 M $Pa^{1/2}$ (attributed to the ionic sulfonate group).[132] By exchanging H^+ on sulfonate group to Li^+ (Li-Nafion), Li-Nafion selectively conducts Li^+ through the ionic cluster formed at sulfonate group (i.e. high transference number of Li^+).

Kim et al. laminated 4 μm-thick Nafion layer on Li metal as the protective coating and used in a carbonate electrolyte (EC/DEC + 1 M $LiPF_6$).[119] FTIR spectroscopy on the Nafion film confirms ion exchange between H^+ and Li^+ takes place during Li plating/stripping. Nafion coating on Li metal maintains smooth surface after 10 cycles of Li||Li cycling at high current density (10 mA cm^{-2}, 4 mAh cm^{-2}), showing the good mechanical stability of Nafion. Under the same condition, Nafion-coated Li metal can be cycled for 250 cycles (2000 h in total). The authors compared the Li||Li cycling result with 50 μm-thick Li-Nafion. The thick Li-Nafion film shows transference number

of Li^+ (t_{Li+}) close to unity, which is higher than 4 μm-thick Nafion film (where t_{Li+} = 0.83). However, the conductivity of thick Nafion is one-order lower (3.33×10^{-6} S cm^{-1}) than 4 μm-thick Nafion layer (1.42×10^{-5} S cm^{-1}). Low ionic conductivity of thick Nafion film resulted in unstable voltage curves and large polarizations in galvanostatic Li||Li cycling, and the cell failed at low current density of 0.2 mA cm^{-2}. The deposited Li metal underneath the thick Nafion film is patchy and dendritic. This comparison experiment highlights the importance of high ionic conductivity of polymer film for depositing Li in uniform and smooth morphology.

Archer et al. dissolved ion-exchanged Li-Nafion in PC and solution-casted on Li metal to form 200 nm-thick Li-Nafion film (**Figure 1-7f**).[21] The Li-Nafion film prepared by this method is even thinner than the film used by Kim et al.[119] and therefore shows higher ionic conductivity (2×10^{-3} S cm^{-1}), while maintaining high transference number of Li^+ (t_{Li+} = 0.88). Additionally, nanoporous Al_2O_3 membrane (20 nm pore size) were combined with the Li-Nafion layer to increase the mechanical strength of the composite coating. In a carbonate electrolyte (EC/DMC (1:1) + 1 M $LiPF_6$), the roughness of Li metal deposited under the 200 nm-thick Li-Nafion/Al_2O_3layer is close to the value of flat deposition (**Figure 1-7g**). On the contrary, the Li dendrites are observed when 9-μm-thick Li-Nafion coating is used. This result agrees with the observation by Kim et al.[119] Because thick Nafion film shows only limited ionic conductivity, Li metal preferentially grows from the defect sites in the polymer film and eventually breaks the coating layer. With a thinner coating with higher ionic conductivity, the ion transport is not hindered and Li deposits underneath the coating layer.

In mixed carbonate electrolyte (EC/DMC + 1 M $LiPF_6$ + 10% FEC + 1% VC), the CE of Li plating/striping is improved from 86% with pristine Li counter electrode to 92% with Li-Nafion/Al_2O_3-protected Li counter

electrode (0.5 mA cm^{-2}/1 mAh cm^{-2}). Similar CE is observed under higher current density and capacity (3 mA cm^{-2}, 3 mAh cm^{-2}).

1.7.4.2 Polyacrylonitrile

EC is less stable on contact with Li metal and susceptible to decomposition reaction compared to ether solvents. Nevertheless, oxidative stability of EC makes it compatible with 4V-cathode. To enhance the reduction-stability of EC with Li metal, Yu et al. recently developed a PAN-based polymer gel film.[133] The film was prepared by thermal crosslinking of PEGDA oligomer mixed in a polymer solution of PAN, EC, and LiTFSI. Dipole-dipole interaction between C≡N group of PAN and C=O group of EC increases the energy level of lowest unoccupied molecular orbital (LUMO) and makes EC resistant toward reduction. FTIR, and Raman spectroscopy on PAN-PEGDA-EC-LiTFSI gel film evidences a coordination between PAN and EC, and decreased number of free EC molecules, respectively. The PAN-gel-protected Li shows stable Li||Li cycling at 10 mA cm^{-2} and 1 mAh cm^{-2} for 100 cycles. The cycled Li is shiny, and SEM shows densely deposited Li. Although CE of Li plating/stripping is not reported, Li||NCM 111 cell shows good capacity retention of 94.0% after 450 cycles at 1C rate.

1.7.4.3 Polyurea

Polyurea film can be directly coated on a Li foils by the MLD technique with ethylenediamine and 1,4-phenylene diisocyanate as the precursors.[45] The growth rate of the film is controlled by the number of reaction cycle, and the typical growth rate is 0.4 nm per cycle. Amide bonding in polyurea makes the film polar, which in turn regulates the ion flux of Li cation. Hildebrand solubility parameter of poly(*N*-methacryl urea) is reported as 30.7 $MPa^{1/2}$, which is close to the value of EC.[129] Sun et al. reported that 4 nm-thick polyurea coating enables

stable Li||Li cycling in a carbonate electrolyte (EC/DEC/DMC (1:1:1) + 1 M $LiPF_6$) at 3 mA cm^{-2} and 1 mAh cm^{-2} for 200 hours.[45]

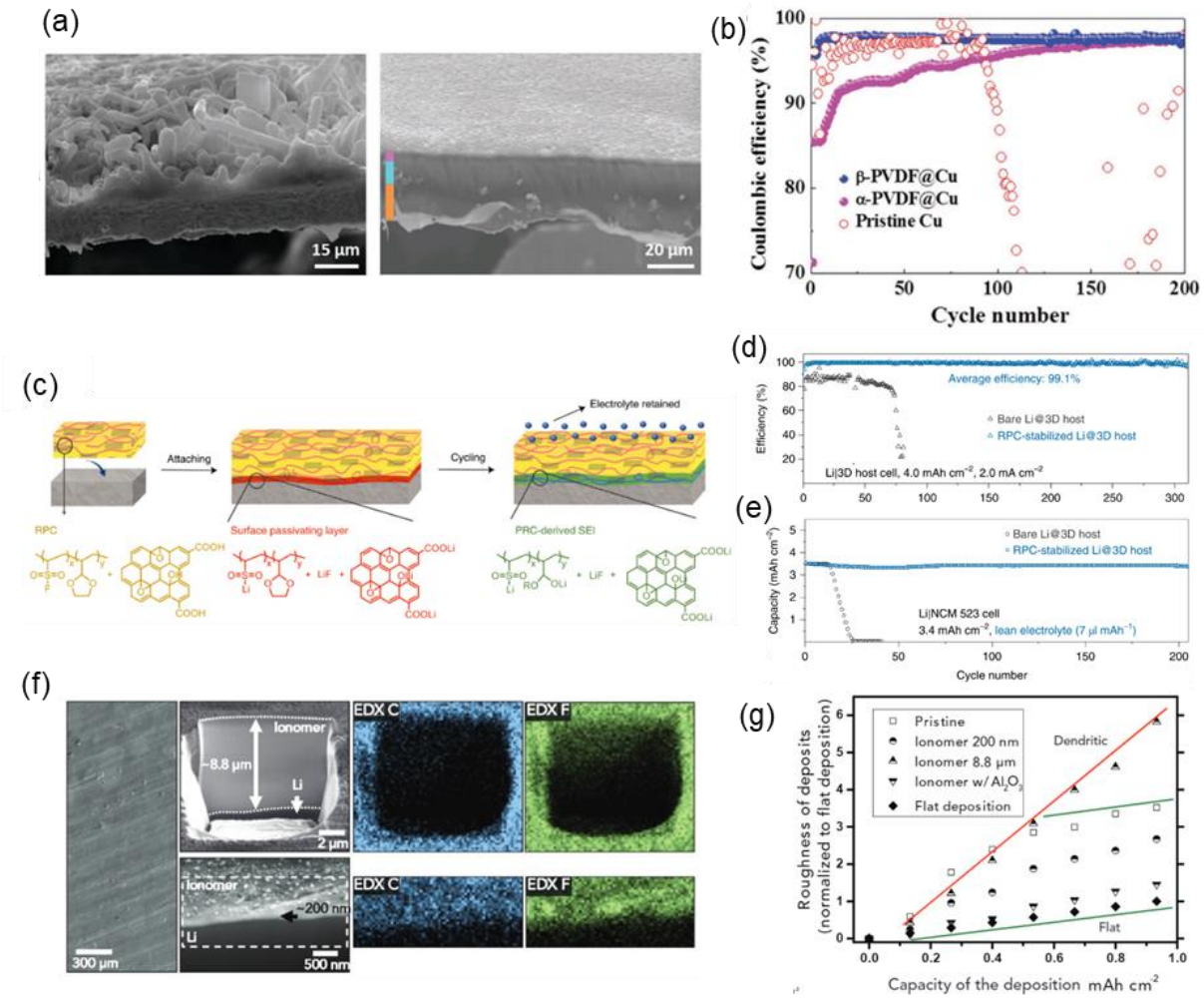

Figure 1-7 (a) SEM image of copper surface after electrodeposition of Li metal (1 mA cm^{-2}, 2 mAh cm^{-2}) without coating (left) and with β-PVDF coating (right). (b) Coulombic efficiency of Li metal plating/stripping with polar β-PVDF coating; nonpolar α-PVDF coating; and without coating.[67] (c) Formation of SEI layer after the application of reactive polymer coating (RPC consisting of poly(SF-DOL) and GO) on Li metal surface. (d) CE of RPC-stabilized Li metal deposited in 3D carbon host, and the comparison with uncoated 3D host (2 mA cm^{-2}, 4 mAh cm^{-2}). (e) Capacity retention of RPC-stabilized 3D Li ||NCM 523 full cell under lean electrolyte condition.[22] (f) Cross-sectional SEM image and EDX mapping of ionomer (Li-Nafion) coating at a thickness of 9 μm (top) and 200 nm (bottom). (g) Roughness of electroplated Li metal at various deposition capacity.[21]

1.8 Summary and future perspectives

The past few years have witnessed a large variety of protective coatings made of both inorganic and polymeric materials that have been reported to give better cycling performance than bare Li metal in either Li||Li symmetric cycling or CE tests. In order for the protective coating approach to help enable Li metal anode to achieve efficiencies of > 99.72% (CE is calculated based on the cell requirement for practical Li metal battery [1]) and ultimately a 500 Wh kg^{-1} lithium metal battery, we advocate for several research directions that merit attention from the research community.

1.8.1 Ion conduction mechanism through the coating layer

Ion conduction is an inherently complex issue for a thin coating layer. For example, a layer of solid ion conductor immersed in liquid electrolyte offers two pathways of ion conduction either through the solid phase, the liquid phase, or both. If the solid conductive layer has no porosity and is also free from any defect, the ion conduction is only possible through the solid phase. However, when the solid conductive layer possesses inherent defects or porosity, permeation of the liquid electrolyte through the pores is possible. In this case, ion conduction through the liquid phase is more probable, because the ionic conductivity of liquid phase is generally higher than solid phase. Although permeation of the liquid electrolyte into the solid phase may increase the overall ionic conductivity of the protective coating, the selectivity towards Li ion inevitably decreases, leading to increasing rate of side reactions with the leaked electrolyte. Therefore, evaluation of the respective ion conductivity in the liquid and the solid phases, by AC impedance technique for example,[39] is essential to understand the ion conduction mechanism and to improve the design of protective coatings. Similarly, evaluation of swelling behavior of polymeric coatings in the liquid electrolyte, the resulting ionic conductivity, and the selectivity toward Li ion (i.e. transference

number) should be studied in detail. A correlation between the dielectric constant of polymers and the size of Li metal nuclei can aid understanding on the electroplating behavior of Li metal through polymer coatings.[134]

1.8.2 Mechanistic understanding of protection layer degradation

Mechanical toughness of the protective coatings should be studied after long cycles of Li plating/stripping. Growing Li metal deposits under the coating layer creates stress and can eventually break the coating. As-formed defect becomes a local hotspot promoting more deposition of Li metal. The local defect in 9-μm-thick Li-Nafion layer promoted dendritic growth of Li metal due to the high current density localized at the defect point (Section 1.7.3.1).[21] In contrast, the cracks in 15-nm-thick LiPON layer resulted in a flat deposition of Li metal growing on top of the LiPON layer (Section 1.6.2.1).[109] Therefore, the improved performance in Li||Li cycling or CE tests may have little relation with the protection mechanisms (i.e. mechanical suppression and chemical selectivity), when the coating layer is fractured during the electroplating. Possibly, when Li metal grows on top of the protective layer, a highly lithiophilic coating layer may promote a flat deposition.

1.8.3 Evaluation of coating layer performance under practical conditions and cell configurations for high energy density

Here, we discuss the practical testing conditions for protective coatings aiming for the high energy density of 500 Wh kg^{-1}.[1] In literature, the specific capacity of Li metal is often claimed as 3860 mAh g^{-1}, however, the excess amount of Li metal on the anode side diminishes the effective capacity of Li metal (**Figure 1-8a**). For example, the effective specific capacity of Li metal anode with 50%, 500%, 5000% excess Li metal drops to 2570, 640, 76 mAh g^{-1}, respectively. The effect of coating layers on thin (less excess) Li metal surface needs to be evaluated to claim the high energy density of Li metal. The CE can be evaluated in a practical cell configuration by

pairing cathode with thin Li metal (Section 1.5.4). Capacity retention versus cycle number with 40% excess Li metal is simulated at varied CE of Li plating/stripping (**Figure 1-8b**). In the plateau region, the excess Li metal is consumed, and then the capacity starts decaying in an exponential manner after all the excess Li is consumed. The 0.2% increase in the CE from 99.6% to 99.8% doubles the cycle life of the plateau region. Recently, increasing number of studies on anode free battery (0% excess Li) and thin-Li metal battery has been published.[80,122,135,136]For example, 83% of capacity retention of thin-Li||LFP battery after 100 cycles was demonstrated by Zhou et al.[135] The CE of Li metal anode is evaluated as 99.3% under 0.2 mA cm^{-2} with 0.8 mAh cm^{-2} of capacity in their study.

Reduction of the amount of liquid electrolyte used in the battery cell is an effective pathway to increasing the energy density (**Figure 1-8d**). However, the cycle life of Li metal battery significantly deteriorates under limited amount of electrolyte.[1] Electrolyte is consumed during the battery cycling by the formation of SEI layer and porous Li metal. This sponge-like Li metal with high surface area accelerates the consumption rate of liquid electrolyte to cause the electrolyte depletion. The high porosity also increases the demand for electrolyte to maintain normal battery operation. Applying a protective coating layer on Li metal is a promising strategy to reduce the rate of electrolyte consumption under lean electrolyte condition.

In recent studies on Li metal anode, the shape of current collector is modified from conventional 2D planar structure to 3D porous scaffold to accommodate the volume expansion of Li metal and simultaneously to reduce the amount of isolated Li particles from the current collector.[13–16] Application of the protective coatings on such 3D scaffold or host is highly anticipated to boost the CE of Li plating (**Figure 1-8e**). As a proof of concept, Wang et al.

recently reported 200 cycles of Li||NCM 523 full cell with limited volume of electrolyte and 90%-excess Li plated on polymer-protected 3D carbon scaffold (Section 1.7.2.5).[22]

The CE of Li metal anode has been steadily increasing thanks to the recent development of high-efficiency electrolytes. The compatibility of such electrolytes with high voltage cathode, for example NMC 811, is also demonstrated.[80,137] The electrolyte contains highly-fluorinated ether or carbonate solvents to form a robust SEI layer on Li metal surface. The challenge in the studies of electrolyte is still to realize the CE of Li metal anode above 99.7%. Interesting future studies would be the combination of protective coatings and state-of-the-art electrolytes to increase the upper limit of the CE (**Figure 1-8f**). Finally, more studies on the cell-level engineering to solve safety issues of liquid electrolyte based Li metal battery will be necessary in conjunction with increasing CE of Li metal anode.[34,138,139]

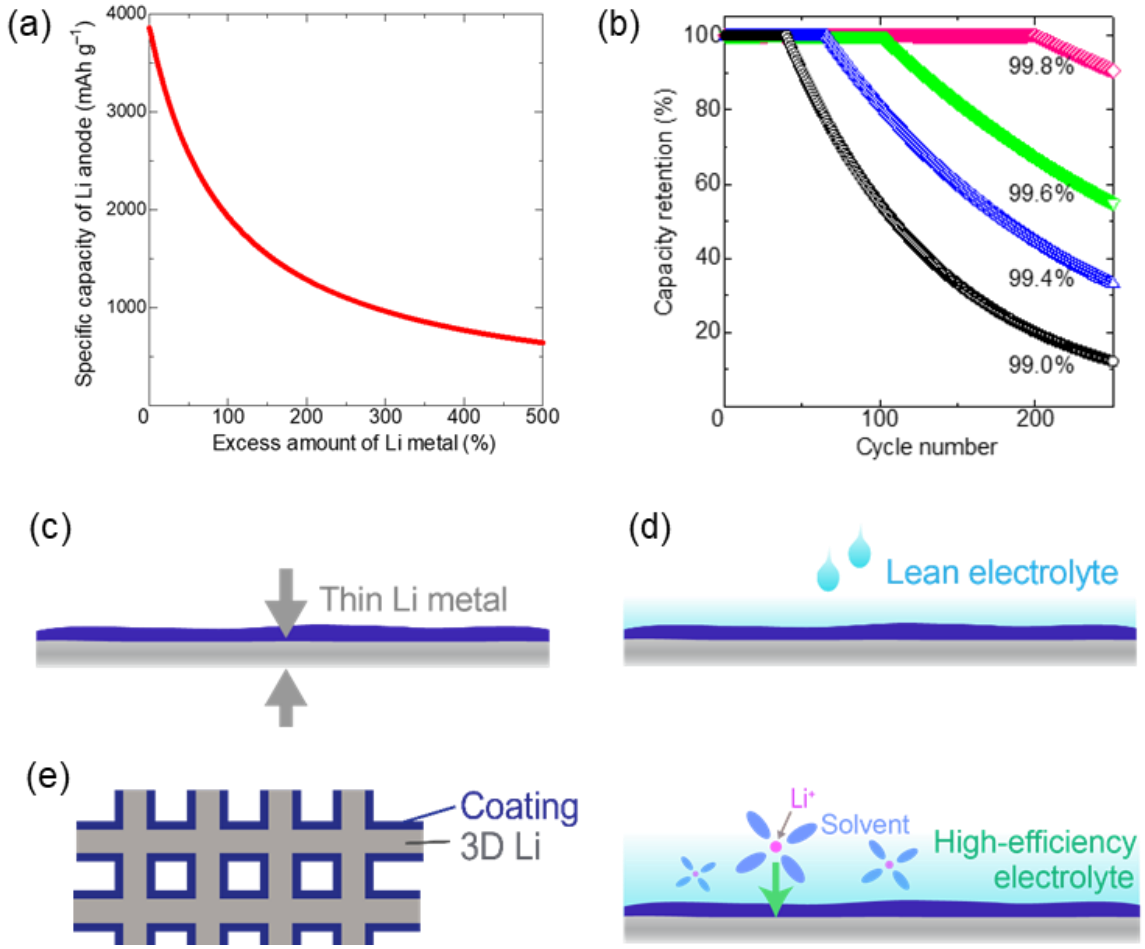

Figure 1-8 (a) Drop of specific capacity of Li metal anode with increasing amount of excess Li metal. 0% excess Li means all Li^+ ions transfer between the anode and the cathode during charging/discharging. (b) Simulated capacity retention of Li metal battery with 40% excess amount of Li metal with increasing coulombic efficiency of the Li anode. Capacity loss at the cathode side is assumed to be negligibly small compared to the anode side. Prospective testing conditions for Li metal anode with the protective coatings: (c) Thin Li metal electrode to reduce the excess amount of Li; (d) Lean electrolyte to reduce the total weight of the battery pack; d) Coating on the 3D-structured Li metal to reduce the influence of volume change during plating/stripping of Li metal; (e) Protective coating used with state-of-the-art electrolyte to further increase the CE of Li metal anode.

1.9 Acknowledgement

Chapter 1, in full, is a reprint of materials published in the following paper: Hongyao Zhou, Sicen Yu, Haodong Liu* and Ping Liu*, “Protective coatings for lithium metal anodes: recent progress and future perspectives” *J. Power Sources*, **2020**, 450, 227632. The dissertation author was the primary researcher for the data presented and was the primary author of this publication. The permissions to reproduce this material were granted by Elsevier, copyright 2020.

Chapter 2 Molecular design of gel polymer electrolyte and the application to lithium metal protection

2.1 Introduction

Gel polymer electrolyte (GPE) is composed of a polymer host swollen in a liquid electrolyte (LE) and is widely used in various electrochemical devices such as lithium (Li) batteries,[106,140,141] supercapacitors,[142] stretchable electronics,[143–145] and as an interfacial protection for Li metal anode.[33,133,146,147] GPE generally shows higher ionic conductivity than solid polymer electrolyte (SPE) and higher mechanical strength than LE.[148,149] The ionic conductivity (σ), transference number (t_+ for cation), and mechanical strength of GPE are dependent on the solvent content absorbed in the polymer host (swelling ratio). Small swelling ratio of the polymer host increases the coupling between the polymer segments and ions, and the selective bindings of anion to the polymer host results in higher t_+.[150,151] GPE is also mechanically stronger at smaller swelling ratio because of higher degree of polymer–polymer interactions.[150,152] In contrast, small swelling ratio often results in reduced values of σ.[150,152–156] For the application in Li batteries, a higher value of t_+ is always desired to minimize the concentration gradient of Li^+ in the electrolyte,[147,157] and at the same time, a higher value of σ is equally important for the efficient ion transport. Therefore, the understandings on the trade-off among σ, t_+, and the mechanical properties of GPE is indispensable for the future development of GPE-based Li batteries. However, the previous research on the correlation between swelling ratio and ion transport/mechanical properties has been focused only on aqueous-based GPEs,[150,158] and much less experimental evidence and no theoretical model have been reported for organic-based GPEs.

To study the relationship between the swelling ratio and the ion-transport/mechanical properties, there are two essential conditions to be satisfied: (1) Cross-link density of the polymer host must be precisely tailored to limit

the swelling ratio at the equilibrium state. In the literature, a cross-linking of polyethylene oxide (PEO) oligomers has been commonly used to prepare organic-based GPEs.[133,152,159–162] However, no attempt on controlling the cross-link density has been reported, and the GPEs were usually used without purification of unreacted cross-linkers in the polymer host. (2) Polarities of the polymer host and the solvent must be matched to cause the swelling and to dissolve the salt in GPE. Unlike aqueous-based GPEs, organic-based GPEs have wide range of choices for the solvents from non-polar to polar ones. A combination of polar polymers (e.g. PEO) and polar solvents (e.g. ethylene carbonate (EC),[133,155,156,163] succinonitrile,[164] ionic liquid [144,165]) is widely used to construct an ion-conductive phase, because the large dipole moment can dissociate the anion and the cation. However, the strong polarity of the polymer host inevitably results in the increasing degree of ion–polymer coupling, higher activation energy (E_a), and reduced diffusion coefficient (D_+ for cation) of the charge carrier.[157,166] In contrast, the ions solvated in a low-polarity solvent absorbed by a non-polar polymer host should cause little ion–polymer coupling. Thus, different ion-transport properties are expected when the GPE is swollen in high-polarity or low-polarity media.

In this article, we systematically study the Li^+ transport properties (σ, t_+, E_a, D_+) and the rheological properties of GPE composed of polyacrylonitrile–polybutadiene copolymer (PAN-PBD) with a wide range of the cross-link densities (10^{-5}–10^{-2} mol cm^{-3}), which is swollen in ether (low-polarity) or carbonate (high-polarity) electrolyte (**Figure 2-1**). We report the σ–t_+ trade-off with respect to the swelling ratio, where the change of σ is simulated by percolation model, for the first time in organic-based GPE. Hansen solubility parameters (HSPs) are used to predict the swelling behavior of PAN-PBD, showing PBD phase favors the swelling in the ether electrolyte, while PAN phase swells in the carbonate electrolyte. The decoupling of Li^+ from the polymer host is realized in PBD

phase swollen in the ether electrolyte, where no change in E_a is observed. To demonstrate a practical application of GPE, the cross-linked PAN-PBD thin film is used as a protective coating for Li metal. Morphology of the electrodeposited Li metal changes from dendritic to spherical with the coating. High σ and viscosity of the GPE (realized in lower cross-link density) are found to be beneficial for the Li deposition without breaking the coating layer. A high shear modulus of the coating, commonly believed to be an essential property to suppress the Li dendrite, appears to be unnecessary for the GPE-based coatings, if sufficiently high σ ($> 10^{-4}$ S cm^{-1}) and viscosity are provided. This study paves the way for a rational design of GPE microstructure through the controlled cross-link density and the polarity-matchings between polymer hosts and organic solvents.

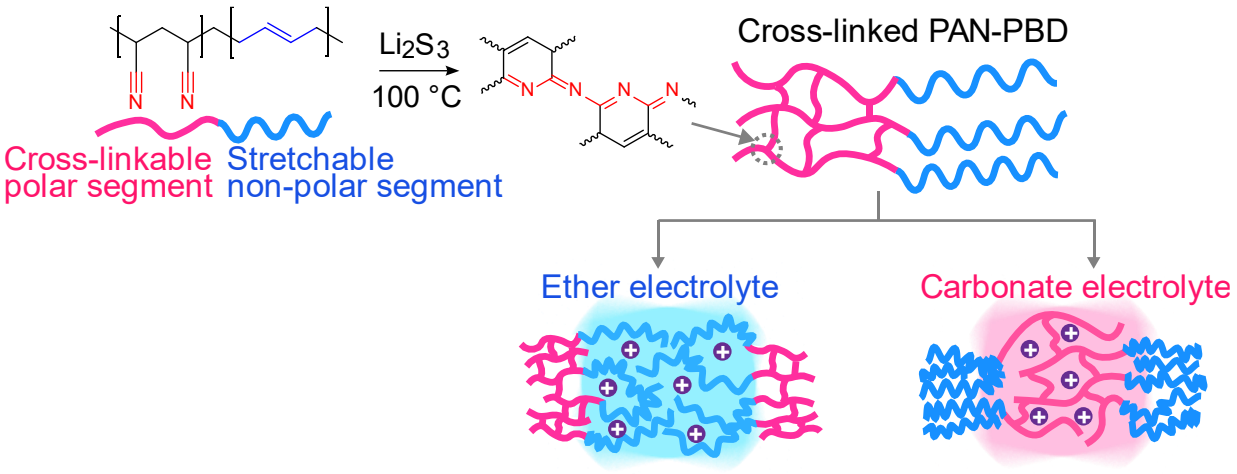

Figure 2-1 Scheme of the cross-linking of PAN-PBD and swelling in the ether and carbonate electrolytes. The cross-link density and the swelling ratio of the resulting polymer is controlled by the concentration of Li_2S_3 during the cross-linking step. Because of the difference in the polarity, the PBD, and PAN segments favor the swelling in ether (lower polarity), and carbonate (higher polarity) electrolytes, respectively. The different degree of ion–polymer interaction in each phase is expected to cause distinctive ion-transport properties in the GPE.

2.2 Results and discussion

2.2.1 Cross-linking reaction of PAN-PBD copolymer with Li_2S_3 catalyst

Self-cyclization of PAN is an attractive approach to form cross-links without introducing additional cross-linking oligomers into the polymer host.[140,167] Conventionally, self-cyclization of PAN was initiated at temperatures above 200 °C,[168–170] and the resulting cross-link density only varied in a narrow range (e.g. 1.5–2.5 × 10^{-4} mol cm^{-3}) regardless of variations in the heating time.[167] The difficulty in varying the cross-link density of PAN can be attributed to the high activation energy (149 kJ mol^{-1}) for the cyclization, and the spontaneous propagation of the cyclization after the activation.[171] Lithium trisulfide (Li_2S_3 = Li_2S + 2S) in dimethyl formamide (DMF) solution was known to catalyze the PAN cyclization and to lower the initiation temperature.[172,173] Here we carry out the cross-linking of PAN-PBD in a mixed solution of DMF and tetrahydrofuran (THF) with varied concentration of Li_2S_3 (Li_2S_3/AN = 0–1.0 in mol/mol) at 100 °C to vary the cross-link density of PAN segments (Figure 2-1). After the cross-linking, residual DMF and Li_2S_3 remaining in the polymer film is removed by the solvent extraction in dimethoxyethane (DME), which has a high solubility for polysulfide species (S_x^-) (**Figure S2-1,** Appendix). Structure of cross-linked PAN-PBD is analyzed by FTIR, and the absorbance is normalized to the peak at 970 cm^{-1} (trans C=C–H of PBD) (**Figure 2-2**). Absorbance at 1440 cm^{-1} (saturated C–H bending of PBD) remains constant after the cross-linking, indicating the PBD segment is unreacted. Increasing absorbance at 1600 cm^{-1} (C=C/C=N stretching) and decreasing absorbance at 2240 cm^{-1} (C≡N stretching of PAN) suggest that the cyclization of C≡N into the conjugate C=C/C=N is catalyzed by Li_2S_3. Appearance of the peaks at 2190 cm^{-1} (conjugate C≡N) and 790 cm^{-1} (1,2,3-trisubstituted =C–H bending) suggests that dehydrogenation of α- and β-hydrogens of PAN takes place and forms C=C double bond in the PAN main chain.

Red shift of the C=C/C=N peak position from 1620 to 1612 cm^{-1} with increasing Li_2S_3/AN ratio indicates extending length of the C=C/C=N conjugation (**Figure S2-2,** Appendix). X-ray photoelectron spectroscopy (XPS) shows increasing intensity of S 2*p* peak at 163.3 eV with increasing Li_2S_3/AN ratio, revealing the possible presence of both S–S and S–C bonds[174] (**Figure S2-3,** Appendix). Based on the above analysis, we propose a following reaction scheme: (1) Li_2S_3 catalyzes the dehydrogenation at PAN backbone (possibly by producing H_2S gas) and forms conjugate C≡N. (2) Nucleophilic attack of S_x^- on C≡N produces S_x–C=N^- anion and initiates intramolecular self-cyclization between adjacent C≡N groups. The cyclization reaction between the conjugate C≡N groups are sterically favored (formation of six-membered ring), compared to between nonconjugate C≡N groups. (3) The cyclization reaction propagates between different PAN chains and result in intermolecular cross-linking. (**Figure S2-4,** Appendix)

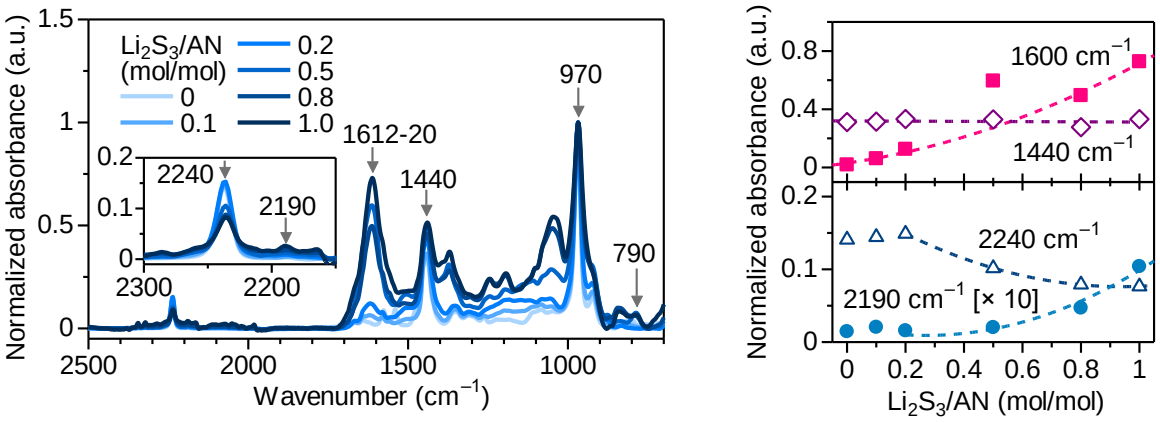

Figure 2-2 (a) FTIR spectra of PAN-PBD cross-linked under varied Li_2S_3/AN ratio (0–1.0). The inset shows the magnified view of the C≡N stretching peaks. The absorbance is normalized to the peak at 970 cm^{-1} (trans C=C–H of PBD). (b) Changes of the absorbance at the selected peaks (1600 cm^{-1} → C=C/C=N; 1440 cm^{-1} → CH_2 of PBD; 2240 cm^{-1} → C≡N; 2190 cm^{-1} (magnified by 10) → conjugate C≡N), showing the cyclization of C≡N into a fused pyridine structure. The dashed lines represent the least-squares fittings to the experimental results.

2.2.2 Swelling ratio and cross-link density of PAN-PBD GPE

Swelling ratio of cross-linked PAN-PBD film is expresses as a volume ratio of the swollen polymer (V) to the volume of dry polymer (V_0) and plotted as a function of Li_2S_3/AN ratio (**Figure 2-3a, b**). The swelling ratio in DME solvent decreases with increasing ratio of Li_2S_3/AN because of the increasing number of the intermolecular cross-links formed in the PAN segments. The swelling ratio in pure dimethyl carbonate (DMC) is lower than the value in DME, and the addition of EC in DMC increased the swelling ratio. An addition of lithium hexafluorophosphate ($LiPF_6$) in DMC/EC solvent reduces the swelling ratio of PAN–PBD film (**Figure 2-3b**). We confirmed that an addition of lithium perchlorate ($LiClO_4$) also reduces the swelling ratio to the same degree as $LiPF_6$ (**Figure S2-5,** Appendix). In contrast, an addition of lithium bis(fluorosulfonyl)imide (LiFSI) causes no change in the swelling ratio in DME (**Figure 2-3a**). FTIR analysis revealed a stronger absorbance of C≡N–Li^+ dipole–ion pair in DMC/EC/$LiPF_6$, compared with DME/LiFSI (**Figure S2-6,** Appendix).

To obtain a theoretical basis of the swelling behavior, we used HSPs and quantified the degree of interaction between the polymers (PAN, PBN) and the solvents (DME, DMC, EC, DMC + EC). Relative energy difference (RED) is a useful parameter to evaluate the solubility of polymers in solvents,[175] which is calculated from the difference of HSPs between the polymer and the solvent (Calculation **A,** Appendix). Typically, a good solvent shows RED < 1 (i.e. the polymer and the solvent have a similar polarity), while a poor solvent shows RED > 1. DME shows low RED with PBD (0.95) and high RED with PAN (1.40), indicating preferential solvation of PBD phase (**Figure 2-3c**). DMC shows high RED with both PBD (1.17) and PAN (1.47), which explains the low swelling ratio of PAN-PBD in DMC. In contrast, pure EC shows low RED with PAN (0.89) and significantly higher RED with PBD (3.05), suggesting only PAN phase can swell in EC. In a mixed solvent of DMC and EC (1:1 in weight

ratio), RED with PAN (0.85) shows the similar value in pure EC. Despite the RED with PBD (1.61) is lower in the DMC/EC mixed solvent than in pure EC, RED > 1 suggests the solvation of PBD phase is still unlikely in DMC/EC. Therefore, the increased swelling ratio in the DMC/EC mixed solvent from the pure DMC is explained by the reduced RED value with PAN phase. The favorable solvation of PAN in DMC/EC also explains that the decrease of swelling ratio by the addition of salt ($LiPF_6$ and $LiClO_4$) is caused by the formation of $C{\equiv}N{-}Li^+$ pair, which behaves as a physical cross-linking.

Cross-link density (N) of PAN-PBD can be calculated from the swelling ratio by using Flory–Rehner equation:[176,177]

$$N = \frac{\ln(1 - v_2) + v_2 + \chi_{12} v_2}{V_1 (v_2/2 - v_2^{1/3})} \qquad (2\text{-}1)$$

where V_1 is the molar volume of the solvent, v_2 is the volume fraction of polymer in the swollen state, which equals the inverse of the swelling ratio ($v_2 = V_0/V$), and χ_{12} is solvent–polymer interaction parameter, which is proportional to the RED squared (Calculation **B,** Appendix).[178] Note that the χ_{12} is averaged by the volume fraction of PAN and PBD in the copolymer (PAN:PBD = 32:68, vol/vol), therefore, the N is also an averaged value of the entire copolymer structure. As a result, the N calculated from the swelling ratio in DME is smaller than the values calculated from the swelling ratio in DMC and DMC/EC at low Li_2S_3/AN ratio (**Figure 2-3d**). This result reflects the influence of polymer microstructure, where the cross-link is formed only in PAN phase, and thus the polymer swelling is more restricted in DMC/EC mixed solvent (the solvents only swell PAN phase). In contrast, the swelling of PBD phase is less restricted in DME (the solvent only swells PBD phase), and thus the effective value of N is lower. The cross-link density estimated from the swelling in DMC is high because of the poor solubility for

both PAN and PBD. The influence of the microstructure is pronounced at larger swelling ratio (i.e. low Li_2S_3/AN ratio) and minimized at smaller swelling ratio, resulting in a convergence of the *N* values at higher Li_2S_3/AN ratio.

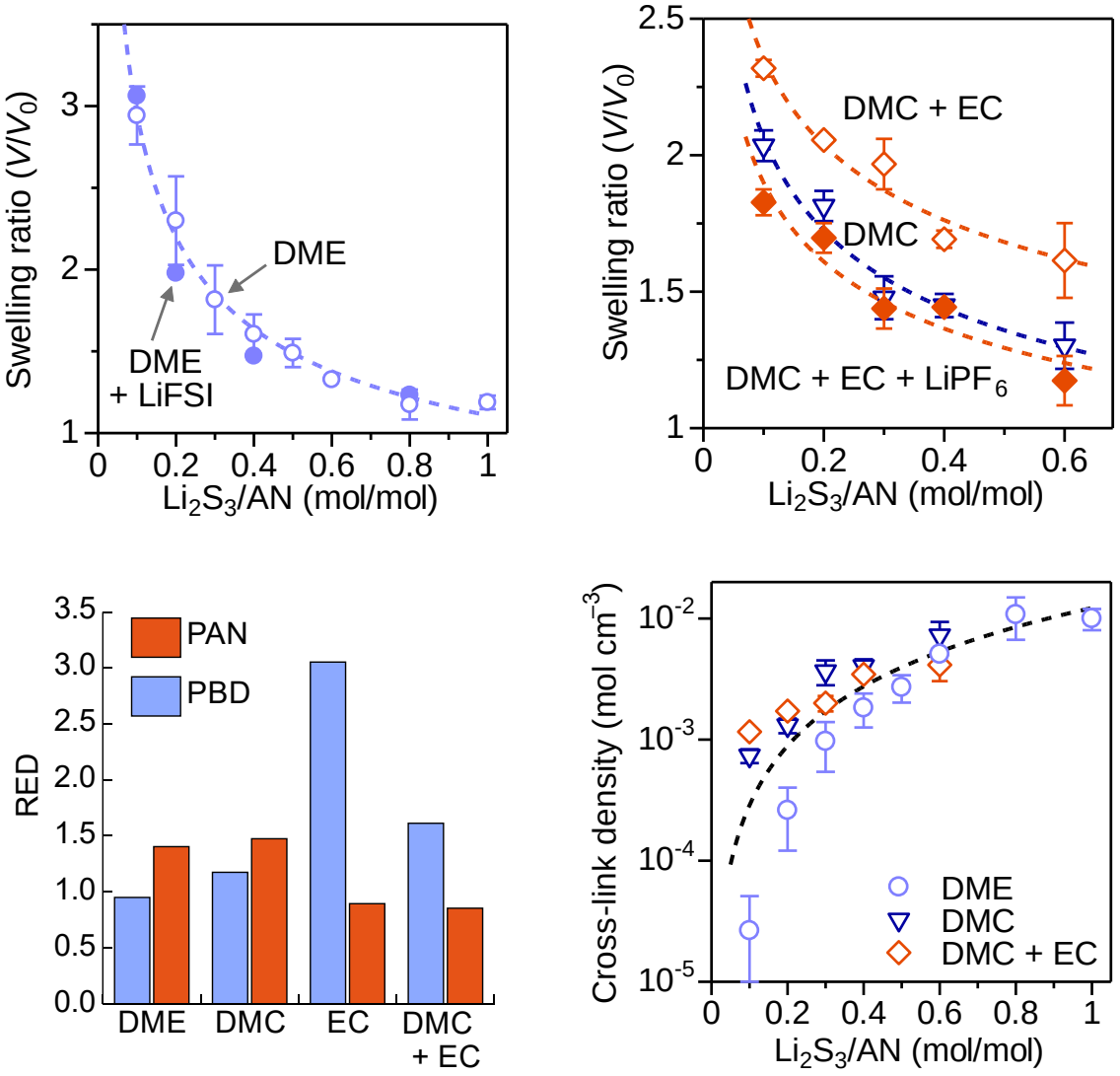

Figure 2-3 Swelling ratio of PAN-PBD in (a) DME (+ LiFSI, 1 ml kg^{-1}), and (b) DMC, DMC + EC (1:1) (+ $LiPF_6$, 1 mol kg^{-1}). Formation of C≡N–Li^+ pairs in DMC + EC decreases the swelling ratio when $LiPF_6$ is added. (c) Relative energy difference (RED) between the polymer (PAN, PBD) and the solvents (DME, DMC, EC, DMC + EC). A good solvent for a polymer generally shows RED < 1. (d) Cross-link density of PAN-PBD calculated from Equation (2-1) and the swelling experiment of (a) and (b). All the dashed curves represent the least-square fittings to the experimental data.

2.2.3 Relationship among ion-transport properties, swelling ratio, and solvent polarity

The σ of cross-linked PAN–PBD GPE swollen in DME/LiFSI, and DMC/EC/$LiPF_6$ is expressed as a function of the volume fraction of LE (ϕ_{LE}) absorbed in the polymer host (**Figure 2-4a**):

$$\phi_{LE} = 1 - \frac{V_0}{V} \qquad (2\text{-}2)$$

In both electrolytes, the change of σ at $\phi_{LE} > 0.4$ is gradual, then the σ sharply decreases as ϕ_{LE} drops to 0.2. A similar σ–ϕ_{LE} relationship was also observed in different organic-based GPEs such as a polymer blend of nitrile-butadiene and styrene-butadiene rubbers (NBR/SBR),[154] PEO,[152,155] and poly(methyl methacrylate) (PMMA).[156] However, no theoretical model has been proposed to explain the σ–ϕ_{LE} relationship.

Here we demonstrate the applicability of percolation model for the first time in organic-based GPEs. Percolation model was firstly proposed by Hsu to explain an insulator-to-conductor transition of a proton-conductive membrane (e.g. Nafion) as a function of the water content:[158]

$$\sigma = \sigma_0(\phi_{LE} - \phi_0)^n \qquad (2\text{-}3)$$

where σ_0 is a constant depending on the combination of polymer and electrolyte, ϕ_0 is a percolation threshold below which no ion-conductive pathway can form, n is a universal constant reported to range between 1.3 and 2 for a three-dimensional percolating system.[158,179–181] The σ_0 and ϕ_0 can be obtained from the linear fitting of $\sigma^{1/n}$ with respect to ϕ_{LE}, and the best fitting was obtained at $n = 2$ for our system (**Figure S2-7**, Calculation **C,** Appendix). The fitted parameters are: $\sigma_0 = 7.36 \times 10^{-3}$ S cm^{-1} (DME), 2.86×10^{-3} S cm^{-1} (DMC/EC); and $\phi_0 =$ 0.178 (DME), 0.201 (DMC/EC), respectively. As a result, the simulated values of σ agrees well with the experimental results (**Figure 2-4a**, **solid lines**).

The t_+ of PAN-PBD GPE is evaluated by the potentiostatic polarization method[182] (Calculation **D, Figure S2-8, S9,** Appendix). The low value of t_+ (< 0.4) is observed at higher swelling ratio (ϕ_{LE} > 0.4) (**Figure 2-4b**), which agrees with the low t_+ generally observed in LE both DME[183] and EC/DMC[184] electrolytes. The t_+ increases with decreasing ϕ_{LE} and reaches the maximum value of t_+ = 0.6, when ϕ_{LE} is close to the percolation limit ($\phi_0 \approx$ 0.2). Previously, a similar increase of t_+ with decreasing ϕ_{H2O} (volume fraction of water) was reported in an aqueous-based GPEs,[150,151] where the polymer is positively charged and can completely trap the counter anion at the lowest value of ϕ_{H2O} = 0.2, to achieve the highest value of $t_+ \approx$ 1.[150] In PAN-PBD GPE, the increase of t_+ could be attributed to the ion–dipole interaction between PAN and the counter anions (FSI^- and PF_6^-) to reduce the relative mobility of the anions, compared with Li^+. The increase of t_+ in DME electrolyte could be attributed to the anion trapping at the interphase between PAN and PBD, because non-polar PBD itself can have little interaction with ions (as evidenced by constant E_a at all range of ϕ_{LE}, see below). To maximize the t_+ in organic-based GPEs, we propose that a positively charged polymer could be used to electrostatically bind with the anions (which is much stronger than ion–dipole interaction) in the future study.

The D_+ of GPE can be calculated from Nernst–Einstein relation[185] as a function of σ, t_+, and ϕ_{LE}:

$$D_+ = \frac{RT\sigma t_+}{(z_+F)^2 c_0 \phi_{LE}} \quad (2\text{-}4)$$

where R is the standard gas constant, T is the temperature, F is the Faraday constant, z_+ is the charge number of the cation (z_+ = 1 for Li^+), c_0 is the bulk concentration of the charge carrier (c_0 = 1 mol kg^{-1}). At ϕ_{LE} > 0.4, the D_+ of PAN–PBD GPE is nearly constant at 1 × 10^{-7} cm^2 s^{-1} in DME, and 3 × 10^{-8} cm^2 s^{-1} in DMC/EC, respectively (**Figure 2-4c**). The D_+ at the plateau in DMC/EC agrees with the D_+ reported for hydrogenated nitrile-butadiene rubber (HNBR) GPE in propylene carbonate (PC) (D_+ = 0.9 × 10^{-8} cm^2 s^{-1}, 36% PAN content).[140]

The D_+ starts to decrease at $\phi_{LE} < 0.4$, and when ϕ_{LE} is close to the percolation limit ($\phi_0 \approx 0.2$), the D_+ drops to 1×10^{-8} cm^2 s^{-1} in DME, and 3×10^{-10} cm^2 s^{-1} in DMC/EC, respectively. The significant reduction of D_+ in DMC/EC electrolyte (where PAN is the ion-conduction phase) can be explained by the increasing degree of the C≡N–Li^+ interactions at lower ϕ_{LE}. This explanation is further supported by the increase of E_a only observed when the PAN–PBD GPE is swollen in DMC/EC (**Figure 2-4d,** the Arrhenius plot in **Figure S2-10,** Appendix). In contrast, the E_a of the GPE swollen in DME electrolyte (where PBD is the ion-conduction phase) remains constant even at low ϕ_{LE}, showing the Li^+ transport is decoupled from the interaction with the polymer host.

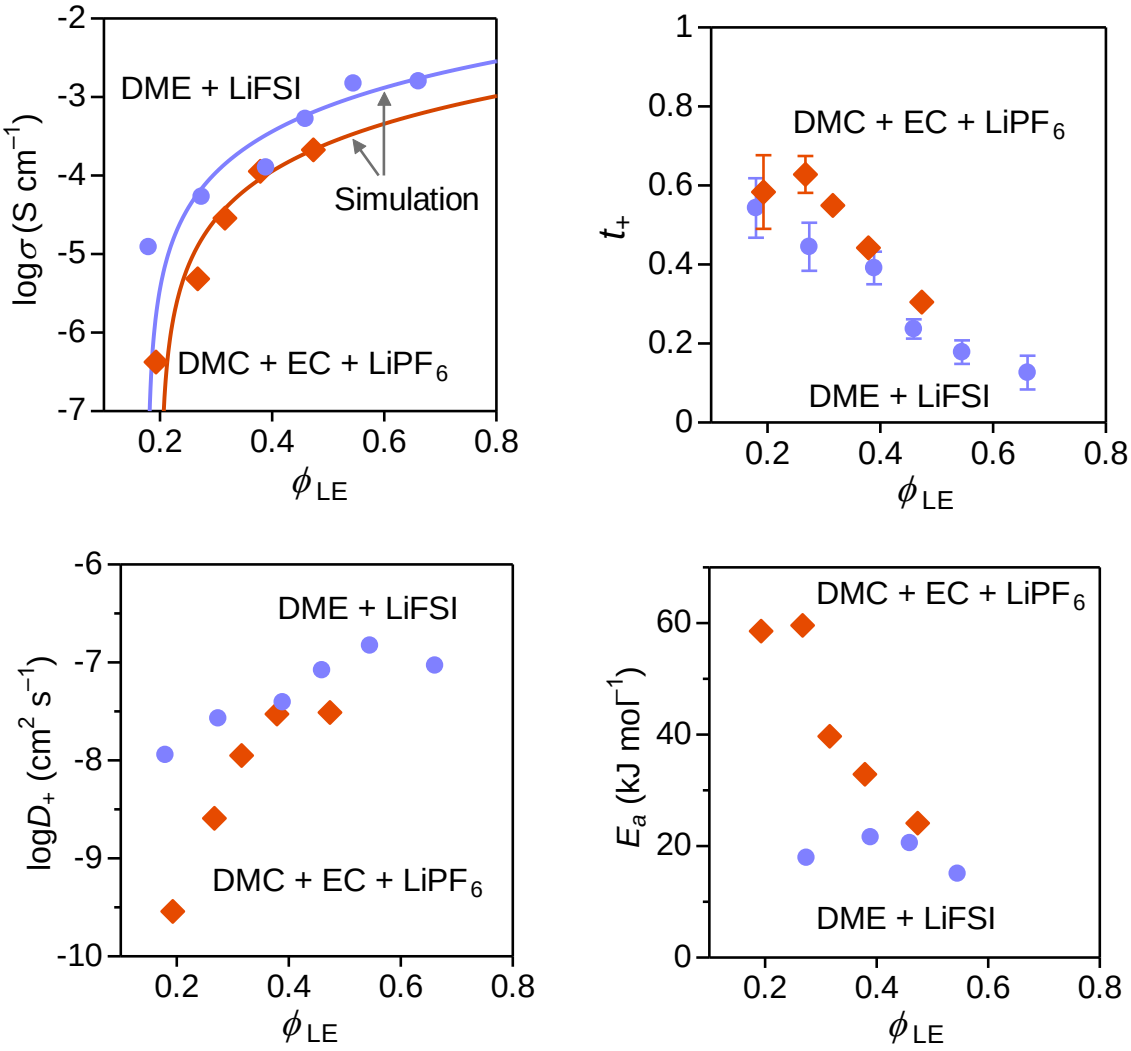

Figure 2-4 (a) Ionic conductivity, (b) cation transference number, (c) cation diffusion coefficient, and (d) activation energy of PAN–PBD GPE swollen in DME + LiFSI (1 mol kg^{-1}), and in DMC + EC (1:1) + $LiPF_6$ (1 mol kg^{-1}). The volume fraction of the liquid electrolyte (ϕ_{LE}) in the swollen polymer is controlled by the cross-link density of PAN–PBD.

2.2.4 Relationship between mechanical properties and cross-link density

Tensile strain is applied to the dry PAN-PBD to study the influence of cross-link density on the mechanical properties (**Figure 2-5a**). At the lowest cross-link density (Li_2S_3/AN = 0.1), PAN-PBD shows rubber-like behavior without any plastic deformation until the fracture. At higher cross-link density, the transition from elastic to plastic deformation appears after approximately 3% of the strain is applied (inset of Figure 2-5a), and the yield strength increases with increasing cross-link density. Young's modulus (E) is calculated from the slope of the stress–strain curve at the elastic region and plotted with the cross-link density estimated from the swelling ratio in DME (**Figure 2-5b**). The value of E increases by a factor of 10^2 when the cross-link density is increased from 3×10^{-5} to 1×10^{-3} mol cm^{-3}, while the elongation at break remains at 200%, showing the increasing toughness of the material. Further increase of the cross-link density to 1×10^{-2} mol cm^{-3} increases the E by a factor of four, while the elongation at break decreases to 50%, transforming into a rigid and brittle material.

Oscillatory shear strain is applied to PAN-PBD swollen in DME/$LiClO_4$ or DMC/EC/$LiClO_4$ to evaluate the rheological properties. $LiClO_4$ was used instead of LiFSI or $LiPF_6$ because of the better stability under the ambient environment. Linear viscoelastic regime is evaluated to be below 1% of the strain (Figure S2-11, Appendix). Frequency dependence of storage (G') and loss (G'') modulus, and phase angle ($\delta = \tan^{-1}(G''/G')$) are evaluated at a constant strain of 0.1% (under the linear viscoelastic regime) (**Figure 2-5c, d**). In both DME and DMC/EC electrolytes, higher cross-link density (Li_2S_3/AN = 0.3) results in larger G' value while the G'' shows little difference from the lower cross-link density (Li_2S_3/AN = 0.1). When the oscillation frequency is reduced from 10 to 0.1 rad s^{-1}, G' of Li_2S_3/AN = 0.1 starts decreasing, and the δ increases from nearly 0° to 20° and 10° in DME and DMC/EC

electrolytes, respectively. The increase of δ indicates the transition of GPE from a purely elastic body to a more viscous material.

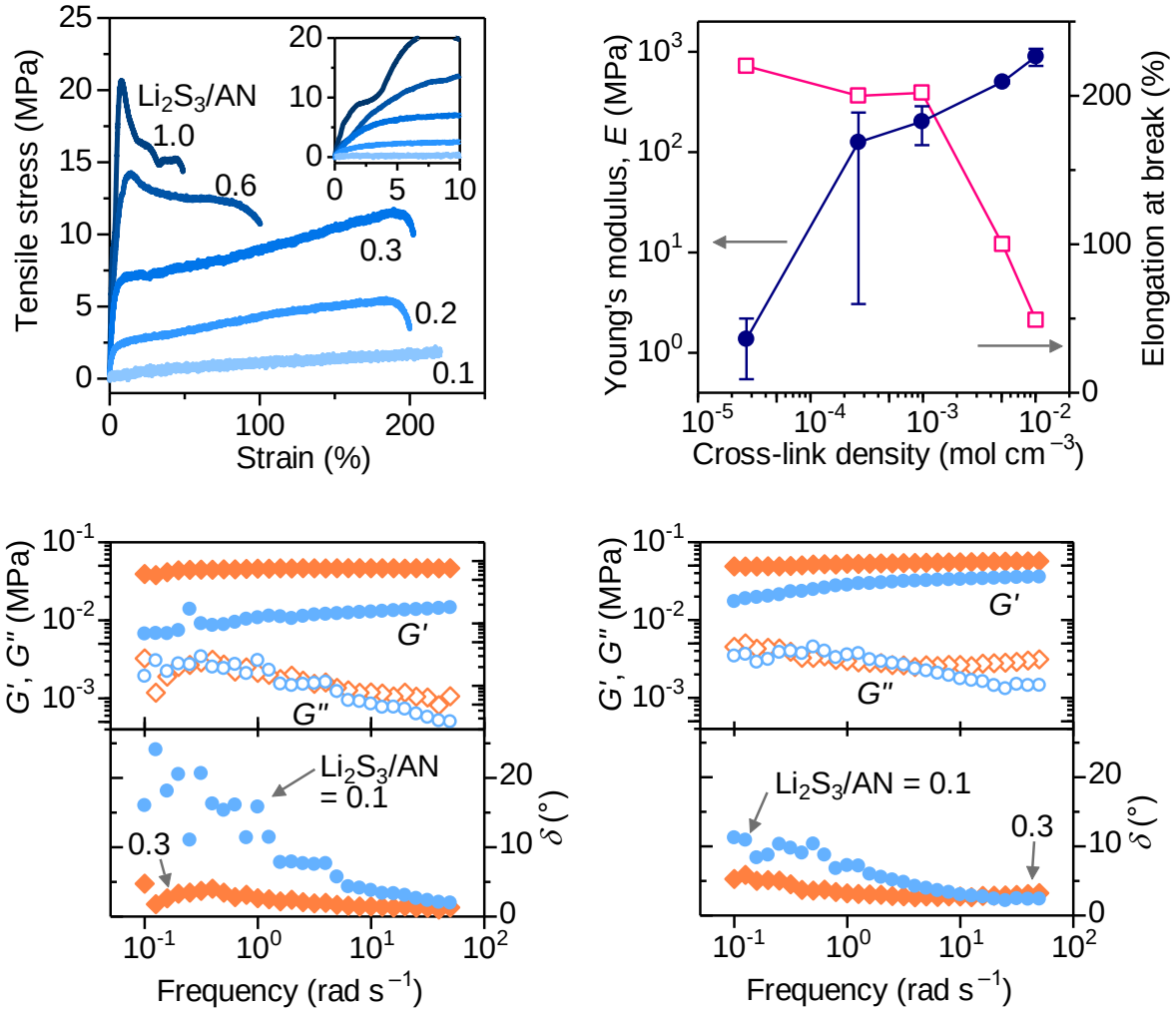

Figure 2-5 (a) Stress–strain curve of the dry PAN–PBD film. (b) Young's modulus and elongation at break evaluated from (a), plotted with the cross-link density. (c, d) Frequency dependence of storage and loss modulus (*G*, *G"*), and phase angle (δ) of PAN–PBD swollen in (c) DME + $LiClO_4$ (sat. 0.3 mol kg^{-1}), and in (d) DMC + EC (1:1 wt) + $LiClO_4$ (1 mol kg^{-1}), evaluated under a constant strain of 0.1%.

2.2.5 Influence of cross-link density in protective coatings for Li metal

Previously, both PAN[133] and PBD[186] were used as protective coatings[147] for Li metal anode. PAN was reported to reduce the reactivity of EC with Li metal through the dipole–dipole interaction,[133] while the PBD copolymer was used as the elastic binder for the inorganic nanofillers.[186] To use the cross-linked PAN–PBD GPE as the protective coating, we reduced the film thickness to 10 μm and placed between the battery separator and the copper (Cu) current collector (**Figure S2-12,** Appendix). The PAN–PBD thin film is swollen to the equilibrium in the LE (DMC + EC (1:1) + LiPF6 (1 mol kg^{-1}) + fluoroethylene carbonate, FEC (5wt%) as additive) before the cell assembly. During the first deposition of Li metal on Cu, the voltage polarization increases with the increasing cross-link density of PAN–PBD coating (**Figure S2-13,** Appendix) because of the reduced σ (Figure 2-4a). After the Li deposition (capacity = 1 mAh cm^{-2}), we observed that the Li metal breaks the coating and deposits on the surface when the Li_2S_3/AN ratio is equal to or greater than 0.4, while all the Li metal is plated underneath the coating below the ratio of 0.4 (**Figure 2-6a,** see **Figure S2-14** for the optical images underneath the coating, Appendix). The observation agrees with the previous study where a thick Nafion coating (50 μm) with low σ (< 10^{-5} S cm^{-1}) resulted in the non-uniform Li deposition concentrated at the local defects in the coating.[119] The conductivity measurement (Figure 2-4a) indicates the σ higher than at least 10^{-5} S cm^{-1} is required to deposit Li metal underneath the 10 μm-thick coatings.

On the uncoated Cu (current density = 0.1 mA cm^{-2}), two different morphologies of the Li metal are observed, showing a flat Li deposit where the Li is deformed by the compressive pressure from the battery separator, and a dendritic shape where the Li is less compressed (**Figure 2-6b, c**). In contrast, the Li metal deposited underneath the coating uniformly shows the spherical morphology with a diameter of 20 μm, and no dendritic Li is

observed (**Figure 2-6d, e**). The spherical Li deposits are also observed underneath the coating with slightly higher cross-link density (Li_2S_3/AN = 0.2, 0.3), however, only the flat and compressed Li deposits (like the morphology on the uncoated Cu) is observed when the Li is plated on the coating surface (Li_2S_3/AN = 0.4) (**Figure S2-15,** Appendix).

When Li metal is deposited at higher current density (0.5 mA cm^{-2}), the Li deposits on the uncoated Cu shows the smaller particle size (< 2 μm), and the more pronounced dendritic morphology (**Figure 2-6f, g,** see **Figure S2-16** for the optical images, and **Figure S2-17** for the SEM images at different magnifications, Appendix). In contrast, the Li deposits underneath the coating shows the granular morphology with the larger particle size (≈ 5 μm) than the Li on the uncoated Cu (**Figure 2-6g**). Furthermore, the Li particles adhered on the least-cross-linked coating (Li_2S_3/AN = 0.1) shows the large spherical morphology (diameter ≈ 15 μm, **Figure 2-6h, i**) which resembles to the Li deposited underneath the coating at 0.1 mA cm^{-2} (Figure 2-6d, e). No spherical Li particle is observed on the coating at Li_2S_3/AN = 0.3. The higher viscosity ($\delta \approx 10°$ at the oscillation frequency of 0.1 rad s^{-1}, Figure 2-5d) of the coating at Li_2S_3/AN = 0.1 appears to be beneficial for the better adhesion with the Li particles. A recent report on the morphological improvement of Li deposits in the viscous LE further supports the merit of using the viscous coating.[31] Contrary to the common belief that high shear modulus is required to suppress the Li dendrite,[27,30] the swollen GPE (with significantly lower shear modulus of $G \sim 10^{-2}$ MPa than the dry SPE, for example, G(PEO) = 26.2 MPa)[30] is proved to be useful as the protective coating for Li metal.

XPS spectra at the F 2*p* and P 2*p* region reveals that LiF and phosphates ($Li_xPO_yF_z$)[187] are invariably present in the solid electrolyte interface (SEI) layer of the Li deposits on the both uncoated and PAN–PBD-coated Cu (**Figure 2-6j, m**). The LiF and phosphates are the decomposition products of $LiPF_6$ or FEC in the LE phase. The

N 1*s* and S 2*p* spectra respectively shows the increasing peak intensity of sp^3-hybridized N,[188] sulfoxide bond (S–O), S–S, and possibly S–C bond[174] with increasing Li_2S_3/AN ratio (**Figure 2-6k, l**). Because the LE contains no N or S species, the N and S compounds must be produced from the decomposition of the PAN–PBD coating. Lower volume fraction of LE ($\phi_{LE} \approx 0.3$, Figure 2-3b) at Li_2S_3/AN = 0.3 represents higher surface concentration of PAN–PBD segment on the Li deposits, and thus the increasing ratio of the SEI products is derived from the coating side. The XPS analysis points out the importance of tuning the cross-link density (the swelling ratio) of the polymeric coating to balance the ratio between the SEI products derived from the LE, or from the protective coating.

The long-term stability of the coating is evaluated by the repetitive deposition/dissolution of Li metal for 50 cycles (**Figure S2-18,** Appendix). All Li is deposited underneath the coating at Li_2S_3/AN < 0.3, while a minor amount of Li is deposited on top of the coating surface at Li_2S_3/AN = 0.3. The low values of ϕ_{LE} (≈ 0.3), σ ($< 10^{-4}$ S cm^{-1}), and also the low viscosity ($\delta < 5°$) are likely to cause a tip-driven growth of Li filament through the local defect, which is commonly observed in more ionically resistive and brittle solid state electrolytes.[189] Therefore, $\sigma > 10^{-4}$ S cm^{-1} is desired for the long-term stability of GPE-based protective coatings. Despite the morphological improvement of the Li deposits, coulombic efficiency (CE) of the Li metal deposition/dissolution for 50 cycles shows no improvement by the surface coating, compared to the CE on the uncoated Cu (**Figure S2-19,** Appendix). The morphology of Li deposits after the 50 cycles shows aggregation of fine Li filaments with the domain size less than 1 μm (**Figure S2-20,** Appendix). The morphological change during the cycling is possibly caused by the build-up of inactive Li deposits[5], which reduces the effective area of Li deposits directly in contact with the coating, and also the effective pressure exerted on the Li deposits. Optimization of the current collector (e.g. 3D

structure),[22] and a rigorous control on the cell stack pressure could be a promising way to enhance the benefits of protective coatings.

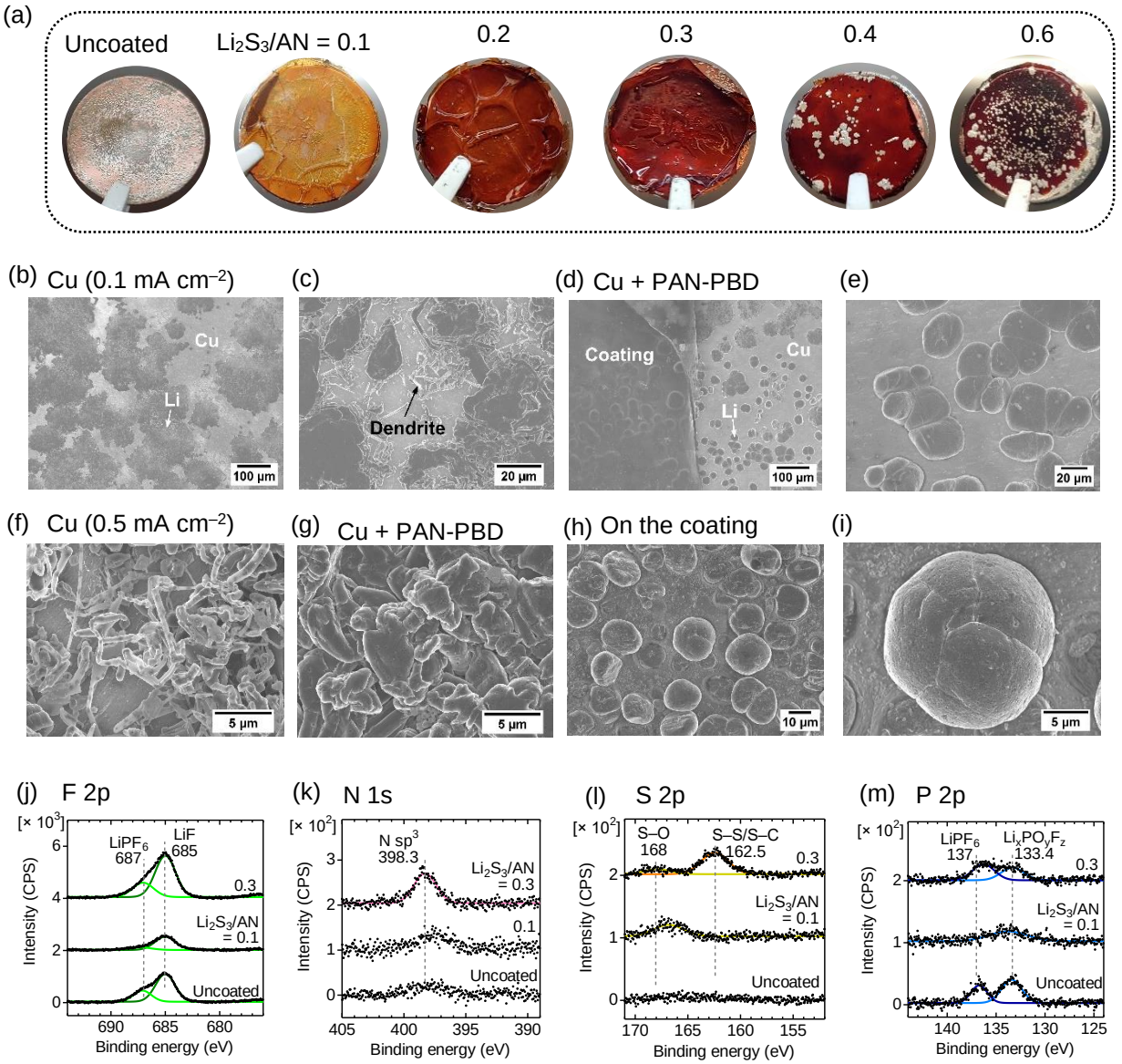

Figure 2-6 (a) Optical images after the first deposition of Li metal on Cu foil with/without a protective coating of PAN–PBD cross-linked at Li_2S_3/AN = 0.1–0.6. (b–g) SEM images after the first deposition of Li metal on (b, c, f) uncoated Cu, and on (d, e, g) PAN–PBD-coated Cu (Li_2S_3/AN = 0.1). (h, i) The Li metal adhered on the coating, showing the spherical morphology resembling to (e). (j–m) XPS spectra of the Li metal after the first deposition on uncoated, and PAN–PBD-coated Cu (Li_2S_3/AN = 0.1, and 0.3).Current density = 0.1 (a, b–e, j–m), and 0.5 (f–i) mA cm^{-2}. Charge capacity = 1 mAh cm^{-2} (a–m). Electrolyte = DMC + EC (1:1) + $LiPF_6$ (1 mol kg^{-1}) + FEC (5wt%) for all the experiment.

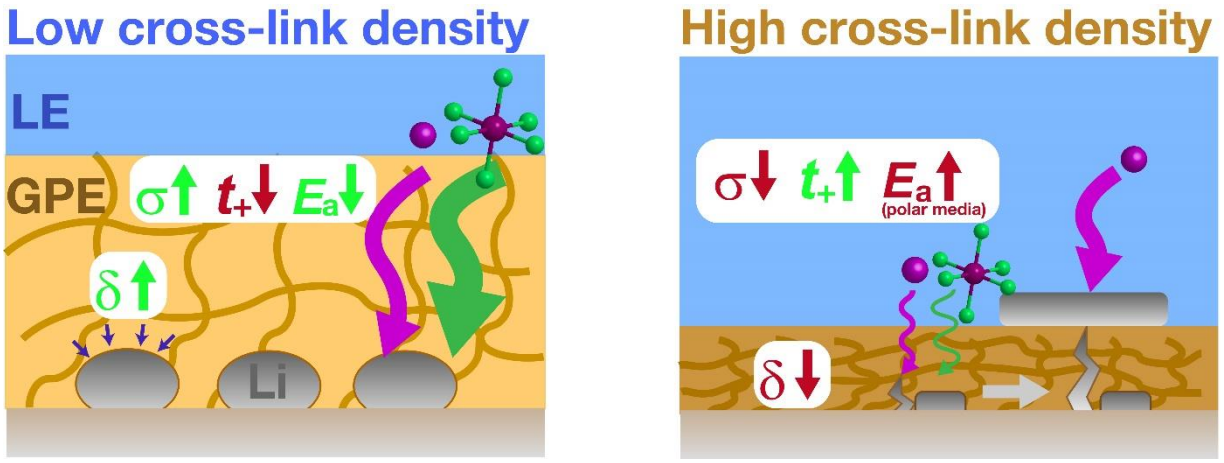

Figure 2-7 Schematic representation of ion-transport properties (σ, t_+, E_a), and rheology (phase angle, δ) of GPE at low/high cross-link density, and the Li deposition process through the protective GPE coating. At low cross-link density, the large swelling ratio increases σ but decreases t_+ (i.e. lower relative mobility of Li^+ than the anion). The higher viscosity (δ) at low cross-link density results in the spherical morphology of Li deposits. At high cross-link density, the low swelling ratio decreases σ but increases t_+. The increasing degree of dipole– Li^+ interaction also increases E_a in the polar polymer swollen in the polar electrolyte. The lower values of σ and δ are prone to cause the tip-driven Li growth through the local defect, eventually leading to the Li plating on top of the coating.

2.3 Conclusions

In summary, we controlled the cross-link density of PAN–PBD copolymer by adjusting the mole ratio of Li_2S_3/AN to study the influence of the swelling ratio to the ion-transport and rheological properties of the GPE. In addition, the presence of both polar and non-polar segments in PAN–PBD enables us to evaluate the influence of the solvent polarity. We used the PAN–PBD GPE as the protective coating for Li metal and made the correlations between the GPE properties and the morphology of Li deposits (**Figure 2-7**). Low cross-link density results in high ϕ_{LE} and σ (which can be simulated by the percolation model), and low E_a (~ 20 kJ mol^{-1}). The higher viscosity ($\delta >$ 10°) of the coating benefits from the better adhesion with the Li deposits and improve the Li morphology from the dendritic to the large spherical particles (15–20 μm). In contrast, high cross-link density results in low ϕ_{LE}, σ, and δ, which are prone to cause the tip-driven Li growth, and the penetration through the coating. Once the electronic pathway is formed in the coating, the Li deposition initiates from the coating surface, leading to the failure of the protective function. To avoid the coating failure over the long cycles, the σ higher than 10^{-4} S cm^{-1} is desirable. The increasing degree of ion–polymer interaction at lower ϕ_{LE} increases E_a (~ 60 kJ mol^{-1}) only when the GPE is swollen in the polar electrolyte (DMC + EC + $LiPF_6$), and no increase of E_a is observed when swollen in the less polar electrolyte (DME + LiFSI). The advantage of reducing ϕ_{LE} is the increase of t_+. However, the trade-off between σ and t_+ significantly limits the performance of GPE-based protective coatings, in terms of enhancing the selectivity towards Li^+ transport. To simultaneously achieve both high σ and t_+, introducing the strong ionic binding between the anions and the positively charged polymer chains (the method widely used in aqueous-based GPEs) could also be a promising structural design for organic-based GPEs.

2.4 Experimental methods

2.4.1 Materials

Poly(acrylonitrile-*co*-butadiene) (37–39wt% acrylonitrile content, Sigma Aldrich, U.S.), lithium sulfide (Li_2S, 99.98%, Sigma Aldrich,) elemental sulfur (S, sublimed, Fisher scientific), lithium bis(fluorosulfonyl)imide (LiFSI, battery grade, Capchem, China), lithium hexafluorophosphate ($LiPF_6$, battery grade, BASF, Germany), lithium perchlorate ($LiClO_4 \geq 95.0\%$ Sigma Aldrich), dimethoxyethane (DME, battery grade, BASF), dimethyl carbonate (DMC, battery grade, BASF), ethylene carbonate (EC, battery grade, BASF), and fluoroethylene carbonate (FEC, battery grade, Capchem) were used as received. Tetrahydrofuran (THF, reagent grade, Spectrum Chemical, U.S.) and dimethyl formamide (DMF, reagent grade, Spectrum Chemical) were dried with activated molecular sieve (4A, Spectrum Chemical) prior to the use.

2.4.2 Preparation of cross-linked PAN-PBD film

The cross-linking reaction was performed inside the argon-filled glove box ($H_2O < 0.5$ ppm, $O_2 < 1$ ppm). 2.0 g of PAN–PBD was dissolved in 18 g of THF to obtain 10wt% PAN-PBD solution (stock solution **1**). 0.37 g (8.0 mmol) of Li_2S and 0.51 g (16 mmol) of S were dissolved in 4.0 mL of DMF to obtain Li_2S_3 (2 mol dm^{-3}) solution (stock solution **2**). Varied volume of the solution **2** (0–1.7 mL) was added into the solution **2** (4.5 g) to obtain a mixed solution **3** with various Li_2S_3/AN (0–1.0 mol/mol). The weight ratio of THF/DMF in the mixed solution **3** was kept constant at 2.3 by dilution with additional DMF. Then, the mixed solution **3** was poured into a Teflon-coated petri dish and heated at 100 °C for 30 hours to complete the cross-linking reaction. THF and DMF were evaporated during the heating and a dark-colored, free-standing film was obtained. The typical thickness of the cross-linked PAN-PBD film ranged between 100 and 200 μm. After the cross-linking, the film was immersed in

DME solvent for three days (which was replaced each day) to extract any residual DMF and unreacted polysulfides. A thinner film with typical thickness of approximately 10 μm was prepared by coating 60 μL of the mixed solution **3** on a stainless-steel substrate (2 cm^2) and heated at 100 °C for 20 hours to complete the cross-linking reaction. The film was immersed in DMF to enable the peeling-off from the substrate and rinsed in DMC for several times (Figure S2-12, Appendix).

2.4.3 Characterization and swelling test of the cross-linked PAN–PBD film

The chemical bonding in the cross-linked PAN-PBD film was analyzed with attenuated total reflectance (ATR)-FTIR (UATR 2, PerkinElmar, U.S.). The swelling ratio of cross-linked PAN-PBD film was measured by comparing the area of the film before and after being immersed in the electrolyte solution. Cross-linked PAN-PBD film was cut into a circle shape (diameter = 13–16 mm) and immersed in the solvents (DME, DMC, DMC + EC) for 24 hours. The influence of the additional salts (LiFSI, $LiPF_6$, $LiClO_4$) was evaluated by transferring the film fully swollen in the solvents to the salt-added electrolyte solution. The swollen film was placed between two glass plates, and the optical image was recorded (Figure S2-21, Appendix). The area was directly evaluated from the digitized image, using an image processing software (ImageJ ver. 1.51h, N.I.H., U.S.). The swelling ratio is converted from the area ratio (A/A_0) to the volume ratio (V/V_0), under the assumption of the isotropic volume change: $V/V_0 = (A/A_0)^{3/2}$. The results obtained from 2–4 samples at each Li_2S_3/AN ratio were averaged, and the standard deviation was evaluated.

2.4.4 Electrochemical measurement of the cross-linked PAN–PBD GPE

Potentiostatic electrochemical impedance spectroscopy (PEIS) and chronoamperometry (CA) were carried out with the potentiostat (VSP-300 Biologic Instruments, U.S.). The Li deposition/dissolution cycles was carried out with the battery cycler (BT2000, Arbin Instruments, U.S.). The t_+ of PAN–PBD GPE was evaluated by a potentiostatic polarization method reported by Newman and Balsara.[182] The cross-linked PAN-PBD film was swollen in DME/LiFSI (1 mol kg^{-1}) or DMC/EC(1:1 in weight ratio)/$LiPF_6$ (1 mol kg^{-1}) and placed between two Li metal foils. Prior to the measurement, the Li was deposited/dissolved at 20 μA cm^{-2} for 2 hours and 5 cycles to stabilize the Li/electrolyte interface. At the open-circuit voltage (OCV), 10 mV of the voltage polarization was applied at a frequency range from 1 MHz to 1 Hz to evaluate the bulk and interface resistances (R_{bulk}, R_{int}). A constant voltage of ±5 and ±10 mV for 2 hours was applied to obtain the steady-state current (I_{ss}). The t_+ was evaluated from the results obtained in the two measurement (see Calculation D for the detailed calculation in Appendix). The conductivity of was measured by the PEIS method described above with two stainless-steel blocking electrodes. The temperature of the cell was controlled by the ribbon heater and the Peltier cooler. The Li deposition was carried out in CR 2032-coin cell with a Cu foil (9 μm) as the working electrode and Li foil (250 μm) as the counter/reference electrode. The PAN–PBD thin film (10 μm) and a polypropylene battery separator (25 μm, Celgard, U.S.) was placed between the Cu and Li electrodes (see Figure S2-12 in Appendix). The electrolyte used for the Li deposition was DMC + EC (1:1 in weight ratio) + $LiPF_6$ (1 mol kg^{-1}) + FEC (5wt%).

2.4.5 Characterization of the Li deposits

The morphology of the Li deposits and the PAN–PBD thin film were observed under the scanning electron microscope (SEM, Sigma 500, Zeiss Instruments, Germany) at the electron high tension (EHT) voltage of 3

kV, and through the in-lens detector. Surface chemistry on the Li deposits was probed using a PHI 3056 X-ray photoelectron spectrometer equipped with a dual Al Kα (1486.7 eV) and Mg Kα (1256.6 eV) anode source, operated at 350 W, and with sample chamber pressure below 10−8 Torr. Samples were dissembled in an argon-filled glovebox, rinsed with a small quantity of anhydrous DME (Sigma-Aldrich), and transferred to the XPS chamber using an airtight vacuum transfer system. High resolution scans were acquired using a pass energy of 23.5 eV and an energy step of 0.05 or 0.075 eV. Survey scans were measured using a pass energy of 93.5 eV and a 0.5 eV energy step. The binding energies were calibrated by setting the hydrocarbon C 1s (C−C, C−H) signal to 284.6 eV, which corresponds mainly to the adventitious carbon. C signal was measured before and after any other signal to precisely calibrate the energy scale.

2.4.6 Tensile and rheological measurements

Tensile strength of the cross-linked PAN–PBD at the dry state was evaluated with the tensile tester (Model 5982, Instron, U.S.), at a constant strain rate of 2 mm min^{-1} (see Figure S2-22 in Appendix for the sample dimension). Rheological properties of the cross-linked PAN–PBD GPE were characterized using the Discovery HR-3 Rheometer (TA Instruments, U.S.) equipped with a 20 mm parallel-plate geometry. An oscillation frequency of 1 Hz was used in the amplitude sweep and an oscillation strain of 0.1% was used in the frequency sweep. During all the measurements, an axial force of 1 N was applied for proper contact between the sample and the plates. All the measurements are conducted at 25°C. Non-corrosive $LiClO_4$ was used as the electrolyte salt at the concentration of 1 mol kg^{-1} in DMC/EC, and 0.3 mol kg^{-1} in DME (saturated).

2.5 Acknowledgement

Chapter 2 contains materials that is currently being prepared for submission for publication. The dissertation author is the primary researcher for the data presented and is the primary author of the manuscript. The work is supervised by Prof. Ping Liu and supported by Dr. Gabriel Veith, Dr. Haodong Liu, Xing Xing, Sicen Yu and Zijun Wang.

2.6 Appendix

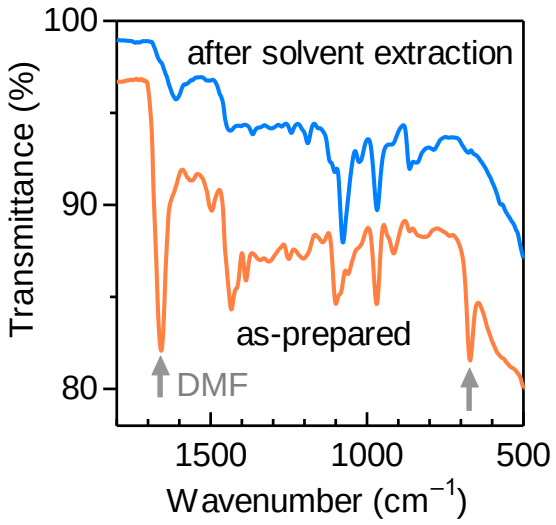

Figure S2-1 FTIR spectra of cross-linked PAN-b-PAB (Li2S3/AN = 1.0) before and after the solvent extraction in DME, showing a complete removal of DMF (the solvent used in the cross-linking step).

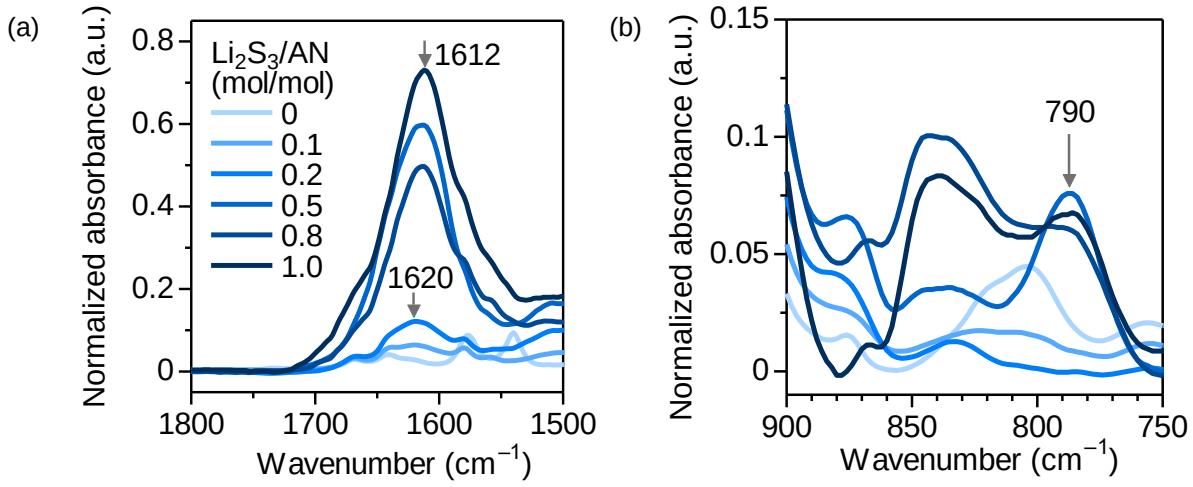

Figure S2-2 (a) Red shift of the C=C/C=N stretching peaks, suggesting the extension of the conjugation length at higher Li_2S_3/AN ratio. (b) Appearance of the 1,2,3-trisubstituted =C–H bending at 790 cm^{-1} at Li_2S_3 > 0.5

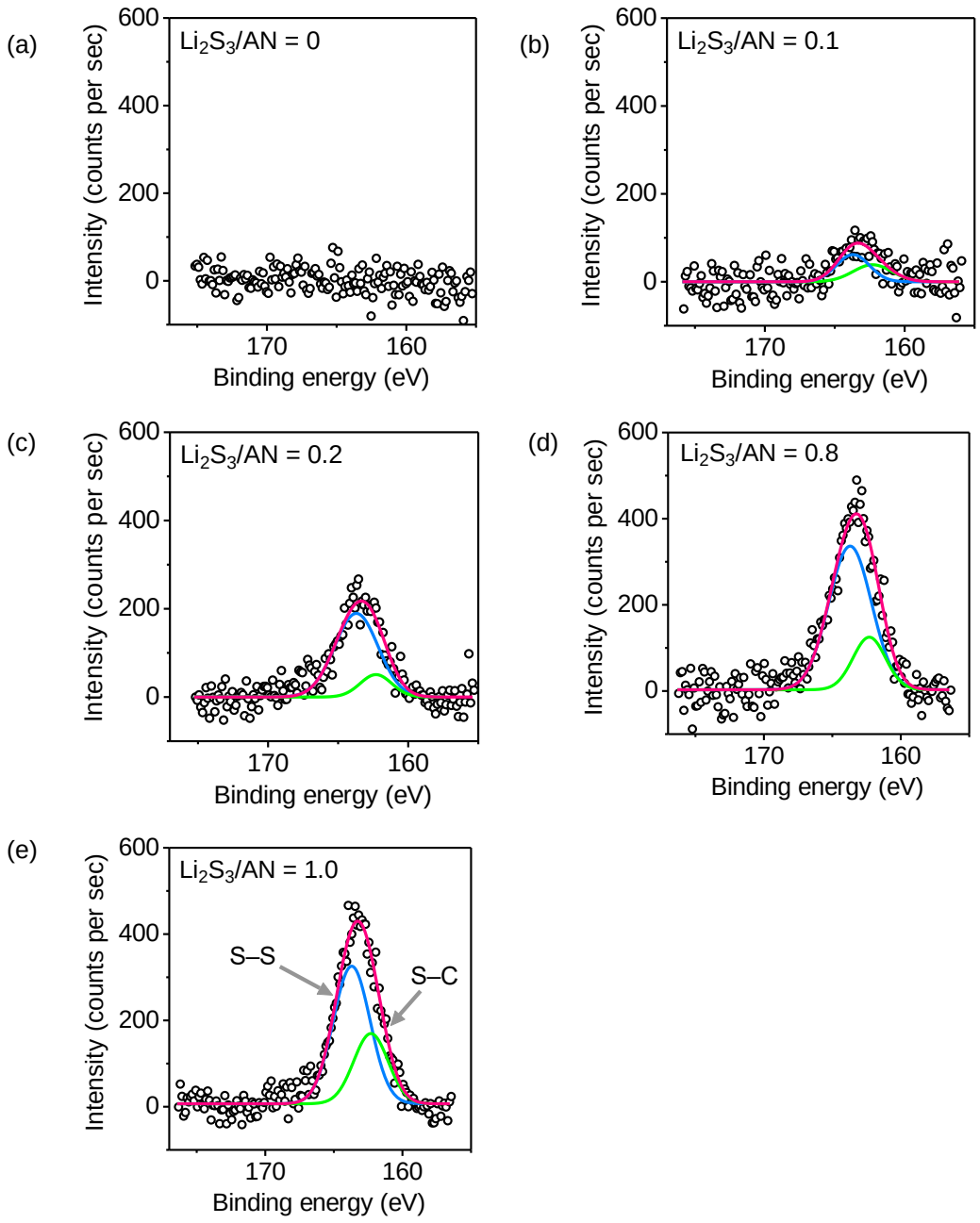

Figure S2-3 (a–e) XPS S 2*p* spectra of PAN-PBD after the solvent extraction in DME (polysulfide dissolves in DME). The deconvolution of the S $2p_{3/2}$ peak at 163.3 eV suggest the possible formation of both S–S (peak at 163.7 eV) and S–C (peak at 162.3 eV)[190] bonding with increasing Li_2S_3/AN ratio (0–1.0).

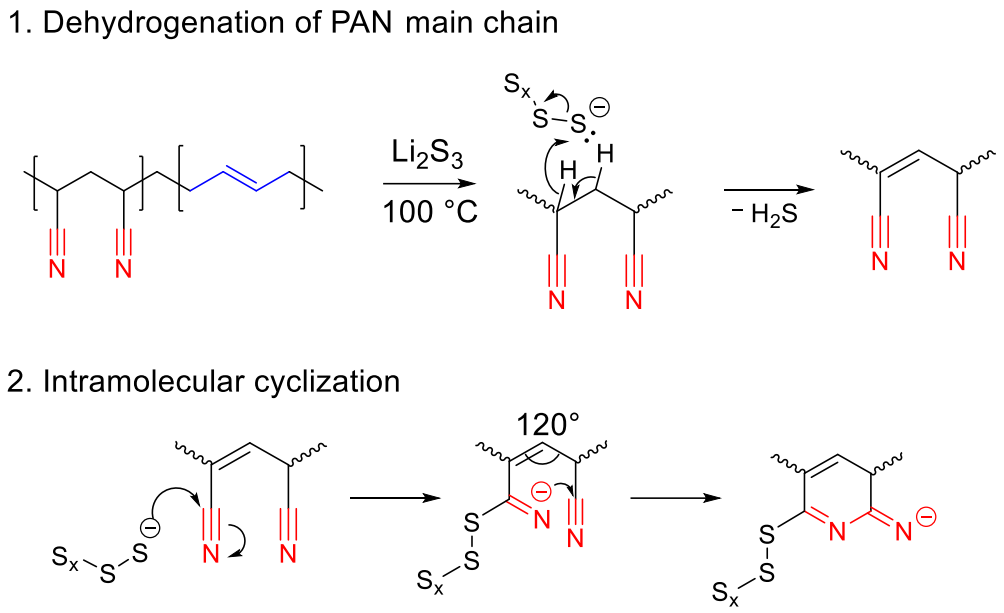

Figure S2-4 Reaction scheme of the cross-linking reaction of PAN-PBD catalyzed by Li_2S_3. (1) Nucleophilic attack of polysulfide (S_x^-) on β-hydrogen of PAN results in dehydrogenation and production of H_2S gas. (2) Nucleophilic attack on C≡N produces S_x–C=N$^-$ anion. The hydrogenation and formation of the C=C in step (1) fixes the bonding angle of PAN main chain to 120° (angle of six-membered ring) and sterically facilitates intramolecular cyclization of C≡N. (3) The cyclization reaction initiated in step (2) transfers to different PAN chains and forms intermolecular cross-links.

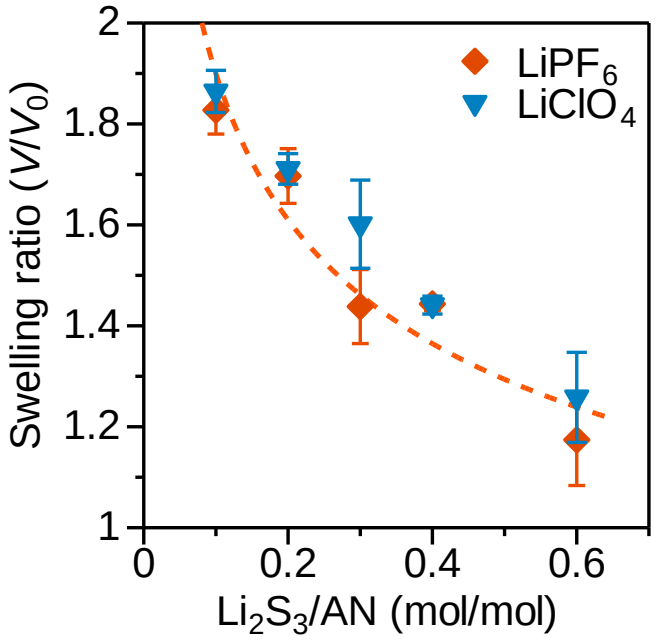

Figure S2-5 Swelling ratio of cross-linked PAN-PBD in DMC/EC mixed solvent added with $LiClO_4$ or $LiPF_6$ (1 mol kg^{-1})

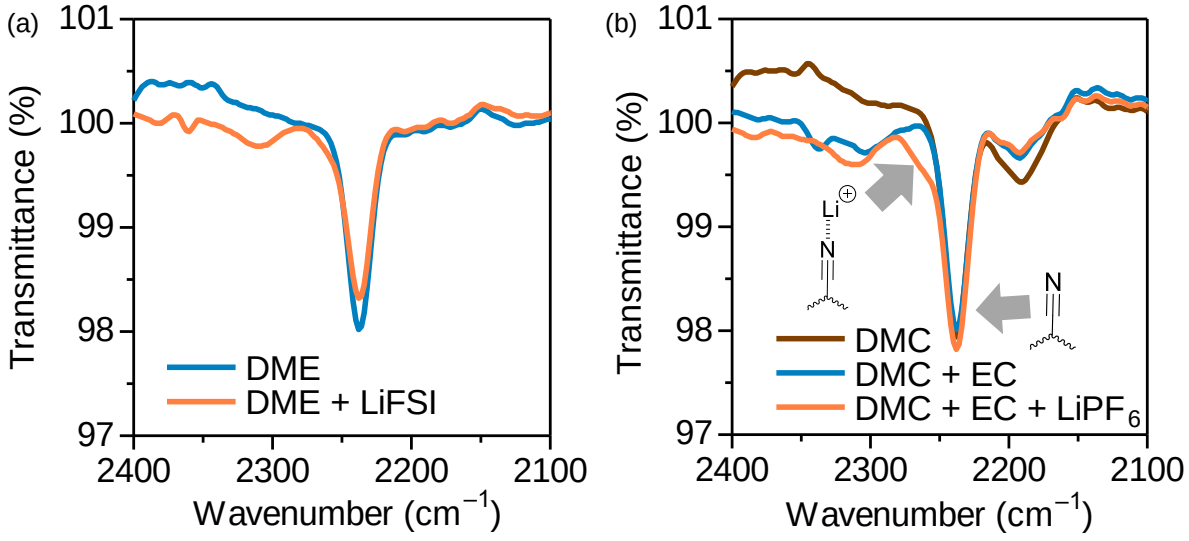

Figure S2-6 FTIR spectra of cross-linked PAN-PBD (Li_2S_3/AN = 0.1) swollen in (a) DME (+ LiFSI, 1 mol kg^{-1}), and (b) DMC, DMC + EC (+ $LiPF_6$, 1 mol kg^{-1}).

Calculation A: Calculation of relative energy difference (RED) between polymer and solvent

HSPs are composed of three independent parameters, which account for dispersion force (δ_D), dipole-dipole interaction (δ_P), and hydrogen-bonding (δ_H), respectively (Table A). The sum of the squared values of HSPs equals to Hildebrand solubility parameter (δ).

$$\delta^2 = \delta_D^2 + \delta_P^2 + \delta_H^2 \quad (A1)$$

RED is expressed as a ratio of R_a to R_o:

$$\mathrm{RED} = \frac{R_a}{R_o} \quad (A2)$$

where R_o is a constant unique to the polymer. R_a is expressed as

$$R_a^2 = 4(\delta_{D1} - \delta_{D2})^2 + (\delta_{P1} - \delta_{P2})^2 + (\delta_{H1} - \delta_{H2})^2 \quad (A3)$$

where the subscript 1 and 2 represents the HSPs of the solvent and the polymer, respectively.

The HSPs for the mixed solvent (e.g. solvent *a* + solvent *b*) can be calculated by taking the volume average of the HSPs of each solvent:

$$\delta_{i,a+b} = v_a \delta_{i,a} + v_b \delta_{i,b}$$

where i = D, P, H, and v_a and v_b is the volume ratio of the solvent. Note EC/DMC = 1/1 in weight ratio converts to 0.448/0.552 in volume ratio.

Table S2-1 Values of HSPs, Ro, and V1 used in this study[175]

δ_D	δ_P	δ_H	R_o	V_1 ($cm^3\ mol^{-1}$)
17.5	2.3	3.4	6.5	-
21.7	14.1	9.1	10.9	-
15.4	6.0	6.0	-	104.5
15.5	3.9	9.7	-	84.2
19.4	21.7	5.1	-	66
17.2	11.9	7.6	-	75 (averaged)

Calculation B: Calculation of χ parameter between polymer and solvent

Flory–Huggins χ parameter can be calculated from the HSPs:

$$\chi_{12} = \frac{\alpha V_1}{RT}[(\delta_{D1} - \delta_{D2})^2 + 0.25(\delta_{P1} - \delta_{P2})^2 + 0.25(\delta_{H1} - \delta_{H2})^2] \quad \text{(B1)}$$

where α is an empirical parameter. Previously, α = 0.6 was reported in the literature and therefore is used in this study.[176,178]

Using Equation (A2) and (A3),

$$\chi_{12} = \frac{\alpha V_1}{RT}\left(\frac{R_a}{2}\right)^2 = \frac{\alpha V_1}{RT}\left(\frac{R_o RED}{2}\right)^2 \quad \text{(B2)}$$

Equation (B2) shows the χ parameter is proportional to the RED squared. Calculated values of the χ_{12} parameters between each of the solvent and the polymer are listed in Table B. The χ_{12} of PAN–PBD copolymer is estimated from the volume average of χ_{12} of the two polymers (AN = 38wt% is used in this study and corresponds to 32vol%).

Table S2-2 Calculated values of χ_{12} parameters between the solvents (DME, DMC, DMC/EC) and the polymers (PBD, PAB, PAN–PBD)

	PBD	PAN	PAN–PBD (AN = 38wt%)
DME	0.241	1.48	0.640
DMC	0.297	1.32	0.625
DMC + EC (1:1 wt)	0.498	0.392	0.464

Calculation C: Parameter fittings for σ_0 and ϕ_0 by using percolation model

In percolation model, the ionic conductivity is expressed as

$$\sigma = \sigma_0(\phi_{\mathrm{LE}} - \phi_0)^n \quad \text{(Eq. 3)}$$

Taking the power of 1/*n* for both sides of the equation gives

$$\sigma^{1/n} = \sigma_0^{1/n}\phi_{\mathrm{LE}} - \sigma_0^{1/n}\phi_0 \quad \text{(C1)}$$

In the linear fitting of $\sigma^{1/n}$ with respect to ϕ_{LE}, σ_0, and ϕ_0 can be evaluated from the slope, and the *x*-intercept, respectively. The best fit is obtained with n = 2 for both ether and carbonate electrolytes (Figure S2-7)

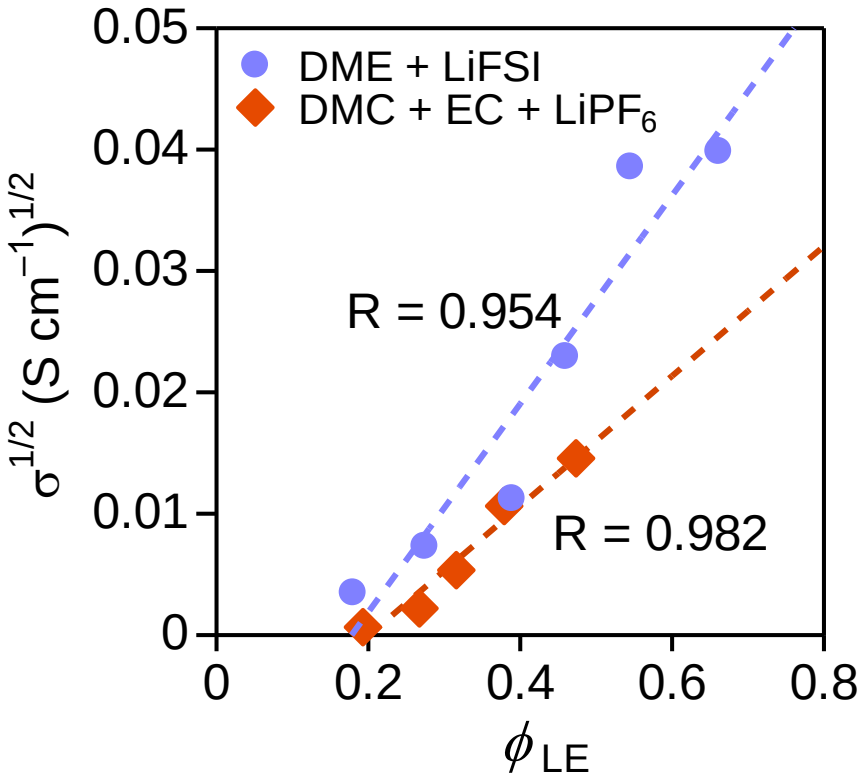

Figure S2-7 Fitting of $\sigma^{1/2}$ with respect to ϕelectrolyte for DME + LiFSI (1 mol kg^{-1}) and DMC + EC (1:1 wt) + $LiPF_6$ (1 mol kg^{-1}).

Calculation D: Measurement of t_+ with potentiostatic polarization method

The t_+ can be evaluated by applying a small voltage bias (ΔV) between the two Li metal electrodes with the GPE in the middle, and by measuring the steady-state current (I_{ss}) under the assumption that only Li^+ moves at the steady state. The t_+ can be calculated from:[182]

$$t_+ = \frac{I_{ss}(\Delta V - I_0 R_{int,0})}{I_0(\Delta V - I_{ss} R_{int,ss})} \quad \text{(D1)}$$

I_0 is the initial current at the beginning of the polarization step, which can be calculated from the Ohm's law:

$$I_0 = \frac{\Delta V}{R_{bulk} + R_{int,0}} \quad \text{(D2)}$$

All the resistance terms in Equation (D1) and (D2) can be evaluated from the impedance spectra before and after each polarization step.

Q_{bulk}, and Q_{int} represent the constant phase element (CPE) of the bulk GPE, and the interface between the GPE and the Li metal, respectively. Similarly, R_{bulk}, and R_{int} represents the bulk, and interface resistance, respectively. W represents the Warburg element, accounting for the diffusion process.

The impedance spectra and the current during the polarization are shown in Figure S2-8 (the GPE swollen in DME + LiFSI) and S9 (the GPE swollen in DMC + EC + $LiPF_6$). The fitted values of R_{bulk} and R_{int} are shown in Table D. We confirmed the ionic conductivity calculated from R_{bulk} (with Li-metal non-blocking electrode) agrees with the conductivity evaluated with stainless-steel blocking electrode.

Table S2-3 Electrode area, thickness of the swollen film, R_{bulk}, R_{int}, and t_+, which are evaluated from Figure S2-8, 9. The ionic conductivity calculated from R_{bulk} with Li-metal non-blocking electrode (σ_{Li}) agrees with the value evaluated with stainless-steel blocking electrode (σ_S). The error interval represents the standard deviation of the results obtained from the different voltage biases. (*a.* R_{bulk} was estimated from the conductivity test measured with stainless-steel blocking electrodes, because R_{bulk} and R_{int} were indistinguishable from the Nyquist plot.)

Electrolyte	Li_2S_3/AN (mol/mol)	Area (cm^2)	Thickness (mm)	R_{bulk} (Ω)	R_{int} (Ω)	t_+	σ_{Li} (S cm^{-1})	σ_S (S cm^{-1})
DME	0.1	0.71	0.097	10.4 ± 0.1	477 ± 15	0.13 ± 0.04	1.3×10^{-3}	1.6×10^{-3}
DME	0.2	2.0	0.26	4.9 ± 0.1	72 ± 8	0.18 ± 0.03	2.7×10^{-3}	1.5×10^{-3}
DME	0.3	2.0	0.11	11.3 ± 0.3	100 ± 3	0.24 ± 0.02	5.2×10^{-4}	5.3×10^{-4}
DME	0.4	2.0	0.13	52 ± 4	240 ± 20	0.39 ± 0.04	1.3×10^{-4}	1.3×10^{-4}
DME	0.6	1.3	0.12	304 ± 3	262 ± 9	0.45 ± 0.06	3.1×10^{-5}	5.4×10^{-5}
DME	1.0	1.3	0.097	608 ± 6	320 ± 20	0.54 ± 0.06	1.2×10^{-5}	3.1×10^{-5}
DMC/EC	0.1	0.71	0.10	91 ± 3	232 ± 2	0.30 ± 0.01	1.6×10^{-4}	2.1×10^{-4}
DMC/EC	0.2	0.71	0.11	244 ± 3	360 ± 7	0.44 ± 0.02	6.6×10^{-5}	1.1×10^{-4}
DMC/EC	0.3	0.71	0.11	820 ± 20	375 ± 2	0.55 ± 0.02	1.8×10^{-5}	2.9×10^{-5}
DMC/EC	0.4	0.71	0.048	1440 ± 40	183 ± 5	0.63 ± 0.05	4.7×10^{-6}	4.8×10^{-6}
DMC/EC	0.6	0.71	0.20	6.7×10^{5} [a]	$(1.7 \pm 0.5) \times 10^{4}$	0.58 ± 0.09	-	4.2×10^{-7}

Figure S2-8 Potentiostatic electrochemical impedance spectra (PEIS: a, c, e, g, i, k) and chronoamperometry (CA: b, d, f, h, j, l) of PAN–PBD GPE swollen in DME + LiFSI (1 mol kg–1). The GPE is cross-linked under the Li2S3/AN ratio = 0.1 (a, b); 0.2 (c, d); 0.3 (e, f); 0.4 (g, h); 0.6 (i, j); 1.0 (k, l). The EIS is measured after the condition cycle, and at the end of each CA step. The CA is measured under the constant potential of ±5, ±10 mV vs. Li+/Li for 2 hours. The lines in the EIS represents the fitting curve to the equivalent circuit shown in Calculation D.

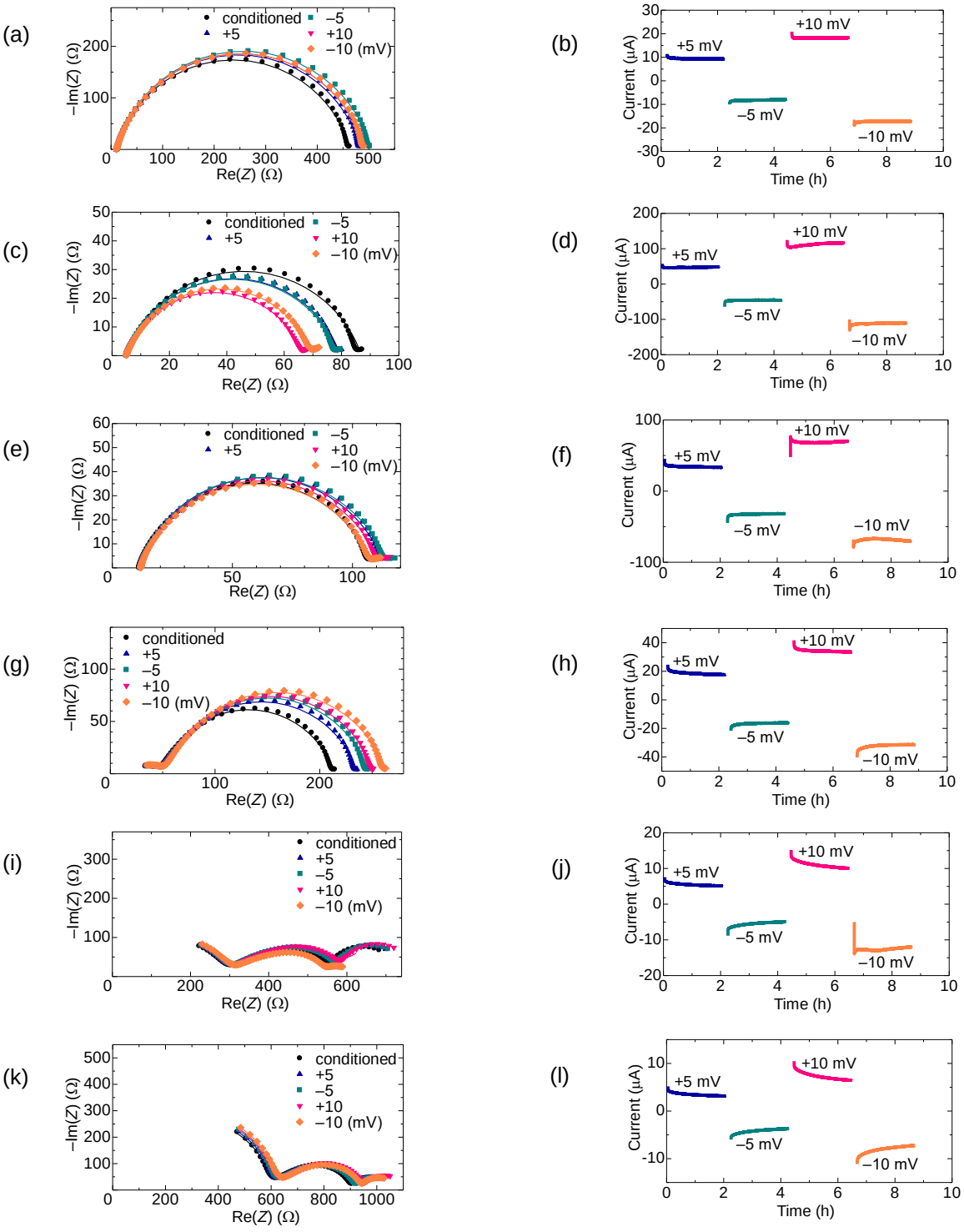
(a)
conditioned
+5
−5
+10
−10 (mV)
−Im(Z) (Ω)
Re(Z) (Ω)
(b)
+10 mV
+5 mV
−5 mV
−10 mV
Current (μA)
Time (h)
(c)
conditioned
+5
−5
+10
−10 (mV)
−Im(Z) (Ω)
Re(Z) (Ω)
(d)
+10 mV
+5 mV
−5 mV
−10 mV
Current (μA)
Time (h)
(e)
conditioned
+5
−5
+10
−10 (mV)
−Im(Z) (Ω)
Re(Z) (Ω)
(f)
+10 mV
+5 mV
−5 mV
−10 mV
Current (μA)
Time (h)
(g)
conditioned
+5
−5
+10
−10 (mV)
−Im(Z) (Ω)
Re(Z) (Ω)
(h)
+10 mV
+5 mV
−5 mV
−10 mV
Current (μA)
Time (h)
(i)
conditioned
+5
−5
+10
−10 (mV)
−Im(Z) (Ω)
Re(Z) (Ω)
(j)
+10 mV
+5 mV
−5 mV
−10 mV
Current (μA)
Time (h)
(k)
conditioned
+5
−5
+10
−10 (mV)
−Im(Z) (Ω)
Re(Z) (Ω)
(l)
+10 mV
+5 mV
−5 mV
−10 mV
Current (μA)
Time (h)

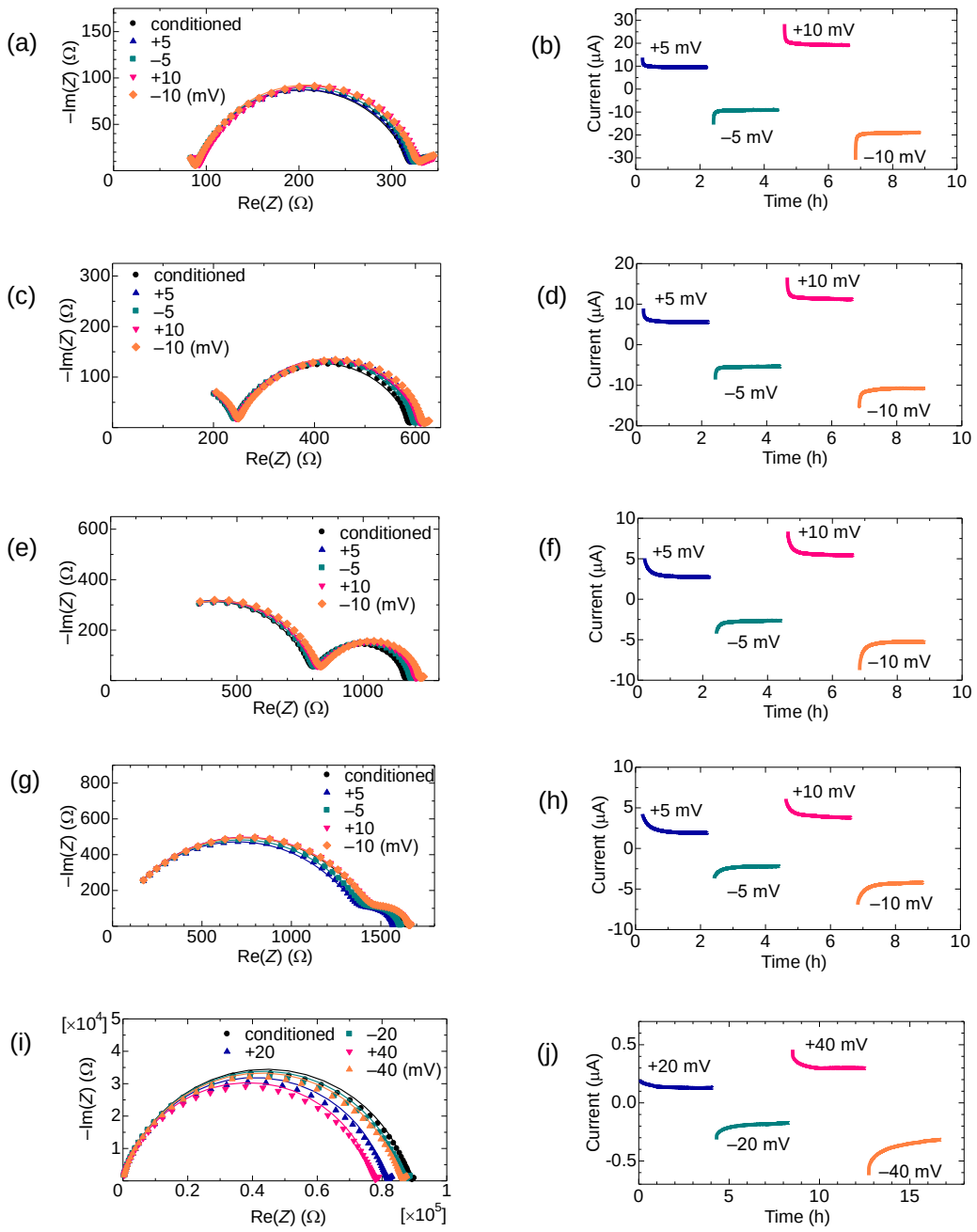

Figure S2-9 PEIS (a, c, e, g, i) and CA (b, d, f, h, j) of PAN–PBD GPE swollen in DMC + EC (1:1 wt) + $LiPF_6$ (1 mol kg^{-1}). The GPE is cross-linked under the Li_2S_3/AN ratio = 0.1 (a, b); 0.2 (c, d); 0.3 (e, f); 0.4 (g, h); 0.6 (i, j). The EIS is measured after the condition cycle, and at the end of each CA step. The CA is measured under the constant potential of ±5, ±10 mV *vs.* Li^+/Li for 2 hours (b, d, f, h), or ±20, ±40 mV for 4 hours (j) because of the low conductivity of the sample. The lines in the EIS represents the fitting curve to the equivalent circuit shown in Calculation D.

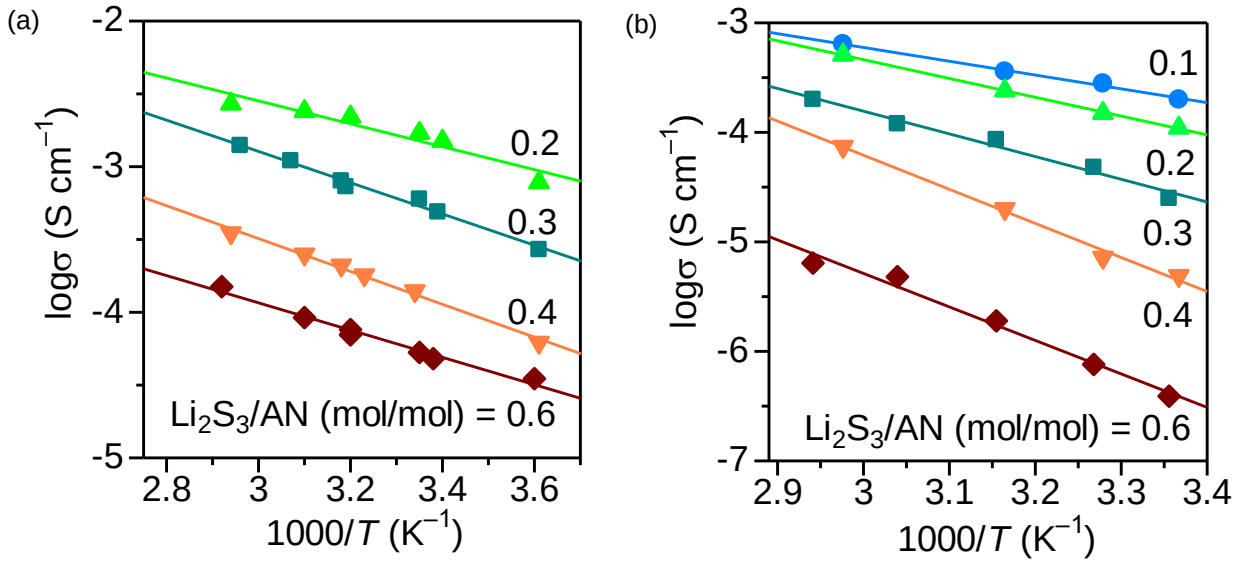

Figure S2-10 Arrhenius plot of PAN–PBD GPE swollen in (a) DME + LiFSI (1 mol kg^{-1}), and in (b) DMC + EC (1:1 wt) + $LiPF_6$ (1 mol kg^{-1})

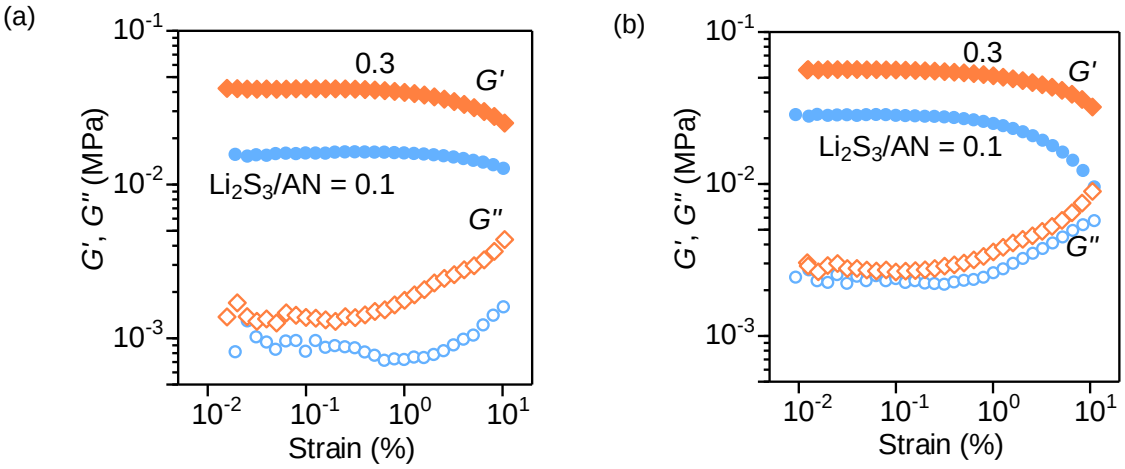

Figure S2-11 Strain dependence of storage (*G'*) and loss (*G"*) modulus of PAN–PBD swollen in (a) DME + $LiClO_4$ (sat. 0.3 mol kg^{-1}), and in (b) DMC + EC (1:1) + $LiClO_4$ (1 mol kg^{-1}), evaluated under a constant frequency of 1Hz. The linear viscoelastic regime is evaluated as a strain range in which the *G'* is constant (i.e. strain < 1% in this study).

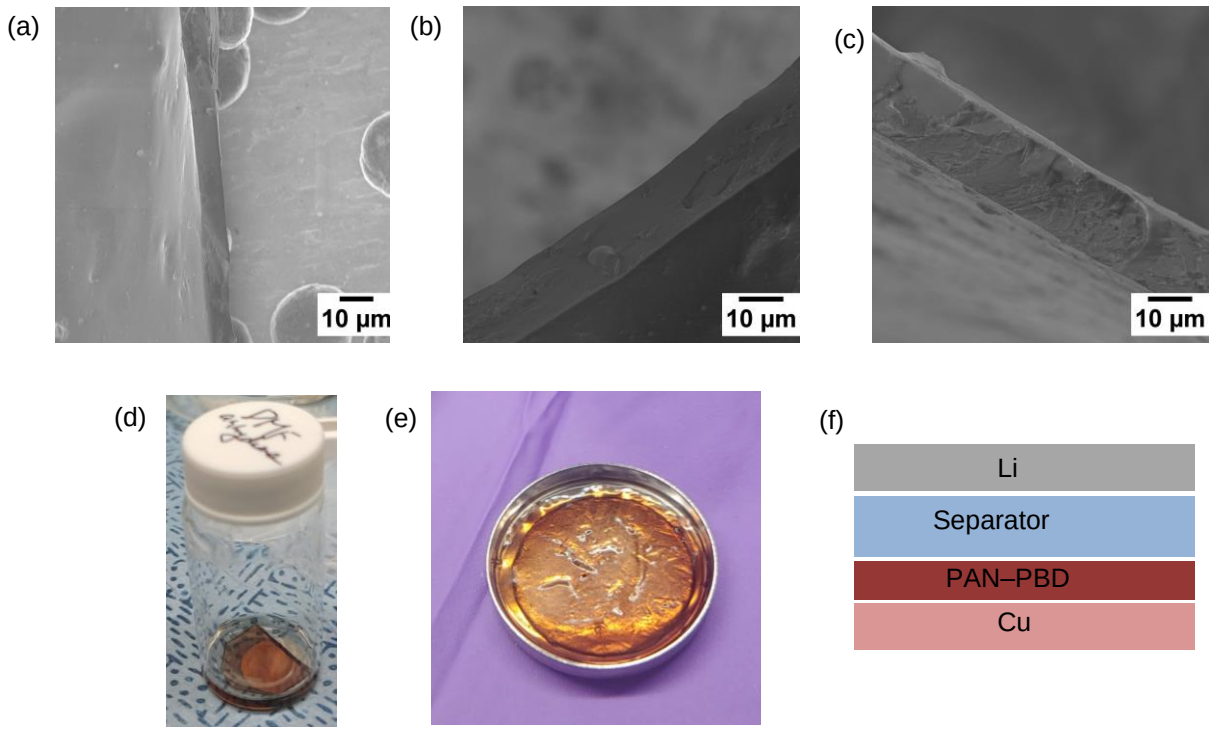

Figure S2-12 (a–c) Cross-sectional images of PAN–PBD thin film used as the protective coating for Li metal anode. Li_2S_3/AN = 0.1 (a), 0.2 (b), 0.4 (c). (d) PAN–PBD thin film peeled off from the stainless-steel substrate by immersing in DMF. (e) Free-standing PAN–PBD thin film transferred on Cu foil after thorough rinsing in DMC. (f) Cell configuration used in the Li deposition on PAN–PBD-coated Cu. The coating is fully swollen in the electrolyte (DMC + EC (1:1) + $LiPF_6$ (1 mol kg^{-1}) + FEC (5wt%)) prior to the cell assembly. A commercial battery separator (Celgard) is placed on top of the coating.

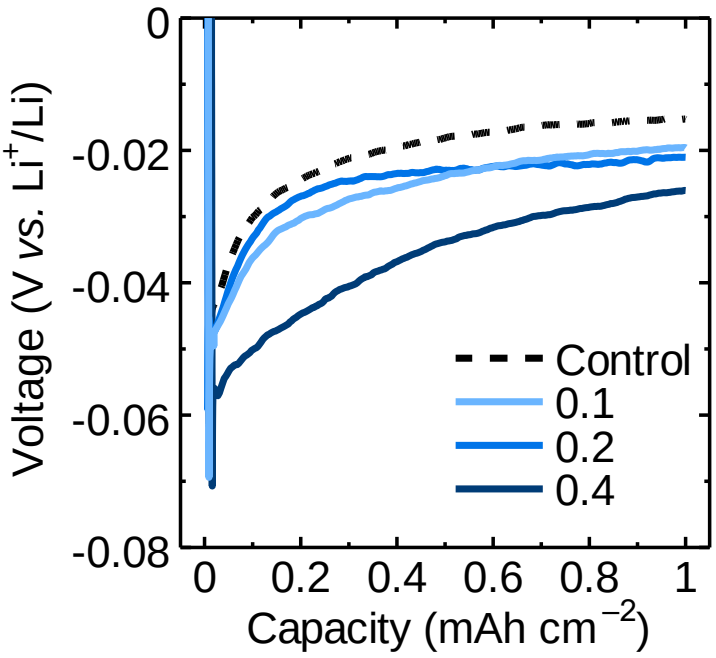

Figure S2-13 Voltage profiles during the first deposition of Li metal on uncoated Cu (control cell), and PAN–PBD-coated Cu (Li_2S_3/AN = 0.1, 0.2, 0.4). Current density = 0.1 mA cm^{-2}. The optical images of the Li metal after the deposition are shown in Figure S2-14.

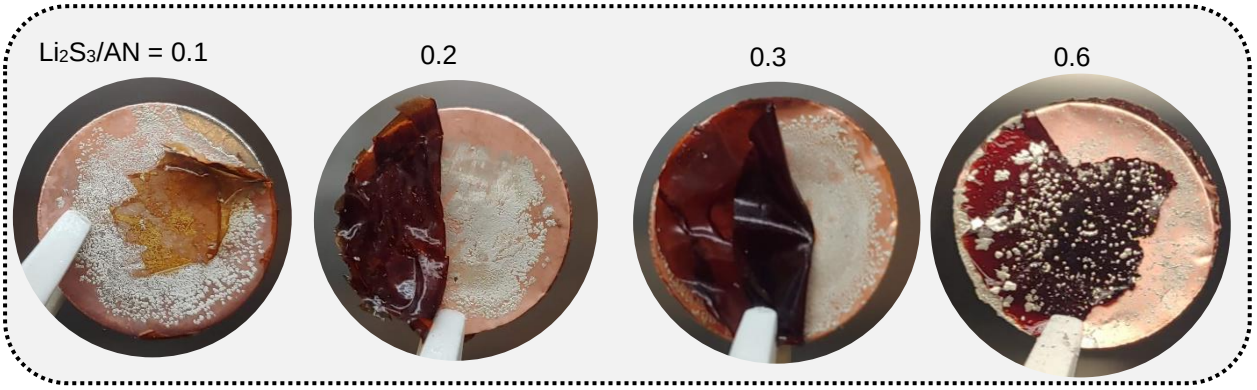

Figure S2-14 Optical images of Li metal underneath the PAN–PBD coating after the first deposition on Cu foil. Current density = 0.1 mA cm^{-2}, deposition capacity = 1 mAh cm^{-2}.

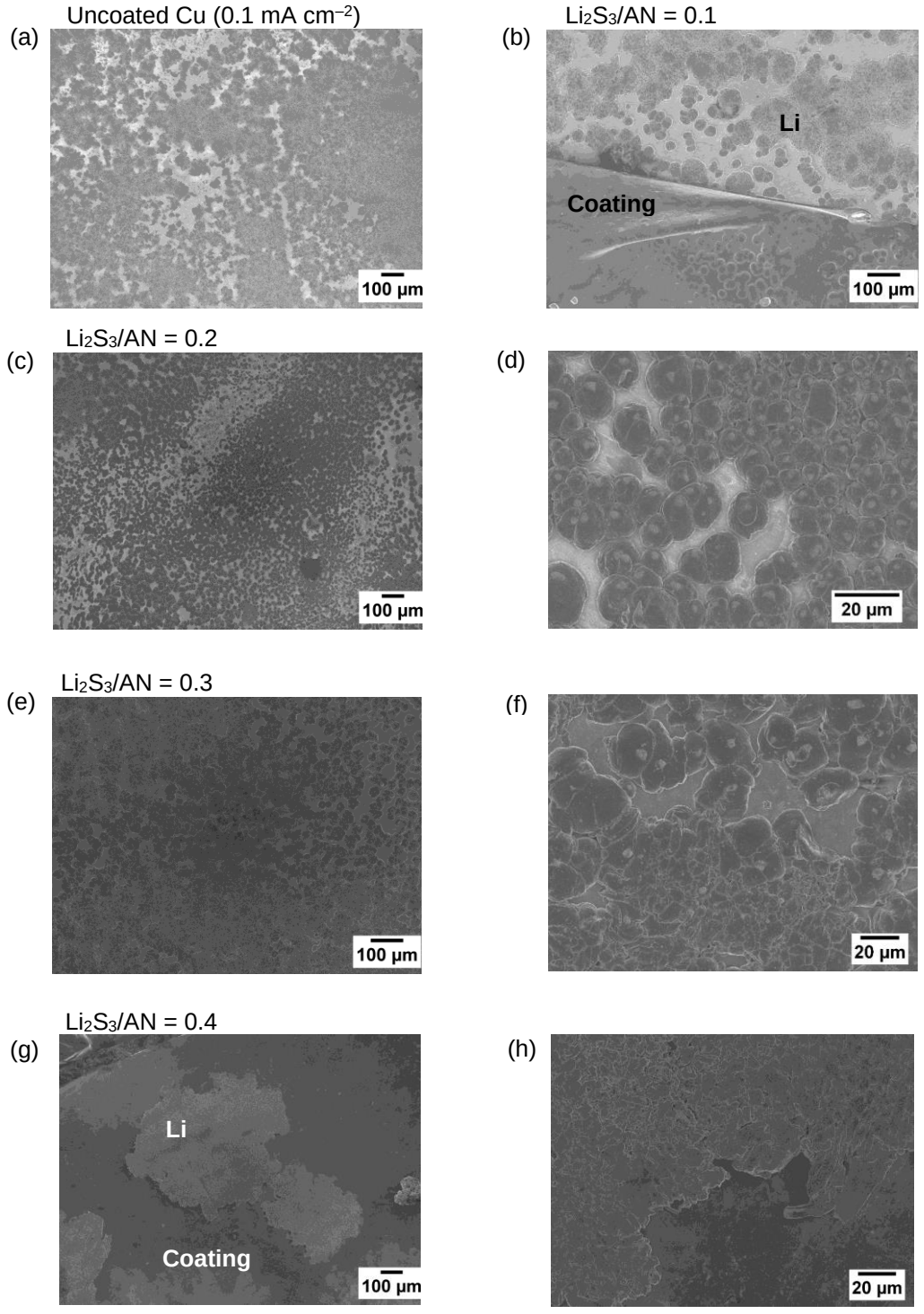

Figure S2-15 SEM images of Li metal after the first deposition on (a) uncoated Cu, and on (b–h) Cu with PAN–PBD coating cross-linked at Li_2S_3/AN = 0.1 (b); 0.2 (c, d); 0.3 (e, f); 0.4 (g, h). Li metal is deposited underneath the coating in (b–f), and on the surface in (g, h). Current density = 0.1 mA cm^{-2}, deposition capacity = 1 mAh cm^{-2}.

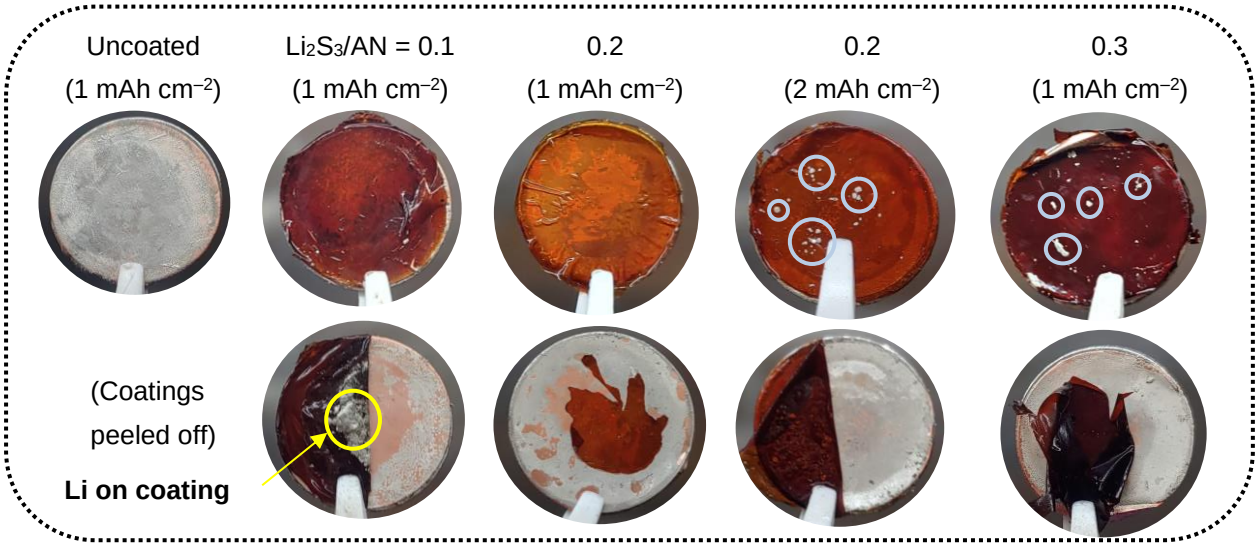

Figure S2-16 Optical images of Li metal after the first deposition on uncoated Cu, and on Cu with PAN–PBD coating cross-linked at Li_2S_3/AN = 0.1–0.3. The highlighted region shows the Li metal adhered on the backside of the coating when peeled off. Li metal plating on the coating surface is observed at Li_2S_3/AN = 0.3, and when the capacity is increased to 2 mAh cm^{-2} (Li_2S_3/AN = 0.2). Current density = 0.5 mA cm^{-2}.

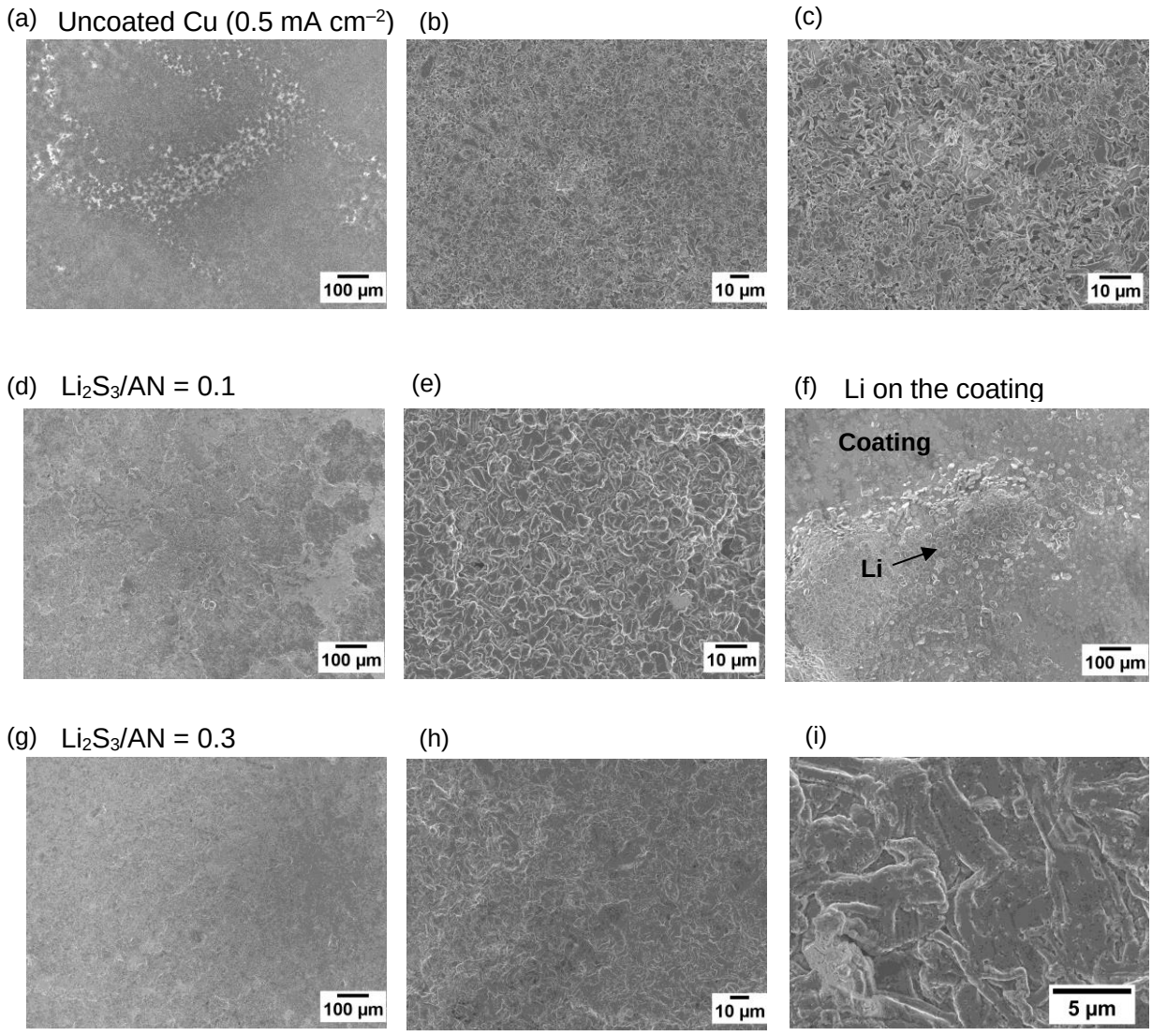

Figure S2-17 SEM images of Li metal after the first deposition on (a–c) uncoated Cu, and on (d, e, g–i) Cu with PAN–PBD coating cross-linked at Li_2S_3/AN = 0.1 (d, e); 0.3 (g–i). (f) Li metal adhered on the coating (Li_2S_3/AN = 0.1). Current density = 0.5 mA cm^{-2}

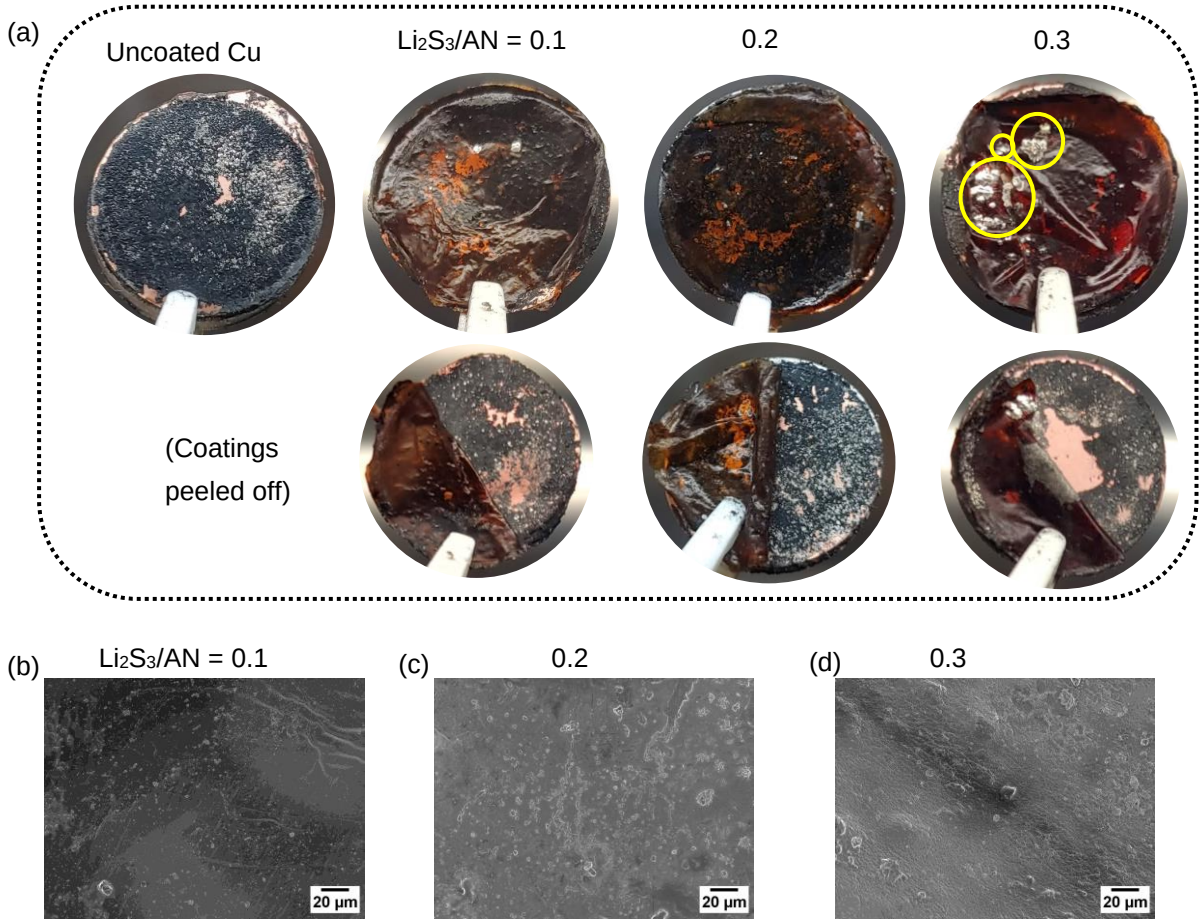

Figure S2-18 (a) Optical images of Li metal after the 51st deposition on uncoated Cu, and on Cu with PAN–PBD coating (Li_2S_3/AN = 0.1–0.3). The highlighted area shows Li metal plating on the coating surface at Li_2S_3/AN = 0.3. (b–d) SEM images of the PAN–PBD coating after 50 cycles of Li deposition/dissolution. Current density = 0.1 mA cm^{-2}, deposition capacity = 1 mAh cm^{-2}.

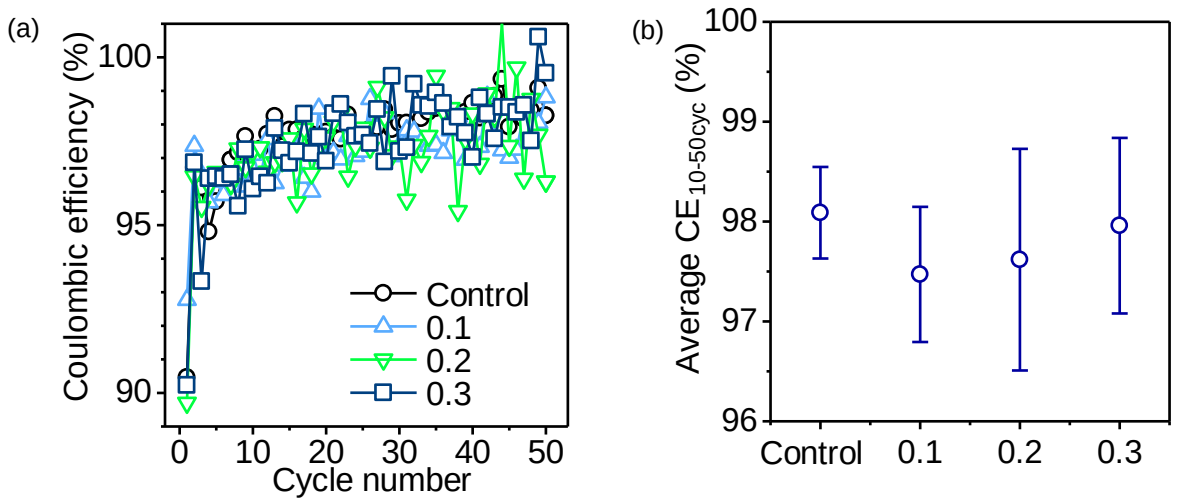

Figure S2-19 (a, b) Coulombic efficiency (CE) of Li metal deposition/dissolution on uncoated Cu (control), and on PAN–PBD-coated Cu (Li_2S_3/AN = 0.1–0.3). (a) CE at each cycle, (b) average CE between 10 and 50 cycle. The error bar represents the standard deviation. Current density = 0.1 mA cm^{-2}, deposition capacity = 1 mAh cm^{-2}.

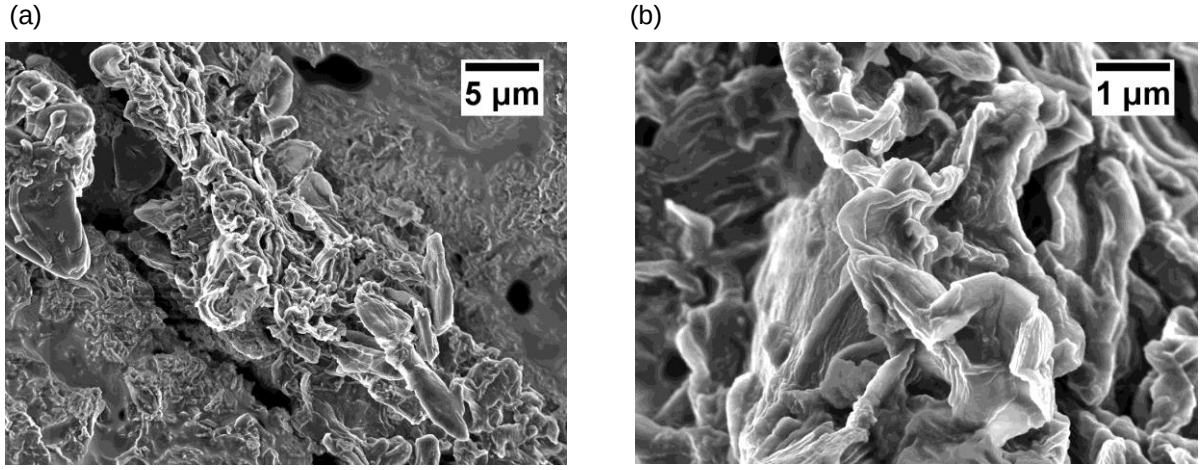

Figure S2-20 (a, b) SEM images of Li metal after the 51st deposition on PAN–PBD-coated Cu (Li_2S_3/AN = 0.3). The sample in the image is the Li deposits adhered on the Cu-side of the coating surface as shown in Figure S2-18. Current density = 0.1 mA cm^{-2}, deposition capacity = 1 mAh cm^{-2}.

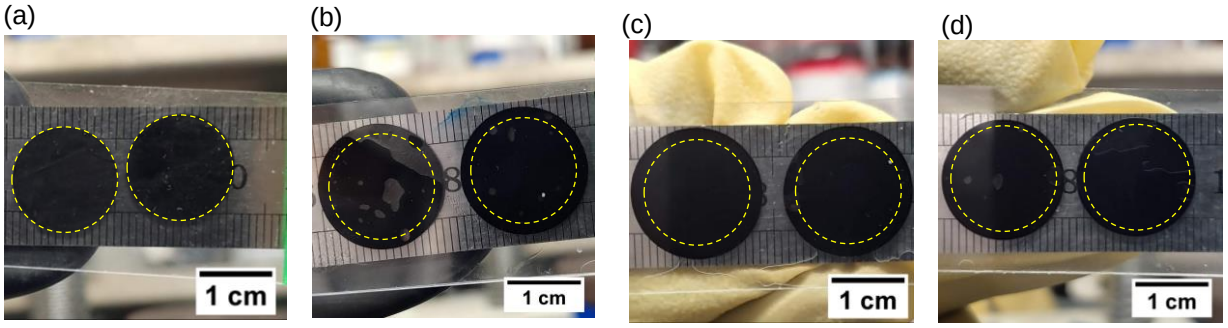

Figure S2-21 Optical images used for the evaluation of the swelling ratio: (a) dry film (b) swollen in pure DMC (c) in DMC/EC (1:1) (d) in DMC/EC/$LiPF_6$ (1 mol kg^{-1}) The circle in the images represents the area of the dry film (a). Sample in image: Li_2S_3/AN = 0.3

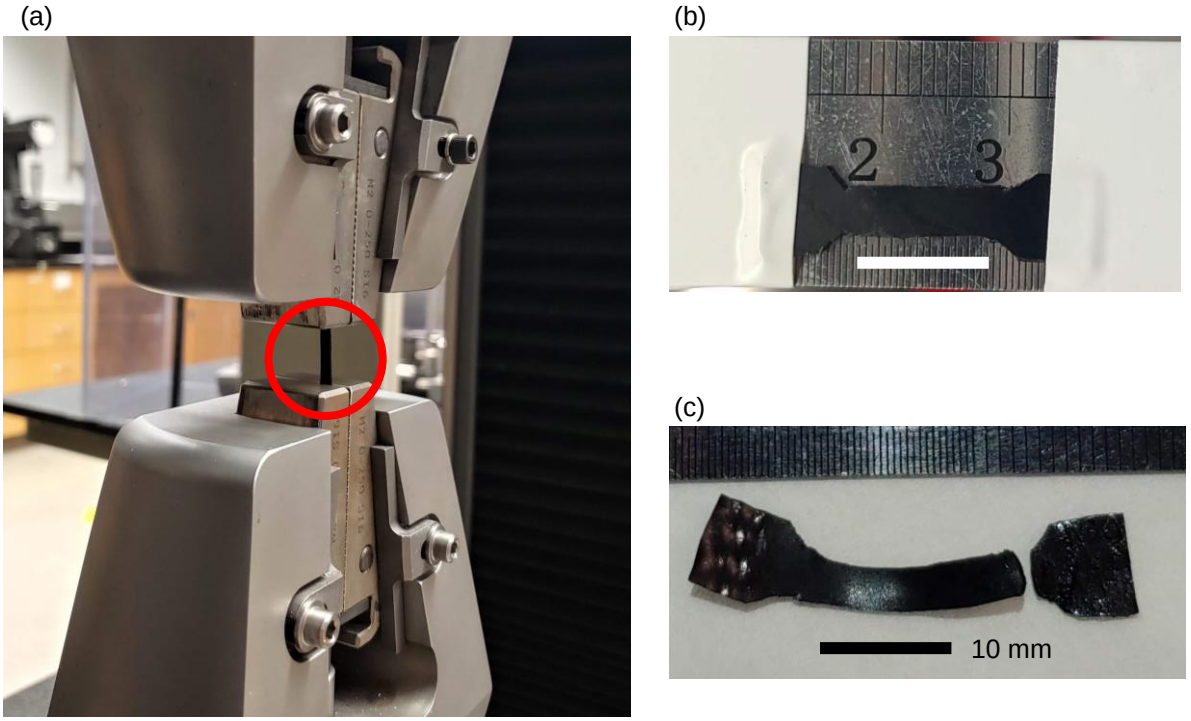

Figure S2-22 Photograph of the tensile test of the dry PAN–PBD film: (a) the film clipped to the instrument (b) the film before the tensile test and (c) after the break. The dimension of the sample is 10 mm (length) × 4 mm (width) × 0.5 ± 0.2 mm (thickness). Sample in image: Li_2S_3/AN = 0.6

Chapter 3 In-situ formed polymer gel electrolytes for lithium batteries with inherent thermal shutdown safety features

3.1 Introduction

Rechargeable lithium (Li) metal batteries are being intensively studied due to their promises of high energy densities.[191] Current research focuses on addressing the cycle life issues of the Li metal anode.[2,20,23] Li metal is known to experience dendrite growth. Coupled with its high reactivity with the organic electrolyte, continuous consumption of electrolyte and the formation of isolated "dead" lithium leads to cell failure.[192] Another challenge of Li metal battery is an increased concern for safety. Flammability of organic solvent is an inherent safety problem of using liquid-based electrolytes including polymer gel electrolytes.[193] The safety issue is more pronounced in Li metal battery, where highly reactive, mossy Li metal grown on the anode is prone to catch fire.

Current research on Li metal anode overwhelmingly focuses on improving its cycling stability by suppressing dendrite (or more generally non-uniform) growth and improving coulombic efficiency. General approaches include: 1) three-dimensional (3D) hosts to minimize macroscopic volume change and reduce local effective current density which discourages dendrite growth;[69,194] 2) new electrolyte chemistry to affect Li deposition.[8,195] For example, ether-based electrolyte was found to be more effective than carbonate-based electrolytes to offer dendrite-free Li deposition;[94,196] and 3) inorganic and polymeric coatings to influence morphology.[48,53,54]

The fundamental reason for non-uniform Li growth is due to uneven current distribution, ion concentration gradient in the solution and the heterogeneous nature of the Li surface especially at a high current density. Li chemically reacts with electrolyte components (both solvent and salts) to form the solid electrolyte interface (SEI) layer, which is a composite of multiple salts and organic and polymeric compounds.[197] The heterogeneous nature

of the SEI layer inherently leads to inhomogeneous Li metal growth. Based on this hypothesis, we previously fabricated a single component layer of lithium methyl carbonate (LMC) on the surface of Li metal by reacting dimethyl carbonate (DMC) and lithium iodide (LiI), and achieved a stable plating/striping of Li in a mixed electrolyte of ethylene carbonate (EC), DMC and LiI.[105,198] LiI works as both a source of lithium ion and a catalyst of the demethylation of DMC, which produces LMC. This rigid inorganic layer on Li metal is chemically homogeneous and suppresses the dendrite growth.

Compared to tremendous efforts to increase the lithium cycling stability and efficiency, much less attention has been paid to the safety implications of electrolyte choices. Although ether-based solvents are favored for high-efficiency lithium cycling, they are highly volatile. Recently, researchers proposed to use electrolytes with very high concentrations of salts to achieve simultaneous excellent cycle life and safety in both lithium-ion and Li metal batteries. Yamada et al. showed high concentration of lithium/sodium bis(fluorosulfonyl)imide (LiFSI/NaFSI) in TMP (trimethyl phosphate) solvent exhibits both fire retarding property and highly reversible cycling of Li^+ or Na^+ ions with graphite anodes.[199] Zhang et al. reported that the highly concentrated LiFSI in triethyl phosphate (TEP) solution can be diluted with fluoroether, a non-solvating solvent, to decrease the total concentration of the salt, while maintaining the fire retarding property and enabling the cycle of Li metal anode at high columbic efficiency (>99%).[92]

Here, we present a new electrolyte for Li metal batteries that enables both stable lithium cycling and a new built-in safety mechanism that is thermally triggered. A polymer gel electrolyte is in-situ formed between the solvent, VC, and the salt, LiI. Contrasted from our previous work on the rigid DMC coating, the product from VC and LiI is a flexible polymer gel, which is more capable of accommodating the volume change of the Li metal anode. The SEI

layer between the gel electrolyte and Li metal is composed of soft polyVC embedded with hard Li_2CO_3 nanoparticles, which enables stable Li metal cycling. The coulombic efficiency of Li plating/stripping on Cu substrate is evaluated as 98.6%. As a safety function, the gel electrolyte can solidify at elevated temperatures, lose its ionic conductivity, and shut down the battery.

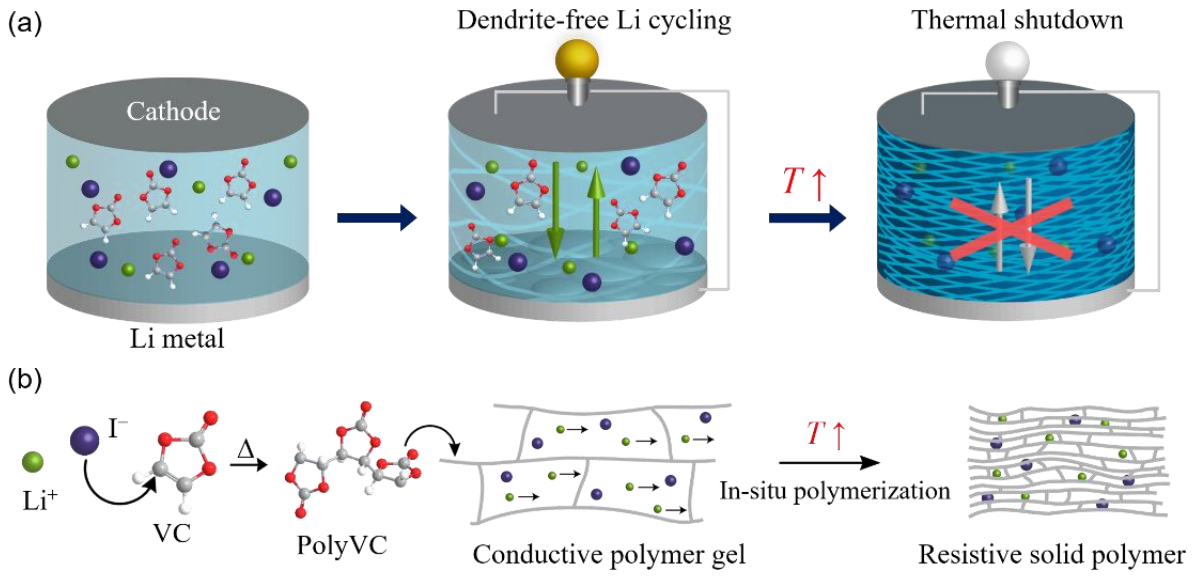

Figure 3-1 Li metal battery enabling dendrite-free Li cycling at room temperature and thermal shutdown when temperatures increase. (b) Chemical reactions and physical state of the polyVC-LiI gel inside the battery represented in (a). Heating of the electrolyte within a controlled time triggers partial polymerizations of VC with I^- anion to form the polymer gel network. Prolonged time of heating leads to full polymerization of VC and results in the resistive solid phase.

3.2 Experimental methods

3.2.1 Preparation of polyVC-LiI gel electrolyte

0.268 g of LiI (Ultra dry, >99%, Alfa Aesar, U.S.) and 2.0 g of VC (BASF, U.S.) were mixed in a 20 mL glass vial, and the solution was stirred by a magnetic stirrer at 350 rpm and heated by a hotplate at 80 °C for 1 hour. The cap of the vial should be slightly open to allow the pressure release because the reaction between VC and LiI generates CO_2 gas. All synthesis was conducted inside an Ar-filled glove box. Free-radical polymerization of VC by AIBN was carried out based on the method reported by Reimschuessel and Creasy.[200] Anionic polymerization of VC by LiOEt was carried out in DMSO at 80 °C with monomer/initiator ratio of 100 : 1. Synthesized polymer was purified in deionized water and dried under vacuum.

3.2.2 Characterization

As-prepared polyVC-LiI gel was purified by a dilution in *N*,*N*-dimethylformamide (DMF, Fisher Scientific, U.S.) followed by a precipitation in methanol and rinsing with deionized water. The sample was dried under vacuum at 100 °C for 4 days. The molecular structure of the dried sample was analyzed with ATR-FTIR (UATR 2, PerkinElmar, U.S.), and 500 MHz NMR (ECA 500, JEOL, Japan). Deuterated dimethylsulfoxide (d_6-DMSO, Sigma Aldrich, U.S.) was used as the solvent in the NMR experiment. The crystal structure of polyVC-LiI electrolyte after the complete polymerization was analyzed with XRD (D2 Phaser, Bruker, Germany).

The cross-sectional image and the surface morphology of polyVC-LiI gel electrolyte on Li metal/Cu foil was characterized by SEM (FEI Quanta FEG 250, Thermo Fisher Scientific, U.S.), paired with EDX analysis of C Kζ, O Kζ and I Lζ lines with an electron beam of 10 keV. Cryo-EM micrographs were recorded on a field emission gun JEM-2100F (JEOL), equipped with an OneView camera and operated at 200 keV.[105] The pristine polyVC-LiI

gel electrolyte was diluted by 10 times in VC and casted on a TEM grid. The electrodeposited Li metal was dispersed in VC under sonication and dropped on a TEM grid. All the sample preparation and transformation were performed with Ar protection.[72] The images were taken after the temperature was equilibrated to 100 K.

3.2.3 Electrochemical tests

The surface of Li metal was cleaned by scrubbing with a plastic blade before use. As-prepared polyVC-LiI gel was soon transferred between two pieces of Li metal and sealed in a CR2016 stainless steel coin cell case for Li//Li symmetric cell.

A copper (Cu) foil which was cleaned with hydrochloric acid was used in Li//Cu cell for the efficiency test. Prior to the test, a conditioning cycle was carried out on all the cells. In this step, a Li film was first deposited onto the Cu foil at 0.5 mA cm^{-2} for 10 hours, and then fully stripped to 1 V. Another Li film (5 mAh cm^{-2}) was deposited again, only 1 mAh cm^{-2} capacity of Li film was stripped and plated for 10 cycles. Finally, the Li film was fully stripped to 1 V. The current density during this test was 0.5 mA cm^{-2}. The distance between the two electrodes was controlled by a polypropylene film (25 μm) or a PTFE washer (125 μm) in the middle. The active diameter of the electrode is 12 mm. Electrochemical test was carried out on LAND-CT2001 battery testing systems (LAND electronics, China) and Arbin-BT2000 battery tester (Arbin Instrument, U.S.).

Conductivity of the polymer gel was measured with a potentiostat VSP-300 (Biologic Instrument, U.S.). The gel was placed between two stainless steel rods (diameter = 6.35 mm, distance = 3.0 mm) and heated with ribbon heater. Alternating voltage (10 mV) was applied after the temperature was stabilized ($dT/dt < 0.1$ °C min^{-1}).

Electrochemical window of the polymer gel electrolyte was evaluated with cyclic voltammetry, using a three-electrode cell: the working electrode was a stainless-steel foil (SUS304, area = 0.7 cm^2); the reference and the

counter electrodes were Li metal foil. The voltage range was between –0.15 and 3.8 V vs. Li/Li^+, and the scan rate was 1 mV s^{-1}.

3.3 Results and discussion

3.3.1 Formation and mechanism of thermal shutdown of polyVC-LiI gel electrolyte

A polymer gel electrolyte is synthesized by the gelation of a solution of VC and LiI (1 mol kg^{-1}) with a controlled reaction time (1 h) at 80 °C. LiI is the catalyst for the polymerization of VC. The polymerization rate significantly reduces at room temperature, especially when the polymer gel electrolyte is sealed in a battery cell. The reduction of VC on the surface of Li metal forms a robust SEI layer and enables dendrite-free cycling of the Li metal battery (**Figure 3-1**a). When the battery is heated, the polymerization of VC is accelerated, and the gel electrolyte turns into a solid phase (Figure 3-1b). Low ionic conductivity of the solidified electrolyte hinders the Li^+ ion transport and stops the charging/discharging of the battery.

3.3.2 Molecular structure of polyVC and the polymerization mechanism of VC catalyzed by LiI

The polymer gel synthesized with LiI was black in color (Figure S3-1, Appendix). Weight ratio of the polymer to VC solvent in the gel is 20% as determined by precipitating the polymer fraction in methanol from a DMF solution. The molecular weight of the polymer shows broad distribution ranging from 10^3 to 10^5 Da, as analyzed by gel permeation chromatography (Figure S3-1c, d Appendix). VC was also polymerized by free-radical and anionic polymerizations with azobisisobutyronitrile (AIBN) and lithium ethoxide (LiOEt) as initiators, respectively, to compare with the molecular structures of polyVC initiated from LiI. Despite the fact that free-radical polymerization of VC by AIBN has been studied for decades,[200–202] to the best of our knowledge, there are no reported studies on anionic polymerization of VC. The polymer products were precipitated in water and dried at 100 ℃ under vacuum overnight. Fourier-transform infrared (FTIR) spectra of three types of polyVCs prepared by

AIBN, LiOEt, and LiI are shown in **Figure 3-2**a. The C-H alkane stretching at 2990 cm^{-1} in those three polyVCs derives from the addition reaction on the double bond of VC. The C=O carbonyl stretching (1800 cm^{-1}) and C-O-C carbonate ester stretching (1160 & 1080 cm^{-1}) are present in those three polyVCs, which indicates the cyclic carbonate unit is preserved after the polymerization.

An additional peak at 970 cm^{-1} is particularly pronounced in polyVCs initiated by LiI and LiOEt. The five-membered ring of VC is not stable on the anionic attack from alkoxide or I^-, and ring-opening reaction can take place. Production of CO_2 gas from the solution of VC and LiI is observed by gas chromatography with a flame ionization detector (GC-FID) (Figure S3-2, Appendix). The rate of CO_2 gas generation increases at a higher temperature. Krapcho reported that nucleophilic attack from anions can promote the decarboxylation of the substrate in concerted fashion.[203] The IR peak at 970 cm^{-1} is assigned to C-O-C ether stretching, resulting from the ring-opening and decarboxylation reaction of the cyclic ester bond. Indeed, anionic polymerization of ethylene carbonate (five-membered cyclic carbonate) also produces ring-opened structure.[204,205]

^{1}H NMR analysis (Figure 3-2b) confirms polyVC initiated by AIBN has the simplest molecular structure, only possessing the cyclic carbonate units (peak **a**, chemical shift: 5.3 ppm). The main peak of polyVC initiated by LiI matches with peak **a**, and two additional peaks (**b**, **c**) are present. A broad peak (**b**) between 6.0 and 6.2 ppm is assigned to H on vinyl group and peak **c** at 4.6 ppm to H on tertiary carbon bonded with oxygen atom and ethylene carbonate unit. The presence of vinyl group supports the ring-opening reaction during the polymerization, and tertiary carbon suggests a branched structure in the cyclic carbonate chain.

According to our observation that the polymerization of VC proceeds with the decarboxylation, lithium iodoalkoxide (by-product of the decarboxylation of VC) is likely the initiator of the polymerization (see Figure S3-3

in the Appendix for the reaction scheme). Alkoxide attacks the double bond of VC and the polymerization propagates. Substitution reaction of iodo group by alkoxide adds vinyl ether group in the polymer structure and regenerates the I^- anion. Ring-opening reaction can occur on the main chain of cyclic carbonate in polyVC. Branching of the polymer chain is then accomplished by the substitution reaction of iodo group by anionic end group of another polymer chain.

A solution of VC and LiI (1 mol kg^{-1}) was stored at room temperature under Ar atmosphere for a prolonged period time to study the composition and the crystal structure. The sample gradually turned to a gel and finally to a hard solid after five months. IR spectra of the solid polyVC-LiI electrolyte only shows the peaks of polyVC and unreacted residual VC (Figure S3-4a, Appendix). The catalytic reaction between LiI and VC is specific, and polyVC and CO_2 are the only major products. Interestingly, powder X-ray diffraction (PXRD) of the polyVC-LiI electrolyte shows only a broad peak of polyVC, and LiI is completely amorphized in the polymer matrix (Figure S3-4b, Appendix).

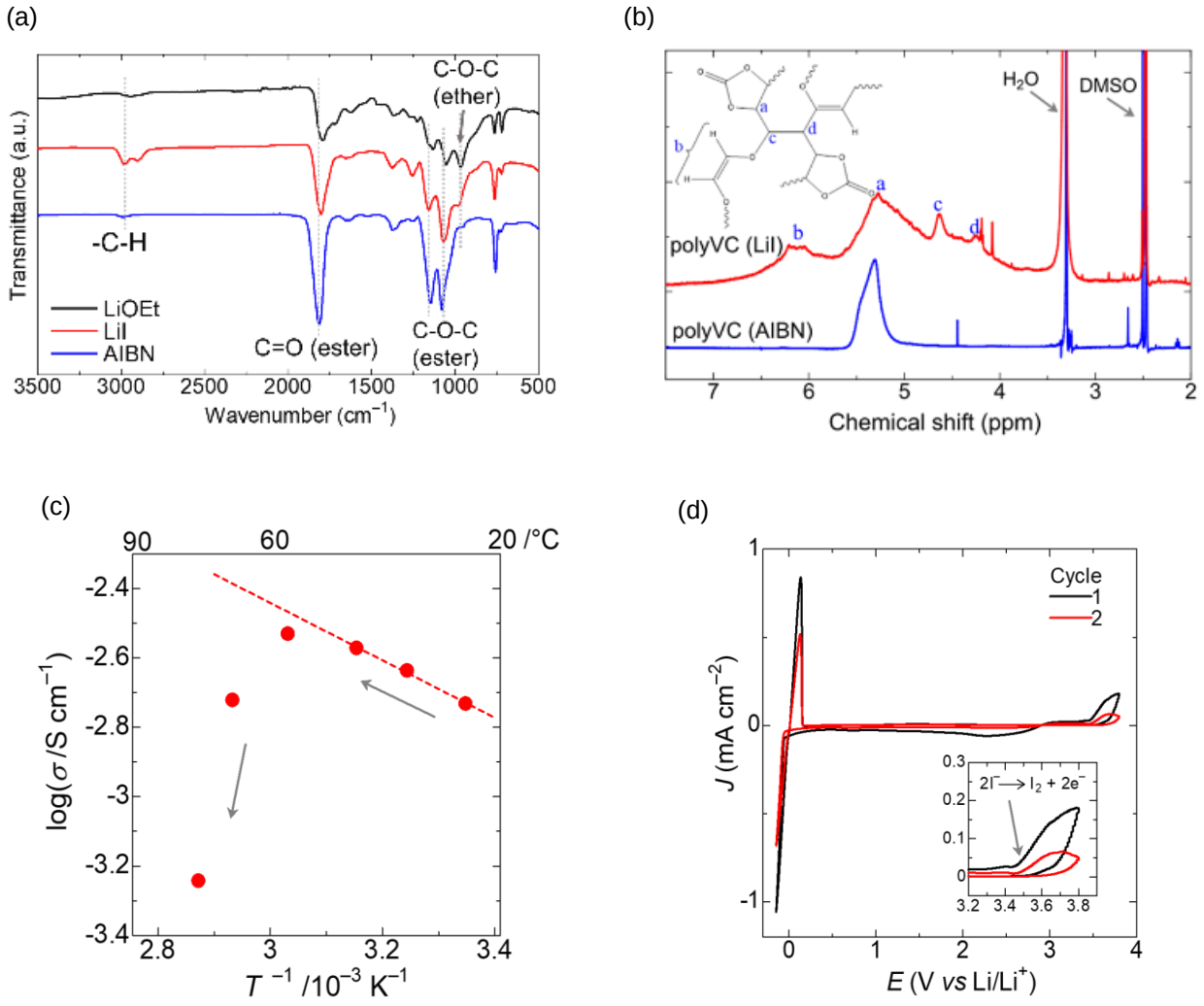

Figure 3-2 (a) IR spectra of polyVCs polymerized with AIBN, LiI, and LiOEt as the initiator. (b) ^{1}H NMR spectra of polyVCs polymerized with AIBN and LiI. (c) Conductivity of polyVC-LiI electrolyte at increasing temperature (average heating rate is 0.3 ℃ min^{-1}). (d) Cyclic voltammetry of the polyVC-LiI electrolyte on a stainless-steel working electrode. Scan rate was 1 mV s^{-1}.

3.3.3 Conductivity and electrochemical window of polyVC-LiI gel electrolyte

The conductivity of the polyVC-LiI gel electrolyte at 25 °C is evaluated as 1.8×10^{-3} S cm^{-2}, which is comparable to the conductivities of other organic liquid electrolytes. The conductivity increases linearly with increasing temperatures (average heating rate was 0.3 °C min^{-1}) until 60 °C, following the Arrhenius equation (Figure 3-2c). However, the conductivity starts decreasing above 60 °C, because polymerization of VC solidifies the electrolyte. Decay of the conductivity at high temperatures is expected to shut down the battery.

The electrochemical window of the polyVC-LiI gel electrolyte was analyzed by cyclic voltammetry (Figure 3-2d). The electrolyte was very stable down to lithium plating potential, but oxidative current was observed above 3.5 V vs. Li/Li^+, which is due to the oxidation of iodide anion in the electrolyte. The oxidation potential of LiI in the polyVC-LiI gel electrolyte is higher than the oxidation potential in a liquid ether electrolyte (2.9 V vs. Li/Li+).[206]

3.3.4 Electrochemical performance of Li metal anode with polyVC-LiI gel electrolyte

The polyVC-LiI gel was directly applied as the electrolyte in Li//Li symmetric cell. In order to examine the intrinsic property of this gel electrolyte, a plastic washer was used to control the thickness of the electrolyte instead of using a membrane support (Figure S3-5, Appendix). With the electrolyte thickness of 25 μm, Li/polyVC-LiI/Li cell can cycle over 1500 hours without shorting at a constant current density of 1 mA cm^{-2} and areal capacity of 1 mAh cm^{-2} (**Figure 3-3**a). With a thicker electrolyte (125 μm), the cell can be cycled at a higher current density of 5 mA cm^{-2} (Figure 3-3b). The polarization in the voltage curve becomes flat after a couple of cycles at the beginning, which indicates stable plating and dissolution of Li metals.[207] Coulombic efficiency of lithium deposition in this polyVC-LiI gel was evaluated by plating/stripping Li metal on Cu foil (Figure 3-3c), and a high efficiency of 98.6% is achieved at 0.5 mA cm^{-2}. As a comparison, the cycling efficiency of Li metal in a carbonate electrolyte of

EC/DMC/$LiPF_6$ with 2 wt% VC additive was reported as only 80%.[208] Recently, Hu and co-workers reported an electrolyte using VC as the major solvent with 1 M lithium bis(trifluoromethanesulfonyl) imide (LiTFSI) salt, and the Li cycling efficiency in this electrolyte is 97%,[209] which is comparable to the efficiency in polyVC-LiI gel electrolyte. The high efficiency of cycling Li metal suggests VC is a promising solvent to protect Li metal from parasitic side reactions with the electrolyte.

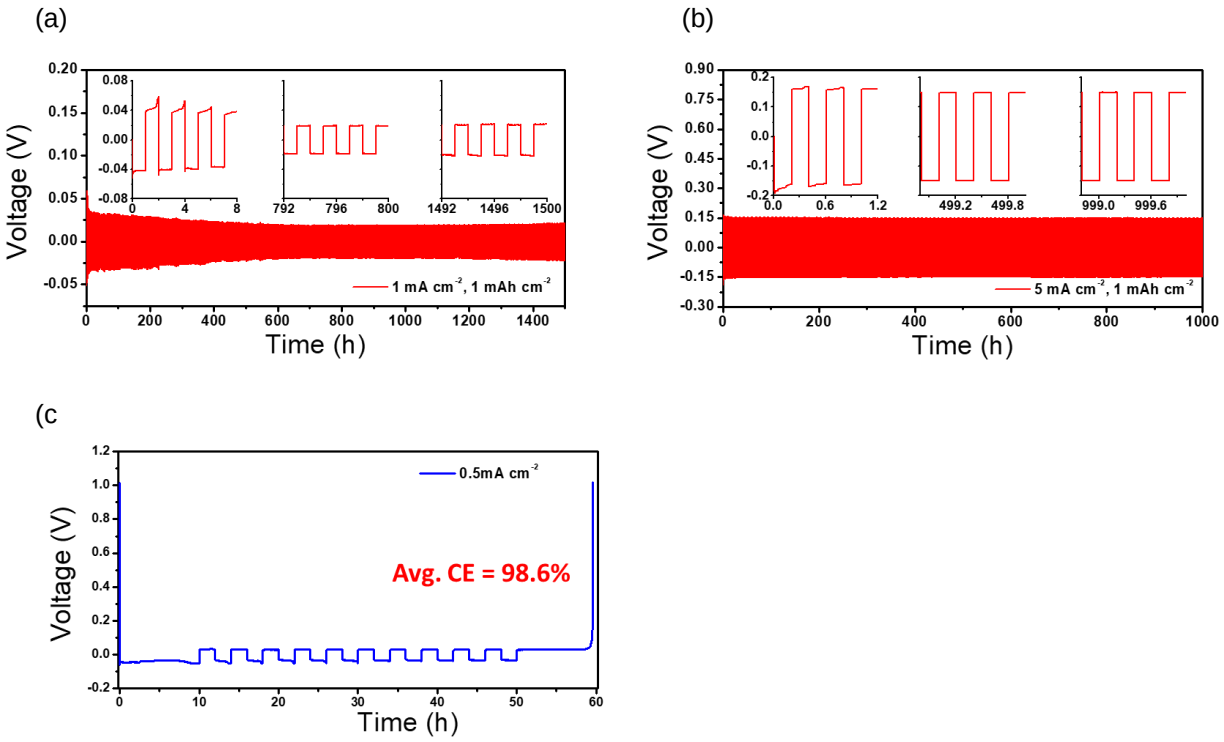

Figure 3-3 Cycling performance of Li//Li symmetric cell with separator-free polyVC-LiI gel electrolyte at a current density of (a) 1 mA cm^{-2} and (b) 5 mA cm^{-2}. Thickness of the electrolyte is: (a) 25 μm; (b) 125 μm. (c) Efficiency test of Li plating/stripping with Li//Cu cell. PolyVC-LiI gel electrolyte with 125 μm thickness was placed between the Cu and Li metal foils.

3.3.5 Characterization of the interface between polyVC-LiI gel electrolyte and Li metal

The morphology of cycled Li metal and the polymer coating layer was observed by scanning electron microscope (SEM) after 1000 hours of lithium plating/stripping in a Li//Li symmetric cell at a current density of 5 mA cm^{-2} and a capacity of 1 mAh cm^{-2} (**Figure 3-4**a). Elemental mapping of the cross section clearly indicates the polymer layer on the lithium surface (Figure 3-4b-d). The surface of the polymer layer is smooth and dense (Figure 3-4e-h) while the cycled Li shows a dendrite-free morphology.

The morphology of Li metal deposited on Cu foil (Current density = 0.5 mA cm^{-2}, areal capacity = 5 mAh cm^{-2}) was also examined (Figure 3-4i-k). The dark region in the elemental mapping of C and O indicates the layer of Li metal. Interestingly, the Li metal deposited near the Cu surface shows fibrous morphology, while the Li metal is dense near the polymer electrolyte (Figure 3-4l). Possibly, as Li metal is deposited from the Cu substrate into the gel electrolyte the pressure on the growing tip of the Li metal increases and results in the dense morphology.

To further prove that the polymerization of VC by LiI contributes to the stabilization of Li metal, Li metal was deposited on Cu foil in VC-LiI electrolyte before and after gelation. The morphology of the electrodeposited Li metal was observed by SEM. A beaker cell was used in this experiment to eliminate the influence of pressure between the polymer gel and the electrode (Figure S3-6, Appendix). Under atmospheric pressure, the Li metal grows into larger particles when deposited in the gel state compared to the liquid state. To note, when $LiPF_6$ is used instead of LiI in the pure VC electrolyte, the polarization of Li plating is significantly higher and Li metal grows in a dendritic form, indicative of a beneficial role of LiI. We postulate that, unlike complex polyanions such as PF_6^-, the irreducible nature of the iodide ion prevents the formation of other inorganic anions which would introduce interfacial inhomogeneity and promote dendrite growth. The formation of the polymer gel electrolyte through

selective decarboxylation and polymerization of VC thus leads to a robust and stable SEI layer consisting of Li_2CO_3 as the inorganic component and enables highly stable lithium cycling. Finally, it is also possible that high viscosity and elasticity of the gelled electrolyte enhances further the stability of the Li metal surface.[31–33]

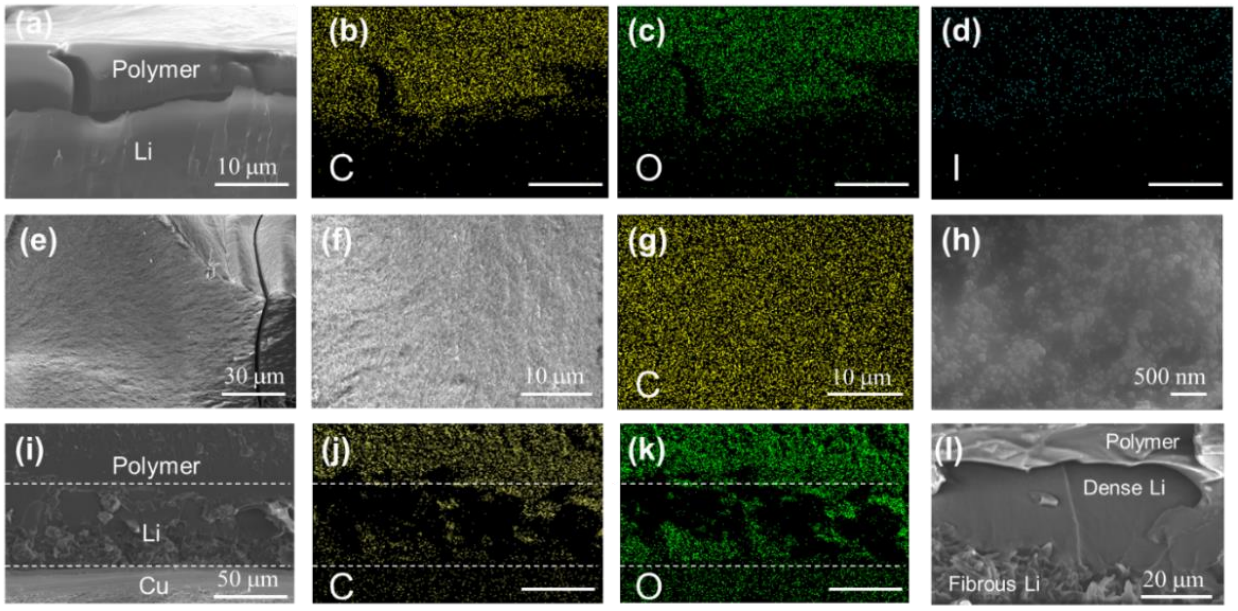

Figure 3-4 SEM image (a) and elemental mapping (b-d) of cross section of Li metal after cycling for 1000 hours at a current density of 5 mA cm^{-2} with a capacity of 1 mAh cm^{-2}. Scale bar = 10 μm. Surface SEM images (e, f, h) of the polymer coating on Li metal at increasing magnifications and the elemental mapping (g) of the image (f). Cross-sectional SEM image (i) and elemental mapping (j, k) of electrodeposited Li metal on Cu substrate at a plating current density of 0.5 mA cm^{-2} with a capacity of 5 mAh cm^{-2} in polyVC-LiI gel electrolyte. Scale bar = 50 μm. (l) Magnified view of the Li metal on Cu substrate. Fibrous, and dense morphologies of Li metal are observed on the Cu side, and the polymer side, respectively.

3.3.6 Cryo-EM analysis of the SEI layer on Li metal

The structure and the composition of the SEI layer is directly visualized with cryogenic electron microscopy (cryo-EM) analysis.[49,72] Pristine polyVC-LiI gel electrolyte before cycling shows an amorphous structure (**Figure 3-5**a), and no diffraction point is observed in the fast Fourier transform (FFT) pattern in Figure 3-5b. This result agrees with the PXRD pattern of polyVC-LiI electrolyte, where LiI is completely amorphized in the polyVC matrix (Figure S3-4b, Appendix). After 10 cycles of Li//Li cycling in polyVC-LiI gel electrolyte, Li_2O, and Li_2CO_3 particles are observed on the electroplated Li metal (Figure 3-5c). The FFT pattern (Figure 3-5d) confirms the lattice space of Li_2CO_3 (110), (200), (002) planes and Li_2O (111) plane. The Li_2O (111) plane in the marked region of Figure 3-5c align in the same direction, and thus those Li_2O particles likely belong to one larger particle. Li_2O comes from either surface oxidation during the sample preparation or the decomposition of VC. The particle size of Li_2CO_3 ranges from 10 to 20 nm and is larger than those (c.a. 3 nm) produced from a carbonate electrolyte of ethylene carbonate (EC)/diethylene carbonate (DEC)with 1 M $LiPF_6$.[71] The in-situ decarboxylation of VC in the electrolyte increases the concentration of CO_2 and promotes the growth of dense and large Li_2CO_3 particles. Except for Li_2CO_3 and Li_2O, no other crystalline SEI component, such as lithium methylcarbonate (LMC), [105] are observed. Amorphous region in Figure 3-5c is likely occupied by polyVC, as the amorphous nature is shown in Figure 3-5a.

We would like to put the composition and function of this unique SEI layer into the context of previous SEI engineering approaches. The chemical composition of SEIs are usually very complex, comprised of a mixture of LiF, Li_2CO_3, Li_2O, various forms of lithium alkyl carbonate, and polymers.[197,210] This is a direct result of the strong reductive ability of Li metal when exposed to organic solvents and lithium salts with complex anions. As a result,

the exact role of different components in determining cycling stability is unclear. To make the case even more complex, it is a popular practice to add additives to improve the SEI. For example, fluorinated organic solvents[211–215] and fluoride salt[8,196,216] additives can preferentially be reduced at the anode, thus forming more desirable SEIs. [10,195,217] Lithium fluoride (LiF) is widely believed to be the key SEI component because of the low solubility in the electrolyte, the high electrochemical stability, and the mechanical robustness.[59] Meanwhile, the addition of CO_2 in the electrolyte is also known to improve the cycle performance, because of the formation of Li_2CO_3 in the SEI layer.[218–220]

The SEI layer made from VC and LiI in this study is free from fluoride compounds. Therefore, it is clear that Li_2CO_3 and amorphous polyVC alone are effective to stabilize the interface between the electrolyte and Li metal. Elimination of the decomposition reaction of lithium salt by using LiI simplifies the interface chemistry and helps to define the composition of SEI layer.

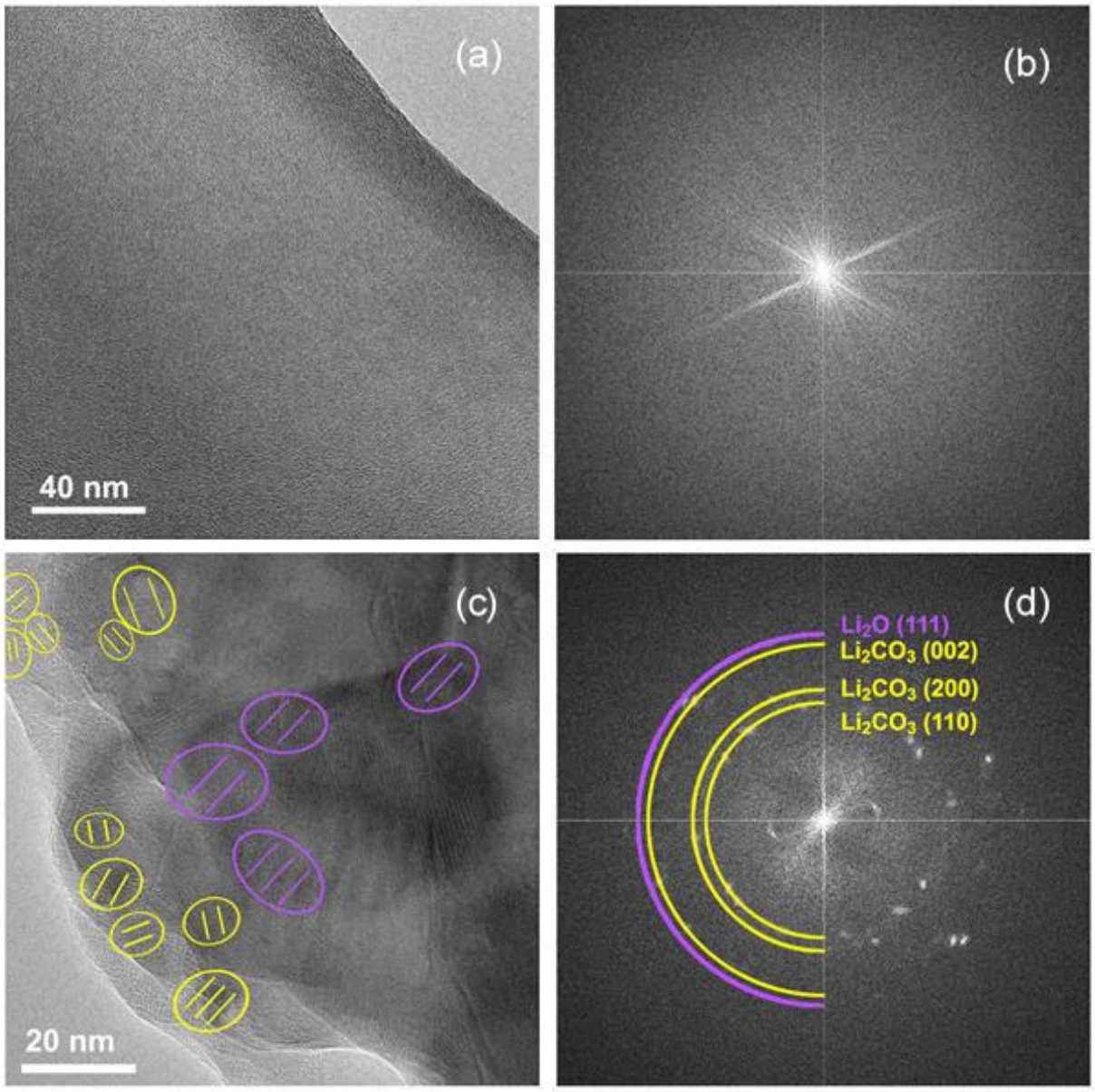

Figure 3-5 Cryo-EM image (a) and FFT pattern (b) of polyVC-LiI gel electrolyte. Cryo-EM image (c) and FFT pattern (d) of the SEI layer on Li metal after Li//Li symmetric cycling for 10 cycles at 1 mA cm^{-2}, 1mAh cm^{-2}. Direction of the lattice planes in each crystal grain are emphasized by the straight lines.

3.3.7 Thermal shutdown of Li//LTO cell test with polyVC-LiI gel electrolyte

PolyVC-LiI gel electrolyte was tested in a full cell to demonstrate its potential application. LTO was selected as the cathode material and cycled between the cutoff voltages of 1 and 2 V vs. Li^+/Li, well below the oxidation potential of I^- (3.5 V svs. Li^+/Li). During the first discharge, an irreversible capacity of 25 mAh g^{-1} is lost in the reductive reaction of the gel electrolyte (**Figure 3-6a**). A passivation layer likely forms on the cathode side during this first discharge, and this irreversible reaction gradually diminishes in the following cycles. The increasing polarization with cycle numbers suggests the formation of a thicker polyVC layer on the cathode side. Since the increase of polarization was not observed in Li//Li symmetric cell during long term cycling (Figure 3-3a, b), polyVC-LiI gel electrolyte is more stable with Li metal compared to LTO cathode. Despite the slow capacity decay, the cell still maintains half of the initial capacity (75 mAh g^{-1}) after 700 cycles of charging/discharging at a rate of 1 C (Figure 3-6b). Recovery of the capacity by slowing down the charging/discharging rate (to 1/4 and 1/8 C after 1203 cycles) indicates kinetic barrier is a source of the capacity degradation.

The temperature of LTO cell was increased in the middle of the charging step at room temperatures to evaluate the thermal shutdown function. When the cell temperature is increased to 60 ℃, the overpotential of the cell decreases by 20 mV, because the ionic conductivity of the electrolyte increases, while the polymerization rate is slow at this temperature (Figure 3-6c). When the temperature reaches 80 ℃, the polymerization rate of VC is accelerated, resulting in a complete loss of the capacity within 30 min (Figure 3-6d). The impedance of the LTO cell increases from 200 Ω to 2×10^5 Ω after heating at 80 ℃ (Figure 3-6e), and the electrolyte turned into a solid (Figure S3-7, Appendix).

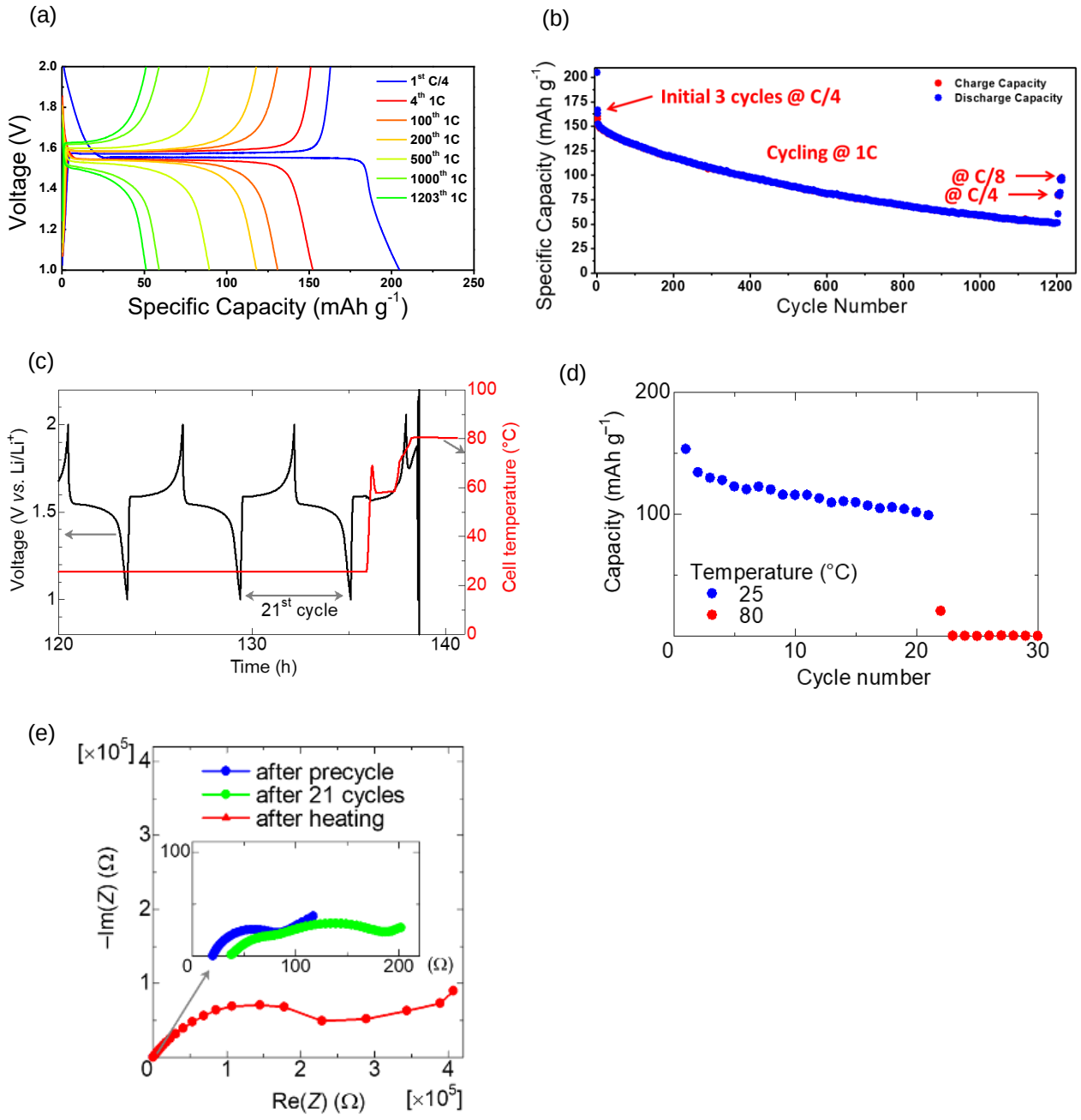

Figure 3-6 Voltage profile (a) and specific capacity (b) of LiI/LTO cell cycled in polyVC-LiI gel electrolyte at the indicated C-rate. (c) Voltage profile and cell temperature of Li//LTO cell. The cell temperature was increased in the middle of 22nd charging step. (d) Discharge capacity of Li//LTO cell and the cycle number. (e) Impedance spectra of Li//LTO cell after precycle (2 cycles at 20 μA cm^{-2}), 21 cycles (at 40 μA cm^{-2}), and heating at 80 °C.

3.4 Conclusions

Thermal shutdown function using a polymer gel electrolyte was demonstrated in Li metal battery for the first time. Thermally activated in-situ polymerization was successfully implemented in the self-protective battery. Combination of VC and LiI also stabilizes the surface Li metal by forming the SEI layer composed of Li_2CO_3 and polyVC. Nucleophilic attack of LiI on VC produces CO_2, and lithium alkoxide, which initiates anionic polymerization of VC. LiI is completely amorphized in the polyVC matrix. The composite SEI layer with 20 nm dense Li_2CO_3 grains embedded in amorphous polyVC matrix results in stable Li//Li symmetric cycling for over 1000 hours at 5 mA cm^{-2} and 1 mAh cm^{-2}, achieving 98.6% coulombic efficiency of Li plating/stripping. The thermal shutdown function of the gel electrolyte is also demonstrated in a Li//LTO cell with promising cycling stability. We are mindful that the use of LiI as the salt limits its upper operating voltage to 3.5 V. As a result, we are actively pursuing the use of LiI-containing polyVC gel electrolyte to enable stable cycling of sulfur-based cathodes, which will be reported elsewhere. The idea of using irreducible lithium salt (LiI) and catalyzed chemical reactions to control the composition of SEI layer leads to a better understanding of the interfacial chemistry inside batteries. The work also clearly shows the potential of a fluorine free electrolyte chemistry for Li metal batteries.

3.5 Acknowledgement

Chapter 3, in full, is a reprint of materials published in the following paper: Hongyao Zhou, Haodong Liu, Yejing Li, Xiujun Yue, Xuefeng Wang, Matthew Gonzalez, Ying Shirley Meng and Ping Liu*, "*In situ* formed polymer gel electrolyte for lithium batteries with inherent thermal shutdown safety features" *J. Mater. Chem. A*, **2019**, 7, 16984. The dissertation author was the primary researcher for the data presented and was the primary author of this publication. The permissions to reproduce this material were granted by Royal Society of Chemistry, copyright 2019.

3.6 Appendix

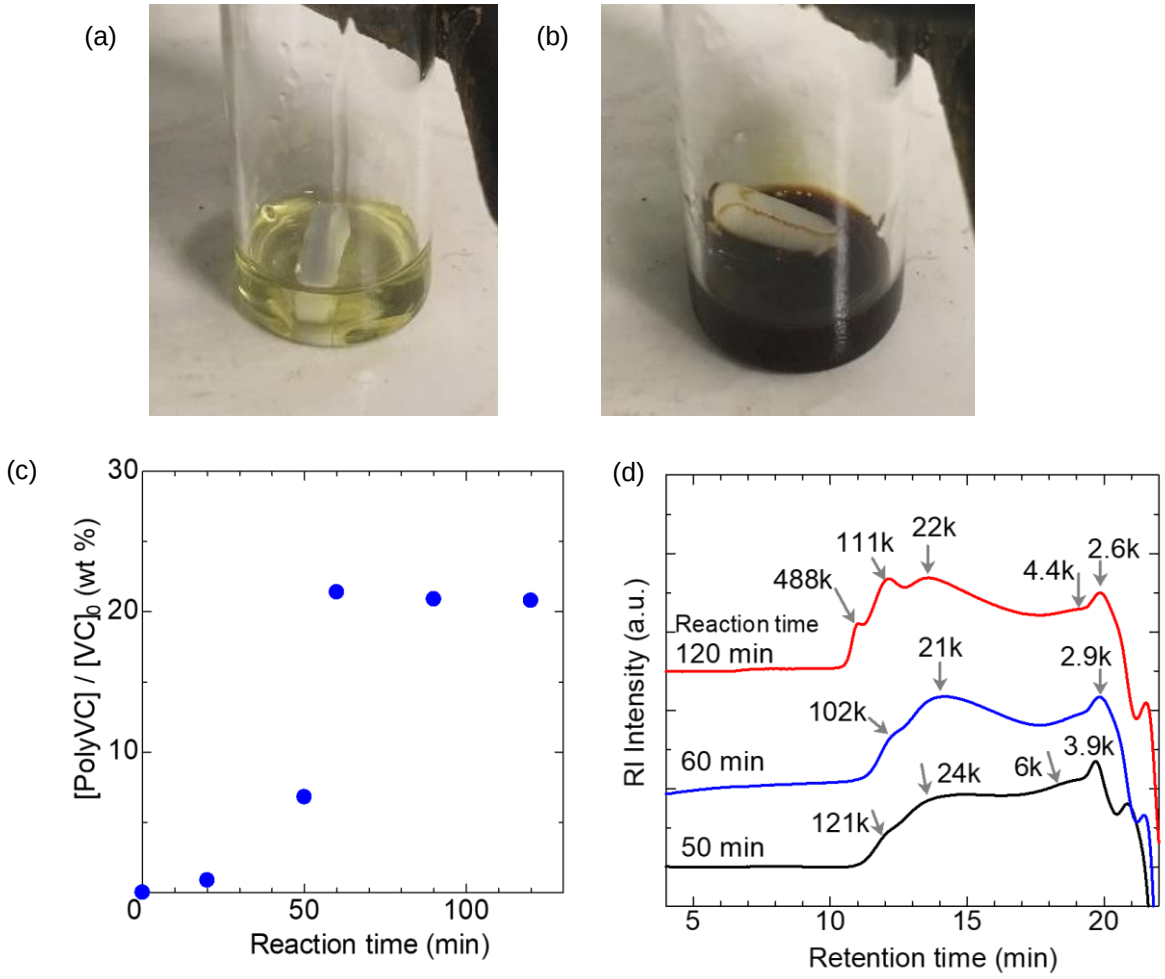

Figure S3-1 Photograph of VC-LiI (1 mol kg^{-1}) solution before heating (a) and after heating (b) at 80 °C. (c) Weight ratio of polyVC to the initial amount of VC ($[VC]_0$ = 2 g) monomer after varied reaction time ($_T$ = 80 ° C). The polymer gel after 60 minutes of reaction is used as the electrolyte in the experiment, and the weight ratio of polyVC to solvent VC in the gel electrolyte is 1:4. (d) Reflective index (RI) intensity vs retention time of polyVC after 50 min, 60 min and 120 min of the reaction. Number-averaged molecular weight (M_n) of the polymer at each peak is labeled in the figure. The polyVC synthesized with LiI shows a broad distribution of the M_n.

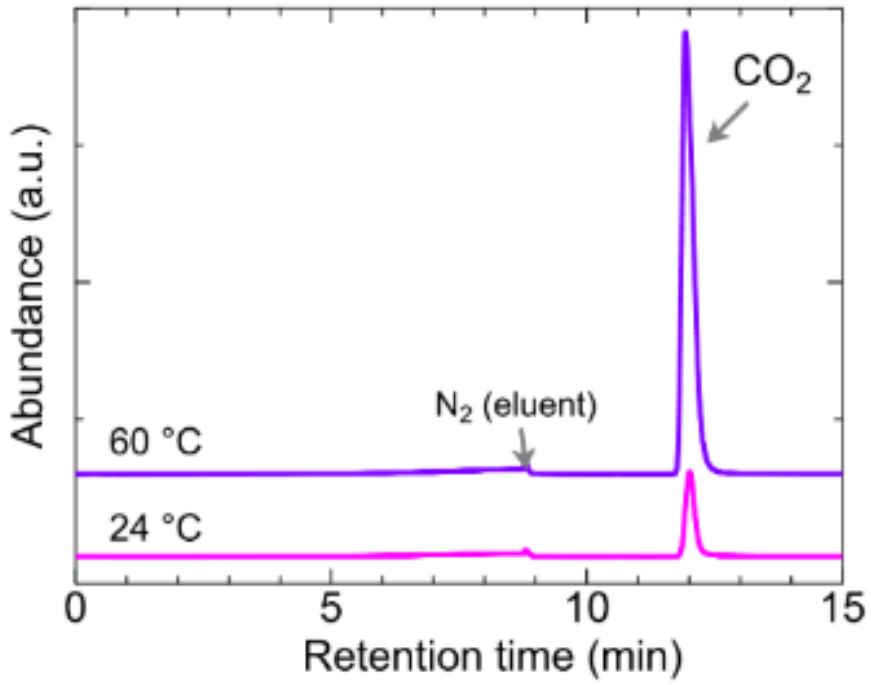

Figure S3-2 Gas chromatography of the gas generated during the polymerization of VC by LiI at 24 and 60 °C.

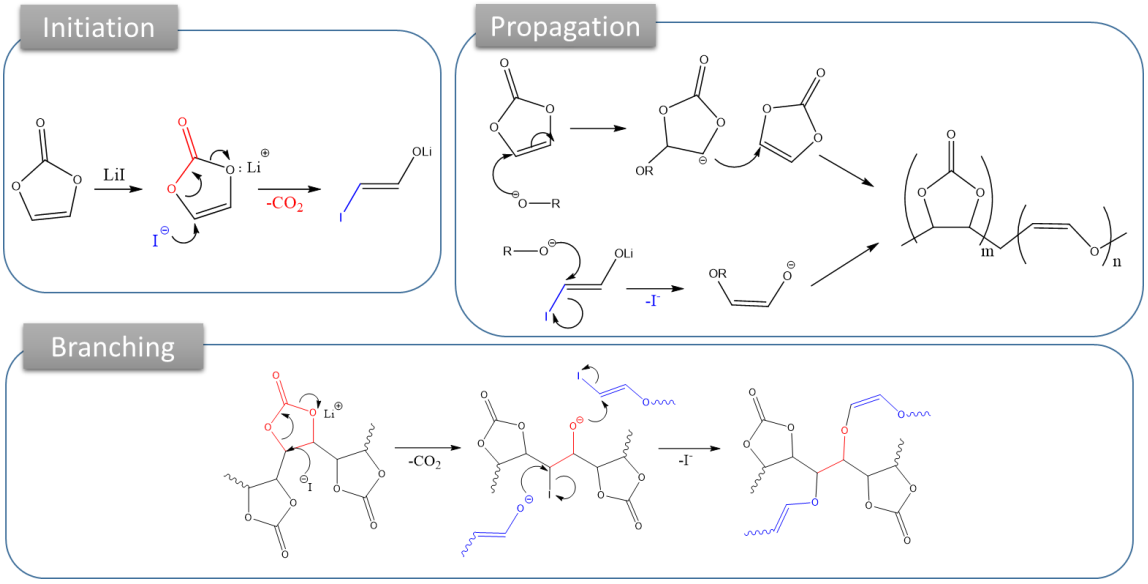

Figure S3-3 Initiation, propagation, and branching reactions of polyVC which is polymerized from VC and LiI.

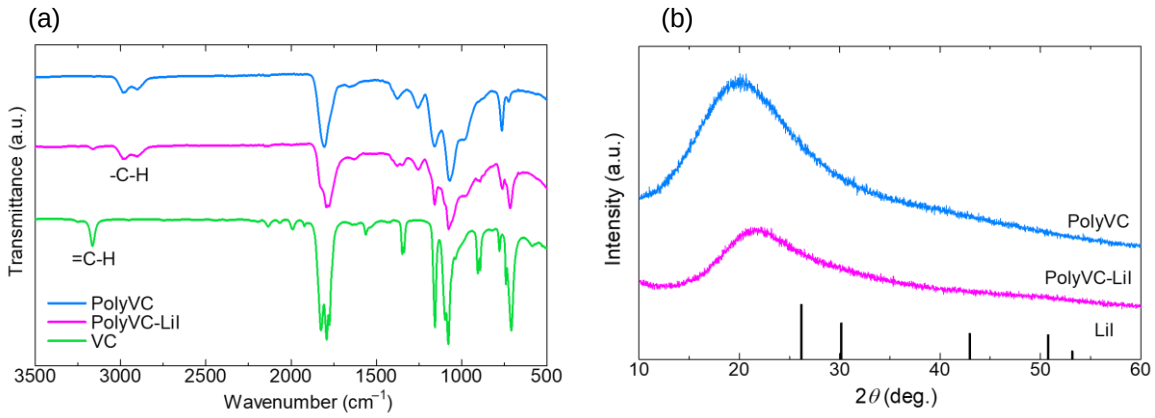

Figure S3-4 (a) IR spectrum of solidified polyVC-LiI gel electrolyte after five months of storage under Ar atmosphere, and the spectrum after removal of LiI. (b) Powder X-ray diffraction pattern of solidified polyVC-LiI electrolyte before (PolyVC-LiI)/after (PolyVC) removal of LiI. No LiI peaks are visible in the polymer gel. Diffraction pattern of LiI is cited from Inorganic Crystal Structure Database (ICSD) 414244.

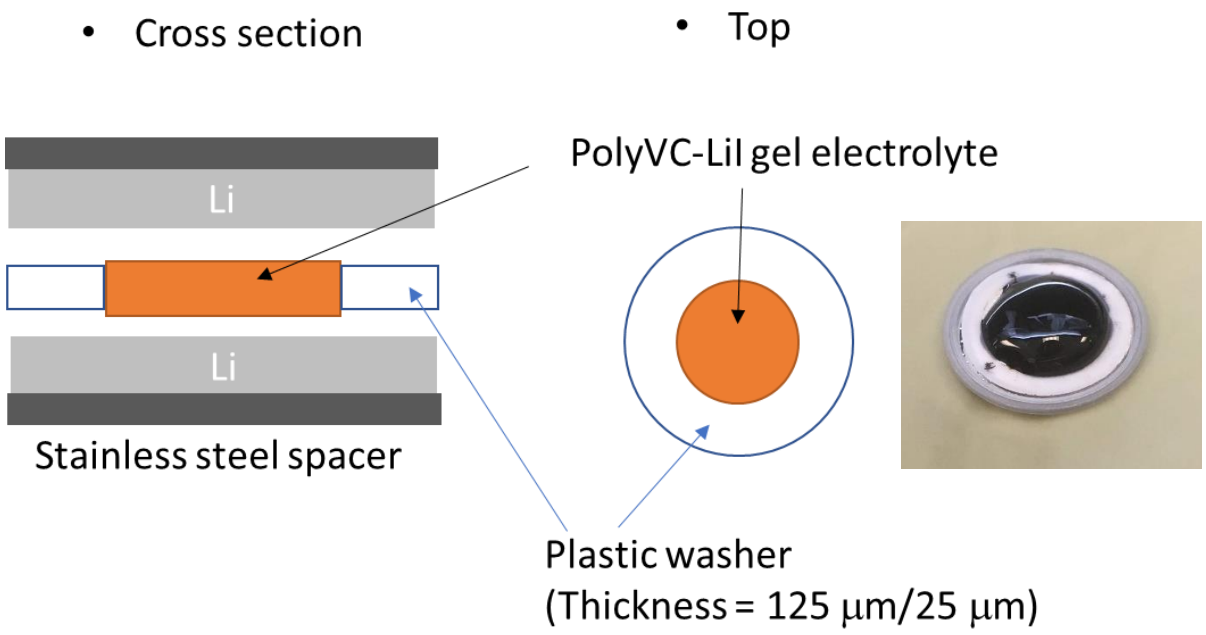

Figure S3-5 Cross section and top view of Li//Li symmetric cell. The two electrodes are separated by a plastic washer with a thickness of 125 μm and 25 μm (PTFE for 125 μm, PE for 25 μm). The inner diameter of the washer is 12 mm. The cell is crimped into CR2016 coin cell case.

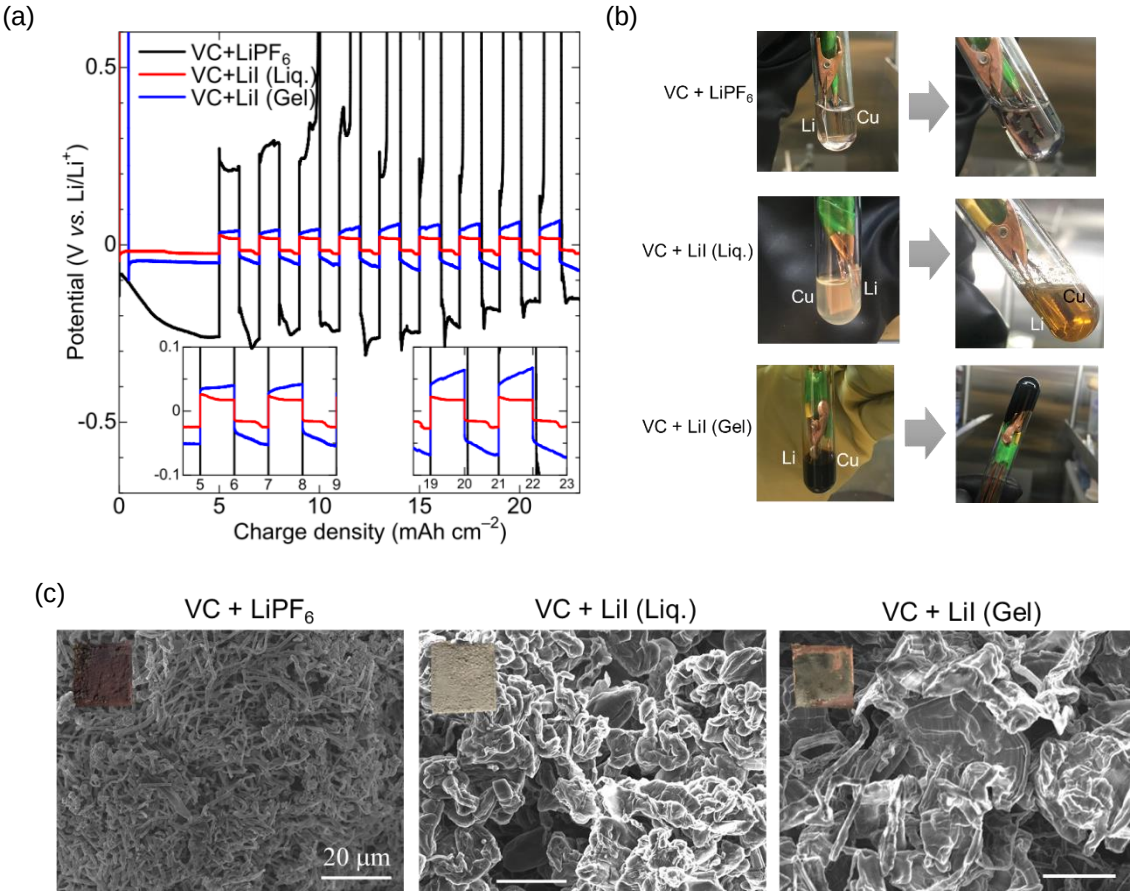

Figure S3-6 (a) Potential profile of Li//Li symmetric cycling in a test tube flooded with various VC-based electrolytes: VC + 1 mol kg^{-1} $LiPF_6$; VC + 1 mol kg^{-1} LiI at liquid state; VC + 1 mol kg^{-1} LiI at gel state. 5 mAh cm^{-2} of Li was deposited on Cu foil and 1 mAh cm^{-2} of Li was stripped/deposited repeatedly for 9 cycles. (b) Photo images of the state of the electrolytes before (left column) and after (right column) Li//Li cycling. (c) SEM images of the deposited Li metal on Cu foil. Scale bar = 20 μm. The inset shows the photo image of the electrodeposited Li on Cu electrode.

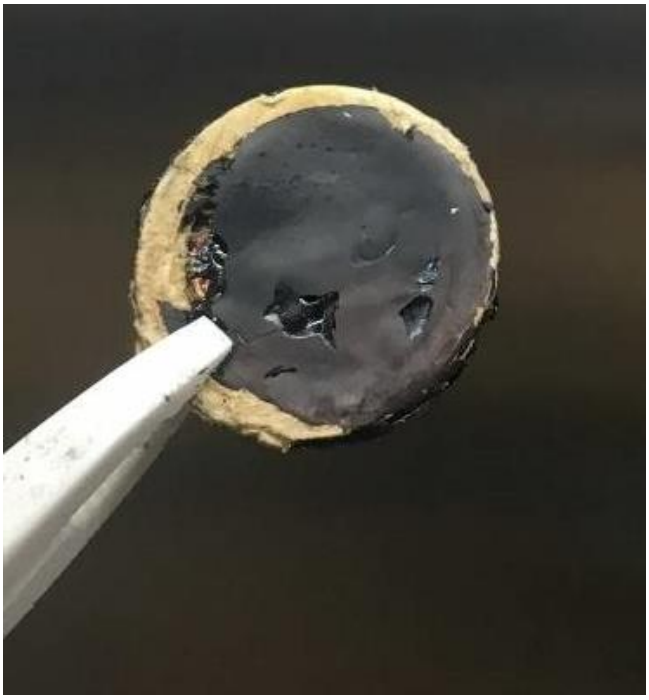

Figure S3-7 VC-based polyVC-LiI gel electrolyte after heating at 80 °C. The gel was completely solidified and covered the surface of Li metal.

Chapter 4 High Seebeck coefficient electrochemical thermocells for efficient waste heat recovery

4.1 Introduction

The electrochemical potentials of reversible electrode reactions are usually functions of temperatures due to entropy changes. This effect can be explored to convert thermal energy into electricity.[221,222] Thermocells are constructed with identical electrochemical redox pairs on both electrodes which operate at different temperatures. As a result, a voltage is generated in the thermocell.[223–226] This simple setup and the use of inexpensive materials as compared to solid thermoelectric materials[227] have stimulated its applications for waste-heat recovery,[223,228,229] power source for wearable devices,[230,231] and liquid cooling system[232].

Seebeck coefficient is a partial derivative of the electrochemical potential with respect to the temperature ($\partial E/\partial T$).[233] Much effort has been devoted to maximize this value since large voltage directly translates to higher thermal efficiency (η):[234]

$$\eta = \frac{\sigma V_{oc}^{-2}}{4\kappa\Delta T} \qquad (4\text{-}1)$$

σ, and κ are, respectively, the ionic, and thermal conductivity of the electrolyte solution, V_{oc} is the open-circuit voltage, and ΔT is the temperature gradient. Consider a reversible redox reaction: $A + ne^- \leftrightharpoons B$

Using the equation of Gibbs free energy and Nernst equation, the Seebeck coefficient is:

$$\frac{\partial E}{\partial T} = -\frac{\Delta S_{redox} + \Delta S_{vap}}{nF} + \frac{\partial}{\partial T}\left(\frac{RT}{nF}\ln\left(\frac{c_{A1}}{c_{A2}}\right)\right) \qquad (4\text{-}2)$$

F is the Faraday constant and R is the standard gas constant. n is the stoichiometric number of electrons in the redox reaction. ΔS_{redox}, and ΔS_{vap} are entropy changes of redox reaction and vaporization, respectively. The first term is negative when oxidation occurs at higher temperatures, and thus the Seebeck coefficient is negative, *vice versa*. c_{A1} and c_{A2} are the respective concentrations of the redox specie A in the hot and cold sides of the thermocell, whereas the

concentration of the specie B is assumed to be constant.[235] ΔS_{redox} of transition metal redox couples was studied by Weaver and coworkers.[236–239] Solvent effect on ΔS_{redox} and Seebeck coefficient has also been systematically studied.[240–242] The Seebeck coefficient can also be increased by introducing the concentration difference between c_{A1} and c_{A2} in equation (2), which is previously achieved by exploring host-guest chemistry.[235,243] However, the Seebeck coefficient is still limited to ca. 2 mV K^{-1}.

The Br_2–Br^- thermocell, which was first proposed by Lalancette[244] and developed by Endo[245], and Shindo,[246,247] can exhibit a Seebeck coefficient of 5.68 mV K^{-1} when the hot side is operated above the boiling point of Br_2.[246] The vaporization of Br_2 increases the Seebeck coefficient, however, the extremely corrosive Br_2 vapor limits its application. Previously, a thermally regenerative fuel cell, using hydrogenation of acetone to iso-propanol, was studied by Ando and coworkers.[248–251] Chemical heat pump involving dehydrogenation of iso-propanol and hydrogenation of acetone was studied by Saito and coworkers.[252–255] However, no study on the Seebeck coefficient and thermoelectric power of a thermocell based on this couple has been reported.

Here we demonstrate a thermocell based on the redox couple of acetone and iso-propanol (Figure4-1). When the hot side is operated at a temperature above the boiling point of acetone, its vaporization is utilized to create a large concentration difference ($c_{A1}/c_{A2} < 1$). The Seebeck coefficient is raised to –9.9 mV K^{-1}, the highest value reported so far for any redox couple. The thermal efficiency is 1.57% with respect to the Carnot efficiency, which is comparable to the conventional ferri/ferrocyanide redox couple.[256] Unlike the Br_2/Br^- couple, this redox couple is environmentally benign. Reversible redox reaction of acetone and iso-propanol is observed for the first time in a neutral pH solution. This is essential for the application of thermocells, because self-condensation of acetone occurs in both acidic and basic solutions at elevated temperatures.[257]

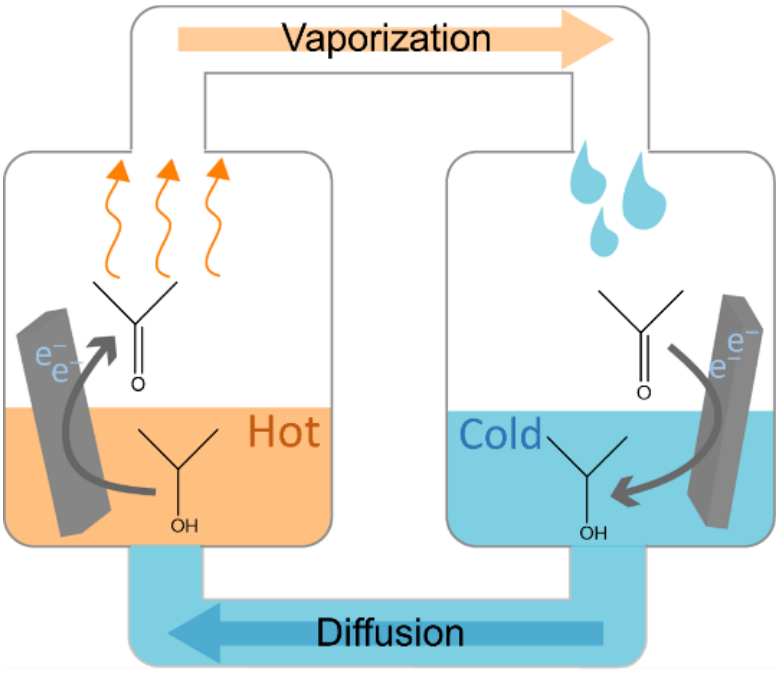

Figure 4-1 Scheme of the acetone–iso-propanol thermocell. Oxidation of iso-propanol to acetone occurs at the hot side, and reverse reaction occurs at the cold side. Acetone vaporizes when hot side temperature is above its boiling point.

4.2 Experimental methods

4.2.1 Materials

H_2PtCl_6 (YSI, Inc, received as 3% aqueous solution), $SnCl_4$ (Sigma Aldrich), concentrated sulfuric acid (Fischer Scientific), Li_2SO_4 H_2O (Fischer Scientific), acetone (Fischer Scientific, HPLC grade), iso-propanol (Macron Fine Chemicals, ACS reagent grade) were used as received.

4.2.2 Preparation of platinum-tin (Pt-Sn) electrode

Platinum foil (5 mm × 15 mm) was polished with fine sandpaper to remove any debris on the surface and further cleaned by scanning to –0.5 V vs. Ag/AgCl (saturated KCl) in 0.5 M sulfuric acid solution. Pt-Sn electrolyte (aqueous solution of 0.012 M H_2PtCl_6, 0.28 M $SnCl_4$, and 0.50 M H_2SO_4) was purged with argon gas for 20 minutes to remove the oxygen in the solution. Pt-Sn was deposited on the cleaned Pt foil by scanning between –0.25 V and 0.55 V vs. Ag/AgCl at a scan rate of 50 mV/s for 100 cycles, with another Pt foil as the counter electrode. The scan was ended at –0.25 V to generate the catalyst in its reduced form. The active area of electrode covered with Pt-Sn is 0.5 cm^2. The density of electrodeposited Pt is 3.90 mg cm^{-2}.

4.2.3 Assembly of thermocell

The thermocell was assembled by simply connecting two flasks with hollow tubes (diameter = 0.7 cm, length = 18 cm) through which electrolytes flow between the hot and cold compartment (Figure S1). Total of 30 mL of aqueous solution of 10 vol% acetone, 10 vol% iso-propanol and 1.0 M Li_2SO_4 was used. The top of the two flasks were connected with a gas bridge which was also heated at the same temperature of the hot-side cell in order to prevent condensation of gaseous acetone in the gas bridge.

4.2.4 Electrochemical testing of thermocell

The electrolyte was vigorously stirred at 400 r.p.m. to homogenize the solution. The thermocell was heated after the open-circuit voltage (OCV) of the cell became stable. The hot-side temperature was increased stepwise and held at constant until the OCV stabilized at plateau values. Linear sweep voltammetry was carried at various temperatures, at a scan rate of 10 mV s^{-1} from OCV to 0 mV in order to evaluate the current-voltage profile of the thermocell (VSP300, Bio-Logic Science instruments). Chronoamperomety was carried out at loading voltages of 0, 50, 70, and 100 mV (Interface1000, Gamry Instruments).

4.2.5 SEM/EDX analysis

Particle size and chemical composition of Pt-Sn catalyst was evaluated with scanning electron microscope (SEM, FEI Quanta FEG 250) and energy dispersive x-ray (EDX). Pt-Sn electrode as prepared was soaked in deionized water overnight and washed thoroughly with water and acetone before the characterization.

4.3 Results and discussion

Oxidation of alcohols including iso-propanol on Sn-modified Pt catalyst has been well studied for the past two decades.[258–263] However, the reaction is usually conducted in strong acidic solutions. When acetone is heated with strong acid, the self-condensation readily occurs to produce phorone and acetone-derived polymers[257]. In addition, the reduction of acetone to iso-propanol on platinum catalysts has not been reported. Here, we electrodeposited a Pt-Sn catalyst on Pt substrate, which forms an aggregation of the nanoparticles with a diameter of 100 nm (Figure4-2a, inset). Energy dispersive x-ray analysis (EDX) reveals atomic ratio of Pt and Sn is 9:2 (Figure4-2a).

Cyclic voltammetry of a mixture of acetone and iso-propanol in a neutral pH solution (Figure4-2b) shows peaks of reduction of acetone and oxidation of iso-propanol at –0.35 V and –0.15 V at 21 °C, respectively. The peak height increases with the square root of the scan rate (Figure S4-4, Appendix), which indicates the reaction is limited by diffusion of the active species.[264] The oxidative current of iso-propanol increases with temperature, while the reductive peak current of acetone decreases (Figure4-2c). Oxidation of one iso-propanol molecule produces one acetone and two protons, which increases ΔS_{redox}. Thus, the reaction equilibrium shifts to the acetone side and oxidation of iso-propanol dominates at higher temperatures. These results indicate that a thermocell with iso-propanol oxidation on the hot side and acetone reduction on the cold side is expected to generate power.

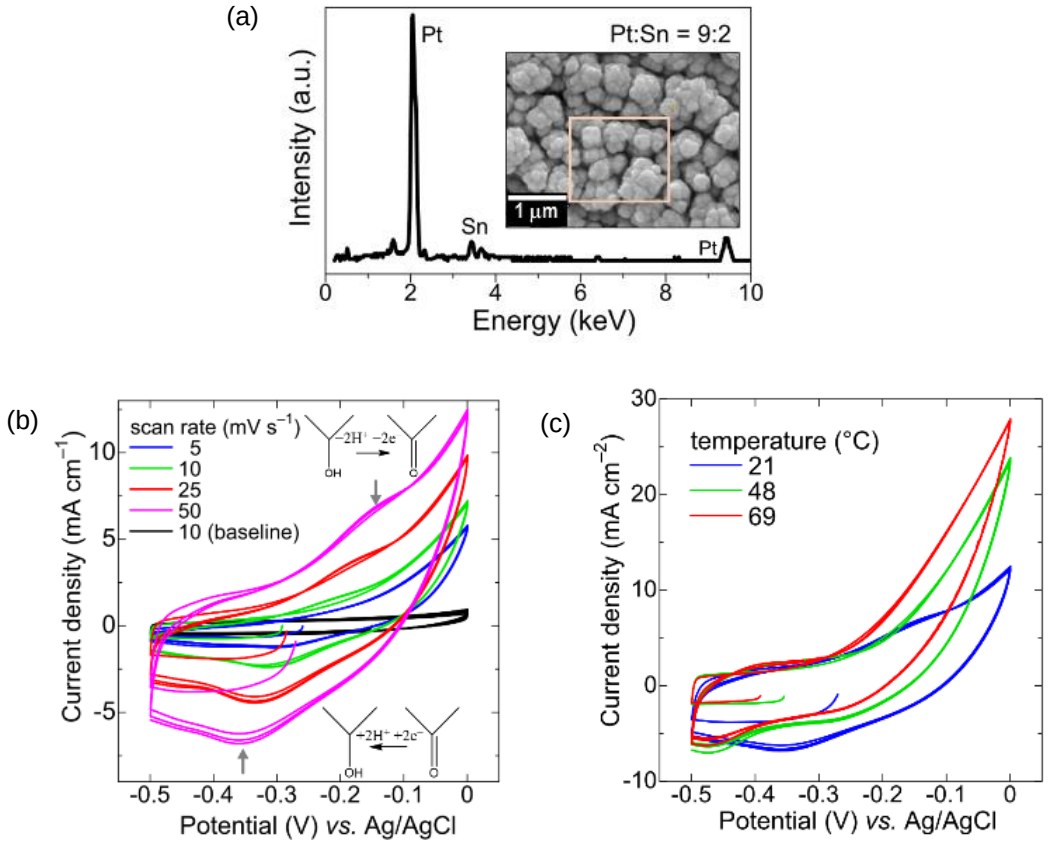

Figure 4-2 (a) Energy dispersive x-ray (EDX) analysis of Sn-modified Pt catalyst. The inset shows the scanning electron microscopy (SEM) image, and EDX was performed at the selected area. (b) Hydrogenation/dehydrogenation of acetone and iso-propaol on Pt-Sn elecctrode at 21 °C with various scan rates. The first three cycles of cyclic voltammetry of an aqueous solution of acetone and iso-propanol (10 vol% each) with 1 M Li_2SO_4 as the supporting electrolyte is shown. Baseline = aqueous solution of 1 M Li_2SO_4. (c) Cyclic voltammetry when the temperature was raised from 21, to 48, and 69 °C. Scan rate = 50 mV s^{-1}.

Open-circuit voltage (V_{oc}) increases linearly with increasing temperature differences between the hot and cold sides (Figure4-3a). The Seebeck coefficient is evaluated as a slope of the least-square fitting to the V_{oc}. The Seebeck coefficient is –3.4 mV K^{-1}, between ΔT = 0 to 40 K, however, the value increases to –9.9 mV K^{-1} as ΔT exceeds 40 K. We found out that the heating of the gas bridge which connects the hot-side and cold-side cells promotes the mass transfer of acetone vapor and is essential for the increase of the Seebeck coefficient (Figure S4-5, Appendix). Because acetone evaporates from the hot side, $c_{A1}/c_{A2} < 1$ in equation (4-2), and the Seebeck coefficient shift to negative values. The concentrations of iso-propanol in the hot side and cold side are approximated to be equal, because the vapor pressure of iso-propanol is much smaller than that of acetone (Figure S4-7a, Appendix).

ΔS_{redox} is evaluated as 656 J K^{-1} mol^{-1} from the Seebeck coefficient (–3.4 mV K^{-1}) at $\Delta T < 40$ K, where vaporization of acetone is negligible. Duan and coworkers[265] evaluated ΔS_{vap} of acetone in water as 230 J K^{-1} mol^{-1}. According to equation (4-2), ΔS_{vap} contributes to the increase of Seebeck coefficient by –1.2 mV K^{-1}, as indicated in Figure4-3b. We evaluated the partial pressure and the concentration of acetone in the hot-side cell from Henry's law[266] (Figure S4-7b c, Appendix). The partial pressure of acetone vapor increases significantly at $\Delta T >$ 40 K, and acetone vapor starts diffusing from the hot-side cell to the cold-side cell. The concentration gradient has greater contribution to the increase of the Seebeck coefficient compared to the vaporization entropy (Figure4-3b).

The Seebeck coefficient and working temperature of the thermocell evaluated in this study, and those results reported in the recent literatures are summarized in Figure4-3c. As mentioned above, Seebeck coefficients of most of redox couples are limited to around 2 mV K^{-1}. Although the Br_2/Br^- redox couple exhibits high Seebeck coefficient, the working temperature is confined in a narrow range, because the V_{oc} rapidly decays to zero below 50 °C.[246]

Acetone–iso-propanol thermocell exhibits high Seebeck coefficient (–3.4 mV K^{-1}) even below the boiling point of acetone (20-60 °C), which effectively increases the range of working temperature. Above 60 °C, the phase change of acetone from liquid to gas state increases the Seebeck coefficient by a factor of three, reaching the highest value ever reported. The working temperature of the organic thermocell can be tailored by selecting the redox species with different boiling points. For example, quinone-related compound, which has been used in organic redox flow batteries,[267,268] possibly increases the working temperature above 100 °C.

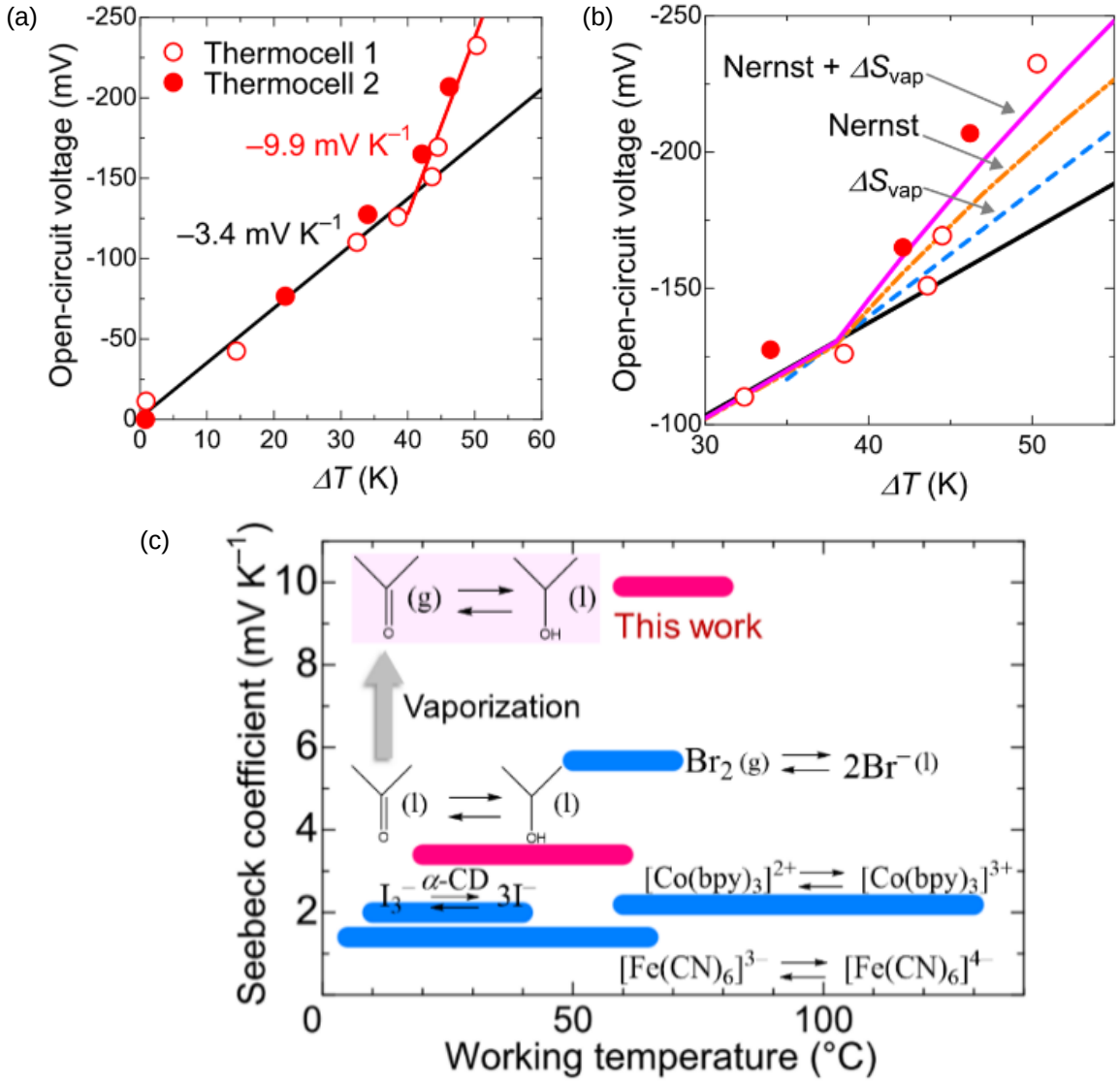

Figure 4-3 Open-circuit voltage of the hot-side electrode *vs.* the cold-side electrode in acetone–iso-propanol thermocell. Experimental data obtained from the two thermocells is plotted. The cold-side temperature is maintained at 20-23 °C. Seebeck coefficient is evaluated from the least-square fitting. (b) Simulation results of the additional voltage due to the vaporization entropy (ΔS_{vap} term) and the concentration gradient (Nernst term) calculated from equation (4-2). Sum of the two terms agrees with the experimental results in (a). (c) Comparison between the Seebeck coefficient (absolute value) and the working temperature of acetone–iso-propanol thermocell (red), and those of other redox systems (blue): $Fe(CN)_6^{3-/4-}$= ferri/ferrocyanide[256]; $Co(bpy)_3^{2+/3+}$= cobalt trisbipyridyl[240]; I_3^-/I^- + α-CD (α-cyclodextrin as a host molecule)[235]; Br_2/Br^-[246]. Vaporization of acetone realizes the highest Seebeck coefficient.

Linear-sweep voltammetry (LSV) shows output current increases with increasing temperature differences (Figure4-4a). The slopes of current-voltage lines are the same, indicating the resistance of the cell is unchanged with temperature. Cyclic voltammetry (CV) at ΔT = 50 K (Figure4-4b) shows a reversible current–voltage profile. It is to note that in LSV measurement, capacitive current (non-Faradaic current) can increase the total current, while CV measurement uses staircase-voltage step (current is measured after voltage change) to minimize the influence of capacitive current. The current–voltage profiles at a scan rate of 5 mV s^{-1} and 50 mV s^{-1} overlap, indicating the current is limited by Ohmic resistance of the cell, which is calculated as 11.5 kΩ. This high Ohmic resistance may be due to the long distance between the hot-side and cold-side electrodes (18 cm), which is designed to reduce the heat flux from the hot side and realizes the large ΔT in our setup. At a slower scan rate (1 mV s^{-1}), reaction kinetics of acetone/iso-propanol starts to limit the output current, and the current–voltage profile deviates from linearity. The output current can be improved by optimizing the cell dimension and decreasing the distance between the electrodes.[269]

The output current measured by chronoamperometry at discharge voltages of 0, 50, 100 mV (Figure4-4c) qualitatively agrees with the current–voltage profile (Figure4-4b). The output current at discharge voltage of 70 mV lasts for 60 hours without degradation, indicating Pt-Sn electrode is free from poisoning of acetone/iso-propanol, and the concentration gradient of acetone is maintained. Neutral pH solution is the key for the long-term stable operation, whereas a precipitation of self-polymerized acetone was observed in the sulfuric acid solution (Figure S4-9, Appendix).

The ionic conductivity of acetone–iso-propanol electrolyte was evaluated as 40 mS cm^{-1} at 47 °C (Figure S4-10, Appendix). Thermal efficiency of the thermocell discharged at 70 °C vs. 23 °C is calculated from equation

(4-1), (see Appendix 2-4 for the full derivations). The absolute efficiency is, η = 0.215%, which is 1.57% of the Carnot efficiency. This value is comparable to the previously reported efficiency of $Fe(CN)_6^{3-/4-}$ redox couple.[256]

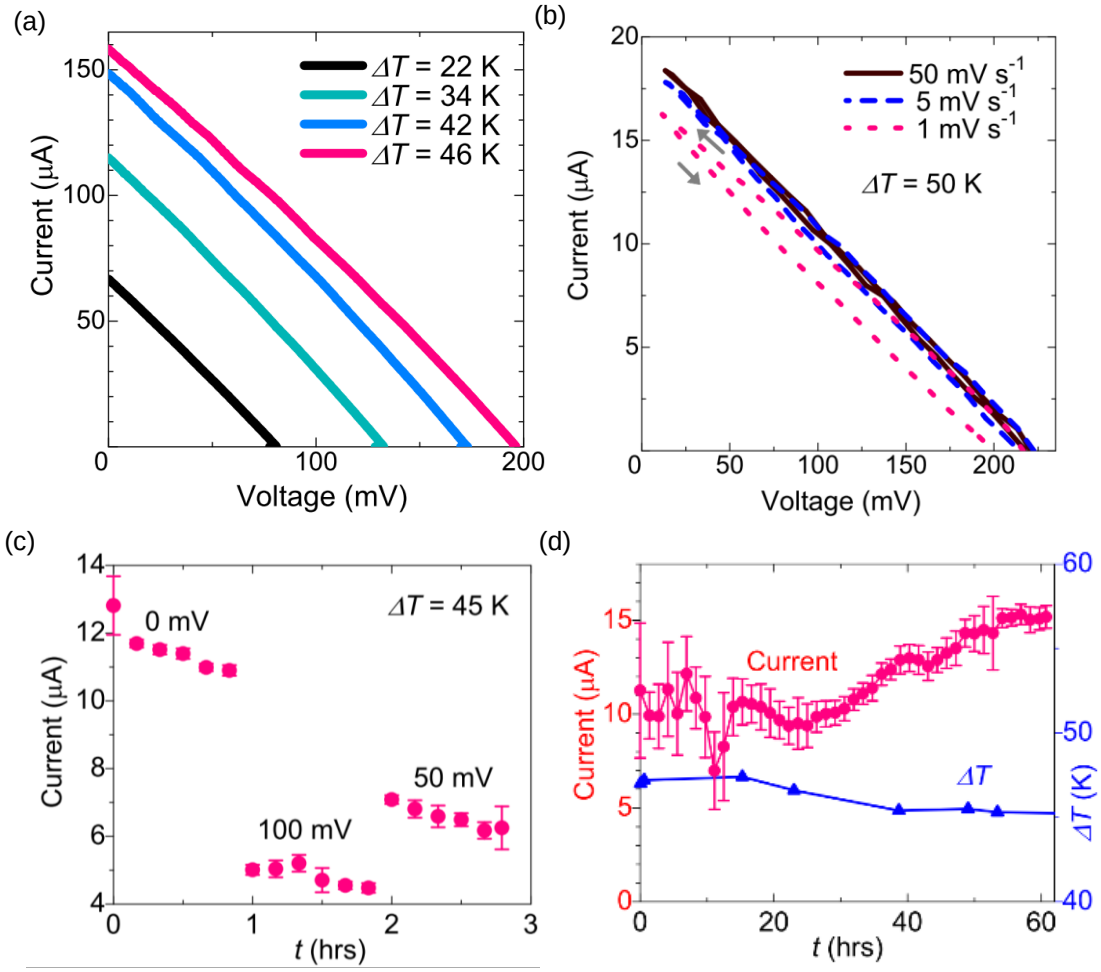

Figure 4-4 *I-V* plot and stability of acetone–iso-propanol thermocell. (a) Linear-sweep voltammetry of the thermocell at various temperature differences applied. Scan rate = 10 mV s^{-1}. Each line is scanned from the open-circuit voltage. (b) Cyclic voltammetry of the thermocell at the temperature difference of 50 K. Each cycle is scanned from the open-circuit voltage to 10 mV. (c) Chronoammperometry of the thermocell discharged at 0, 50, and 100 mV for 1 hrs, respectively, and (d) the thermocell discharged at 70 mV for 60 hrs. Current values between each dots were averaged for clarity, and error bars indicate the standard deviation. Active area of Pt-Sn electrode was 0.5 cm^2 (a-d).

4.4 Conclusions

In summary, the Seebeck coefficient of acetone–iso-propanol redox couple is reported, which increases from –3.4 mV K^{-1} to an unprecedented value of –9.9 mV K^{-1} above the boiling point of acetone. We circumvented the problematic poisoning of the catalyst, and self-condensation reaction of acetone by using a Sn-modified Pt catalyst, and a neutral pH solution, respectively. In addition, neutral pH solution is free from corrosions and enables the use of metal containers, which will facilitate the cell design.

4.5 Acknowledgement

Chapter 4, in full, is a reprint of materials published in the following paper: Hongyao Zhou and Ping Liu*, "High Seebeck Coefficient Electrochemical Thermocells for Efficient Waste Heat Recovery" *ACS Appl. Energy Mater.* **2018**, 1, 1424. The dissertation author was the primary researcher for the data presented and was the primary author of this publication. The permissions to reproduce this material were granted by American Chemical Society, copyright 2018.

4.6 Appendix

Figures

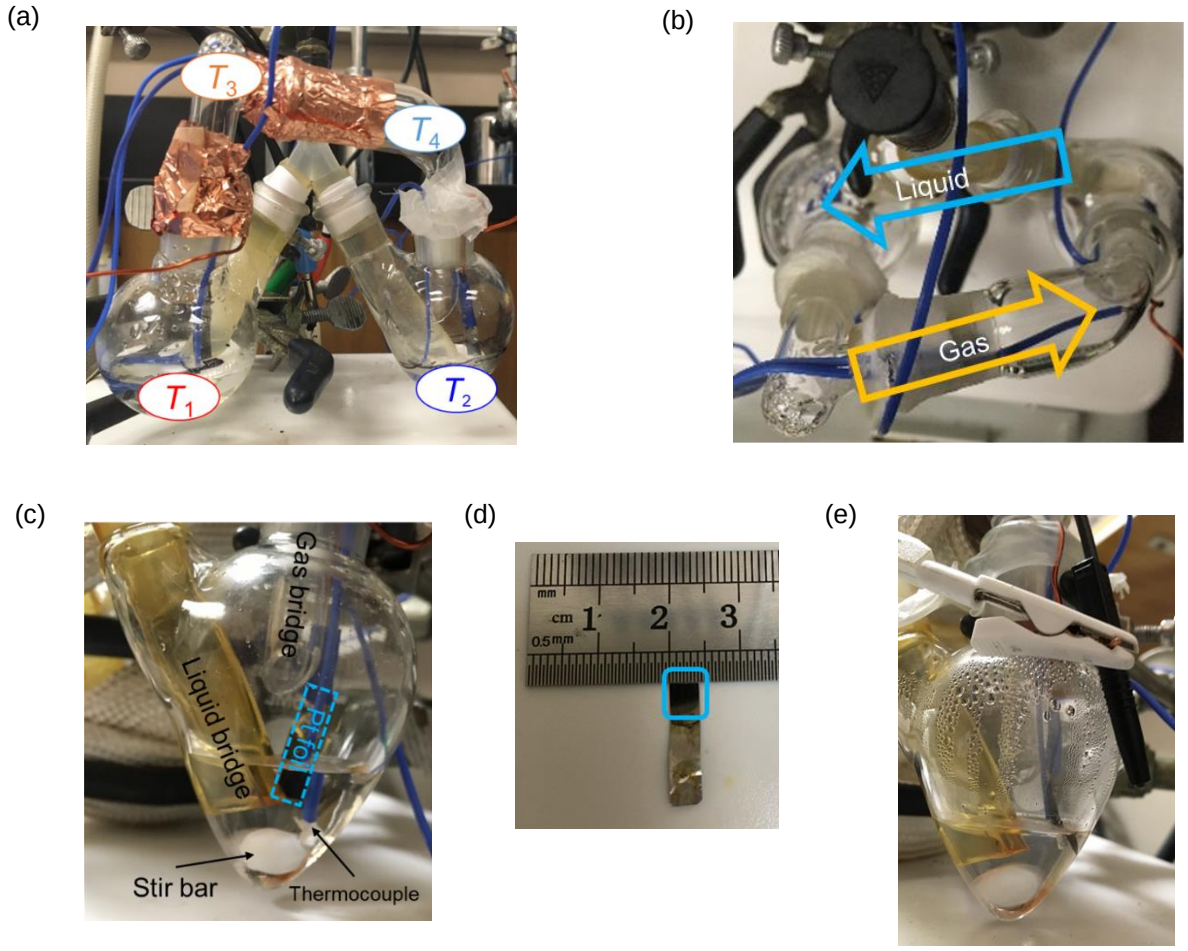

Figure S4-1 Setup of the acetone–iso-propanol thermocell (all photos taken by the author). (a) Two round flasks are connected with liquid bridge (back) and gas bridge (front). The hot-side flask and the gas bridge are rapped and heated with ribbon heater which is not shown in the picture. Liquid temperature of the hot side (T1), that of cold side (T2), and temperature inside the gas bridge (T3 is hot side; T4 is cold side) were measured with four thermocouples (see Figure S4-2). (b) Liquid bridge is filled with an electrolyte solution. Acetone evaporates from the hot side and condenses at the cold sides via gas bridge. (c) The whole cell is on the stirring plate, and a stir bar is placed on the bottom of the flask. The solution is stirred at 400 r.p.m. The tip of a Pt foil on which is covered with Pt-Sn catalyst is dipped in the solution. (d) The total area of Pt-Sn deposited on a Pt foil is 0.5 cm^2 (including both sides), as indicated in the picture. (e) Cold-side cell where acetone vapor condensed, and the liquid droplets were observed on the flask wall.

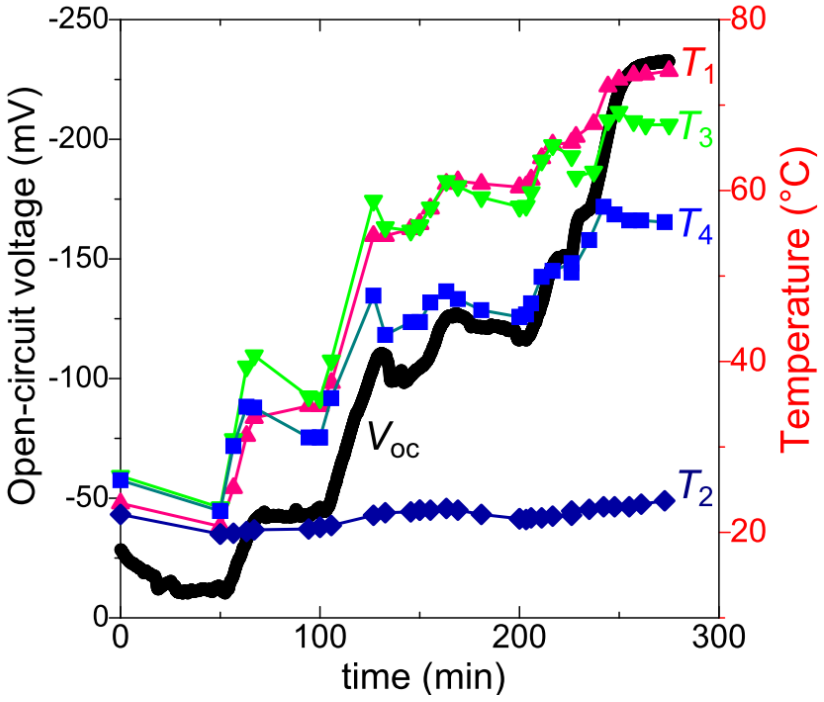

Figure S4-2 Open-circuit voltage and temperatures indexed in Figure S4-1a: T_1 hot-side liquid temperature; T_2 cold side liquid temperature; T_3 hot-side gas temperature; T_4 cold-side gas temperature. The data corresponds to Thermocell 1 in Figure 4-3a, main text. The open-circuit voltage increases with increasing T_1 (T_3) and stabilizes when temperatures are maintained at constant value.

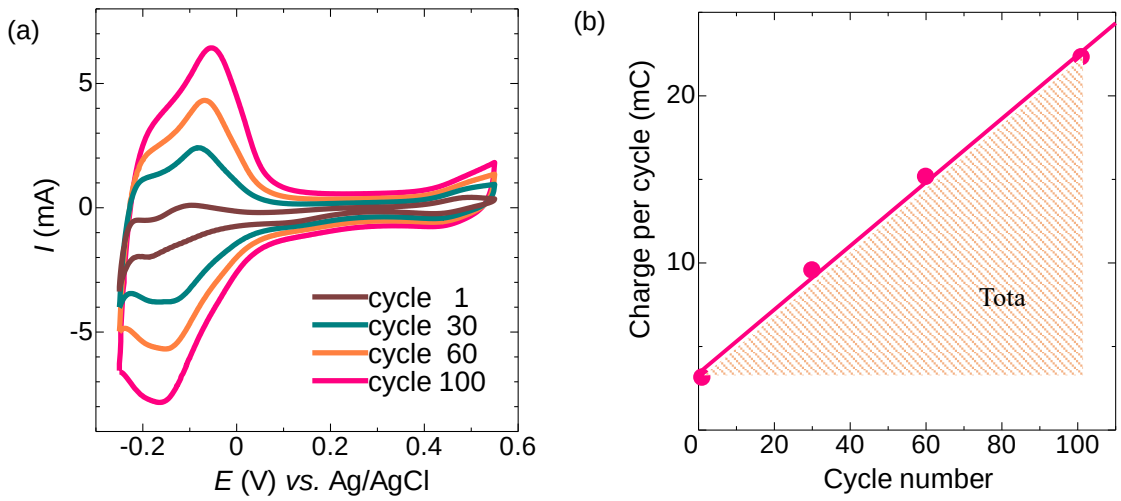

Figure S4-3 (a) Cyclic voltammetry of electrodeposition of PtSn on Pt foil. Broad reductive peak between –0.25 and 0 V corresponds to adsorption of hydrogen atom on Pt surface: $Pt + H^+ + e^- \rightarrow Pt\text{-}H$. (b) Charge passed between –0.25 and 0 V increases with increasing cycle numbers, because surface area of active Pt increases. Assuming a new layer of PtSn is deposited on the preceding layer at every cycle, the loading amount of Pt is calculated from the total charge, which is equal to the area of shaded triangle: 3.90 mg cm^{-2}

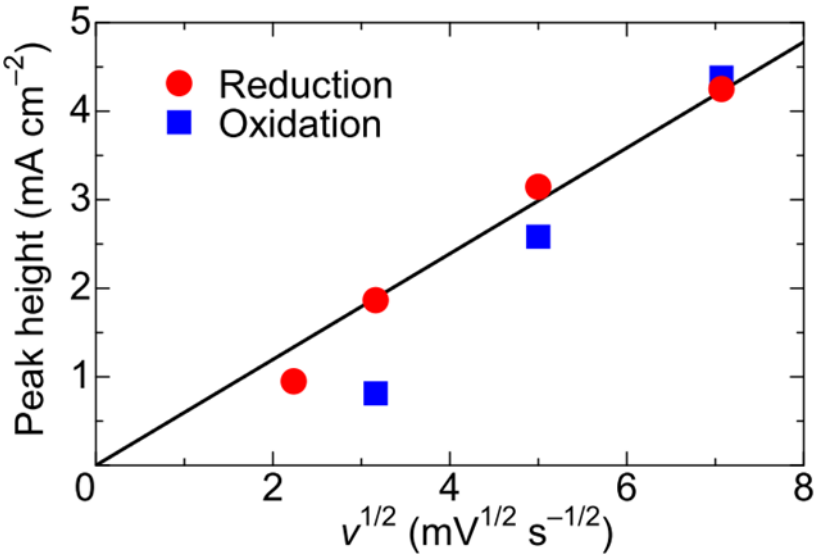

Figure S4-4 Peak height of the reductive/oxidative current density *vs.* the square root of the scan rate ($v^{1/2}$) evaluated from Figure 4-2b in the text. A fitting line is shown as a guide to the eye.

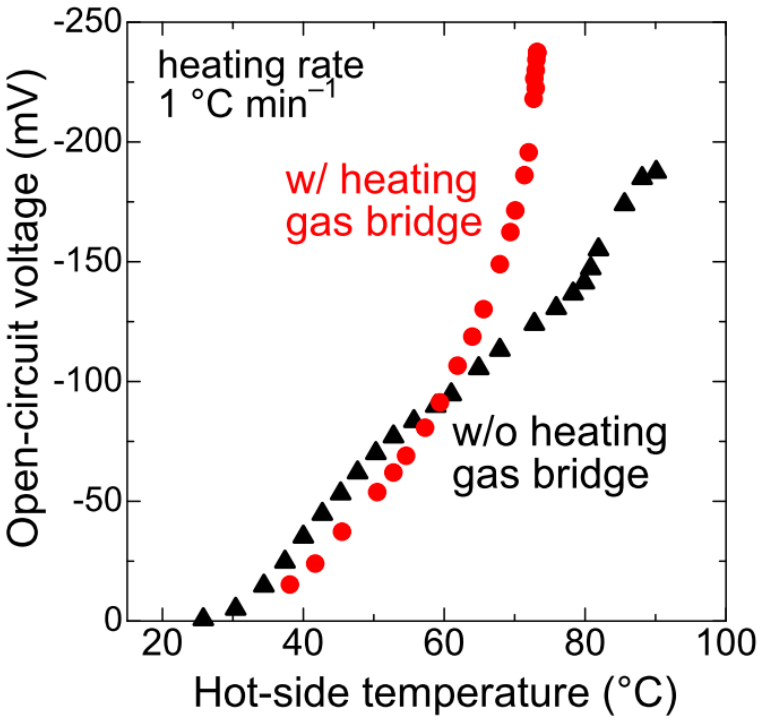

Figure S4-5 Open-circuit voltage (V_{oc}) between the hot-side electrode and the cold-side electrode in acetone–iso-propanol thermocell. The cold-side temperature was maintained at 20-23 °C. The heating of the gas bridge (Figure 4-1 and Figure S4-1) allows acetone vapor to transfer from the hot side to the cold side and increases the V_{oc}. Without heating the gas bridge, acetone vapor condenses at the neck of the hot-side cell and keeps refluxing inside. Average heating rate = 1 °C min^{-1}.

Calculation E: Calculation of vaporization rate through gas bridge

Two flasks, cell 1 and cell 2 are connected by a gas bridge and a liquid bridge. Temperature gradient is given between cell 1 and cell 2 by heating cell 1. Mole fractions of acetone vapor in the cells are

$$y_1 = \frac{p_{A1}}{p_0}$$

$$y_2 = \frac{p_{A2}}{p_0}$$

p_{A1} and p_{A2} is vapor pressure of acetone in cell 1 and cell 2. p_0 is total pressure in the cell, and p_0 = 1 atm.

Flux of acetone gas is caused by molecular diffusion and convection of gas:

$$J_{gas} = \frac{p_0 D_{gas}}{RT}\frac{dy}{dz} + yJ_{gas} \qquad \text{(S1.1)}$$

R is standard gas constant, D_{gas} is diffusion constant of acetone in gas phase, z is a distance from the surface of aqueous phase in cell 1 to that in cell 2.

Integrating equation (S1.1),

$$J_{gas} = \frac{p_0 D_{gas}}{RT(z_2 - z_1)} \ln\left(\frac{1-y_2}{1-y_1}\right) \qquad \text{(S1.2)}$$

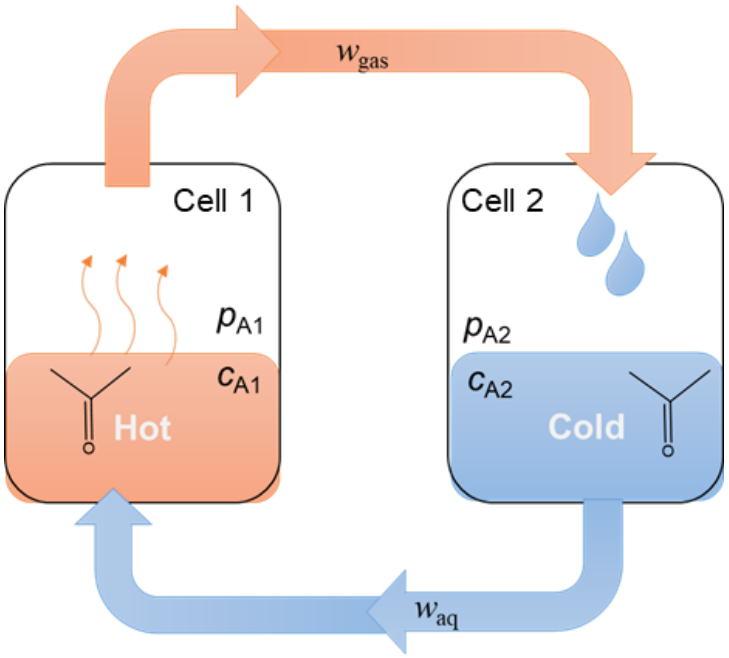

Figure S4-6 Model of acetone–iso-propanol thermocell which is used in the calculation of the concentration of acetone in the solution (c_{A1}, c_{A2}), vapor pressure of acetone (p_{A1}, p_{A2}), mass transfer rate of acetone vapor (w_{gas}), and that of aqueous acetone (w_{aq}).

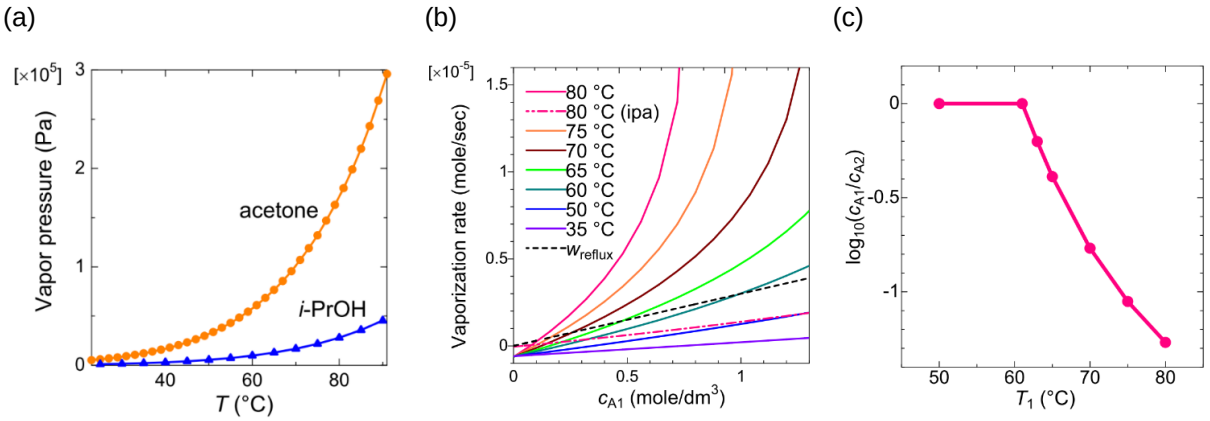

Figure S4-7 (a) Vapor pressures of acetone and iso-propanol calculated from Henry's law. The concentration of acetone and iso-propanol in aqueous phase is 1.36 and 1.32 mol L^{-1} (corresponding to10 vol% in water), respectively. (b) Vaporization rate of acetone as a function of the concentration of acetone in aqueous phase at various temperatures (T_1). ipa = iso-propanol. T_2 = 23 °C. (c) Concentration ratio, c_{A1}/c_{A2}, at the equilibrium condition, $w_{vap} = w_{reflux}$. A concentration gradient of acetone between the hot and cold cells is produced above 60 °C.

Vapor pressure and mole fraction of acetone can be evaluated from Henry's law constant of acetone dissolving into aqueous phase.[266]

$$H^{cp} = \frac{c_A}{p_A} \qquad \text{(S1.3)}$$

c_A is the concentration of the gas molecule in water phase, and p_A is the vapor pressure.

H^{cp} changes with temperature in Arrhenius form:

$$H(T)^{cp} = H_0^{cp} \exp\left(\frac{dlnH^{cp}}{dT^{-1}}\left(\frac{1}{T} - \frac{1}{T_0}\right)\right) \qquad \text{(S1.4)}$$

H_0^{cp} is the Henry's law constant at the standard temperature T_0 = 298 K. The differential form in the exponential is derived from Van't Hoff equation

$$\frac{d\ln H^{cp}}{dT^{-1}} = -\frac{\Delta H}{R}$$

ΔH is a solvation enthalpy of the gas molecule dissolving into aqueous phase.

Mole fraction of acetone vapor is derived from equation (S1.3).

$$y_1 = \frac{c_{A1}}{p_0 H(T_1)^{cp}} \qquad \text{(S1.5)}$$

$$y_2 = \frac{c_{A2}}{p_0 H(T_2)^{cp}} \qquad \text{(S1.6)}$$

Assume all acetone gas vaporizing from the hot side condenses at the cold side, mass balance of acetone is

$$c_{\mathrm{A1}} + c_{\mathrm{A2}} = 2c_0 \quad \text{(S1.7)}$$

c_0 is the initial concentration of acetone.

Vaporization rate of acetone (mass transfer rate from hot side to cold side) is

$$w_{\mathrm{vap}} = J_{\mathrm{gas}} A \quad \text{(S1.8)}$$

A is the interface area between gas and aqueous phase in the cell.

Ideally, the concentration of acetone in the hot side (c_1) decreases to a value where the vaporization rate reaches to zero (mass transfer through liquid bridge is negligibly small compared to that of gas; $w_{\mathrm{liq}} \approx 10^{-4}\, w_{\mathrm{gas}}$, see below). However, in reality, certain amount of acetone gas refluxes back to the hot side, especially when the temperature and the vaporization rate is low. Here we introduce a reflux rate of acetone (w_{reflux}) as an empirical parameter to fit the result.

w_{reflux} must be proportional to c_{A1}, because as $c_{\mathrm{A1}} \to 0$, $w_{\mathrm{reflux}} \to 0$. As a result of fitting, w_{reflux} is evaluated

$$w_{\mathrm{reflux}} = 3 \times 10^{-4} c_{\mathrm{A1}} V \quad \text{(S1.9)}$$

V is the volume of the aqueous phase (V = 0.01 dm^3). w_{reflux} is shown as a dashed line in the Figure S4-5. Vaporization rate (w_{vap}) starts to exceed the reflux rate at 60 °C, and acetone is transported from the hot side to the cold side, causing the concentration gradient. The equilibrium condition where the net transport of acetone gas becomes zero is

$$w_{\mathrm{vap}} = w_{\mathrm{reflux}} \quad \text{(S1.10)}$$

Calculation F: Calculation of diffusion rate through liquid bridge

Flux of acetone through liquid bridge is caused by molecular diffusion and Soret diffusion, which is due to thermal gradient[270]

$$J_{\mathrm{aq}} = -\rho\left(D^M \frac{dx}{dz} + D^T x_0(1-x_0)\frac{dT}{dz}\right) \quad \text{(S2.1)}$$

ρ is density of aqueous phase,[271] D^M is molecular diffusion constant of acetone in aqueous phase,[272] D^T is thermal diffusion constant,[273] x is mole fraction of acetone in aqueous phase, x_0 is the initial mole fraction.

Integration of equation (S2.1) gives

$$J_{\mathrm{aq}} = -\rho\left(D^M \frac{x_2 - x_1}{z_2 - z_1} + D^T x_0(1-x_0)\frac{T_2 - T_1}{z_2 - z_1}\right) \quad \text{(S2.2)}$$

Diffusion rate of acetone in aqueous phase is

$$w_{\mathrm{aq}} = J_{\mathrm{aq}} A_{\mathrm{liq}} \quad \text{(S2.3)}$$

A_{liq} is a cross-sectional area of liquid bridge.

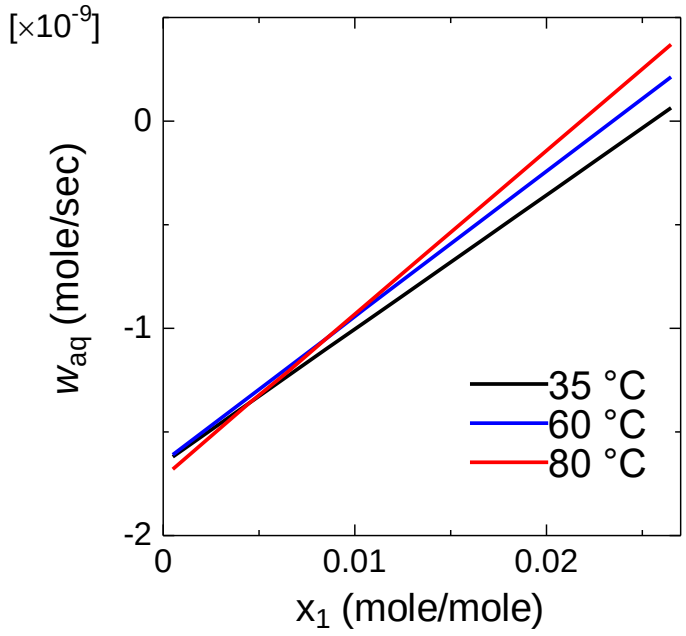

Figure S4-8 Diffusion rate of acetone through liquid bridge at different mole fraction of acetone. Hot-side temperature (T_1) is indicated in the graph. Cold-side temperature, T_2 = 23 °C. x_0 = 0.0265 (corresponding to 10 vol% in aqueous solution). At $x = x_0$, w_{aq} is positive (diffusion toward cold side) due to Soret diffusion. As mole fraction of acetone (x_1) decreases, the concentration gradient increases, and molecular diffusion becomes dominant ($w_{\mathrm{aq}} < 0$, diffusion towards hot side).

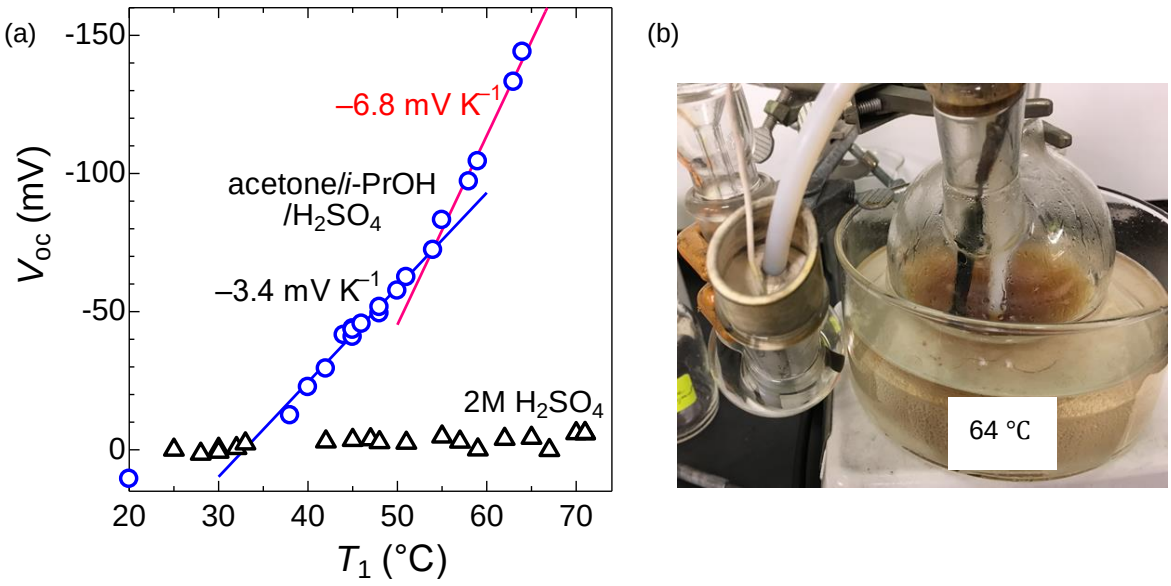

Figure S4-9 (a) Hot-side temperature and open-circuit voltage of acetone–iso-propanol thermocell in acidic solution (acetone = 30vol%; iso-propanol = 30 vol%; sulfuric acid = 2 M). PtSn catalyst is electrodeposited on glassy carbon electrodes. No voltage is generated in pure sulfuric acid solution (black triangle), which proves the Seebeck coefficient is caused by redox reaction between acetone and iso-propanol. (b) Photograph of the thermocell in 2 M sulfuric acid after two days of heating (ca. 64 °C). The solution in the hot cell turned brown due to self-condensation reaction of acetone.

Calculation G: Calculation of thermal efficiency of the thermocell

In this section, we calculate the thermal efficiency of the thermocell discharged at 70 °C vs. 23 °C.

The thermal efficiency of thermocell is expressed as

$$\eta = \frac{W_{\text{out}}}{Q_{\text{diff}}} \qquad \text{(S3.1)}$$

W_{out} is the output power of thermocell, Q_{diff} is heat transfer due to thermal diffusion.

Q_{diff} is calculated from Fourie's law,

$$Q_{\text{diff}} = \kappa A \frac{\Delta T}{\Delta x} \qquad \text{(S3.2)}$$

κ is thermal conductivity of an aqueous solution of 10 vol% acetone and 10 vol% iso-propanol ($\kappa = 5.0 \times 10^{-3}$ W cm^{-1} K^{-1}) reported by Wang et al.,[274] A is a cross-sectional area of the liquid bridge, and Δx is a length of the liquid bridge.

Output voltage is chosen as a half of the open-circuit voltage ($V_{\text{out}} = 1/2V_{\text{oc}}$), where W_{out} is maximum. V_{oc} = 3.4 mV K^{-1}× 37 K + 9.9 mV K^{-1}× 10 K = 225 mV.

$$W_{\text{out}} = \frac{V_{\text{out}}^2}{R} = \frac{\sigma A {V_{\text{oc}}}^2}{4\Delta x} \qquad \text{(S3.3)}$$

σ is the ionic conductivity of the electrolyte and $\sigma = 4.0 \times 10^{-2}$ S cm^{-1} at the average temperature, T = 47 °C (Figure S4-7).

Therefore,

$$\eta = \frac{\sigma {V_{\text{oc}}}^2}{4\kappa\Delta T} = \frac{4.0 \times 10^{-2}\text{S cm}^{-1} \times (0.225\text{ V})^2}{4 \times 5.0 \times 10^{-3}\text{ W cm}^{-1}\text{ K}^{-1} \times 47\text{ K}} = 2.15 \times 10^{-3}$$

Note that Δx and A cancels out in the calculation above, and the efficiency is solely evaluated from V_{oc}, ΔT, ionic and thermal conductivity of the solution.

Meanwhile, Carnot efficiency is

$$\eta_{\text{Carnot}} = 1 - \frac{296\text{ K}}{343\text{ K}} = 0.137$$

Thus, the relative efficiency is

$$\eta' = \frac{\eta}{\eta_{\text{Carnot}}} \times 100 = 1.57\%$$

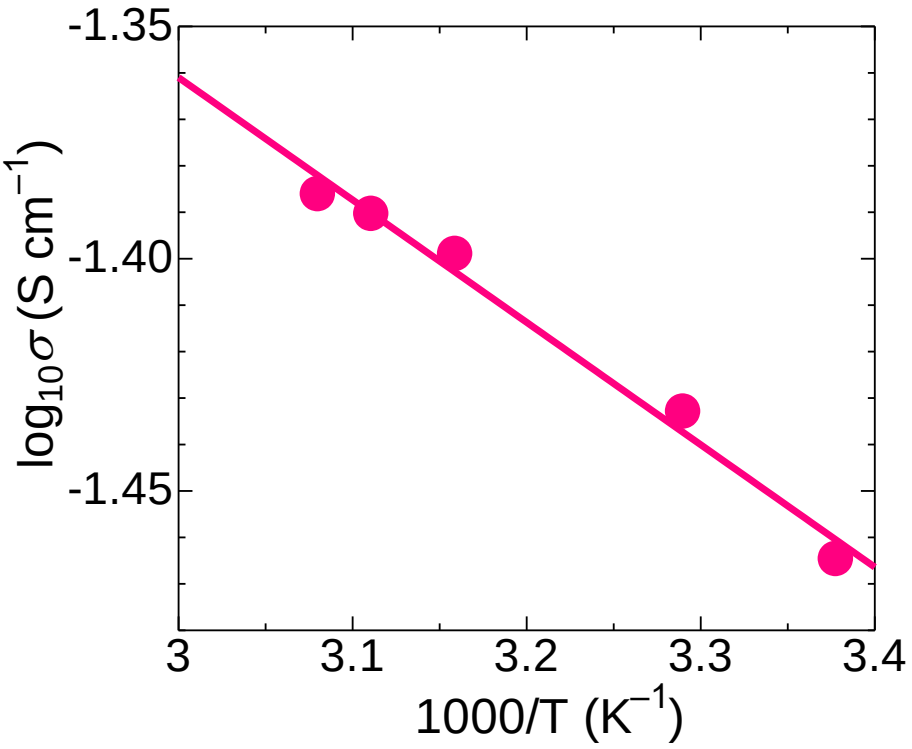

Figure S4-10 Arrhenius plot of the ionic conductivity of the aqueous electrolyte (acetone 10vol%; iso-propanol 10vol%; Li_2SO_4 1 M). Oakton PC 700 conductivity meter was used.

REFERENCES

[1] J. Liu, Z. Bao, Y. Cui, E.J. Dufek, J.B. Goodenough, P. Khalifah, Q. Li, B.Y. Liaw, P. Liu, A. Manthiram, Y.S. Meng, V.R. Subramanian, M.F. Toney, V. V Viswanathan, M.S. Whittingham, J. Xiao, W. Xu, J. Yang, X.-Q. Yang, J.-G. Zhang, Pathways for practical high-energy long-cycling lithium metal batteries, Nat. Energy. 4 (2019) 180–186. doi:10.1038/s41560-019-0338-x.

[2] X. Cheng, R. Zhang, C. Zhao, Q. Zhang, Toward Safe Lithium Metal Anode in Rechargeable Batteries : A Review, Chem. Rev. 117 (2017) 10403–10473. doi:10.1021/acs.chemrev.7b00115.

[3] C. Niu, H. Lee, S. Chen, Q. Li, J. Du, W. Xu, J.G. Zhang, M.S. Whittingham, J. Xiao, J. Liu, High-energy lithium metal pouch cells with limited anode swelling and long stable cycles, Nat. Energy. 4 (2019) 551–559. doi:10.1038/s41560-019-0390-6.

[4] S.S. Zhang, Problem, Status, and Possible Solutions for Lithium Metal Anode of Rechargeable Batteries, ACS Appl. Energy Mater. 1 (2018) 910–920. doi:10.1021/acsaem.8b00055.

[5] C. Fang, J. Li, M. Zhang, Y. Zhang, F. Yang, J.Z. Lee, M.-H. Lee, J. Alvarado, M.A. Schroeder, Y. Yang, B. Lu, N. Williams, M. Ceja, L. Yang, M. Cai, J. Gu, K. Xu, X. Wang, Y.S. Meng, Quantifying inactive lithium in lithium metal batteries, Nature. 572 (2019) 511–515. doi:10.1038/s41586-019-1481-z.

[6] Z. Zeng, V. Murugesan, K.S. Han, X. Jiang, Y. Cao, L. Xiao, X. Ai, H. Yang, J.G. Zhang, M.L. Sushko, J. Liu, Non-flammable electrolytes with high salt-to-solvent ratios for Li-ion and Li-metal batteries, Nat. Energy. 3 (2018) 674–681. doi:10.1038/s41560-018-0196-y.

[7] J. Alvarado, M.A. Schroeder, T.P. Pollard, X. Wang, J.Z. Lee, M. Zhang, T. Wynn, M. Ding, O. Borodin, Y.S. Meng, K. Xu, Bisalt ether electrolytes: A pathway towards lithium metal batteries with Ni-rich cathodes, Energy Environ. Sci. 12 (2019) 780–794. doi:10.1039/c8ee02601g.

[8] L. Yu, S. Chen, H. Lee, L. Zhang, M.H. Engelhard, Q. Li, S. Jiao, J. Liu, W. Xu, J.G. Zhang, A Localized High-Concentration Electrolyte with Optimized Solvents and Lithium Difluoro(oxalate)borate Additive for Stable Lithium Metal Batteries, ACS Energy Lett. 3 (2018) 2059–2067. doi:10.1021/acsenergylett.8b00935.

[9] W. Li, H. Yao, K. Yan, G. Zheng, Z. Liang, Y.M. Chiang, Y. Cui, The synergetic effect of lithium polysulfide and lithium nitrate to prevent lithium dendrite growth, Nat. Commun. 6 (2015) 7436. doi:10.1038/ncomms8436.

[10] G. Li, Q. Huang, X. He, Y. Gao, D. Wang, S.H. Kim, D. Wang, Self-Formed Hybrid Interphase Layer on Lithium Metal for High-Performance Lithium-Sulfur Batteries, ACS Nano. 12 (2018) 1500–1507. doi:10.1021/acsnano.7b08035.

[11] P.J. Kim, V.G. Pol, High Performance Lithium Metal Batteries Enabled by Surface Tailoring of Polypropylene Separator with a Polydopamine/Graphene Layer, Adv. Energy Mater. 8 (2018) 1802665. doi:10.1002/aenm.201802665.

[12] Y. Liu, Q. Liu, L. Xin, Y. Liu, F. Yang, E.A. Stach, J. Xie, Making Li-metal electrodes rechargeable by controlling the dendrite growth direction, Nat. Energy. 2 (2017) 17083. doi:10.1038/nenergy.2017.83.

[13] H. Liu, X. Yue, X. Xing, Q. Yan, J. Huang, V. Petrova, H. Zhou, P. Liu, A scalable 3D lithium metal anode, Energy Storage Mater. 16 (2019) 505–511. doi:10.1016/j.ensm.2018.09.021.

[14] J. Xie, J. Wang, H.R. Lee, K. Yan, Y. Li, F. Shi, W. Huang, A. Pei, G. Chen, R. Subbaraman, J. Christensen, Y. Cui, Engineering stable interfaces for three-dimensional lithium metal anodes, Sci. Adv. 4 (2018)

eaat5168. doi:10.1126/sciadv.aat5168.

[15] K.H. Chen, A.J. Sanchez, E. Kazyak, A.L. Davis, N.P. Dasgupta, Synergistic Effect of 3D Current Collectors and ALD Surface Modification for High Coulombic Efficiency Lithium Metal Anodes, Adv. Energy Mater. 9 (2019) 1802534. doi:10.1002/aenm.201802534.

[16] C. Niu, H. Pan, W. Xu, J. Xiao, J.G. Zhang, L. Luo, C. Wang, D. Mei, J. Meng, X. Wang, Z. Liu, L. Mai, J. Liu, Self-smoothing anode for achieving high-energy lithium metal batteries under realistic conditions, Nat. Nanotechnol. 14 (2019) 594–601. doi:10.1038/s41565-019-0427-9.

[17] R. Weber, M. Genovese, A.J. Louli, S. Hames, C. Martin, I.G. Hill, J.R. Dahn, Long cycle life and dendrite-free lithium morphology in anode-free lithium pouch cells enabled by a dual-salt liquid electrolyte, Nat. Energy. 4 (2019) 683–689. doi:10.1038/s41560-019-0428-9.

[18] M. Genovese, A.J. Louli, R. Weber, S. Hames, J.R. Dahn, Measuring the Coulombic efficiency of lithium metal cycling in anode-free lithium metal batteries, J. Electrochem. Soc. 165 (2018) A3321–A3325. doi:10.1149/2.0641814jes.

[19] Q. Cheng, L. Wei, Z. Liu, N. Ni, Z. Sang, B. Zhu, W. Xu, M. Chen, Y. Miao, L.Q. Chen, W. Min, Y. Yang, Operando and three-dimensional visualization of anion depletion and lithium growth by stimulated Raman scattering microscopy, Nat. Commun. 9 (2018) 2942. doi:10.1038/s41467-018-05289-z.

[20] M.D. Tikekar, S. Choudhury, Z. Tu, L.A. Archer, Design principles for electrolytes and interfaces for stable lithium-metal batteries, Nat. Energy. 1 (2016) 16114. doi:10.1038/nenergy.2016.114.

[21] Z. Tu, S. Choudhury, M.J. Zachman, S. Wei, K. Zhang, L.F. Kourkoutis, L.A. Archer, Designing Artificial Solid-Electrolyte Interphases for Single-Ion and High-Efficiency Transport in Batteries, Joule. 1 (2017) 394–406. doi:10.1016/j.joule.2017.06.002.

[22] Y. Gao, Z. Yan, J.L. Gray, X. He, D. Wang, T. Chen, Q. Huang, Y.C. Li, H. Wang, S.H. Kim, T.E. Mallouk, D. Wang, Polymer–inorganic solid–electrolyte interphase for stable lithium metal batteries under lean electrolyte conditions, Nat. Mater. 18 (2019) 384–389. doi:10.1038/s41563-019-0305-8.

[23] D. Lin, Y. Liu, Y. Cui, Reviving the lithium metal anode for high-energy batteries, Nat. Nanotechnol. 12 (2017) 194–206. doi:10.1038/nnano.2017.16.

[24] X.Q. Zhang, X.B. Cheng, Q. Zhang, Advances in Interfaces between Li Metal Anode and Electrolyte, Adv. Mater. Interfaces. 5 (2018) 1701097. doi:10.1002/admi.201701097.

[25] R. Xu, X.-B. Cheng, C. Yan, X.-Q. Zhang, Y. Xiao, C.-Z. Zhao, J.-Q. Huang, Q. Zhang, Artificial Interphases for Highly Stable Lithium Metal Anode, Matter. 1 (2019) 317–344. doi:10.1016/j.matt.2019.05.016.

[26] C. Monroe, J. Newman, The Effect of Interfacial Deformation on Electrodeposition Kinetics, J. Electrochem. Soc. 151 (2004) A880. doi:10.1149/1.1710893.

[27] C. Monroe, J. Newman, The Impact of Elastic Deformation on Deposition Kinetics at Lithium/Polymer Interfaces, J. Electrochem. Soc. 152 (2005) A396. doi:10.1149/1.1850854.

[28] S. Yu, R.D. Schmidt, R. Garcia-Mendez, E. Herbert, N.J. Dudney, J.B. Wolfenstine, J. Sakamoto, D.J. Siegel, Elastic Properties of the Solid Electrolyte Li7La3Zr2O12 (LLZO), Chem. Mater. 28 (2016) 197–206. doi:10.1021/acs.chemmater.5b03854.

[29] H.Z. Geng, R. Rosen, B. Zheng, H. Shimoda, L. Fleming, J. Liu, O. Zhou, Fabrication and properties of

composites of poly(ethylene oxide) and functionalized carbon nanotubes, Adv. Mater. 14 (2002) 1387–1390. doi:10.1002/1521-4095(20021002)14:19<1387::AID-ADMA1387>3.0.CO;2-Q.

[30] P. Barai, K. Higa, V. Srinivasan, Lithium dendrite growth mechanisms in polymer electrolytes and prevention strategies, Phys. Chem. Chem. Phys. 19 (2017) 20493–20505. doi:10.1039/c7cp03304d.

[31] S. Wei, Z. Cheng, P. Nath, M.D. Tikekar, G. Li, L.A. Archer, Stabilizing electrochemical interfaces in viscoelastic liquid electrolytes, Sci. Adv. 4 (2018) eaao6243. doi:10.1126/sciadv.aao6243.

[32] M.D. Tikekar, G. Li, L.A. Archer, D.L. Koch, Electroconvection and Morphological Instabilities in Potentiostatic Electrodeposition across Liquid Electrolytes with Polymer Additives, J. Electrochem. Soc. 165 (2018) A3697–A3713. doi:10.1149/2.0271816jes.

[33] Q. Zhao, X. Liu, S. Stalin, K. Khan, L.A. Archer, Solid-state polymer electrolytes with in-built fast interfacial transport for secondary lithium batteries, Nat. Energy. 4 (2019) 365–373. doi:10.1038/s41560-019-0349-7.

[34] H. Zhou, H. Liu, Y. Li, X. Yue, X. Wang, M. Gonzalez, Y.S. Meng, P. Liu, In situ formed polymer gel electrolytes for lithium batteries with inherent thermal shutdown safety features , J. Mater. Chem. A. 7 (2019) 16984–16991. doi:10.1039/c9ta02341k.

[35] R.J. Blint, Binding of Ether and Carbonyl Oxygens to Lithium Ion, J. Electrochem. Soc. 142 (1995) 696–702. doi:10.1149/1.2048519.

[36] C.M. Tenney, R.T. Cygan, Analysis of molecular clusters in simulations of lithium-ion battery electrolytes, J. Phys. Chem. C. 117 (2013) 24673–24684. doi:10.1021/jp4039122.

[37] G. Yang, I.N. Ivanov, R.E. Ruther, R.L. Sacci, V. Subjokova, D.T. Hallinan, J. Nanda, Electrolyte Solvation Structure at Solid/Liquid Interface Probed by Nanogap Surface-Enhanced Raman Spectroscopy, ACS Nano. 12 (2018) 10159–10170. doi:10.1021/acsnano.8b05038.

[38] Y. Yamada, F. Sagane, Y. Iriyama, T. Abe, Z. Ogumi, Kinetics of lithium-ion transfer at the interface between Li 0.35La0.55TiO3 and binary electrolytes, J. Phys. Chem. C. 113 (2009) 14528–14532. doi:10.1021/jp9043539.

[39] M.R. Busche, T. Drossel, T. Leichtweiss, D.A. Weber, M. Falk, M. Schneider, M.L. Reich, H. Sommer, P. Adelhelm, J. Janek, Dynamic formation of a solid-liquid electrolyte interphase and its consequences for hybrid-battery concepts, Nat. Chem. 8 (2016) 426–434. doi:10.1038/nchem.2470.

[40] J.N. Lee, C. Park, G.M. Whitesides, Solvent Compatibility of Poly(dimethylsiloxane)-Based Microfluidic Devices, Anal. Chem. 75 (2003) 6544–6554. doi:10.1021/ac0346712.

[41] S.M. George, Atomic layer deposition: An overview, Chem. Rev. 110 (2010) 111–131. doi:10.1021/cr900056b.

[42] L. Chen, K.S. Chen, X. Chen, G. Ramirez, Z. Huang, N.R. Geise, H.G. Steinrück, B.L. Fisher, R. Shahbazian-Yassar, M.F. Toney, M.C. Hersam, J.W. Elam, Novel ALD Chemistry Enabled Low-Temperature Synthesis of Lithium Fluoride Coatings for Durable Lithium Anodes, ACS Appl. Mater. Interfaces. 10 (2018) 26972–26981. doi:10.1021/acsami.8b04573.

[43] C. Ban, S.M. George, Molecular Layer Deposition for Surface Modification of Lithium-Ion Battery Electrodes, Adv. Mater. Interfaces. 3 (2016) 1600762. doi:10.1002/admi.201600762.

[44] L. Chen, Z. Huang, R. Shahbazian-Yassar, J.A. Libera, K.C. Klavetter, K.R. Zavadil, J.W. Elam, Directly

Formed Alucone on Lithium Metal for High-Performance Li Batteries and Li-S Batteries with High Sulfur Mass Loading, ACS Appl. Mater. Interfaces. 10 (2018) 7043–7051. doi:10.1021/acsami.7b15879.

[45] Y. Sun, Y. Zhao, J. Wang, J. Liang, C. Wang, Q. Sun, X. Lin, K.R. Adair, J. Luo, D. Wang, R. Li, M. Cai, T.-K. Sham, X. Sun, A Novel Organic “Polyurea” Thin Film for Ultralong-Life Lithium-Metal Anodes via Molecular-Layer Deposition, Adv. Mater. (2018) 1806541. doi:10.1002/adma.201806541.

[46] L. Wang, Q. Wang, W. Jia, S. Chen, P. Gao, J. Li, Li metal coated with amorphous Li3PO4via magnetron sputtering for stable and long-cycle life lithium metal batteries, J. Power Sources. 342 (2017) 175–182. doi:10.1016/j.jpowsour.2016.11.097.

[47] L. Wang, L. Zhang, Q. Wang, W. Li, B. Wu, W. Jia, Y. Wang, J. Li, H. Li, Long lifespan lithium metal anodes enabled by Al2O3 sputter coating, Energy Storage Mater. 10 (2018) 16–23. doi:10.1016/j.ensm.2017.08.001.

[48] E. Cha, M.D. Patel, J. Park, J. Hwang, V. Prasad, K. Cho, W. Choi, 2D MoS2as an efficient protective layer for lithium metal anodes in high-performance Li-S batteries, Nat. Nanotechnol. 13 (2018) 337–343. doi:10.1038/s41565-018-0061-y.

[49] X. Wang, M. Zhang, J. Alvarado, S. Wang, M. Sina, B. Lu, J. Bouwer, W. Xu, J. Xiao, J.G. Zhang, J. Liu, Y.S. Meng, New Insights on the Structure of Electrochemically Deposited Lithium Metal and Its Solid Electrolyte Interphases via Cryogenic TEM, Nano Lett. 17 (2017) 7606–7612. doi:10.1021/acs.nanolett.7b03606.

[50] D.B. Hall, P. Underhill, J.M. Torkelson, Spin coating of thin and ultrathin polymer films, Polym. Eng. Sci. 38 (1998) 2039–2045. doi:10.1002/pen.10373.

[51] N.F. Himma, A.K. Wardani, I.G. Wenten, Preparation of Superhydrophobic Polypropylene Membrane Using Dip-Coating Method: The Effects of Solution and Process Parameters, Polym. - Plast. Technol. Eng. 56 (2017) 184–194. doi:10.1080/03602559.2016.1185666.

[52] U. Siemann, Solvent cast technology -- a versatile tool for thin film production, in: N. Stribeck, B. Smarsly (Eds.), Scatt. Methods Prop. Polym. Mater., Springer Berlin Heidelberg, Berlin, Heidelberg, 2005: pp. 1–14. doi:10.1007/b107336.

[53] Y. Gao, Y. Zhao, Y.C. Li, Q. Huang, T.E. Mallouk, D. Wang, Interfacial Chemistry Regulation via a Skin-Grafting Strategy Enables High-Performance Lithium-Metal Batteries, J. Am. Chem. Soc. 139 (2017) 15288–15291. doi:10.1021/jacs.7b06437.

[54] K. Liu, A. Pei, H.R. Lee, B. Kong, N. Liu, D. Lin, Y. Liu, C. Liu, P. chun Hsu, Z. Bao, Y. Cui, Lithium Metal Anodes with an Adaptive “Solid-Liquid” Interfacial Protective Layer, J. Am. Chem. Soc. 139 (2017) 4815–4820. doi:10.1021/jacs.6b13314.

[55] W. Liu, W. Li, D. Zhuo, G. Zheng, Z. Lu, K. Liu, Y. Cui, Core-Shell Nanoparticle Coating as an Interfacial Layer for Dendrite-Free Lithium Metal Anodes, ACS Cent. Sci. 3 (2017) 135–140. doi:10.1021/acscentsci.6b00389.

[56] F. Aziz, A.F. Ismail, Spray coating methods for polymer solar cells fabrication: A review, Mater. Sci. Semicond. Process. 39 (2015) 416–425. doi:10.1016/j.mssp.2015.05.019.

[57] M. Bai, K. Xie, K. Yuan, K. Zhang, N. Li, C. Shen, Y. Lai, R. Vajtai, P. Ajayan, B. Wei, A Scalable Approach to Dendrite-Free Lithium Anodes via Spontaneous Reduction of Spray-Coated Graphene Oxide Layers, Adv.

Mater. 30 (2018) 1801213. doi:10.1002/adma.201801213.

[58] H. Chen, A. Pei, D. Lin, J. Xie, A. Yang, J. Xu, K. Lin, J. Wang, H. Wang, F. Shi, D. Boyle, Y. Cui, Uniform High Ionic Conducting Lithium Sulfide Protection Layer for Stable Lithium Metal Anode, Adv. Energy Mater. 9 (2019) 1900858. doi:10.1002/aenm.201900858.

[59] D. Lin, Y. Liu, W. Chen, G. Zhou, K. Liu, B. Dunn, Y. Cui, Conformal Lithium Fluoride Protection Layer on Three-Dimensional Lithium by Nonhazardous Gaseous Reagent Freon, Nano Lett. 17 (2017) 3731–3737. doi:10.1021/acs.nanolett.7b01020.

[60] J. Zhao, L. Liao, F. Shi, T. Lei, G. Chen, A. Pei, J. Sun, K. Yan, G. Zhou, J. Xie, C. Liu, Y. Li, Z. Liang, Z. Bao, Y. Cui, Surface Fluorination of Reactive Battery Anode Materials for Enhanced Stability, J. Am. Chem. Soc. 139 (2017) 11550–11558. doi:10.1021/jacs.7b05251.

[61] F. Liu, Q. Xiao, H. Bin Wu, L. Shen, D. Xu, M. Cai, Y. Lu, Fabrication of Hybrid Silicate Coatings by a Simple Vapor Deposition Method for Lithium Metal Anodes, Adv. Energy Mater. 8 (2018) 1701744. doi:10.1002/aenm.201701744.

[62] J. Lang, Y. Long, J. Qu, X. Luo, H. Wei, K. Huang, H. Zhang, L. Qi, Q. Zhang, Z. Li, H. Wu, One-pot solution coating of high quality LiF layer to stabilize Li metal anode, Energy Storage Mater. 16 (2019) 85–90. doi:10.1016/j.ensm.2018.04.024.

[63] Z. Hu, S. Zhang, S. Dong, W. Li, H. Li, G. Cui, L. Chen, Poly(ethyl α-cyanoacrylate)-Based Artificial Solid Electrolyte Interphase Layer for Enhanced Interface Stability of Li Metal Anodes, Chem. Mater. 29 (2017) 4682–4689. doi:10.1021/acs.chemmater.7b00091.

[64] Q. Pang, X. Liang, A. Shyamsunder, L.F. Nazar, An In Vivo Formed Solid Electrolyte Surface Layer Enables Stable Plating of Li Metal, Joule. 1 (2017) 871–886. doi:10.1016/j.joule.2017.11.009.

[65] A.M. Tripathi, W.N. Su, B.J. Hwang, In situ analytical techniques for battery interface analysis, Chem. Soc. Rev. 47 (2018) 736–751. doi:10.1039/c7cs00180k.

[66] R. Xu, X.Q. Zhang, X.B. Cheng, H.J. Peng, C.Z. Zhao, C. Yan, J.Q. Huang, Artificial Soft–Rigid Protective Layer for Dendrite-Free Lithium Metal Anode, Adv. Funct. Mater. 28 (2018) 1705838. doi:10.1002/adfm.201705838.

[67] J. Luo, C.C. Fang, N.L. Wu, High Polarity Poly(vinylidene difluoride) Thin Coating for Dendrite-Free and High-Performance Lithium Metal Anodes, Adv. Energy Mater. 8 (2018) 1701482. doi:10.1002/aenm.201701482.

[68] N. Saqib, C.M. Ganim, A.E. Shelton, J.M. Porter, On the decomposition of carbonate-based lithium-ion battery electrolytes studied using operando infrared spectroscopy, J. Electrochem. Soc. 165 (2018) A4051–A4057. doi:10.1149/2.1051816jes.

[69] H. Liu, X. Yue, X. Xing, Q. Yan, J. Huang, V. Petrova, H. Zhou, P. Liu, A scalable 3D lithium metal anode, Energy Storage Mater. 16 (2019) 505–511. doi:10.1016/j.ensm.2018.09.021.

[70] H. Zheng, D. Xiao, X. Li, Y. Liu, Y. Wu, J. Wang, K. Jiang, C. Chen, L. Gu, X. Wei, Y.S. Hu, Q. Chen, H. Li, New insight in understanding oxygen reduction and evolution in solid-state lithium-oxygen batteries using an in situ environmental scanning electron microscope, Nano Lett. 14 (2014) 4245–4249. doi:10.1021/nl500862u.

[71] Y. Li, Y. Li, A. Pei, K. Yan, Y. Sun, C.L. Wu, L.M. Joubert, R. Chin, A.L. Koh, Y. Yu, J. Perrino, B. Butz, S.

Chu, Y. Cui, Atomic structure of sensitive battery materials and interfaces revealed by cryo–electron microscopy, Science (80-.). 358 (2017) 506–510. doi:10.1126/science.aam6014.

[72] X. Wang, Y. Li, Y.S. Meng, Cryogenic Electron Microscopy for Characterizing and Diagnosing Batteries, Joule. 2 (2018) 2225–2234. doi:10.1016/j.joule.2018.10.005.

[73] M.J. Zachman, Z. Tu, S. Choudhury, L.A. Archer, L.F. Kourkoutis, Cryo-STEM mapping of solid–liquid interfaces and dendrites in lithium-metal batteries, Nature. 560 (2018) 345–349. doi:10.1038/s41586-018-0397-3.

[74] H. Liu, X. Wang, H. Zhou, H.D. Lim, X. Xing, Q. Yan, Y.S. Meng, P. Liu, Structure and Solution Dynamics of Lithium Methyl Carbonate as a Protective Layer for Lithium Metal, ACS Appl. Energy Mater. 1 (2018) 1864–1869. doi:10.1021/acsaem.8b00348.

[75] L. Lin, F. Liang, K. Zhang, H. Mao, J. Yang, Y. Qian, Lithium phosphide/lithium chloride coating on lithium for advanced lithium metal anode, J. Mater. Chem. A. 6 (2018) 15859–15867. doi:10.1039/c8ta05102j.

[76] L. Chen, J.G. Connell, A. Nie, Z. Huang, K.R. Zavadil, K.C. Klavetter, Y. Yuan, S. Sharifi-Asl, R. Shahbazian-Yassar, J.A. Libera, A.U. Mane, J.W. Elam, Lithium metal protected by atomic layer deposition metal oxide for high performance anodes, J. Mater. Chem. A. 5 (2017) 12297–12309. doi:10.1039/c7ta03116e.

[77] T. Liu, L. Lin, X. Bi, L. Tian, K. Yang, J. Liu, M. Li, Z. Chen, J. Lu, K. Amine, K. Xu, F. Pan, In situ quantification of interphasial chemistry in Li-ion battery, Nat. Nanotechnol. 14 (2019) 50–56. doi:10.1038/s41565-018-0284-y.

[78] B.D. Adams, J. Zheng, X. Ren, W. Xu, J.G. Zhang, Accurate Determination of Coulombic Efficiency for Lithium Metal Anodes and Lithium Metal Batteries, Adv. Energy Mater. 8 (2018) 1702097. doi:10.1002/aenm.201702097.

[79] Y. Xu, T. Li, L. Wang, Y. Kang, Interlayered Dendrite-Free Lithium Plating for High-Performance Lithium-Metal Batteries, Adv. Mater. 37 (2019) 1901662. doi:10.1002/adma.201901662.

[80] X. Fan, L. Chen, O. Borodin, X. Ji, J. Chen, S. Hou, T. Deng, J. Zheng, C. Yang, S.C. Liou, K. Amine, K. Xu, C. Wang, Non-flammable electrolyte enables li-metal batteries with aggressive cathode chemistries, Nat. Nanotechnol. 13 (2018) 715–722. doi:10.1038/s41565-018-0183-2.

[81] A. Sakuda, A. Hayashi, M. Tatsumisago, Sulfide solid electrolyte with favorable mechanical property for all-solid-state lithium battery, Sci. Rep. 3 (2013) 2261. doi:10.1038/srep02261.

[82] H. Yildirim, A. Kinaci, M.K.Y. Chan, J.P. Greeley, First-Principles Analysis of Defect Thermodynamics and Ion Transport in Inorganic SEI Compounds: LiF and NaF, ACS Appl. Mater. Interfaces. 7 (2015) 18985–18996. doi:10.1021/acsami.5b02904.

[83] S. Hao, C. Wolverton, Lithium transport in amorphous Al2O3 and AlF 3 for discovery of battery coatings, J. Phys. Chem. C. 117 (2013) 8009–8013. doi:10.1021/jp311982d.

[84] X. Yu, J.B. Bates, G.E. Jellison, F.X. Hart, A stable thin-film lithium electrolyte: Lithium phosphorus oxynitride, J. Electrochem. Soc. 144 (1997) 524–532. doi:10.1149/1.1837443.

[85] G. Nazri, Preparation, structure and ionic conductivity of lithium phosphide, Solid State Ionics. 34 (1989) 97–102. doi:10.1016/0167-2738(89)90438-4.

[86] M. Prencipe, A. Zupan, R. Dovesi, E. Apr??, V.R. Saunders, Ab initio study of the structural properties of

LiF, NaF, KF, LiCl, NaCl, and KCl, Phys. Rev. B. 51 (1995) 3391–3396. doi:10.1103/PhysRevB.51.3391.

[87] R.M. SPRIGGS, L.A. BRISSETTE, Expressions for Shear Modulus and Poisson's Ratio of Porous Refractory Oxides, J. Am. Ceram. Soc. 45 (1962) 198–199. doi:10.1111/j.1151-2916.1962.tb11121.x.

[88] E.G. Herbert, W.E. Tenhaeff, N.J. Dudney, G.M. Pharr, Mechanical characterization of LiPON films using nanoindentation, Thin Solid Films. 520 (2011) 413–418. doi:10.1016/j.tsf.2011.07.068.

[89] A. Sakuda, A. Hayashi, Y. Takigawa, K. Higashi, M. Tatsumisago, Evaluation of elastic modulus of Li2S-P2S5glassy solid electrolyte by ultrasonic sound velocity measurement and compression test, J. Ceram. Soc. Japan. 121 (2013) 946–949. doi:10.2109/jcersj2.121.946.

[90] H. Peelaers, C.G. Van De Walle, Elastic constants and pressure-induced effects in MoS2, J. Phys. Chem. C. 118 (2014) 12073–12076. doi:10.1021/jp503683h.

[91] R.R. Nair, W. Ren, R. Jalil, I. Riaz, V.G. Kravets, L. Britnell, P. Blake, F. Schedin, A.S. Mayorov, S. Yuan, M.I. Katsnelson, H.M. Cheng, W. Strupinski, L.G. Bulusheva, A. V. Okotrub, I. V. Grigorieva, A.N. Grigorenko, K.S. Novoselov, A.K. Geim, Fluorographene: A two-dimensional counterpart of Teflon, Small. 6 (2010) 2877–2884. doi:10.1002/smll.201001555.

[92] S. Chen, J. Zheng, L. Yu, X. Ren, M.H. Engelhard, C. Niu, H. Lee, W. Xu, J. Xiao, J. Liu, J.G. Zhang, High-Efficiency Lithium Metal Batteries with Fire-Retardant Electrolytes, Joule. 2 (2018) 1548–1558. doi:10.1016/j.joule.2018.05.002.

[93] X. Fan, X. Ji, F. Han, J. Yue, J. Chen, L. Chen, T. Deng, J. Jiang, C. Wang, Fluorinated solid electrolyte interphase enables highly reversible solid-state Li metal battery, Sci. Adv. 4 (2018) eaau9245.

[94] S. Jiao, X. Ren, R. Cao, M.H. Engelhard, Y. Liu, D. Hu, D. Mei, J. Zheng, W. Zhao, Q. Li, N. Liu, B.D. Adams, C. Ma, J. Liu, J.G. Zhang, W. Xu, Stable cycling of high-voltage lithium metal batteries in ether electrolytes, Nat. Energy. (2018) 1–8. doi:10.1038/s41560-018-0199-8.

[95] N.D. Trinh, D. Lepage, D. Aymé-Perrot, A. Badia, M. Dollé, D. Rochefort, An Artificial Lithium Protective Layer that Enables the Use of Acetonitrile-Based Electrolytes in Lithium Metal Batteries, Angew. Chemie - Int. Ed. 57 (2018) 5072–5075. doi:10.1002/anie.201801737.

[96] J. Pan, Y.T. Cheng, Y. Qi, General method to predict voltage-dependent ionic conduction in a solid electrolyte coating on electrodes, Phys. Rev. B. 91 (2015) 134116. doi:10.1103/PhysRevB.91.134116.

[97] C. Li, L. Gu, J. Maier, Enhancement of the Li conductivity in LiF by introducing glass/crystal interfaces, Adv. Funct. Mater. 22 (2012) 1145–1149. doi:10.1002/adfm.201101798.

[98] J. Yang, C. Hu, Y. Jia, Y. Pang, L. Wang, W. Liu, X. Sun, Surface Restraint Synthesis of an Organic-Inorganic Hybrid Layer for Dendrite-Free Lithium Metal Anode, ACS Appl. Mater. Interfaces. 11 (2019) 8717–8724. doi:10.1021/acsami.9b00507.

[99] S.T. Myung, K. Izumi, S. Komaba, Y.K. Sun, H. Yashiro, N. Kumagai, Role of alumina coating on Li-Ni-Co-Mn-O particles as positive electrode material for lithium-ion batteries, Chem. Mater. 17 (2005) 3695–3704. doi:10.1021/cm050566s.

[100] S. Mo, B. Zhang, K. Zhang, S. Li, F. Pan, LiAl 5 O 8 as a potential coating material in lithium-ion batteries: a first principles study, Phys. Chem. Chem. Phys. 21 (2019) 13758–13765. doi:10.1039/c9cp02650a.

[101] X. Han, Y. Gong, K. Fu, X. He, G.T. Hitz, J. Dai, A. Pearse, B. Liu, H. Wang, G. Rubloff, Y. Mo, V. Thangadurai, E.D. Wachsman, L. Hu, Negating interfacial impedance in garnet-based solid-state Li metal

batteries, Nat. Mater. 16 (2017) 572–579. doi:10.1038/nmat4821.

[102] Y. Shen, Y. Zhang, S. Han, J. Wang, Z. Peng, L. Chen, Unlocking the Energy Capabilities of Lithium Metal Electrode with Solid-State Electrolytes, Joule. 2 (2018) 1674–1689. doi:10.1016/j.joule.2018.06.021.

[103] D.M. Seo, D. Chalasani, B.S. Parimalam, R. Kadam, M. Nie, B.L. Lucht, Reduction Reactions of Carbonate Solvents for Lithium Ion Batteries, ECS Electrochem. Lett. 3 (2014) A91–A93. doi:10.1149/2.0021409eel.

[104] H. Liu, H. Zhou, B.S. Lee, X. Xing, M. Gonzalez, P. Liu, Suppressing Lithium Dendrite Growth with a Single-Component Coating, ACS Appl. Mater. Interfaces. 9 (2017) 30635–30642. doi:10.1021/acsami.7b08198.

[105] H. Liu, X. Wang, H. Zhou, H.-D. Lim, X. Xing, Q. Yan, Y.S. Meng, P. Liu, Structure and Solution Dynamics of Lithium Methyl Carbonate as a Protective Layer For Lithium Metal, ACS Appl. Energy Mater. 1 (2018) 1864–1869. doi:10.1021/acsaem.8b00348.

[106] H. Zhou, H. Liu, Y. Li, X. Yue, X. Wang, M. Gonzalez, Y.S. Meng, P. Liu, In situ formed polymer gel electrolytes for lithium batteries with inherent thermal shutdown safety features, J. Mater. Chem. A. 7 (2019) 16984–16991. doi:10.1039/C9TA02341K.

[107] Y. Han, X. Duan, Y. Li, L. Huang, D. Zhu, Y. Chen, Effects of sulfur loading on the corrosion behaviors of metal lithium anode in lithium-sulfur batteries, Mater. Res. Bull. 68 (2015) 160–165. doi:10.1016/j.materresbull.2015.03.042.

[108] W. Liu, R. Guo, B. Zhan, B. Shi, Y. Li, H. Pei, Y. Wang, W. Shi, Z. Fu, J. Xie, Artificial Solid Electrolyte Interphase Layer for Lithium Metal Anode in High-Energy Lithium Secondary Pouch Cells, ACS Appl. Energy Mater. 1 (2018) 1674–1679. doi:10.1021/acsaem.8b00132.

[109] A.C. Kozen, C.F. Lin, O. Zhao, S.B. Lee, G.W. Rubloff, M. Noked, Stabilization of Lithium Metal Anodes by Hybrid Artificial Solid Electrolyte Interphase, Chem. Mater. 29 (2017) 6298–6307. doi:10.1021/acs.chemmater.7b01496.

[110] J. Lau, R.H. DeBlock, D.M. Butts, D.S. Ashby, C.S. Choi, B.S. Dunn, Sulfide Solid Electrolytes for Lithium Battery Applications, Adv. Energy Mater. 8 (2018) 1800933. doi:10.1002/aenm.201800933.

[111] H.D. Lim, H.K. Lim, X. Xing, B.S. Lee, H. Liu, C. Coaty, H. Kim, P. Liu, Solid Electrolyte Layers by Solution Deposition, Adv. Mater. Interfaces. 5 (2018) 1701328. doi:10.1002/admi.201701328.

[112] J. Liang, X. Li, Y. Zhao, L. V. Goncharova, G. Wang, K.R. Adair, C. Wang, R. Li, Y. Zhu, Y. Qian, L. Zhang, R. Yang, S. Lu, X. Sun, In Situ Li 3 PS 4 Solid-State Electrolyte Protection Layers for Superior Long-Life and High-Rate Lithium-Metal Anodes, Adv. Mater. 30 (2018) 1804684. doi:10.1002/adma.201804684.

[113] X. Liang, Q. Pang, I.R. Kochetkov, M.S. Sempere, H. Huang, X. Sun, L.F. Nazar, A facile surface chemistry route to a stabilized lithium metal anode, Nat. Energy. 2 (2017) 17119. doi:10.1038/nenergy.2017.119.

[114] Z. Jiang, L. Jin, Z. Han, W. Hu, Z. Zeng, Y. Sun, J. Xie, Facile Generation of Polymer-Alloy Hybrid Layer towards Dendrite-free Lithium Metal Anode with Improved Moisture Stability, Angew. Chemie Int. Ed. 58 (2019) 11374–11378. doi:10.1002/anie.201905712.

[115] C. Yan, X.B. Cheng, Y.X. Yao, X. Shen, B.Q. Li, W.J. Li, R. Zhang, J.Q. Huang, H. Li, Q. Zhang, An Armored Mixed Conductor Interphase on a Dendrite-Free Lithium-Metal Anode, Adv. Mater. 30 (2018) 1804461. doi:10.1002/adma.201804461.

[116] K. Yan, H.W. Lee, T. Gao, G. Zheng, H. Yao, H. Wang, Z. Lu, Y. Zhou, Z. Liang, Z. Liu, S. Chu, Y. Cui,

Ultrathin two-dimensional atomic crystals as stable interfacial layer for improvement of lithium metal anode, Nano Lett. 14 (2014) 6016–6022. doi:10.1021/nl503125u.

[117] X. Shen, Y. Li, T. Qian, J. Liu, J. Zhou, C. Yan, J.B. Goodenough, Lithium anode stable in air for low-cost fabrication of a dendrite-free lithium battery, Nat. Commun. 10 (2019) 900. doi:10.1038/s41467-019-08767-0.

[118] H. Zhang, X. Liao, Y. Guan, Y. Xiang, M. Li, W. Zhang, X. Zhu, H. Ming, L. Lu, J. Qiu, Y. Huang, G. Cao, Y. Yang, L. Mai, Y. Zhao, H. Zhang, Lithiophilic-lithiophobic gradient interfacial layer for a highly stable lithium metal anode, Nat. Commun. 9 (2018) 3729. doi:10.1038/s41467-018-06126-z.

[119] J. Song, H. Lee, M.-J. Choo, J.-K. Park, H.-T. Kim, Ionomer-Liquid Electrolyte Hybrid Ionic Conductor for High Cycling Stability of Lithium Metal Electrodes, Sci. Rep. 5 (2015) 14458. doi:10.1038/srep14458.

[120] A.F.M. Barton, Handbook of Solubility Parameters and Other Cohesion Parameters, 2nd Editio, 1991. doi:10.1002/9781119403647.ch305.

[121] U. Eduok, O. Faye, J. Szpunar, Recent developments and applications of protective silicone coatings: A review of PDMS functional materials, Prog. Org. Coatings. 111 (2017) 124–163. doi:10.1016/j.porgcoat.2017.05.012.

[122] X. Xing, Y. Li, X. Wang, V. Petrova, H. Liu, P. Liu, Cathode electrolyte interface enabling stable Li–S batteries, Energy Storage Mater. 21 (2019) 474–480. doi:10.1016/j.ensm.2019.06.022.

[123] Q. Li, F.L. Zeng, Y.P. Guan, Z.Q. Jin, Y.Q. Huang, M. Yao, W.K. Wang, A.B. Wang, Poly (dimethylsiloxane) modified lithium anode for enhanced performance of lithium-sulfur batteries, Energy Storage Mater. 13 (2018) 151–159. doi:10.1016/j.ensm.2018.01.002.

[124] C.H. Tsao, P.L. Kuo, Poly(dimethylsiloxane) hybrid gel polymer electrolytes of a porous structure for lithium ion battery, J. Memb. Sci. 489 (2015) 36–42. doi:10.1016/j.memsci.2015.03.087.

[125] B. Zhu, Y. Jin, X. Hu, Q. Zheng, S. Zhang, Q. Wang, J. Zhu, Poly(dimethylsiloxane) Thin Film as a Stable Interfacial Layer for High-Performance Lithium-Metal Battery Anodes, Adv. Mater. 29 (2017) 1603755. doi:10.1002/adma.201603755.

[126] G. Zheng, C. Wang, A. Pei, J. Lopez, F. Shi, Z. Chen, A.D. Sendek, H.W. Lee, Z. Lu, H. Schneider, M.M. Safont-Sempere, S. Chu, Z. Bao, Y. Cui, High-Performance Lithium Metal Negative Electrode with a Soft and Flowable Polymer Coating, ACS Energy Lett. 1 (2016) 1247–1255. doi:10.1021/acsenergylett.6b00456.

[127] Q. Pang, L. Zhou, L.F. Nazar, Elastic and Li-ion–percolating hybrid membrane stabilizes Li metal plating, Proc. Natl. Acad. Sci. 115 (2018) 12389–12394. doi:10.1073/pnas.1809187115.

[128] V.A. Ganesh, A.S. Nair, H.K. Raut, T.T. Yuan Tan, C. He, S. Ramakrishna, J. Xu, Superhydrophobic fluorinated POSS-PVDF-HFP nanocomposite coating on glass by electrospinning, J. Mater. Chem. 22 (2012) 18479–18485. doi:10.1039/c2jm33088a.

[129] A.F.M. Barton, Handbook of Polymer-Liquid Interaction Parameters and Solubility Parameters, 1st Editio, CRC Press, 1990.

[130] I.S. Kang, Y.-S. Lee, D.-W. Kim, Improved Cycling Stability of Lithium Electrodes in Rechargeable Lithium Batteries, J. Electrochem. Soc. 161 (2014) A53–A57. doi:10.1149/2.029401jes.

[131] J.H. Kim, H.S. Woo, W.K. Kim, K.H. Ryu, D.W. Kim, Improved Cycling Performance of Lithium-Oxygen Cells by Use of a Lithium Electrode Protected with Conductive Polymer and Aluminum Fluoride, ACS Appl.

Mater. Interfaces. 8 (2016) 32300–32306. doi:10.1021/acsami.6b10419.

[132] R.S. Yeo, Dual cohesive energy densities of perfluorosulphonic acid (Nafion) membrane, Polymer (Guildf). 21 (1980) 432–435. doi:10.1016/0032-3861(80)90015-4.

[133] J. Bae, Y. Qian, Y. Li, X. Zhou, J.B. Goodenough, G. Yu, Polar polymer–solvent interaction derived favorable interphase for stable lithium metal batteries, Energy Environ. Sci. 12 (2019) 3319–3327. doi:10.1039/C9EE02558H.

[134] J. Lopez, A. Pei, J.Y. Oh, G.-J.J.N. Wang, Y. Cui, Z. Bao, Effects of Polymer Coatings on Electrodeposited Lithium Metal, J. Am. Chem. Soc. 140 (2018) 11735–11744. doi:10.1021/jacs.8b06047.

[135] F. Qiu, X. Li, H. Deng, D. Wang, X. Mu, P. He, H. Zhou, A Concentrated Ternary-Salts Electrolyte for High Reversible Li Metal Battery with Slight Excess Li, Adv. Energy Mater. 9 (2019) 1803372. doi:10.1002/aenm.201803372.

[136] T.T. Beyene, H.K. Bezabh, M.A. Weret, T.M. Hagos, C.-J. Huang, C.-H. Wang, W.-N. Su, H. Dai, B.-J. Hwang, Concentrated Dual-Salt Electrolyte to Stabilize Li Metal and Increase Cycle Life of Anode Free Li-Metal Batteries, J. Electrochem. Soc. 166 (2019) A1501–A1509. doi:10.1149/2.0731908jes.

[137] X. Cao, X. Ren, L. Zou, M.H. Engelhard, W. Huang, H. Wang, B.E. Matthews, H. Lee, C. Niu, B.W. Arey, Y. Cui, C. Wang, J. Xiao, J. Liu, W. Xu, J.-G. Zhang, Monolithic solid–electrolyte interphases formed in fluorinated orthoformate-based electrolytes minimize Li depletion and pulverization, Nat. Energy. 4 (2019) 796–805. doi:10.1038/s41560-019-0464-5.

[138] X. Zhang, A. Wang, X. Liu, J. Luo, Dendrites in Lithium Metal Anodes: Suppression, Regulation, and Elimination, Acc. Chem. Res. 52 (2019) 3223–3232. doi:10.1021/acs.accounts.9b00437.

[139] Y. Zhu, J. Xie, A. Pei, B. Liu, Y. Wu, D. Lin, J. Li, H. Wang, H. Chen, J. Xu, A. Yang, C.L. Wu, H. Wang, W. Chen, Y. Cui, Fast lithium growth and short circuit induced by localized-temperature hotspots in lithium batteries, Nat. Commun. 10 (2019) 2067. doi:10.1038/s41467-019-09924-1.

[140] N. Verdier, D. Lepage, R. Zidani, A. Prébé, D. Aymé-Perrot, C. Pellerin, M. Dollé, D. Rochefort, Cross-Linked Polyacrylonitrile-Based Elastomer Used as Gel Polymer Electrolyte in Li-Ion Battery, ACS Appl. Energy Mater. 3 (2020) 1099–1110. doi:10.1021/acsaem.9b02129.

[141] F. Baskoro, H.Q. Wong, H.-J. Yen, Strategic Structural Design of a Gel Polymer Electrolyte toward a High Efficiency Lithium-Ion Battery, ACS Appl. Energy Mater. 2 (2019) 3937–3971. doi:10.1021/acsaem.9b00295.

[142] H. Park, J.W. Kim, S.Y. Hong, G. Lee, H. Lee, C. Song, K. Keum, Y.R. Jeong, S.W. Jin, D.S. Kim, J.S. Ha, Dynamically Stretchable Supercapacitor for Powering an Integrated Biosensor in an All-in-One Textile System, ACS Nano. 13 (2019) 10469–10480. doi:10.1021/acsnano.9b04340.

[143] H. Wang, Z. Wang, J. Yang, C. Xu, Q. Zhang, Z. Peng, Ionic Gels and Their Applications in Stretchable Electronics, Macromol. Rapid Commun. 39 (2018) 1800246. doi:10.1002/marc.201800246.

[144] T.P. Lodge, T. Ueki, Mechanically Tunable, Readily Processable Ion Gels by Self-Assembly of Block Copolymers in Ionic Liquids, Acc. Chem. Res. 49 (2016) 2107–2114. doi:10.1021/acs.accounts.6b00308.

[145] D.G. Seo, H.C. Moon, Mechanically Robust, Highly Ionic Conductive Gels Based on Random Copolymers for Bending Durable Electrochemical Devices, Adv. Funct. Mater. 28 (2018) 1706948. doi:10.1002/adfm.201706948.

[146] T. Liu, J. Zhang, W. Han, J. Zhang, G. Ding, S. Dong, G. Cui, Review—In Situ Polymerization for Integration and Interfacial Protection Towards Solid State Lithium Batteries, J. Electrochem. Soc. 167 (2020) 070527. doi:10.1149/1945-7111/ab76a4.

[147] H. Zhou, S. Yu, H. Liu, P. Liu, Protective coatings for lithium metal anodes : Recent progress and future perspectives, J. Power Sources. 450 (2020) 227632. doi:10.1016/j.jpowsour.2019.227632.

[148] V. Bocharova, A.P. Sokolov, Perspectives for Polymer Electrolytes: A View from Fundamentals of Ionic Conductivity, Macromolecules. 53 (2020) 4141–4157. doi:10.1021/acs.macromol.9b02742.

[149] Y. Cho, C. Hwang, D.S. Cheong, Y. Kim, H. Song, Gel/Solid Polymer Electrolytes Characterized by In Situ Gelation or Polymerization for Electrochemical Energy Systems, Adv. Mater. 31 (2019) 1804909. doi:10.1002/adma.201804909.

[150] S.T. Russell, R. Pereira, J.T. Vardner, G.N. Jones, C. Dimarco, A.C. West, S.K. Kumar, Hydration Effects on the Permselectivity-Conductivity Trade-Off in Polymer Electrolytes, Macromolecules. 53 (2020) 1014–1023. doi:10.1021/acs.macromol.9b02291.

[151] G.M. Geise, M.A. Hickner, B.E. Logan, Ionic Resistance and Permselectivity Tradeoffs in Anion Exchange Membranes, ACS Appl. Mater. Interfaces. 5 (2013) 10294–10301. doi:10.1021/am403207w.

[152] M. Kono, E. Hayashi, M. Watanabe, Preparation, Mechanical Properties, and Electrochemical Characterization of Polymer Gel Electrolytes Prepared from Poly(alkylene oxide) Macromonomers, J. Electrochem. Soc. 146 (1999) 1626–1632. doi:10.1149/1.1391817.

[153] E. Guler, Y. Zhang, M. Saakes, K. Nijmeijer, Tailor-made anion-exchange membranes for salinity gradient power generation using reverse electrodialysis, ChemSusChem. 5 (2012) 2262–2270. doi:10.1002/cssc.201200298.

[154] M. Matsumoto, J.E. Soc, M. Matsumoto, T. Ichino, J.S. Rutt, S. Nishi, New Dual - Phase Polymer Electrolytes Prepared from NBR / SBR Latices New Dual-Phase Polymer Electrolytes Prepared from NBR / SBR Latices, J. Electrochem. Soc. 140 (1993) L151.

[155] G.B. Appetecchi, Y. Aihara, B. Scrosati, Investigation of swelling phenomena in PEO-based polymer electrolytes: II. Chemical and electrochemical characterization, Solid State Ionics. 170 (2004) 63–72. doi:10.1016/j.ssi.2003.12.019.

[156] S. Kuwabata, M. Tomiyori, Rechargeable Lithium Battery Cells Fabricated Using Poly(methyl methacrylate) Gel Electrolyte and Composite of V2O5 and Polypyrrole, J. Electrochem. Soc. 149 (2002) A988. doi:10.1149/1.1487834.

[157] K.M. Diederichsen, E.J. McShane, B.D. McCloskey, Promising Routes to a High Li+ Transference Number Electrolyte for Lithium Ion Batteries, ACS Energy Lett. 2 (2017) 2563–2575. doi:10.1021/acsenergylett.7b00792.

[158] W.Y. Hsu, J.R. Barkley, P. Meakin, Ion Percolation and Insulator-to-Conductor Transition in Nafion Perfluorosulfonic Acid Membranes, Macromolecules. 13 (1980) 198–200. doi:10.1021/ma60073a041.

[159] G. Tian, Z. Zhao, T. Zinkevich, K. Elies, F. Scheiba, H. Ehrenberg, A Crosslinked Polyethyleneglycol Solid Electrolyte Dissolving Lithium Bis(trifluoromethylsulfonyl)imide for Rechargeable Lithium Batteries, ChemSusChem. 12 (2019) 4708–4718. doi:10.1002/cssc.201901587.

[160] J.H. Baik, S. Kim, D.G. Hong, J.C. Lee, Gel Polymer Electrolytes Based on Polymerizable Lithium Salt and

Poly(ethylene glycol) for Lithium Battery Applications, ACS Appl. Mater. Interfaces. 11 (2019) 29718–29724. doi:10.1021/acsami.9b05139.

[161] A. Nishimoto, K. Agehara, N. Furuya, T. Watanabe, M. Watanabe, High Ionic Conductivity of Polyether-Based Network Polymer Electrolytes with Hyperbranched Side Chains, Macromolecules. 32 (1999) 1541–1548. doi:10.1021/ma981436q.

[162] S. Park, B. Jeong, D.A. Lim, C.H. Lee, K.H. Ahn, J.H. Lee, D.W. Kim, Quasi-Solid-State Electrolyte Synthesized Using a Thiol-Ene Click Chemistry for Rechargeable Lithium Metal Batteries with Enhanced Safety, ACS Appl. Mater. Interfaces. 12 (2020) 19553–19562. doi:10.1021/acsami.0c02706.

[163] N. Ihrner, W. Johannisson, F. Sieland, D. Zenkert, M. Johansson, Structural lithium ion battery electrolytes: Via reaction induced phase-separation, J. Mater. Chem. A. 5 (2017) 25652–25659. doi:10.1039/c7ta04684g.

[164] S.A. Chopade, J.G. Au, Z. Li, P.W. Schmidt, M.A. Hillmyer, T.P. Lodge, Robust Polymer Electrolyte Membranes with High Ambient-Temperature Lithium-Ion Conductivity via Polymerization-Induced Microphase Separation, ACS Appl. Mater. Interfaces. 9 (2017) 14561–14565. doi:10.1021/acsami.7b02514.

[165] F. Wu, L. Luo, Z. Tang, D. Liu, Z. Shen, X.-H. Fan, Block Copolymer Electrolytes with Excellent Properties in a Wide Temperature Range, ACS Appl. Energy Mater. 3 (2020) 6536–6543. doi:10.1021/acsaem.0c00737.

[166] K.M. Diederichsen, H.G. Buss, B.D. McCloskey, The Compensation Effect in the Vogel-Tammann-Fulcher (VTF) Equation for Polymer-Based Electrolytes, Macromolecules. 50 (2017) 3831–3840. doi:10.1021/acs.macromol.7b00423.

[167] N. Verdier, D. Lepage, A. Prébé, D. Aymé-Perrot, M. Dollé, D. Rochefort, Crosslinker free thermally induced crosslinking of hydrogenated nitrile butadiene rubber, J. Polym. Sci. Part A Polym. Chem. 56 (2018) 1825–1833. doi:10.1002/pola.29063.

[168] Z. Fu, B. Liu, Y. Liu, B. Li, H. Zhang, Detailed Cyclization Pathways Identification of Polyacrylonitrile and Poly(acrylonitrile- co -itaconic acid) by in Situ FTIR and Two-Dimensional Correlation analysis, Ind. Eng. Chem. Res. 57 (2018) 8348–8359. doi:10.1021/acs.iecr.8b01162.

[169] E. Cipriani, M. Zanetti, P. Bracco, V. Brunella, M.P. Luda, L. Costa, Crosslinking and carbonization processes in PAN films and nanofibers, Polym. Degrad. Stab. 123 (2016) 178–188. doi:10.1016/j.polymdegradstab.2015.11.008.

[170] S. Dalton, F. Heatley, P.M. Budd, Thermal stabilization of polyacrylonitrile fibres, Polymer (Guildf). 40 (1999) 5531–5543. doi:10.1016/S0032-3861(98)00778-2.

[171] B. Barua, M.C. Saha, Studies of reaction mechanisms during stabilization of electrospun polyacrylonitrile carbon nanofibers, Polym. Eng. Sci. 58 (2018) 1315–1321. doi:10.1002/pen.24708.

[172] J. Guo, Z. Yang, Y. Yu, H.D. Abruña, L.A. Archer, Lithium-sulfur battery cathode enabled by lithium-nitrile interaction, J. Am. Chem. Soc. 135 (2013) 763–767. doi:10.1021/ja309435f.

[173] B.S. Lee, S. Cui, X. Xing, H. Liu, X. Yue, V. Petrova, H.D. Lim, R. Chen, P. Liu, Dendrite Suppression Membranes for Rechargeable Zinc Batteries, ACS Appl. Mater. Interfaces. 10 (2018) 38928–38935. doi:10.1021/acsami.8b14022.

[174] Z. Wang, Y. Dong, H. Li, Z. Zhao, H. Bin Wu, C. Hao, S. Liu, J. Qiu, X.W. Lou, Enhancing lithium–sulphur battery performance by strongly binding the discharge products on amino-functionalized reduced graphene oxide, Nat. Commun. 5 (2014) 5002. doi:10.1038/ncomms6002.

[175] C.M. Hansen, Hansen Solubility Parameters, 2nd Editio, CRC Press, 2007. doi:10.1201/9781420006834.

[176] S.G. Croll, Application of the Flory-Rehner equation and the Griffith fracture criterion to paint stripping, J. Coatings Technol. Res. 7 (2010) 49–55. doi:10.1007/s11998-009-9166-4.

[177] J.L. Valentín, J. Carretero-González, I. Mora-Barrantes, W. Chassé, K. Saalwächter, Uncertainties in the determination of cross-link density by equilibrium swelling experiments in natural rubber, Macromolecules. 41 (2008) 4717–4729. doi:10.1021/ma8005087.

[178] T. Lindvig, M.L. Michelsen, G.M. Kontogeorgis, A Flory-Huggins model based on the Hansen solubility parameters, Fluid Phase Equilib. 203 (2002) 247–260. doi:10.1016/S0378-3812(02)00184-X.

[179] D.R. Morris, X. Sun, Water-sorption and transport properties of Nafion 117 H, J. Appl. Polym. Sci. 50 (1993) 1445–1452. doi:10.1002/app.1993.070500816.

[180] T. Thampan, S. Malhotra, H. Tang, R. Datta, Modeling of conductive transport in proton-exchange membranes for fuel cells, J. Electrochem. Soc. 147 (2000) 3242–3250. doi:10.1149/1.1393890.

[181] P. Knauth, L. Pasquini, R. Narducci, E. Sgreccia, R.-A. Becerra-Arciniegas, M.L. Di Vona, Effective ion mobility in anion exchange ionomers: Relations with hydration, porosity, tortuosity, and percolation, J. Memb. Sci. 617 (2020) 118622. doi:10.1016/j.memsci.2020.118622.

[182] D.M. Pesko, S. Sawhney, J. Newman, N.P. Balsara, Comparing Two Electrochemical Approaches for Measuring Transference Numbers in Concentrated Electrolytes, J. Electrochem. Soc. 165 (2018) A3014–A3021. doi:10.1149/2.0231813jes.

[183] T.P. Liyana-Arachchi, J.B. Haskins, C.M. Burke, K.M. Diederichsen, B.D. McCloskey, J.W. Lawson, Polarizable Molecular Dynamics and Experiments of 1,2-Dimethoxyethane Electrolytes with Lithium and Sodium Salts: Structure and Transport Properties, J. Phys. Chem. B. 122 (2018) 8548–8559. doi:10.1021/acs.jpcb.8b03445.

[184] S.A. Krachkovskiy, J.D. Bazak, S. Fraser, I.C. Halalay, G.R. Goward, Determination of Mass Transfer Parameters and Ionic Association of LiPF 6 : Organic Carbonates Solutions, J. Electrochem. Soc. 164 (2017) A912–A916. doi:10.1149/2.1531704jes.

[185] J. Newman, K.E. Thomas, Electrochemical Systems, Third Edit, John Wiley & Sons, Inc., Hoboken, New Jersey, 2004. https://www.wiley.com/en-us/Electrochemical+Systems%2C+3rd+Edition-p-9780471477563.

[186] Y. Liu, D. Lin, P.Y. Yuen, K. Liu, J. Xie, R.H. Dauskardt, Y. Cui, An Artificial Solid Electrolyte Interphase with High Li-Ion Conductivity, Mechanical Strength, and Flexibility for Stable Lithium Metal Anodes, Adv. Mater. 29 (2017) 1605531. doi:10.1002/adma.201605531.

[187] B. Philippe, R. Dedryvère, M. Gorgoi, H. Rensmo, D. Gonbeau, K. Edström, Role of the LiPF 6 Salt for the Long-Term Stability of Silicon Electrodes in Li-Ion Batteries – A Photoelectron Spectroscopy Study, Chem. Mater. 25 (2013) 394–404. doi:10.1021/cm303399v.

[188] W.J. Gammon, O. Kraft, A.C. Reilly, B.C. Holloway, Experimental comparison of N(1s) X-ray photoelectron spectroscopy binding energies of hard and elastic amorphous carbon nitride films with reference organic compounds, Carbon N. Y. 41 (2003) 1917–1923. doi:10.1016/S0008-6223(03)00170-2.

[189] K.B. Hatzell, X.C. Chen, C.L. Cobb, N.P. Dasgupta, M.B. Dixit, L.E. Marbella, M.T. McDowell, P.P. Mukherjee, A. Verma, V. Viswanathan, A.S. Westover, W.G. Zeier, Challenges in Lithium Metal Anodes for Solid-State Batteries, ACS Energy Lett. 5 (2020) 922–934. doi:10.1021/acsenergylett.9b02668.

[190] S. Sato, Y. Honda, M. Kuwahara, H. Kishimoto, N. Yagi, K. Muraoka, T. Watanabe, Microbial Scission of Sulfide Linkages in Vulcanized Natural Rubber by a White Rot Basidiomycete, Ceriporiopsis s ubvermispora, Biomacromolecules. 5 (2004) 511–515. doi:10.1021/bm034368a.

[191] P. Albertus, S. Babinec, S. Litzelman, A. Newman, Status and challenges in enabling the lithium metal electrode for high-energy and low-cost rechargeable batteries, Nat. Energy. 3 (2017) 16–21. doi:10.1007/978-3-319-15458-9.

[192] D. Lv, Y. Shao, T. Lozano, W.D. Bennett, G.L. Graff, B. Polzin, J. Zhang, M.H. Engelhard, N.T. Saenz, W.A. Henderson, P. Bhattacharya, J. Liu, J. Xiao, Failure mechanism for fast-charged lithium metal batteries with liquid electrolytes, Adv. Energy Mater. 5 (2015) 1400993. doi:10.1002/aenm.201400993.

[193] S. Hess, M. Wohlfahrt-Mehrens, M. Wachtler, Flammability of Li-Ion Battery Electrolytes: Flash Point and Self-Extinguishing Time Measurements, J. Electrochem. Soc. 162 (2015) A3084–A3097. doi:10.1149/2.0121502jes.

[194] K.-H. Chen, A.J. Sanchez, E. Kazyak, A.L. Davis, N.P. Dasgupta, Synergistic Effect of 3D Current Collectors and ALD Surface Modification for High Coulombic Efficiency Lithium Metal Anodes, Adv. Energy Mater. (2018) 1802534. doi:10.1002/aenm.201802534.

[195] G. Li, Y. Gao, X. He, Q. Huang, S. Chen, S.H. Kim, D. Wang, Organosulfide-plasticized solid-electrolyte interphase layer enables stable lithium metal anodes for long-cycle lithium-sulfur batteries, Nat. Commun. 8 (2017) 850. doi:10.1038/s41467-017-00974-x.

[196] J. Qian, W.A. Henderson, W. Xu, P. Bhattacharya, M. Engelhard, O. Borodin, J.-G. Zhang, High rate and stable cycling of lithium metal anode., Nat. Commun. 6 (2015) 6362. doi:10.1038/ncomms7362.

[197] X.B. Cheng, R. Zhang, C.Z. Zhao, F. Wei, J.G. Zhang, Q. Zhang, A review of solid electrolyte interphases on lithium metal anode, Adv. Sci. 3 (2015) 1500213. doi:10.1002/advs.201500213.

[198] H. Liu, H. Zhou, B.S. Lee, X. Xing, M. Gonzalez, P. Liu, Suppressing Lithium Dendrite Growth with a Single-Component Coating, ACS Appl. Mater. Interfaces. 9 (2017) 30635–30642. doi:10.1021/acsami.7b08198.

[199] J. Wang, Y. Yamada, K. Sodeyama, E. Watanabe, K. Takada, Y. Tateyama, A. Yamada, Fire-extinguishing organic electrolytes for safe batteries, Nat. Energy. 3 (2018) 22–29. doi:10.1038/s41560-017-0033-8.

[200] H.K. Reimschuessel, W.S. Creasy, Polymerization of Vinylene Carbonate in Dimethyl Sulfoxide., J. Polym. Sci. 16 (1978) 845–860. doi:10.1002/pol.1978.170160410.

[201] N.D. Field, J.R. Schaefgen, High Molecular Weight Poly (vinylene Carbonate) and Derivatives, J. Polym. Sci. 58 (1962) 533–543.

[202] L. Ding, Y. Li, Y. Li, Y. Liang, J. Huang, Polymerization of vinylene carbonate as well as aminolysis and hydrolysis of poly(vinylene carbonate), Eur. Polym. J. 37 (2001) 2453–2459. doi:10.1016/S0014-3057(01)00145-8.

[203] A.P. Krapcho, J.F. Weimaster, J.M. Eldridge, E.G.E. Jahngen, A.J. Lovey, W.P. Stephens, Synthetic Applications and Mechanism Studies of the Decarbalkoxylations of Geminal Diesters and Related Systems Effected in MeaSO by Water and/or by Water with Added Salts, J. Org. Chem. 43 (1978) 138–147. doi:10.1021/jo00395a032.

[204] J. Lee, M.H. Litt, Ring-Opening Polymerization of Ethylene Carbonate and Depolymerization of Poly

(ethylene oxide- co -ethylene carbonate) acids , transesterification catalysts , or bases as initiators, Macromolecules. 33 (2000) 1618–1627. doi:10.1021/ma9914321.

[205] Y.C. Jung, M.S. Park, D.H. Kim, M. Ue, A. Eftekhari, D.W. Kim, Room-Temperature Performance of Poly(Ethylene Ether Carbonate)-Based Solid Polymer Electrolytes for All-Solid-State Lithium Batteries, Sci. Rep. 7 (2017) 17482. doi:10.1038/s41598-017-17697-0.

[206] F. Wu, J.T. Lee, N. Nitta, H. Kim, O. Borodin, G. Yushin, Lithium iodide as a promising electrolyte additive for lithium-sulfur batteries: Mechanisms of performance enhancement, Adv. Mater. 27 (2015) 101–108. doi:10.1002/adma.201404194.

[207] G. Bieker, M. Winter, P. Bieker, Electrochemical in situ investigations of SEI and dendrite formation on the lithium metal anode, Phys. Chem. Chem. Phys. 17 (2015) 8670–8679. doi:10.1039/c4cp05865h.

[208] H. Ota, K. Shima, M. Ue, J. Yamaki, Effect of vinylene carbonate as additive to electrolyte for lithium metal anode, Electrochim. Acta. 49 (2004) 565–572. doi:10.1016/j.electacta.2003.09.010.

[209] Z. Hu, S. Zhang, S. Dong, Q. Li, G. Cui, L. Chen, Self-stabilized solid electrolyte interface on host-free Li metal anode towards high areal capacity and rate utilization, Chem. Mater. 30 (2018) 4039–4047. doi:10.1021/acs.chemmater.8b00722.

[210] G. Wan, F. Guo, H. Li, Y. Cao, X. Ai, J. Qian, Y. Li, H. Yang, Suppression of Dendritic Lithium Growth by in Situ Formation of a Chemically Stable and Mechanically Strong Solid Electrolyte Interphase, ACS Appl. Mater. Interfaces. 10 (2018) 593–601. doi:10.1021/acsami.7b14662.

[211] I.A. Shkrob, J.F. Wishart, D.P. Abraham, What Makes Fluoroethylene Carbonate Different?, J. Phys. Chem. C. 119 (2015) 14954–14964. doi:10.1021/acs.jpcc.5b03591.

[212] X.Q. Zhang, X.B. Cheng, X. Chen, C. Yan, Q. Zhang, Fluoroethylene Carbonate Additives to Render Uniform Li Deposits in Lithium Metal Batteries, Adv. Funct. Mater. 27 (2017) 1605989. doi:10.1002/adfm.201605989.

[213] S. Chen, J. Zheng, D. Mei, K.S. Han, M.H. Engelhard, W. Zhao, W. Xu, J. Liu, J.G. Zhang, High-Voltage Lithium-Metal Batteries Enabled by Localized High-Concentration Electrolytes, Adv. Mater. 30 (2018) 1706102. doi:10.1002/adma.201706102.

[214] C. Yan, X.B. Cheng, Y. Tian, X. Chen, X.Q. Zhang, W.J. Li, J.Q. Huang, Q. Zhang, Dual-Layered Film Protected Lithium Metal Anode to Enable Dendrite-Free Lithium Deposition, Adv. Mater. 30 (2018) 1707629. doi:10.1002/adma.201707629.

[215] X. Ren, Y. Zhang, M.H. Engelhard, Q. Li, J.G. Zhang, W. Xu, Guided Lithium Metal Deposition and Improved Lithium Coulombic Efficiency through Synergistic Effects of LiAsF6and Cyclic Carbonate Additives, ACS Energy Lett. 3 (2018) 14–19. doi:10.1021/acsenergylett.7b00982.

[216] L. Suo, W. Xue, M. Gobet, S.G. Greenbaum, C. Wang, Y. Chen, W. Yang, Y. Li, J. Li, Fluorine-donating electrolytes enable highly reversible 5-V-class Li metal batteries, Proc. Natl. Acad. Sci. 115 (2018) 1156–1161. doi:10.1073/pnas.1712895115.

[217] K. Xu, Electrolytes and interphases in Li-ion batteries and beyond, Chem. Rev. 114 (2014) 11503–11618. doi:10.1021/cr500003w.

[218] L.J. Krause, V.L. Chevrier, L.D. Jensen, T. Brandt, The Effect of Carbon Dioxide on the Cycle Life and Electrolyte Stability of Li-Ion Full Cells Containing Silicon Alloy, J. Electrochem. Soc. 164 (2017) A2527–

A2533. doi:10.1149/2.1121712jes.

[219] Y. Carmeli, M. Babai, H. Yamin, The correlation between the surface chemistry and the performance of Li-Carbon intercalation anodes for rechatgeable “Rocking-Chair” type batteries, J. Electrochem. Soc. 141 (1994) 603–611.

[220] D. Aurbach, B. Markovsky, A. Shechter, Y. Ein-Eli, H. Cohen, A Comparative Study of Synthetic Graphite and Li Electrodes in Electrolyte Solutions Based on Ethylene Carbonate-Dimethyl Carbonate Mixtures, J. Electrochem. Soc. 143 (1996) 3809–3820. doi:10.1149/1.1837300.

[221] S.W. Lee, Y. Yang, H.-W. Lee, H. Ghasemi, D. Kraemer, G. Chen, Y. Cui, An electrochemical system for efficiently harvesting low-grade heat energy., Nat. Commun. 5 (2014) 3942. doi:10.1038/ncomms4942.

[222] Y. Yang, S.W. Lee, H. Ghasemi, J. Loomis, X. Li, D. Kraemer, G. Zheng, Y. Cui, G. Chen, Charging-free electrochemical system for harvesting low-grade thermal energy, Proc. Natl. Acad. Sci. 111 (2014) 17011–17016. doi:10.1073/pnas.1415097111.

[223] M.F. Dupont, D.R. MacFarlane, J.M. Pringle, Thermo-electrochemical cells for waste heat harvesting – progress and perspectives, Chem. Commun. (2017) 6288–6302. doi:10.1039/C7CC02160G.

[224] T.I. Quickenden, Y. Mua, A Review of Power Generation in Aqueous Thermogalvanic Cells, J. Electrochem. Soc. 142 (1995) 3985–3994.

[225] H.L. Chum, R.A. Osteryoung, Review of Thermally Regenerative Electrochemical Systems, Rep. SERI/TR-332416,. 1 (1980).

[226] T. Ikeshoji, F.N.B. de Nahui, New electrochemical system of high thermoelectric power, J. Electroanal. Chem. Interfacial Electrochem. 305 (1991) 147–151. doi:10.1016/0022-0728(91)85210-G.

[227] S. Twaha, J. Zhu, Y. Yan, B. Li, A comprehensive review of thermoelectric technology: Materials, applications, modelling and performance improvement, Renew. Sustain. Energy Rev. 65 (2016) 698–726. doi:10.1016/j.rser.2016.07.034.

[228] H. Im, T. Kim, H. Song, J. Choi, J.S. Park, R. Ovalle-Robles, H.D. Yang, K.D. Kihm, R.H. Baughman, H.H. Lee, T.J. Kang, Y.H. Kim, High-efficiency electrochemical thermal energy harvester using carbon nanotube aerogel sheet electrodes, Nat. Commun. 7 (2016) 10600. doi:10.1038/ncomms10600.

[229] L. Zhang, T. Kim, N. Li, T.J. Kang, J. Chen, J.M. Pringle, M. Zhang, A.H. Kazim, S. Fang, C. Haines, D. Al-Masri, B.A. Cola, J.M. Razal, J. Di, S. Beirne, D.R. MacFarlane, A. Gonzalez-Martin, S. Mathew, Y.H. Kim, G. Wallace, R.H. Baughman, High Power Density Electrochemical Thermocells for Inexpensively Harvesting Low-Grade Thermal Energy, Adv. Mater. 29 (2017) 1–7. doi:10.1002/adma.201605652.

[230] P. Yang, K. Liu, Q. Chen, X. Mo, Y. Zhou, S. Li, G. Feng, J. Zhou, Wearable Thermocells Based on Gel Electrolytes for the Utilization of Body Heat, Angew. Chemie - Int. Ed. 55 (2016) 12050–12053. doi:10.1002/anie.201606314.

[231] W.B. Chang, C.M. Evans, B.C. Popere, B.M. Russ, J. Liu, J. Newman, R.A. Segalman, Harvesting Waste Heat in Unipolar Ion Conducting Polymers, ACS Macro Lett. 5 (2016) 94–98. doi:10.1021/acsmacrolett.5b00829.

[232] A.H. Kazim, A.S. Booeshaghi, S.T. Stephens, B.A. Cola, Thermo-electrochemical generator: energy harvesting & thermoregulation for liquid cooling applications, Sustain. Energy Fuels. (2017). doi:10.1039/C7SE00161D.

[233] P.F. Salazar, S. Kumar, B.A. Cola, Design and optimization of thermo-electrochemical cells, J. Appl. Electrochem. 44 (2014) 325–336. doi:10.1007/s10800-013-0638-y.

[234] T. Ikeshoji, Thermoelectric Conversion by Thin-Layer Thermogalvanic Cells with Soluble Redox Couples, Bull. Chem. Soc. Japan. 60 (1987) 1505–1514.

[235] H. Zhou, T. Yamada, N. Kimizuka, Supramolecular Thermo-Electrochemical Cells: Enhanced Thermoelectric Performance by Host–Guest Complexation and Salt-Induced Crystallization, J. Am. Chem. Soc. 138 (2016) 10502–10507. doi:10.1021/jacs.6b04923.

[236] E.L. Yee, R.J. Cave, K.L. Guyer, P.D. Tyma, M.J. Weaver, A survey of ligand effects upon the reaction entropies of some transition metal redox couples, J. Am. Chem. Soc. 101 (1979) 1131–1137. doi:10.1021/ja00499a013.

[237] S. Sahami, M.J. Weaver, Entropic and Enthalpic Contributions To the Solvent Dependence of the Thermodynamics of Transition-Metal Redox Couples Part I. Couples containing aromatic ligands, J. Electroanal. Chem. 122 (1981) 155–170.

[238] S. Sahami, M.J. Weaver, Entropic and Enthalpic Contributions To the Solvent Dependence of the Thermodynamics of Transition-Metal Redox Couples Part II. Couples containing amine and ethylenediamine ligands, J. Electroanal. Chem. 122 (1981) 171–181.

[239] J. Hupp, M. Weaver, Solvent, Ligand, and Ionic Charge Effects on Reaction Entropies for Simple Transition-Metal Redox Couples, Inorg. Chem. 23 (1984) 3639–3644.

[240] T.J. Abraham, D.R. MacFarlane, J.M. Pringle, High Seebeck coefficient redox ionic liquid electrolytes for thermal energy harvesting, Energy Environ. Sci. 6 (2013) 2639–2645. doi:Doi 10.1039/C3ee41608a.

[241] M.A. Lazar, D. Al-Masri, D.R. MacFarlane, J.M. Pringle, Enhanced thermal energy harvesting performance of a cobalt redox couple in ionic liquid-solvent mixtures, Phys. Chem. Chem. Phys. 18 (2016) 1404–1410. doi:10.1039/C5CP04305K.

[242] T. Kim, J.S. Lee, G. Lee, H. Yoon, J. Yoon, T.J. Kang, Y.H. Kim, High thermopower of ferri/ferrocyanide redox couple in organic-water solutions, Nano Energy. 31 (2017) 160–167. doi:10.1016/j.nanoen.2016.11.014.

[243] H. Zhou, T. Yamada, N. Kimizuka, Thermo-electrochemical cells empowered by selective inclusion of redox-active ions by polysaccharides, Sustain. Energy Fuels. 2 (2018) 472–478. doi:10.1039/C7SE00470B.

[244] J.-M. Lalancette, R. Roussel, Metals intercalated in graphite. V. A concentration cell with intercalated bromine, Can. J. Chem. 54 (1976) 3541–3544. doi:10.1139/v76-508.

[245] M. Endo, Y. Yamagishi, M. Inagaki, Thermocell with graphite fiber-bromine intercalation compounds, Synth. Met. 7 (1983) 203–209. doi:10.1016/0379-6779(83)90049-8.

[246] K. Shindo, M. Arakawa, T. Hirai, Effect of non-graphitized carbon electrodes on the electrochemical characteristics of a thermocell with a Br2/Br− redox couple, J. Power Sources. 70 (1998) 228–234. doi:10.1016/S0378-7753(97)02676-1.

[247] K. Shindo, M. Arakawa, T. Hirai, Influence of electrode materials on open-circuit voltage profiles with a temperature difference for a thermocell using a Br2/Br--redox reaction, J. Power Sources. 110 (2002) 46–51. doi:10.1016/S0378-7753(02)00216-1.

[248] Y. Ando, T. Tanaka, T. Doi, T. Takashima, A study on a thermally regenerative fuel cell utilizing

low-temperature thermal energy, Energy Convers. Manag. 42 (2001) 1807–1816. doi:10.1016/S0196-8904(01)00042-5.

[249] Y. Ando, Y. Aoyama, T. Sasaki, Y. Saito, H. Hatori, T. Tanaka, Effect of catalytic and electrochemical acetone hydrogenation on the I-V characteristics of an acetone/hydrogen-based thermally regenerative fuel cell, Bull. Chem. Soc. Jpn. 77 (2004) 1855–1859. doi:10.1246/bcsj.77.1855.

[250] Y. Ando, T. Tanaka, M. Amano, Influence of the internal structure and temperature in the reaction layer on the electric output in a solar thermal cell, Energy Convers. Manag. 44 (2003) 2811–2819. doi:10.1016/S0196-8904(03)00026-8.

[251] P.B.L. Chaurasia, Y. Ando, T. Tanaka, Investigation on proton exchange membrane fuel cell for solar power generation., Int. J. Sustain. Energy. 26 (2007) 107–119. doi:10.1080/14786450701552786.

[252] Y. Saito, H. Kameyama, K. Yoshida, Catalyst-assisted chemical heat pump with reaction couple of acetone hydrogenation/2–propanol dehydrogenation for upgrading low-level thermal energy: Proposal and evaluation, Int. J. Energy Res. 11 (1987) 549–558. doi:10.1002/er.4440110411.

[253] M. Noda, S. Shinoda, Y. Saito, Liquid-phase dehydrogenation of 2-propanol by suspended nickel fine-particle catalyst, Bull. Chem. Soc. Japan. 61 (1988) 961–965.

[254] Y. Saito, M. Yamashita, E. Ito, N. Meng, Hydrogen production from 2-propanol as a key reaction for a chemical heat pump with reaction couple of 2-propanol dehydrogenation/acetone hydrogenation, Int. J. Hydrogen Energy. 19 (1994) 223–226.

[255] N. Meng, S. Shinoda, Y. Saito, Improvements on thermal efficiency of chemical heat pump involving the reaction couple of 2-propanol dehydrogenation and acetone hydrogenation, Int. J. Hydrogen Energy. 22 (1997) 361–367.

[256] R. Hu, Baratunde A Cola, N. Haram, J.N. Barisci, S. Lee, S. Stoughton, G. Wallace, C. Too, M. Thomas, A. Gestos, M.E. Dela Cruz, J.P. Ferraris, A. a. Zakhidov, R.H. Baughman, Harvesting waste thermal energy using a carbon-nanotube-based thermo-electrochemical cell, Nano Lett. 10 (2010) 838–846. doi:10.1021/nl903267n.

[257] F. Cataldo, Synthesis of ketonic resins from self-polymerization of acetone, 1. Action of protic and lewis acids on acetone, Die Angew. Makromol. Chemie. 236 (1996) 1–19. doi:10.1002/apmc.1996.052360101.

[258] M.J. Gonzalez, C.T. Hable, M.S. Wrighton, Electrocatalytic Oxidation of Small Carbohydrate Fuels at Pt-Sn Modified Electrodes, J. Phys. Chem. B. 102 (1998) 9881–9890. doi:10.1021/jp982792d.

[259] W.J. Zhou, S.Q. Song, W.Z. Li, Z.H. Zhou, G.Q. Sun, Q. Xin, S. Douvartzides, P. Tsiakaras, Direct ethanol fuel cells based on PtSn anodes: The effect of Sn content on the fuel cell performance, J. Power Sources. 140 (2005) 50–58. doi:10.1016/j.jpowsour.2004.08.003.

[260] E. Antolini, Catalysts for direct ethanol fuel cells, J. Power Sources. 170 (2007) 1–12. doi:10.1016/j.jpowsour.2007.04.009.

[261] M. Zhu, G. Sun, Q. Xin, Effect of alloying degree in PtSn catalyst on the catalytic behavior for ethanol electro-oxidation, Electrochim. Acta. 54 (2009) 1511–1518. doi:10.1016/j.electacta.2008.09.035.

[262] V.K. Puthiyapura, D.J.L. Brett, A.E. Russell, W.F. Lin, C. Hardacre, Biobutanol as Fuel for Direct Alcohol Fuel Cells-Investigation of Sn-Modified Pt Catalyst for Butanol Electro-oxidation, ACS Appl. Mater. Interfaces. 8 (2016) 12859–12870. doi:10.1021/acsami.6b02863.

[263] Z.D. Wei, L.L. Li, Y.H. Luo, C. Yan, C.X. Sun, G.Z. Yin, P.K. Shen, Electrooxidation of methanol on upd-Ru and upd-Sn modified Pt electrodes, J. Phys. Chem. B. 110 (2006) 26055–26061. doi:10.1021/jp0651891.

[264] T. Huang, S. Mao, G. Zhou, Z. Zhang, Z. Wen, X. Huang, S. Ci, J. Chen, A high-performance catalyst support for methanol oxidation with graphene and vanadium carbonitride, Nanoscale. 7 (2015) 1301–1307. doi:10.1039/C4NR05244G.

[265] S.X. Duan, J.T. Jayne, P. Davidovits, D.R. Worsnop, M.S. Zahniser, C.E. Kolb, Uptake of gas-phase acetone by water surfaces, J. Phys. Chem. 97 (1993) 2284–2288. doi:10.1021/j100192a049.

[266] R. Sander, Compilation of Henry's law constants (version 4.0) for water as solvent, Atmos. Chem. Phys. 15 (2015) 4399–4981. doi:10.5194/acp-15-4399-2015.

[267] B. Huskinson, M.P. Marshak, C. Suh, S. Er, M.R. Gerhardt, C.J. Galvin, X. Chen, A. Aspuru-Guzik, R.G. Gordon, M.J. Aziz, A metal-free organic-inorganic aqueous flow battery., Nature. 505 (2014) 195–198. doi:10.1038/nature12909.

[268] K. Lin, Q. Chen, M.R. Gerhardt, L. Tong, S.B. Kim, L. Eisenach, A.W. Valle, D. Hardee, R.G. Gordon, M.J. Aziz, M.P. Marshak, Alkaline quinone flow battery, Science (80-.). 349 (2015) 1529–1532. doi:10.1126/science.aab3033.

[269] Y. Mua, T.I. Quickenden, Power Conversion Efficiency, Electrode Separation, and Overpotential in the Ferricyanide/Ferrocyanide Thermogalvanic Cell, J. Electrochem. Soc. 143 (1996) 2558–2564. doi:10.1149/1.1837047.

[270] J.K. Platten, The Soret Effect: A Review of Recent Experimental Results, J. Appl. Mech. 73 (2006) 5. doi:10.1115/1.1992517.

[271] K. Noda, M. Ohashi, K. Ishida, Viscosities and Densities at 298.15 K for Mixtures of Methanol, Acetone, and Water, J. Chem. Eng. Data. 27 (1982) 326–328. doi:10.1021/je00029a028.

[272] A. Perera, F. Sokolić, Modeling nonionic aqueous solutions: The acetone-water mixture, J. Chem. Phys. 121 (2004) 11272–11282. doi:10.1063/1.1817970.

[273] A. Abbasi, M.Z. Saghir, M. Kawaji, A new approach to evaluate the thermodiffusion factor for associating mixtures, J. Chem. Phys. 130 (2009) 064506. doi:10.1063/1.3076926.

[274] P. Wang, A. Anderko, R.D. Young, Modeling viscosity of concentrated and mixed-solvent electrolyte systems, Ind. Eng. Chem. Res. 47 (2008) 5698–5709. doi:10.1016/j.fluid.2004.09.008.